ANA RITA ALVES DOS SANTOS RODRIGUES

METHODS FOR FACILITATING NONINVASIVE AMBULATORY MONITORING OF BLOOD ELECTROLYTE LEVELS

DOCTORAL DISSERTATION

Kaunas
2023

KAUNAS UNIVERSITY OF TECHNOLOGY

ANA RITA ALVES DOS SANTOS RODRIGUES

METHODS FOR FACILITATING NONINVASIVE AMBULATORY MONITORING OF BLOOD ELECTROLYTE LEVELS

Doctoral dissertation
Technological Sciences, Electrical and Electronic Engineering (T 001)

Kaunas, 2023

This doctoral dissertation was prepared at Kaunas University of Technology, Biomedical Engineering Institute during the period of 2017–2023. The studies were supported by the Research Council of Lithuania (LMT).

Scientific Supervisor:
Prof. Dr. Vaidotas MAROZAS (Kaunas University of Technology, Technological Sciences, Electrical and Electronic Engineering, T 001).

Edited by: English language editor dr. Armandas Rumšas (Publishing House *Technologija*), Lithuanian language editor Aurelija Gražina Rukšaitė (Publishing House *Technologija*).

The official defense of the dissertation will be held at 10 a.m. on 27 September 2023 at the public meeting of the Dissertation Defense Board of the Electrical and Electronic Engineering Science Field in Rectorate Hall at Kaunas University of Technology.

Address: K. Donelaičio 73-402, Kaunas, LT-44249, Lithuania.
Phone: (+370) 608 28 527; e-mail: doktorantura@ktu.lt.

Doctoral dissertation was sent on 27 August 2023.
The doctoral dissertation is available on the internet http://ktu.edu and at the library of Kaunas University of Technology (Donelaičio 20, Kaunas, LT-44239, Lithuania).

KAUNO TECHNOLOGIJOS UNIVERSITETAS

ANA RITA ALVES DOS SANTOS RODRIGUES

NEINVAZINIAI KRAUJO ELEKTROLITŲ LYGIO AMBULATORINĖS STEBĖSENOS METODAI

Daktaro disertacija
Technologijos mokslai, elektros ir elektronikos inžinerija (T 001)

2023, Kaunas

Disertacija rengta 2017–2023 metais Kauno technologijos universiteto Biomedicininės inžinerijos institute. Mokslinius tyrimus rėmė Lietuvos mokslo taryba.

Mokslinis vadovas:
prof. dr. Vaidotas MAROZAS (Kauno technologijos universitetas, technologijos mokslai, elektros ir elektronikos inžinerija, T 001).

Redagavo: anglų kalbos redaktorius dr. Armandas Rumšas (leidykla „Technologija“), lietuvių kalbos redaktorė Aurelija Gražina Rukšaitė (leidykla „Technologija“).

Elektros ir elektronikos inžinerija mokslo krypties disertacijos gynimo taryba:
prof. dr. Arminas RAGAUSKAS (Kauno technologijos universitetas, technologijos mokslai, elektros ir elektronikos inžinerija, T 001) – **pirmininkas**;
doc. dr. Esther PUEYO (Saragosos universitetas, Ispanija, technologijos mokslai, elektros ir elektronikos inžinerija, T 001);
prof. dr. Rūta VAIČIŪNIENĖ (Lietuvos sveikatos mokslų universitetas, medicinos ir sveikatos mokslai, medicina, M 001);
prof. dr. Algimantas VALINEVIČIUS (Kauno technologijos universitetas, technologijos mokslai, elektros ir elektronikos inžinerija, T 001);
prof. dr. Darius VIRŽONIS (Kauno technologijos universitetas, technologijos mokslai, elektros ir elektronikos inžinerija, T 001).

Disertacija bus ginama viešame elektros ir elektronikos inžinerijos mokslo krypties disertacijos gynimo tarybos posėdyje 2023 m. rugsėjo 27 d. 10 val. Kauno technologijos universiteto Rektorato salėje.

Adresas: K. Donelaičio g. 73-402, Kaunas, LT-44249, Lietuva.
Tel. (+370) 608 28 527; el. paštas doktorantura@ktu.lt.

Disertacija išsiųsta 2023 m. rugpjūčio 27 d.
Su disertacija galima susipažinti interneto svetainėje http://ktu.edu ir Kauno technologijos universiteto bibliotekoje (K. Donelaičio g. 20, Kaunas LT-44239).

> *It seems that for success in science or art, a dash of autism is essential.*
>
> **— Hans Asperger**
>
> (Inhumane psychiatrist, accurate observation)

Contents

List of terms and abbreviations

1D	One dimensional
3D	Three dimensional
ACE	Angiotensin-converting enzyme
ADH	Antidiuretic hormone
AF	Atrial fibrillation
α	Spatial QRS-T angle
ANP	Atrial natriuretic peptide
AP	Action potential
APB	Atrial premature beat
AV	Atrioventricular node
BNP	B-type natriuretic peptide
BP	Blood pressure
Ca^{2+}	Calcium
CD	Conduction disturbance
CKD	Chronic kidney disease
CNN	Convolutional neural network
CVD	Cardiovascular disease
CVI	Clustering validation indices
δ	Surrogate parameter for T-wave elongation
ECF	Extracellular fluid
ECG	Electrocardiogram
ϵ	Absolute estimation error
ESRD	End-stage renal disease
FIR	Finite impulse response
FM	Fowlkes-Mallows index
FN	False negative
FP	False positive
GFR	Glomerular filtration rate
GI	Gastrointestinal
HCO_3^+	Bicarbonate
HD	Hemodialysis
HF	Heart failure
HR	Heart rate
HYP	Hypertrophy
ICF	Intracellular fluid
ICU	Intensive care unit
iqr	Interquartile range
K^+	Potassium

$\mathcal{K}_m$	Maximum number of clusters
Leaky ReLU	Leaky Rectified Linear Unit
LVH	Left ventricular hypertrophy
MCC	Matthews Correlation Coefficient
Mg^{2+}	Magnesium
MI	Myocardial infarction
Na^{+}	Sodium
NORM	Normal (healthy)
PAA	Piecewise Aggregate Approximation
PTH	Parathyroid hormone
θ	Surrogate parameter for T-wave peakedness
θ_δ	Descriptor of T-wave morphology
RAAS	Renin-angiotensin-aldosterone system
RMSE	Root-mean-squared-error
$\mathcal{V}_m$	Membrane potential
$\mathcal{V}_{rest}$	Resting membrane potential
SA	Sinoatrial node
SAX	Symbolic Aggregation approXimation
SCD	Sudden cardiac death
STTC	ST-T changes
$T_c(n)$	Composite T-wave
$T_d(n)$	Downward slope of the T-wave
$T_u(n)$	Upward slope of the T-wave
$T(n)$	T-wave
TCRT	Total cosine R-to-T
TN	True negative
TP	True positive
VCG	Vectorcardiography

INTRODUCTION

Research contextualization

Electrolytes are electrically charged minerals dissolved in the blood and body fluids essential for maintaining homeostasis [1]. Electrolytes participate in various physiological processes, including action potential generation for proper nerve conduction and cardiac muscle contraction [2]. Like many other vital variables in the human biological system, blood electrolyte levels must be tightly regulated within pre-defined limits to allow cells to function normally [2]. When electrolyte levels deviate from their optimal range, neurological and cardiovascular functions can become severely compromised, resulting in disruptions of homeostasis with possible lifelong—or fatal—consequences [1, 2].

Electrolyte imbalance, or dyselectrolytemia, occurs when the level of an electrolyte in the blood falls outside its homeostatic range and is associated with increased all-cause mortality among various populations [3–6]. One of the most worrisome consequences of electrolyte imbalance, particularly that of potassium [7], is arrhythmias with the potential to instigate sudden cardiac death (SCD) [8, 9]. Unfortunately, such dangerous arrhythmias usually emerge without any apparent signs of electrolyte imbalance that could warn patients to seek preemptive medical treatment [10]. The symptomatology of early (and mild) dyselectrolytemia is broad and often nonspecific, varying from symptomless to general fatigue and malaise to ordinary digestive issues [11]. Thus, without a blood test, mild dyselectrolytemia is virtually undetectable. By the time patients manifest more prominent clinical signs, blood electrolytes have already reached life-threatening levels, and emergency care is required.

Since the kidneys are the primary regulators of the homeostatic blood electrolyte profile [2], patients with renal dysfunction are the most susceptible to dyselectrolytemia. Kidney damage, as seen in chronic kidney disease (CKD), evidently hampers renal function, making CKD patients particularly vulnerable to SCD-triggering electrolyte derangements [6, 12]. About 39.5% to 74.2% of CKD patients display at least one dyselectrolytemia [13], although the incidence rate varies for each specific electrolyte and CKD stage [12]. The degree of renal damage further aggravates the susceptibility to electrolyte imbalance, with end-stage renal disease (ESRD) patients requiring hemodialysis (HD) every two-to-three days to rectify their electrolyte levels to survive [2].

Therapeutical drugs are, however, the most recurrent cause of dyselectrolytemia in everyday clinical practice [14, 15]. Many conventional therapies for treating various chronic diseases induce renal dysfunction even if the kidney tissue is healthy [16]. One notable example is antihypertensive agents and other prescribed drugs for CVD, such as diuretics and β-blockers. Around 10% of patients manifest one dyselectrolytemia

episode within a year after initiating hypertension treatment [14], and 26.8% develop sodium imbalance recurrently [17]. Mild potassium derangements are present in 19% [18]—and even 80% [14]—of patients receiving diuretics, depending on the prescribed diuretic class. Similar therapies are also reckoned to promote dyselectrolytemia in 20% to 48% of patients during hospitalization, despite only 3% to 8% of them displaying abnormal levels at admission [19, 20].

Even though sporadic episodes of mild dyselectrolytemia do not typically pose an imminent threat to the patient, recent studies speculate that recurrent episodes can have long-lasting health ramifications [5]. Chronic mild dyselectrolytemia predisposes hypertensive patients to syncope and falls [5], whereas hospitalized patients discharged with uncorrected mild electrolyte imbalance have higher rehospitalization and 60-day [21], 90-day [22], and one-year [23] mortality rates. Albeit not yet proven, these recurrent mild dyselectrolytemia episodes may be involved in the genesis of *cardiorenal syndrome* (CRS), which, as suggested by its name, is characterized by a deterioration of the cardiac and renal functions. This syndrome worsens long-term health, not only because it accelerates the clinical progression of the pre-existent chronic disease, but also because it predisposes patients to develop CVD, CKD, and even ESRD [24]. Furthermore, mild dyselectrolytemia can amplify the odds of a fatal outcome in more advanced stages of chronic disease, especially if coupled with comorbid CVD [21]. Prompt correction of abnormal electrolyte levels is hence paramount for averting unfavorable outcomes.

While some clinicians deem such mild episodes harmless—and often overlook them unless they develop into severe ones—many other clinicians end up underprescribing or underdosing indispensable drugs out of fear of adverse events [25]. However, in the long run, underdosing becomes a double-edged sword strategy that further complicates chronic disease management. Without an appropriate drug regimen, the body cannot maintain homeostasis and activates maladaptive compensatory mechanisms that ultimately damage multiple organs [2, 26], inducing CRS and a declining health status [1].

Research relevance

Many people worldwide are at risk of electrolyte imbalance since CKD, hypertension, and CVD are global epidemics. CKD affects >10% of the world population [27], while hypertension is present in nearly 32% of women and 34% of men [28] and in about 60% of people older than 60 [17]. Almost half of the people with hypertension are on antihypertensive therapy [28]. Roughly 8.8% of the global population suffers from diabetes [29], and 70% to 80% exhibit comorbid hypertension alongside diabetes [30]. CVD is found in 5.5% [31] to 21.3% [32] of adults in the US and UK and already accounts for 32% of deaths globally [33], while CKD kills an estimated

5–10 million people annually [34]. The incidence of these chronic diseases—and, consequently, the occurrence of dangerous dyselectrolytemia—is forecasted to rise further by 2030 due to the aging population [27, 34].

On top of the heightened risk of all-cause mortality, electrolyte imbalance is economically burdensome [35]. The treatment of dyselectrolytemia inflates the already substantial healthcare costs of CKD and CVD, particularly the severe episodes that require hospitalization [36]. In CKD patients, each severe dyselectrolytemia episode costs up to $31,212 in the US, whereas only $1,782 suffices to treat a mild one [35]. Hospitalization for dyselectrolytemia is estimated to have an additional healthcare cost burden of 7% to 39% on average [37], with the US reporting to have spent $1.6–3.6 billion in 2009 to treat sodium imbalance alone [38].

Regular monitoring of blood electrolyte levels could avert unfavorable health outcomes in the short and long term. In addition to enabling a prompt correction of electrolyte derangements before the onset of SCD-triggering arrhythmias [39], regular monitoring could facilitate drug titration, helping clinicians to continually adjust the dosage of life-saving medications for the maximum benefits without adverse effects [25]. In those at risk of drug-induced dyselectrolytemia, regular monitoring could delay—or even prevent—the development of CRS and the disease progression, thus promoting general long-term health. Furthermore, regular blood electrolyte monitoring could also decrease the economic burden of chronic diseases. For instance, the timely detection of mild dyselectrolytemia may help avoid at least 22% of hospitalizations of elderly patients [40], while halting the progression of CKD to ESRD could reduce the CKD cost by six times [41]. The average annual cost of ESRD is $100,593 per patient, whereas $16,112 suffices to treat CKD in the USA [41].

Despite being potentially life-saving and advisable in vulnerable patients, regular monitoring is poorly implemented in clinical practice, primarily due to the lack of practical methods to assess blood electrolyte levels. Blood tests are the only clinically valid method for capturing electrolyte imbalance, but blood testing can be expensive and logistically burdensome for healthcare facilities to perform regularly. Moreover, blood tests are infeasible outside clinical settings, thus precluding ambulatory blood electrolyte monitoring. Inexpensive—and ideally noninvasive—technologies to assess blood electrolyte levels could facilitate regular monitoring in both in- and outpatients and would, therefore, be of clinical significance [25, 39].

The scientific-technological problem

Non-homeostatic blood electrolyte levels disrupt the action potential of heart cells [7], leading to ventricular repolarization disturbances that can be reflected in the electrocardiogram (ECG) [42]. For instance, an altered T-wave morphology is a well-known manifestation of potassium-induced repolarization disturbances [42]. Thus, ECG

ventricular repolarization markers may be surrogates for blood electrolytes.

In recent years, novel T-wave morphology parameters were devised to quantify blood potassium levels [43–45]. Albeit with promising results, the performance of such parameters was investigated exclusively in ESRD patients during HD sessions, where electrolyte levels fluctuate much more rapidly than in everyday ambulatory settings. While rapid electrolyte fluctuations are known to induce perceptible T-wave morphology changes [46,47], whether an ECG can capture the gradual electrolyte fluctuations expected in an everyday scenario remains unexplored.

Alongside the T-wave morphology, various other ECG features, such as the spatial QRS-T angle, have been extensively studied as ventricular repolarization markers [48–50]. Although their relationship with blood electrolytes is yet unclear, some of these markers are strong indicators of cellular electrical activity [48], thus spurring scientific interest as prospective solutions for noninvasive blood electrolyte monitoring. However, nearly all existing T-wave-based parameters [43, 45, 51–56] and other ventricular repolarization markers [48, 57] are estimated exclusively from 12-lead or precordial-lead ECG systems, thereby sharing the same *core technological problem*—they are impractical for ambulatory applications. Therefore, methods to estimate ventricular repolarization markers from a set of reduced-lead ECGs are necessary. Such methods could be deployed in consumer healthcare devices and facilitate noninvasive monitoring of blood electrolyte levels.

Research problem: The lack of practical methods to estimate ventricular repolarization markers in ambulatory settings encumbers the scientific-technological advancement of solutions for noninvasive blood electrolyte monitoring. It hinders the: *(i)* performance investigation of currently available solutions in everyday ambulatory scenarios, and *(ii)* development of other potential solutions that could harness the value of some well-known ventricular repolarization markers, such as the spatial QRS-T angle.

Research questions

The lack of adequate technological solutions for ambulatory settings challenges the feasibility of noninvasive blood electrolyte monitoring in everyday scenarios, thereby raising the following central questions:

1. Can reduced-lead ECGs capture gradual blood electrolyte fluctuations in ambulatory settings?

2. What possible confounding factors can affect the performance of potential ECG-derived markers of blood electrolyte levels in ambulatory settings?

3. Can well-established ventricular repolarization markers such as the spatial QRS-T angle be derived from reduced-lead ECGs with sufficient accuracy to be prospective solutions for ambulatory noninvasive blood electrolyte monitoring?

4. How can the efficiency of heartbeat annotation algorithms be improved so that cardiovascular research of noninvasive blood electrolyte markers in long-term ECGs can be expedited?

Working hypothesis

Ventricular repolarization markers can be estimated from reduced-lead ECGs using model-based parametrization and machine-learning approaches with sufficient accuracy to be potential surrogates for blood electrolytes in ambulatory monitoring applications.

Research aim

This doctoral dissertation aims to research and develop methods for facilitating noninvasive ambulatory monitoring of blood electrolyte levels.

Research object

The research focuses on developing signal-processing algorithms for capturing ventricular repolarization changes from reduced-lead ECGs.

Research objectives

1. To analyze the significance of electrolyte balance in health and discuss the clinical value of regular blood electrolyte monitoring for long-term general health.

2. To propose T-wave morphology descriptors that can be estimated from single-lead ECGs to be suitable for ambulatory monitoring. Such descriptors are necessary to explore the feasibility of capturing gradual potassium-induced repolarization disturbances in out-of-hospital settings and thus identify possible confounding factors that can affect noninvasive blood electrolyte monitoring.

3. To engineer algorithms for deriving well-established ventricular repolarization markers such as the spatial QRS-T angle from reduced-lead ECGs. Such methods can enable harnessing the clinical value of these markers to propel research and development of new technological solutions for the noninvasive monitoring of blood electrolyte levels.

4. To develop methods for accelerating the analysis and annotation of heartbeats in long-term ECG recordings. Such methods would expedite the scientific investigation of new ECG markers of blood electrolyte levels.

Scientific novelty

This doctoral dissertation presents a comprehensive overview of the clinical consequences of electrolyte imbalance in long-term health by addressing the impact of

recurrent episodes of mild dyselectrolytemia on the cardiac and renal functions and homeostasis. In contrast to previous research, this dissertation contextualizes the importance of regular blood electrolyte monitoring beyond the need to capture electrolyte derangements solely for SCD prevention. This dissertation argues that it is plausible that recurrent mild dyselectrolytemia episodes can have long-lasting health ramifications while further cementing the need to expand the scientific-technological research and development of methods for facilitating noninvasive ambulatory monitoring of blood electrolyte levels.

The first method uses a model-based-parameterization approach to derive a T-wave morphology descriptor from single-lead ECGs. Unlike the other proposed T-wave-based parameters, the developed descriptor accounts for the global T-wave morphology instead of only local T-wave features. In addition, the descriptor is more robust to noise, which is propitious for ambulatory ECG recordings.

The second method uses a deep-learning-based approach to estimate the spatial QRS-T angle from sets of reduced-lead ECGs. Since the QRS-T angle reflects the angle between the QRS and T vectors in the three-dimensional (3D) space, the model was designed to return the coordinates of each vector as output. An original composite loss function that combines the QRS-T angle and the Euclidean distance is proposed to guide the model throughout the 3D space. Besides proposing the first method for estimating the spatial QRS-T angle from reduced-lead ECGs, this dissertation also explores the conceivability of measuring the angle from solely frontal-lead ECGs.

This doctoral dissertation also presents the first study exploring the feasibility of capturing gradual blood potassium fluctuations in ambulatory settings from single-lead ECGs. No other study had previously investigated the feasibility of noninvasive monitoring of electrolyte levels outside HD sessions. Two T-wave morphology descriptors were employed to quantify potassium-induced ventricular repolarization changes: the proposed model-based descriptor and the only currently available single-lead-derived descriptor sensitive to blood potassium levels in HD sessions. The presented study identifies what possible confounding factors can affect the performance of potential ECG-derived markers of blood potassium levels, thus unraveling the challenges of noninvasive monitoring of blood electrolytes. Since the scientific research of noninvasive blood electrolyte monitoring is still in its infancy, such feasibility studies provide valuable insights for future research and are thus essential to deepen scientific knowledge and impel further development of the research field.

Lastly, an unsupervised symbolic clustering algorithm for faster semiautomatic heartbeat annotation in long-term ECGs is presented. The algorithm compresses heartbeats into short strings by using a classic discretization technique employed in many time-series data mining problems. Beats represented by equal strings are grouped into the same pre-clusters to reduce the computational demands. Instead of every individ-

ual heartbeat, the human expert is presented with the hierarchical clustering results of the generated pre-clusters for manual investigation and annotation. By clustering heartbeats in an unsupervised fashion, the algorithm allows researchers to discover unexpected morphological ECG changes that can be related to blood electrolyte fluctuations.

Practical significance

1. Methods enabling an accurate assessment of the electrolyte profile in ambulatory settings can:

   (a) Allow a timely detection of severe dyselectrolytemia before the onset of SCD-triggering arrhythmias.

   (b) Aid in drug titration and personalization for patients at risk of drug-induced dyselectrolytemia.

   (c) Clarify the causal relationship between electrolyte fluctuations and arrhythmia occurrence and progression.

   (d) Provide insights into the interrelationship of the cardio-renal function, homeostasis, blood electrolytes, and their long-term health ramifications.

2. The engineered algorithms and methods presented in this doctoral dissertation can be used in the following applications:

   (a) The proposed T-wave morphology descriptor can facilitate the development of technological solutions to quantify blood potassium levels in ambulatory settings.

   (b) Since single-lead ECGs suffice to derive the proposed T-wave morphology descriptor, comfortable consumer healthcare devices can be used to collect long-term data instead of Holter devices. Databases of long-term ECGs and synchronous blood samples are still largely unavailable and are pivotal for the research field of noninvasive monitoring of blood electrolyte fluctuations.

   (c) The relationship between the spatial QRS-T angle and blood electrolyte levels can be explored since the proposed deep-learning-based approach estimates the angle from sets of reduced-lead ECGs. The spatial QRS-T angle could be a potential solution for noninvasive blood electrolyte monitoring.

   (d) Estimating the spatial QRS-T angle from reduced-lead ECGs opens up the possibility of harnessing its well-known diagnostic value for SCD risk stratification and early detection of dangerous cardiac events in vulnerable populations, such as CKD and CVD patients.

(e) Similar architectures to the proposed deep-learning model could be developed to derive other 3D-based repolarization markers, such as the ventricular gradient.

(f) The symbolic clustering algorithm may enable researchers to annotate long-term data much faster. Large annotated databases can improve the development of machine-learning models for interpreting ECG signals.

(g) The symbolic clustering algorithm can help researchers discover unexpected morphological ECG changes related to blood electrolyte fluctuations.

3. The feasibility study results provide valuable insights to improve future research on noninvasive monitoring of blood electrolyte levels, namely of what confounding factors that can affect the performance of potential ECG-derived markers of blood electrolytes.

4. The algorithms described in this thesis have been devised in the framework of the project *Personalized wearable technologies for evaluating life-threatening health conditions in chronic kidney disease patients—KidneyLife* funded by the European Regional Development Fund with the Research Council of Lithuania (LMTLT) under Project No. 01.2.2-LMT-K-718-01-0030 from 2018–2022.

Approval of results

The doctoral thesis relies on two primary papers published in international scientific journals with an impact factor listed in the *Clarivate Analytics Web of Science* database. The key results have been presented at four international conferences recognized worldwide: the 2017 IEEE Biomedical Circuits and Systems Conference (*BioCAS*), the 45^{th} and 48^{th} Computing in Cardiology (*CinC*) conferences, and the 15^{th} International Conference on Bio-inspired Systems and Signal Processing, Biosignals (*BIOSTEC 2022*).

The research has been commended both internationally and in Lithuania. In 2018, Kaunas University of Technology awarded the author of the research as one of the most active Ph.D. students in Electrical and Electronics Engineering. At the 45^{th} Computing in Cardiology conference, the research received the *Gary and Bill Sanders Poster Award*. In 2021, the research received a promotion scholarship for academic research granted by the Research Council of Lithuania.

Statements prepared for defense

1. The clinical consequences of electrolyte imbalance stretch beyond dangerous arrhythmias. In patients with chronic diseases, even mild and recurring episodes of dyselectrolytemia can initiate a cascade of maladaptive compensatory mechanisms, resulting in the deterioration of cardiac and renal functions. This deterioration can

ultimately threaten long-term health and hasten the progression of the disease. Therefore, regular monitoring of blood electrolyte levels is essential not only for preventing sudden cardiac death in the short term, but also for maintaining homeostasis and promoting overall health in the long term.

2. T-wave morphology descriptors can capture ventricular repolarization disturbances induced by gradual blood potassium fluctuations in ambulatory single-lead ECGs. However, ambulatory recordings are vulnerable to noise, thus warranting model-based parameterization to generate ECG descriptors. Nonetheless, concurrent electrolyte imbalances and alternating T-wave morphologies are confounding factors that can influence the effectiveness of potential ECG-derived markers of blood potassium.

3. Leveraging deep learning makes it possible to estimate the spatial QRS-T angle with sufficient accuracy from a set of reduced-lead ECGs. Adopting metrics that guide the model through the 3D space improves the model's performance, enabling the estimation of spatial ventricular repolarization markers even when the input ECG leads provide limited spatial information. This approach offers a promising solution for ambulatory QRS-T angle monitoring.

4. Symbolic clustering algorithms can enhance the efficiency of annotating and analyzing heartbeats in long-term ECGs. These algorithms significantly reduce the computational demands of various machine-learning clustering techniques. In addition, symbolic clustering allows researchers to explore how heartbeats naturally fall into different classes and even identify unexpected sub-classes for further study.

Structure of the doctoral dissertation

The doctoral dissertation is organized as follows. Chapter 1 provides a clinical background in electrolyte physiology and its significance for homeostasis. The Chapter introduces the physiological role of electrolytes in the body, their primary regulatory mechanisms, and the etiology and epidemiology of electrolyte imbalance. Chapter 1 contextualizes the short- and long-term health ramifications of electrolyte imbalance.

Chapter 2 is devoted to analyzing the state-of-the-art scientific literature and available technological solutions for the noninvasive assessment of blood electrolyte levels. This Chapter also showcases the theoretical framework upon which the currently available solutions and the ones proposed in this doctoral dissertation are built.

Chapters 3–5 describe the engineered algorithms and methods for facilitating noninvasive ambulatory monitoring of blood electrolyte levels. Chapter 3 explores the feasibility of capturing gradual potassium fluctuations by quantifying T-wave morphology changes in single-lead ECGs via model-based parameterization. Chapter 4 introduces a deep-learning-based approach to estimating the spatial QRS-T from reduced-lead ECGs. Chapter 5 presents a symbolic clustering algorithm for faster heartbeat annotation and analysis in long-term ECGs. Performance evaluation, results, and dis-

cussion of each of the three methods are presented in their respective Chapter.

The doctoral dissertation finishes with the general conclusions in Chapter 6.

Parts of Chapters 3–5 have been quoted verbatim from the previously published articles: [58–61].

The dissertation consists of 194 pages, 48 figures, and eight tables. It presents 221 references.

1. CLINICAL BACKGROUND IN ELECTROLYTE PHYSIOLOGY AND HOMEOSTASIS

1.1. Electrolytes and Homeostasis: The Importance for Life and Health

Homeostasis is the term coined to describe the body's ability to preserve a nearly constant internal environment in response to the changing external conditions, including in settings of injury or disease [1,2]. All cells, tissues, and organs work systematically to maintain homeostasis and sustain life. For example, the lungs provide oxygen to replenish cells, the kidneys eliminate toxic substances, and the gastrointestinal (GI) system supplies nutrients for energy production. Optimal organ functioning hinges on many variables that must be kept within pre-defined limits to be compatible with life. Body temperature, arterial blood pressure, oxygen, fluid and electrolyte levels, and blood pH are some of the variables essential for the survival of the human biological system. Robust homeostatic mechanisms tightly regulate these variables to permit the cells to perform their normal functions and uphold life [2].

Many problems encountered in clinical practice emerge from impaired homeostatic mechanisms that can no longer maintain biological variables within their optimal range [1]. When one or more functional systems lose their ability to contribute their share to homeostasis, all cells in the body become endangered—extreme dysfunction will lead to death, while moderate dysfunction leads to disease [2]. The state of *disease* is hence considered one of *disrupted homeostasis*.

While any disruption of the homeostatic state adversely impacts health, the body continues to operate on multiple compensations to support vital functions even in disease [2]. Albeit restorative of balance, these compensations are only life-sustaining in the short term. When activated for prolonged periods, such compensatory mechanisms become maladaptive, ultimately damaging multiple organs in an attempt to restore homeostasis [26]. Recurrent disruptions of homeostasis not only induce chronic disease but also exacerbate it, thus limiting the quality—and expectancy—of life [1,2].

One of the many crucial variables for maintaining homeostasis is electrolytes [2]. Abnormal electrolyte levels jeopardize proper cell functioning, including that of the heart, and endanger life [7]. While physicians acknowledge the timely detection of electrolyte derangements as pivotal to avert unfavorable outcomes, mild electrolyte imbalance episodes are often overlooked if they do not pose an imminent threat to patients. Such mild episodes usually precede the severe ones and can be early manifestations of disrupted homeostasis, thus suggestive of worsening health status. Regular blood electrolyte monitoring could enable prompt administration of life-saving procedures to restore homeostasis [25].

This Chapter introduces the physiological fundamentals of homeostasis, the importance of electrolytes in the body, and their regulatory mechanisms. The Chapter analyzes the significance of electrolyte balance in health to contextualize the impor-

tance of regularly monitoring blood electrolyte levels for short- and long-term health in those populations most susceptible to electrolyte imbalance.

1.1.1. Composition of the internal environment

About 50% to 70% of the adult human body is fluid, mainly a water solution of ions (i.e., electrolytes) and other substances [2]. The total body fluid is distributed between two compartments: almost two-thirds is *intracellular* (inside the cell), and the remaining is *extracellular* (outside the cell). Blood plasma comprises most of the body's extracellular fluid, constantly moving throughout the body to bathe cells with ions and nutrients needed for survival. Cells can live and function as long as the extracellular fluid embodies the proper concentration of oxygen, electrolytes, pH, and other constituents. Organs and tissues, therefore, collaborate to maintain homeostasis in the extracellular fluid—the body's *internal environment* [1, 2].

Ionic profiles of the intra- and extracellular fluids

The intra- and extracellular fluids differ in ionic composition [2], as illustrated in Fig. 1.1. The two fluid compartments are kept separate by cell membranes, which help maintain the ionic profile of each fluid by regulating ion transport across them. Large amounts of sodium, calcium, chloride, and bicarbonate ions, plus nutrients, are available in the extracellular fluid (ECF). In contrast, the intracellular fluid (ICF) is abundant in potassium, magnesium, phosphate, and large anionic proteins. Optimal cell function crucially depends on the two fluids having these ionic profile differences [62], as will be covered in Sec. 2.1.

Constituents of the extracellular fluid in homeostasis

Ions and other ECF constituents are regulated within a pre-defined range of values., i.e., their homeostatic range, rather than fixed values [2]. For some substances, this range is markedly minuscule. Table 1.1 lists the optimal range and maximum non-

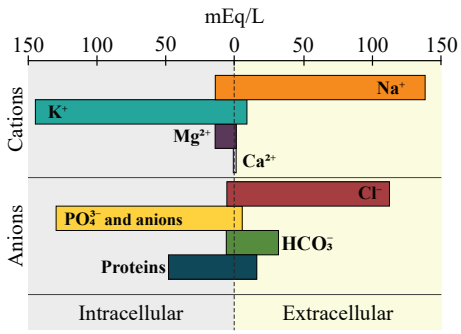

Fig. 1.1. Major cations and anions of the intracellular and extracellular fluids. Adapted from [2].

Table 1.1. Constituents of the extracellular fluid. Adapted from [2].

Constituent	Normal value	Normal range	Nonlethal limits	Unit
Oxygen[1] (O_2)	40	25–40	10–1000	mmHg
Carbon dioxide[1] (CO_2)	45	41–51	5–80	mmHg
Sodium	142	135–145	115–175	mmol L^{-1}
Potassium	4.2	3.5–5.4	1.5–9.0	mmol L^{-1}
Calcium[2]	1.2	1.0–1.4	0.5–2.0	mmol L^{-1}
Chloride	106	98–108	70–130	mmol L^{-1}
Bicarbonate	24	22–29	8–45	mmol L^{-1}
Acid-base[1] (pH)	7.4	7.3–7.5	6.9–8.0	–
Glucose	90	70–115	20–1500	mg dL

[1] In the venous blood;
[2] Ionized calcium.

lethal limits of some of the ECF constituents. Since the blood plasma contains most of these substances, the terms 'extracellular' and 'blood' will be used interchangeably from this point onwards.

Homeostatic control systems and feedback mechanisms

Various homeostatic control systems carefully regulate the composition of the internal environment [1, 2]. Control systems consist of four components: a *stimulus*, a *sensory receptor*, a *control center*, and an *effector*. The *sensory receptor* is a cell, tissue, or organ that senses a change in a physiological variable, i.e., the *stimulus*. Whenever a pertinent change in the stimulus is detected, the receptor conveys a nerve impulse response to the *control center* which processes the information and signals the *effector* to produce a response that will revert the physiological variable to its optimal range. Homeostatic mechanisms respond to a perturbation with a looping mechanism (*feedback mechanism*), either positive or negative. *Positive feedback* accelerates the effect of the stimulus (e.g., labor contractions), whereas *negative feedback* inhibits the source of the stimulus or lessens the metabolic process (e.g., thermoregulation). Most homeostatic control systems rely on negative feedback processes to reverse a change in a physiological condition [2].

1.1.2. The physiological role of electrolytes in the body

Electrolytes are electrically charged minerals (i.e., ions) dissolved in the blood and body fluids. Living systems assimilate many electrolytes, such as zinc and iron. However, some of the most important for cellular processes include *sodium*, *potassium*, *calcium*, *magnesium*, and *bicarbonate*. These electrolytes play a vital role in various

physiological processes, such as generating and conducting action potentials in neurons and muscles, stabilizing enzymatic reactions, or aiding in releasing hormones from endocrine glands [2, 62]. They also contribute to balancing mechanisms of two other crucial biological variables—fluid volume and acid-base levels (i.e., blood pH) [2]. Proper nervous system functioning and muscular relaxation and contraction, including that of the heart, requires these five electrolytes to be within their homeostatic range (Table 1.1) [7]. The physiological role of these five electrolytes is briefly summarized below.

Sodium (Na^+)

Sodium is the most abundant ECF cation and the main osmotic solute of the body, meaning that water moves towards the site of higher Na^+ concentration via *osmosis* [2]. Na^+ determines the fluid distribution between the ICF and ECF compartments, carrying an essential role in the intravascular volume, overall fluid balance, and blood pressure (BP) regulation. Na^+ is also paramount for generating and propagating action potentials in excitable cells. Its homeostatic range is $[Na^+]$=135–145 mmol/L.

Potassium (K^+)

Potassium is the most predominant cation inside the cells [7]. Potassium is pivotal in establishing the resting membrane potential necessary to spur optimum action potentials [63]. Abnormal potassium levels impair cellular excitability, hampering communication between neurons and contractility of both skeletal and cardiac muscle fibers [7,42]. Rapid or substantial fluctuations in K^+ levels can instigate life-threatening neurological changes and cardiac arrhythmias [7, 64]. Thus, blood K^+ must be regulated precisely between $[K^+]$=3.5–5.5 mmol/L, but preferably within the narrow range of 4.2±0.3 mmol/L [2].

Calcium (Ca^{2+})

Calcium is the most abundant mineral in the body, making up 1.5–2% of the total body weight [65]. The bones store 99% of all calcium in the body. Only 0.99% is present in the blood, and 0.01% inside the cells [2]. Nearly 50% of all calcium in the blood, i.e., the total blood calcium (Ca), is ionized (Ca^{2+}), which is its only biologically active form. The remaining 40% is bound to plasma proteins (mainly albumin), and the other 10% to anions (e.g., phosphate). Calcium is essential for bone strength, neuromuscular function, and many intracellular processes, such as enzymatic reactions, blood coagulation, and the release of neurotransmitters and hormones from endocrine glands [2, 66]. Ca^{2+} ions stabilize cell membranes in action potentials and mediate the excitation-contraction coupling mechanism in muscle contraction [2].

Magnesium (Mg^{2+})

Magnesium is the fourth most common mineral [64] and is a primarily ICF cation involved in energy-production metabolism, neurotransmitter release, proper neurological function, and muscular contraction and relaxation. Less than 1% of the body's total Mg^{2+} is present in the ECF, with bones storing more than half of the body's magnesium. Although Mg^{2+} does not directly alter the cellular action potential, it contributes to excitable membrane stabilization. Mg^{2+} controls the activity of various ion channels necessary to move Na^+, K^+, and Ca^{2+} ions across cell membranes [7].

Bicarbonate (HCO_3^-)

Bicarbonate is the second most abundant ECF anion. Its principal function is to regulate blood pH and acid-base balance by acting as a buffer of hydrogen ions (H^+). The bicarbonate buffer system is the most critical extracellular buffer [2], which helps the body to maintain an adequate blood pH by neutralizing metabolic waste products, such as lactic acid and ketones. HCO_3^- ions are the byproduct of a chemical reaction that starts with carbon dioxide (CO_2) and water, which makes bicarbonate a significant component of CO_2 elimination: $CO_2 + H_2O \leftrightarrow H_2CO_3 \leftrightarrow H^+ + HCO_3^-$.

1.1.3. The kidneys and their functions in homeostasis

The *kidneys* oversee multiple vital functions for sustaining an optimal internal environment: excretion of metabolic waste products, regulation of water and electrolytes, blood pH balance, management of arterial pressure, activation of vitamin D, and stimulation of red cell production [2]. Aside from CO_2, the kidneys remove most substances in the blood that cells do not need [2], making them the body's primary *effector* for maintaining the extracellular constituents within their homeostatic range.

Renal dysfunction, whether caused by kidney disease or other factors, results in substantial derangements of homeostasis [25]. If enough fluids, electrolytes, and other substances accumulate in the body, death occurs within a few days unless clinical interventions are initiated to restore, at least partially, water, and electrolyte balances [2]. Such is the case with complete renal failure, in which patients require hemodialysis every two-to-three days to survive.

Functional anatomy of the kidneys

The kidneys are a pair of bean-shaped organs lying on the abdomen's posterior wall. Together with the ureters, bladder, and urethra, the kidneys comprise the *urinary system* (Fig. 1.2a).

Each kidney contains two main structures: the outer *cortex* and the inner *medulla* (Fig. 1.2b). Spanning across the cortex and medulla are the *nephrons*, the functional

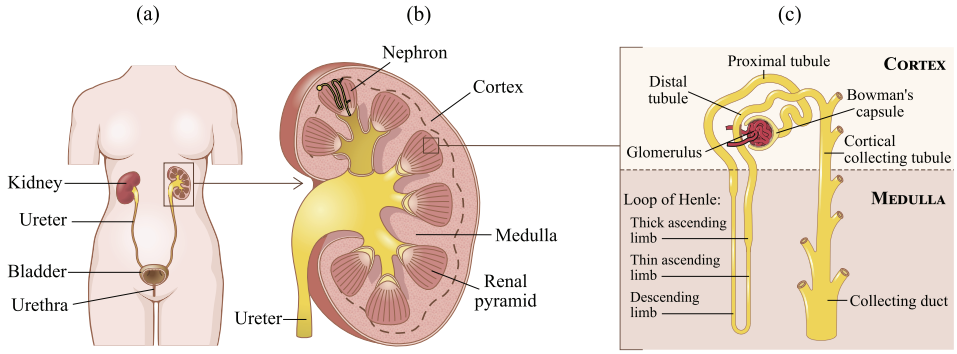

Fig. 1.2. The components of **(a)** the urinary system, the **(b)** general organization of the kidney, and **(c)** basic tubular segments of the nephron (not drawn to scale). The proximal and distal tubules, the loop of Henle, and the collecting duct are the four components of the renal tubule. Adapted from [2].

units of the kidneys that cleanse the blood and produce urine [67]. Along with urine formation, the nephrons control BP regulation, red blood cell production, and calcium absorption [67]. Up to one million nephrons exist in each kidney, but this number gradually decreases with renal injury, disease, or aging, as kidneys cannot regenerate new ones [2].

Each nephron contains a cluster of filtering capillaries known as the glomerulus surrounded by the *Bowman's capsule* and a pipe-like structure called *renal tubule*. The renal tubule comprises four components: the *proximal tubule*, the *loop of Henle*, the *distal tubule*, and the *collecting ducts* (Fig. 1.2c). The loop of Henle is a U-shaped component lying in the medulla composed of three segments: the *descending limb* and the *thin* and *thick ascending limbs* [2].

Urine formation

There are three main steps of urine formation: *glomerular filtration*, *reabsorption*, and *secretion* [67]. Upon the arrival of blood at the glomerulus, large amounts of fluid and most non-proteic substances are filtered as blood moves into the Bowman's capsule (*filtration*), resulting in what is known as the filtrate. The filtrate enters the proximal tubule, which reabsorbs most ions, water, and nutrients (*reabsorption*) but not metabolic waste products [2]. The concentration of dissolved ions in the filtrate (i.e., the osmolality) varies as it passes through each renal tubule component, as water and electrolytes continue to be reabsorbed. Excess ions and other substances are secreted in the distal and collecting tubules. Hormones modulate the rates of reabsorption and secretion of ions and water according to the body's needs [68], thus affecting the volume and composition of the filtrate. Finally, the yielded fluid at the end of the collecting duct is ready to be excreted as urine, moving into the ureter onto the bladder.

1.2. Electrolyte Metabolism: Homeostatic Regulation of Electrolyte Balance

Homeostatic regulation of electrolytes and fluids falls primarily (but not exclusively) under the responsibility of one of the most pivotal organs for preserving homeostasis—the *kidneys* [1,2,67]. The kidneys have the task of adjusting the excretion rate of electrolytes and water to match the intake of these substances precisely so that a relatively constant fluid volume and stable blood electrolyte composition can be maintained [2].

Almost all electrolytes come from food and fluids, which means that a person's eating and drinking habits govern the overall daily intake of water and electrolytes. However, depending on the diet, level of activity, or climatic conditions, the amount of electrolytes a person consumes per day typically surpasses their daily needs. If the intake of a substance exceeds its excretion, its bodily amount increases; likewise, if excretion is higher than its intake, its bodily amount decreases. Hence, it is up to the homeostatic control systems to balance the daily consumption and excretion of electrolytes, as well as compensate for excessive losses whenever possible [2].

While the kidneys and the urinary system are the most preeminent blood electrolyte regulator, the renal excretion rate is usually not fast enough to correct any electrolyte or fluid derangements in case of abrupt fluctuations. Other mechanisms operate as the first line of defense against such rapid fluctuations, thus preserving homeostasis in the short term until the kidneys can restore balance. This Section outlines the regulatory mechanisms of electrolyte balance.

1.2.1. Endocrine control of electrolyte metabolism

Hormones modulate the renal function and the water and electrolytes absorption rate. They stimulate or inhibit the renal blood flow to control the glomerular filtration rate (GFR) so that adequate fluids and electrolyte levels are maintained in the filtered blood [68].

Hormonal modulation of tubular reabsorption/secretion is electrolyte specific, which means that each electrolyte is reabsorbed/secreted at a specific anatomic site [2]. Such specificity allows the kidneys to excrete different electrolytes at variable rates, often independently of one another. In settings where only one individual electrolyte is outside its homeostatic range, this mechanism permits the correction of excessive levels of that electrolyte without compromising the balance of the others.

The primary hormones in electrolyte balance regulation are the ones of the *renin-angiotensin-aldosterone system* (RAAS), the *antidiuretic hormone* (ADH), *natriuretic peptides*, the *parathyroid hormone* (PTH), and, albeit to a lesser extent, vitamin D, calcitonin, insulin, and sympathetic adrenergic activity [68].

Renin-angiotensin-aldosterone system (RAAS)

The RAAS is a hormonal system critical for regulating blood volume and systemic vascular resistance. It consists of three main hormones—renin, angiotensin II, and aldosterone—that impact the cardiovascular, neural, and renal functions. The RAAS involves the kidneys, lungs, systemic vasculature, and the brain, and its primary function is to regulate BP by modulating blood volume, Na^+ and water (H_2O) reabsorption, K^+ secretion, and vascular tone [69]. The body activates the RAAS in response to: BP drops (↓), a rise (↑) in blood [K^+], or low (↓) blood [Na^+] [2, 68].

Renin. Renin secretion is the *first stage* of RAAS activation. The kidneys release renin in response to one of three factors: *(i)* decreased BP (that can be linked to a drop in blood volume), *(ii)* increased renal Na^+ excretion, or *(iii)* sympathetic adrenergic stimulation [2].

Angiotensin. Angiotensin-conversion is the *second stage*. Once renin has been released into the blood, it initiates a biochemical chain of events that converts its target, angiotensinogen, into angiotensin I. Angiotensinogen is produced in the liver but is constantly circulating in the plasma. Angiotensin I is then transformed into angiotensin II by the angiotensin-converting enzyme (ACE), which is found primarily on the surface of the pulmonary and renal endothelium. Angiotensin II exerts various actions throughout the body. It induces vasoconstriction of the arterioles, elicits renal Na^+ reabsorption in the proximal tubules, and stimulates the release of noradrenaline, ADH, and aldosterone [2, 68, 69]. Increased blood Na^+ levels promote water retention, subsequently leading to a rise in ECF volume and, therefore, BP restoration. Angiotensin II also acts in the hypothalamus to evoke the sensation of thirst, so more fluids are consumed to raise the circulating fluid volume (and, in turn, BP). In instances of blood loss or dehydration, angiotensin II also restores BP by reducing GFR and renal blood flow, thereby limiting further fluid loss and blood volume decrease [2, 68, 69].

Aldosterone. The *last stage* of RAAS activation is aldosterone secretion stimulated by angiotensin II. Aldosterone exercises its function in the Na^+-K^+-ATPase pumps of the cells in the collecting ducts of the nephron. It prompts Na^+ reabsorption in exchange for K^+ ions. However, the effects of aldosterone on potassium and sodium balances, i.e., Na^+ reabsorption in unison with K^+ loss, do not always go hand in hand. Whether aldosterone results in Na^+ retention without losing potassium, or K^+ loss without retaining sodium depends on a biochemical process called phosphorylation. Angiotensin II influences phosphorylation and inhibits K^+ secretion: if present, aldosterone triggers Na^+ retention without K^+ loss; if absent, aldosterone increases K^+ excretion without altering sodium and fluid balance. This mechanism allows the body to increase the blood Na^+ levels in states of blood volume depletion without significantly altering K^+ levels and to excrete excess K^+ without affecting sodium or blood volume balance. Since

aldosterone is a steroid hormone, its effects may take hours to days to begin, while the effects of angiotensin II are rapid [69].

Antidiurectic hormone (ADH)

The ADH, or vasopressin, is the primary regulator of tonicity, i.e., the capability of an extracellular solution to enable water to migrate into or out of a cell via osmosis. The body releases ADH when a change in blood osmolality is detected, caused either by increased Na^+ levels, or by volume depletion. ADH controls renal H_2O secretion and is particularly important during states of water deprivation and fluid loss. It essentially enables the kidneys to form a small volume of concentrated urine while excreting normal amounts of Na^+ [2, 68]. ADH promotes H_2O reabsorption in the distal and collecting tubules, thus minimizing further decreases in fluid volume and arterial pressure that would otherwise occur during a state of volume depletion [2, 68].

Natriuretic peptides

Natriuretic peptides are hormones secreted by heart cells when changes in blood pressure occur [2]. Atrial natriuretic peptide (ANP) and B-type natriuretic peptide (BNP) are two examples of this family of hormones that inhibit aldosterone and ADH release by stimulating the kidneys to excrete sodium (*natriuresis*) and water (*diuresis*) [2, 68]. A slight change in blood volume causes a marked change in the cardiac output, which induces BP changes that, in turn, cause substantial changes in urine output [26]. Raised blood volume elicits the release of ANP and BNP from the heart. These hormones promote natriuresis to reduce the circulating blood volume by reducing aldosterone secretion, thereby decreasing Na^+ reabsorption. ANP and BNP also increase GFR by dilating glomerular arterioles, meaning that more blood moves through the nephrons [2].

Parathyroid hormone (PTH)

The PTH is the preeminent hormone in the metabolism of calcium and phosphate (PO_4^{3-}). PTH is secreted in response to low blood calcium levels and exerts its action in the bones, kidneys, and small intestines. Among its targets are the proximal tubules and the ascending loop of Henle, where PTH elicits Ca^{2+} reabsorption while reducing PO_4^{3-} reabsorption [2]. Eliminating PO_4^{3-} from the blood is necessary to increase the levels of circulating Ca^{2+} since PO_4^{3-} binds to Ca^{2+} to form calcium phosphate, a mineral that is not biologically active. Thus, the reduction of PO_4^{3-} levels results in more Ca^{2+} ions available in the blood. Other PTH-mediated mechanisms that lead to an increase of blood Ca^{2+} levels include bone remodeling and vitamin D activation. Bone remodeling releases Ca^{2+} as a byproduct, while vitamin D stimulates calcium absorption in the small intestine [2].

Insulin

Although its effects on electrolyte metabolism are not as critical as that of other hormones, insulin still has a meaningful impact on electrolyte regulation. Insulin influences the renal handling of Na^+, K^+, Ca^{2+}, and PO_4^{3-} [70] and modulates the cellular distribution of K^+ [2, 71]. Its main role is to prevent electrolyte imbalance, namely K^+ surplus and Na^+ and volume loss, immediately after meals until the kidneys can restore balance.

1.2.2. Sympathetic control of electrolyte metabolism

Since the kidneys have extensive sympathetic innervation, the *sympathetic nervous system* (SNS) modulates multiple renal functions, such as renal blood flow, GFR, urinary sodium and water excretion, and hormonal production and secretion [72]. Renal sympathetic nerve activity (RSNA) plays a crucial role in BP regulation and is activated in response to hypotension or volume depletion. Heightened RSNA promotes Na^+ reabsorption in the proximal tubule to increase fluid retention and, thereby, intravascular volume and BP [2].

The physiological association between SNS activation and the kidneys explains why many medications, such as β-blockers, β_2-agonists, and α_2-agonists which are used to treat hypertension, asthma, and CVD, can induce renal dysfunction—and thus a heightened susceptibility to electrolyte imbalance—in the patients taking them. Sympathetic innervation of the renal vasculature is predominantly adrenergic with α and β adrenoceptors [72]. Thus, norepinephrine and other adrenergic agonists stimulate RSNA. These neurohumoral substances induce renin release and vasoconstriction of the renal vasculature, reducing renal blood flow and increasing Na^+ retention. The interrelationship between RSNA and BP substantially impacts the cardiovascular function and vice versa, hence why kidney and heart diseases often co-exist. The cardiovascular and renal systems work in tandem to maintain homeostasis, displaying an intricate cardio interrelationship in which the dysfunction in one of the organs leads to the dysfunction of the other.

1.2.3. Renal and extrarenal regulatory mechanisms

As mentioned above, the responsibility to regulate electrolyte levels and fluid volume is placed primarily on the kidneys [2]. They eliminate most daily excess of H_2O, Na^+, K^+, and Mg^{2+}, while urine usually contains only traces of Ca^{2+} and PO_4^{3-}. While renal excretion of Ca^{2+} and PO_4^{3-} is still relevant for maintaining their homeostatic blood range, the renal hormones control the GI absorption of these two electrolytes, meaning that most excessive Ca^{2+} and PO_4^{3-} intake is eliminated through the feces [73]. In contrast, most daily consumed H_2O, Na^+, K^+, are absorbed and thus must be excreted in the

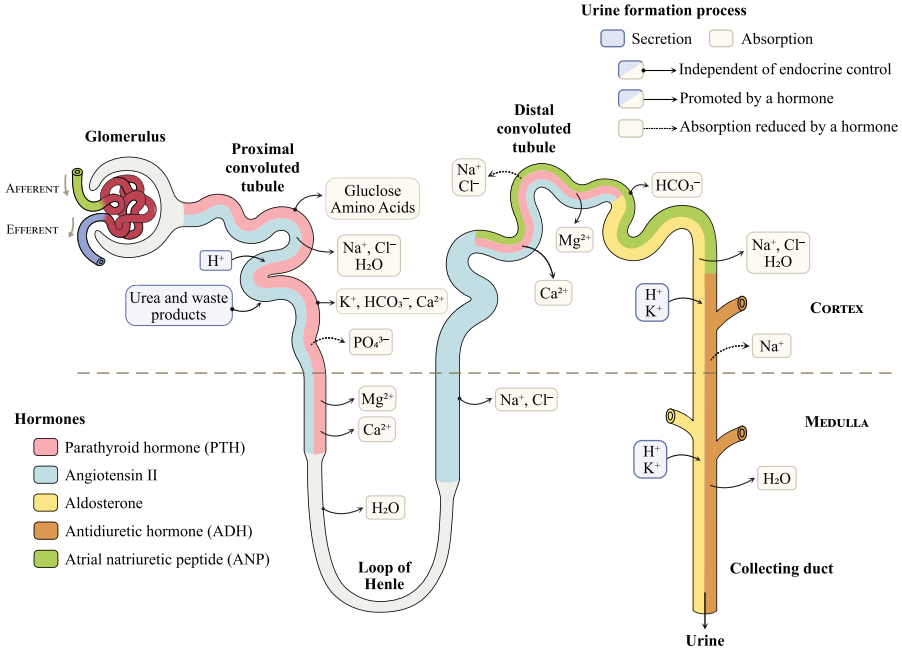

Fig. 1.3. Renal electrolyte secretion and reabsorption in their specific anatomic site and respective hormonal control. Adapted from: [74].

urine. The renal end extrarenal mechanisms of electrolyte metabolism are summarized below.

Sodium and fluid balance

The regulation of sodium and fluid volume are intertwined, and the mechanisms of one cannot be conveyed without the other. Because cell membranes are porous to H_2O but impermeable to most solutes, water swiftly diffuses between the ICF and ECF compartments whenever there is a difference in $[Na^+]$ on either side of the membrane [2]. Thus, any change in blood $[Na^+]$ will be equated with H_2O (and ergo blood) volume changes.

About 80% of Na^+ and water consumed daily is absorbed in the GI tract and is mostly excreted by the kidneys. The daily excreted amount is adjusted by the glomerular filtration and tubular reabsorption rates, each modulated by various feedback mechanisms. Sodium reabsorption varies in different sections of the nephron: 65% is reabsorbed in the proximal tubule, 20% in the loop of Henle, 10% in the distal tube, and 4% in the collecting duct [2]. Other Na^+ and water excretion sources include feces and sweat, albeit in significantly lower amounts than that contained in the urine.

Changes in Na^+ or H_2O alter the plasma osmolarity and blood volume, resulting in BP variations. The body responds to such changes by activating one of the three homeostatic control mechanisms: the RAAS (↓BP), the ADH (↑osmolarity), or na-

Table 1.2. Factors inducing transcellular K^+ shifts. Adapted from [2, 74].

Shifts K^+ into cells (↓blood $[K^+]$)	Shifts K^+ out of cells (↑blood $[K^+]$)
Insulin	Insulin deficiency (High blood sugar)
Alkalosis	Acidosis
β-adrenergic agonist	β-blocker
Hypoosmolarity	Hyperosmolarity
Aldosterone	Aldosterone deficiency (Addison disease)
	Cell lysis (e.g., crush injury, rhabdomyolysis)
	Digitalis
	Strenuous exercise

triuretic peptides (↑atrial pressure) [74]. These mechanisms are detailed in Sec. 1.2.1 and illustrated in Fig. 1.3.

Potassium balance

Nearly 90% of the ingested K^+ is absorbed in the GI tract [71]. About 90–95% of excess K^+ is excreted in the urine, whereas the rest is eliminated through the feces and sweat [2]. Most of the filtered K^+ in the kidneys is reabsorbed in the proximal tubule (65%) and the loop of Henle (25–30%) [2]. When blood $[K^+]$ increases, the body secretes aldosterone, which prompts the cells in the distal and collecting tubules to secrete K^+ (Fig. 1.3), resulting in an increased K^+ excretion [71, 74]. As explained in Sec 1.2.1, aldosterone-mediated renal K^+ secretion occurs without affecting sodium and fluid balance and vice versa [69]. Unlike other electrolytes, the kidneys always excrete a minimum daily amount of K^+ (~580 mg) and are thus unable to reduce its excretion to virtually zero in settings of potassium-deficient diets [71].

Another important mechanism of potassium balance is its *internal distribution* between the ICF and ECF. Since the ICF contains more than 98% of the body's potassium, cells can serve as an overflow site for excess K^+ or as a source of K^+ in the event of depletion [2]. Without this distribution, blood $[K^+]$ would rise to dangerous levels after any potassium-containing meal. Thus, transcellular K^+ shifts are the first line of defense against rapid blood K^+ fluctuations. Table 1.2 summarizes the factors that can induce transcellular K^+ shifts.

Calcium balance

In contrast to Na^+ and K^+, not all calcium ingested daily is absorbed in the small intestine. GI absorption of Ca^{2+} is subject to endocrine regulation by vitamin D, and most excess Ca^{2+} is excreted in the feces and not by the kidneys [66]. Urine contains only trace amounts of Ca^{2+} as kidneys reabsorb 99% of the filtered Ca^{2+} [2]. The kidneys, therefore, play a more vital role in calcium retention rather than excretion. Renal Ca^{2+} reabsorption is controlled by hormones, fluid volume, and other electrolytes (Ta-

Table 1.3. Factors that alter renal calcium excretion. Adapted from [2].

Decreases Ca^{2+} excretion	Increases Ca^{2+} excretion
↑PTH	↓PTH
↓Fluid volume	↑Fluid volume
↓Blood pressure	↑Blood pressure
↑Blood PO_4^{3-} levels	↓Blood PO_4^{3-} level
Metabolic alkalosis	Metabolic acidosis
1,25-Vitamin D_3 (calcitriol)	

ble 1.3). In the proximal tubule, Ca^{2+} reabsorption is passive, paralleling that of Na^+ and H_2O. Thus, urinary Ca^{2+} excretion is inadvertently increased when the body decreases renal Na^+ and H_2O reabsorption in response to increased fluid volume and BP [2].

Bone remodeling is the primary regulatory mechanism of calcium balance [66], and is the first line of defense against abnormal Ca^{2+} levels. This mechanism balances blood $[Ca^{2+}]$ through a dynamic exchange of Ca^{2+} ions between the blood and the bones. When $[Ca^{2+}]$ drops, the body elicits bone resorption, which releases Ca^{2+} into the bloodstream. Conversely, when blood $[Ca^{2+}]$ rises, the body prompts bone formation, thus depositing Ca^{2+} into the bones. Nevertheless, the bones do not have an endless supply of Ca^{2+}, and the kidneys and GI tract must adjust Ca^{2+} absorption/excretion accordingly [2].

Calcium metabolism is modulated mainly by PTH, vitamin D (calcitriol), and calcitonin [2, 66]. PTH is secreted in response to low blood $[Ca^{2+}]$, and mediates bone remodeling, vitamin D activation, and renal Ca^{2+} reabsorption. In the kidneys, PTH elicits Ca^{2+} reabsorption in the distal and PO_4^{3-} excretion in the proximal tubules (Fig. 1.3) to raise the levels of circulating Ca^{2+} (Sec. 1.2.1). Calcitonin inhibts PTH secretion, thus producing the opposite effect, i.e., reduced blood $[Ca^{2+}]$.

Magnesium balance

About 30–40% of dietary Mg^{2+} intake is absorbed by the GI tract. This number rises to 65% at a low intake and drops to 11% at a high Mg^{2+} intake, but the factors controlling Mg^{2+} absorption are not yet clear. PTH is believed to play a role, but other dietary factors such as proteins, K^+, and zinc also affect Mg^{2+} absorption [75].

While the physiological mechanisms of magnesium regulation are not well understood, excretion of excess Mg^{2+} falls under the responsibility of the kidneys. Unlike K^+, renal Mg^{2+} excretion decreases to virtually zero in settings of magnesium depletion [2]. The loop of Henle is the primary site of Mg^{2+} reabsorption (65%), followed by the proximal tubule (25%) [75]. No single hormone seems to be explicitly related to magnesium metabolism, but PTH, calcitonin, acid-base levels, blood volume status, ADH, insulin, high blood Ca^{2+} and low PO_4^{3-} levels are known factors which influence renal Mg^{2+} reabsorption [2, 75]. PTH is the most significant of these, and it stimulates

Mg^{2+} reabsorption in the distal tubule [75].

Bicarbonate and acid-base balance

In contrast to other electrolytes, HCO_3^- is conserved rather than reabsorbed in the kidneys since tubular cells are not permeable to HCO_3^- [2]. Essentially, the kidneys reabsorb Na^+ in exchange for H^+ ions to generate HCO_3^-. However, it is possible that certain molecules in the filtrate, such as phosphates and ammonia, will capture H^+, which will result in fewer available H^+ ions to generate HCO_3^-. In such cases, HCO_3^- is not conserved, which can lead to pH imbalance and metabolic acidosis. If more blood K^+ is present than normal, K^+, rather than H^+, will be exchanged, subsequently excreting higher concentrations of K^+. When this occurs, fewer H^+ ions will also be available, and less HCO_3^- will be conserved. Conversely, if there is less K^+, more H^+ ions enter the filtrate to be exchanged with Na^+, and more HCO_3^- is conserved.

While the kidneys primarily regulate bicarbonate levels, the respiratory system also plays a role. When CO_2 levels in the blood increase, the body responds by increasing the rate and depth of breathing. This causes more CO_2 to be exhaled, which helps to restore the balance of blood $[HCO_3^-]$. Similarly, when $[CO_2]$ decreases, the body slows down breathing to retain more CO_2, which can then be converted into HCO_3^- [2, 74].

1.3. Electrolyte Imbalance—a Byproduct of Disrupted Homeostasis

Electrolyte imbalance, or dyselectrolytemia, occurs when the concentration of an electrolyte in the blood falls outside its homeostatic range. More often than not, electrolyte (and fluid) imbalances arise due to disrupted homeostatic mechanisms [5] rather than environmental causes (e.g., excessive sweat in a tropical climate) [1, 2, 76]. The disruption of a homeostatic mechanism is usually of pathological genesis, caused either by direct damage/failure of an effector organ, as in kidney disease [77], or by dysregulation of their hormonal control centers, such as overactivation of the RAAS in heart failure (HF) [26] or undersecretion of aldosterone in Addison's disease. Electrolyte imbalance instigated by an inadequate diet or environmental factors, while possible, rarely occurs in clinical practice without any associated comorbidity unless in extreme settings. Such is the case of prolonged starvation, rapid loss (or intake) of water or electrolytes within a short time, or continuous small losses without replenishment (e.g., strenuous exercise devoid of rehydration). Despite representing a medical emergency, dyselectrolytemia caused by such extreme settings can generally be corrected without long-term health consequences, provided that patients display normal renal, cardiovascular, and endocrine function. Thus, electrolyte imbalance becomes particularly relevant—and clinically challenging to manage—in patients with chronic diseases.

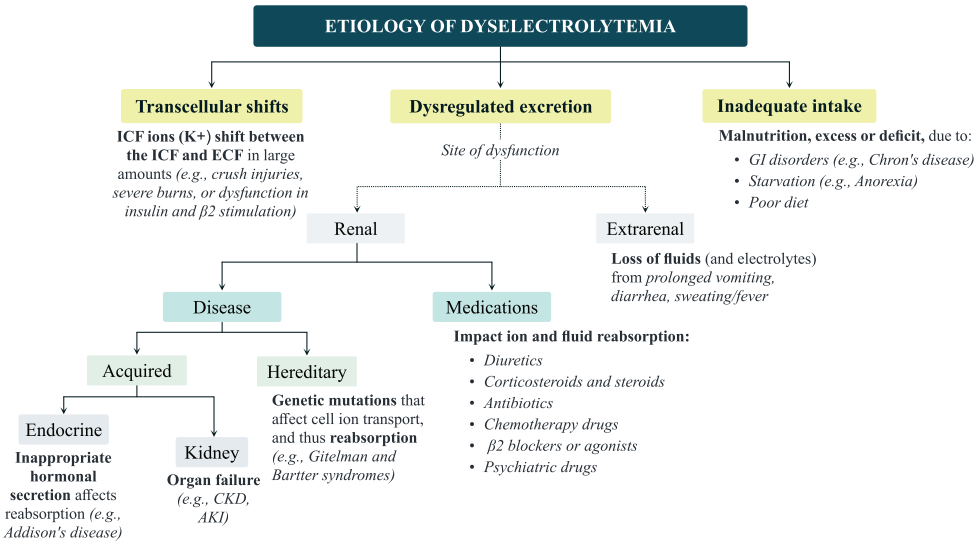

Fig. 1.4. Graphical overview of the three etiologies of electrolyte imbalance.

1.3.1. Etiology

Whenever one of the mechanisms mentioned in Sec. 1.2 malfunctions, electrolyte regulation is compromised, and dyselectrolytemia can develop. Dyselectrolytemia emerges primarily from two-to-three etiologies (Fig. 1.4): *inadequate intake*, *dysregulated excretion*, and *transcellular shifts* in the case of ICF ions (K^+ and Mg^{2+}). Excessive electrolyte intake, insufficient excretion, or the release of large quantities of an intracellular ion into the blood raises electrolyte levels above their ideal range. Conversely, a deficient intake, excessive excretion, or an increased cellular uptake can result in low blood electrolyte disorders. Each of the three etiologies is summarized below.

Dysregulated excretion

Dysregulated excretion is the root of most dyselectrolytemias. It is primarily due to *renal dysfunction* and can lead to excessive, insufficient, or even nonexistent elimination of fluids and electrolytes, depending on the degree of renal failure. Etiologically, renal dysfunction is the byproduct of *diseases* (acquired or hereditary) or *medications*. In *hereditary diseases*, genetic mutations affect ion transport in specific components of the renal tubule, impairing adequate electrolyte reabsorption in the kidneys. *Acquired diseases*, on the other hand, encompass all those caused by the malfunction of an effector organ or the endocrine system that controls it [68]. The most obvious example is kidney disease, in which the degeneration of the renal tissue compromises electrolyte and fluid excretion [77].

Inappropriate hormonal secretion or usage of certain *medications*, such as loop and thiazide diuretics, also dysregulate renal function even if the kidney tissue is unin-

jured and capable of normal excretion [2, 14, 68]. Low secretion of any hormone that stimulates excretion (e.g., aldosterone) results in electrolyte retention. Conversely, hormonal oversecretion (e.g., ADH) prompts increased renal excretion or inadequate reabsorption, thus dropping electrolyte levels below their optimal range. Endocrine diseases, such as Addison's disease or Cushing's syndrome, are examples of acquired diseases that result in dysregulated electrolyte metabolism.

Low electrolyte levels are also a common side effect of *diuretics* and other medications [5]. The usage of diuretics in settings of healthy kidney function works similarly to hormonal oversecretion, causing the kidneys to eliminate fluid and electrolytes excessively.

Extrarenal losses are other sources of electrolyte excretion, such as through the skin (e.g., burns or sweat) or GI tract (e.g., chronic vomiting).

Inadequate intake

Inadequate dietary habits or impaired GI absorption (i.e., malabsorption) usually cause electrolyte deficiencies rather than high blood electrolyte levels. Albeit possible, overconsumption of an electrolyte rarely leads to imbalance if renal function is adequate. The kidneys can cope with copious amounts of electrolytes, provided that only an excessive—but not unreasonably high—amount is ingested at once [2]. Thus, excessive intake is mainly concerning in CKD. Insufficient dietary consumption can induce electrolyte deficiencies, but only after prolonged periods of malnourishment, as seen in *anorexia nervosa* [78], continuous poor diets, and alcoholism. However, malabsorption hinders the body's ability to obtain its daily electrolyte needs and can lead to low levels regardless of the diet [2].

Transcellular shifts

Derangements in the internal distribution of ICF ions such as K^+ can lead to dyselectrolytemia [71]. A release of large amounts of electrolytes from cells into the blood can raise their levels above the normal range. By contrast, an increased cellular uptake lowers blood electrolyte levels. Transcellular shifts arise from cell lysis provoked by trauma or crush injuries or altered ion-transport activity in cell membranes [2], mediated by pathological dysregulations of hormones (e.g., insulin) or other electrolytes (Table 1.2).

Acid-base imbalance

Another frequent cause of dysregulated electrolyte excretion is an *acid-base imbalance* [79], often caused by metabolic disorders that alter blood $[HCO_3^-]$. Acid-base imbalance regularly co-occurs with dyselectrolytemia. Although the mechanisms are not entirely understood, abnormal $[HCO_3^-]$ hampers the activity of the Na^+/K^+-ATPase

Table 1.4. Reference values of blood electrolyte concentration for each classification of each dyselectrolytemia.

Dyselectrolytemia	Classification (mmol/L)		
	Mild	*Moderate*	*Severe*
Potassium (K^+): 3.6 – 5.4 mmol/L[1]			
Hypokalemia	3.5 – 3.0	2.9 – 2.5	< 2.5
Hyperkalemia	5.5 – 5.9	6.0 – 6.9	⩾7.0
Calcium (Ca^{2+}): 1.15 – 1.31 mmol/L[2]			
Hypocalcemia	1.14 – 1.00	0.99 – 0.8	< 0.8
Hypercalcemia	1.32 – 1.50	1.51 – 1.75	> 1.75
Magnesium (Mg^{2+}): 0.71 – 0.94 mmol/L[3]			
Hypomagnesemia	0.70 – 0.66	0.65 – 0.50	< 0.50
Hypermagnesemia	0.95 – 2.0	2.1 – 5.0	> 5.0
Sodium (Na^+): 137 – 145 mmol/L			
Hyponatremia	136 – 130	129 – 125	< 125
Hypernatremia	146 – 154	155 – 165	> 165
Bicarbonate (HCO_3^-): 22 – 26 mmol/L			
Metabolic acidosis	22 – 18		< 18
Metabolic alkalosis		> 26	

[1] Reference value according to the European Society of Cardiology. The American Heart Association considers the normal range of [K^+] to be 3.5–5.0 mmol/L.
[2] Ionized calcium. The values of total corrected calcium (Ca) differ.
[3] Some clinicians are advocating for the reference range of Mg^{2+} to be 0.75–0.85 mmol/L.

pump, perturbing the normal cellular uptake of K^+ and renal secretion of K^+, Na^+, and water in the renal tubules [2].

1.3.2. Classification, symptoms, and treatment

Electrolyte disorders are named based on which ion is out of balance. Each disorder is called: *hypo/hyper* + ion *chemical name* + *emia*, and can be classified as mild, moderate, or severe. *Emia* means 'blood', and the prefixes *hypo* or *hyper* define whether the electrolyte level in the blood is *too low* or *too high*. The exception to this nomenclature is acid-base disorders, i.e., bicarbonate imbalance: low blood [HCO_3^-] is known as *metabolic acidosis*, whereas high blood [HCO_3^-] is *metabolic alkalosis*. Table 1.4 outlines the classification of each dyselectrolytemia.

Symptomatology

The symptomatology of dyselectrolytemia is broad and usually nonspecific, varying from symptomless to general fatigue and malaise to neuromuscular paralysis and

Table 1.5. Symptoms of moderate-to-severe dyselectrolytemia.

Dyselectrolytemia	Symptoms			
	Neuromuscular and neurologic	*Cardiovascular*	*Digestive*	*Others*
Sodium				
Hyponatremia	Seizures, lethargy, confusion, stupor, coma	Possible heart failure	Nausea	Headache
Hypernatremia	Confusion, stupor, coma		Nausea	Thirst
Potassium				
Hypokalemia	Muscle weakness, ascending paralysis, lethargy, delirium, depression	Palpitations, abnormal repolarization (flat T-waves), arrhythmias	Paralytic ileus	Worsening diabetes control, polyuria
Hyperkalemia	Frank muscle paralysis, paraesthesia, lethargy	Palpitations, abnormal repolarization (peaked T-waves), arrhythmias	Nausea, vomiting	Dyspnea
Calcium				
Hypocalcemia	Tetany, dysphagia, circumoral numbness, seizures, lethargy, syncope, depression, cognitive impairment, personality changes	Systole prolongation, hypotension, angina, heart failure	Nausea, heartburn, constipation	Wheezing, dermatological issues (dry skin)
Hypercalcemia	Muscle weakness, lethargy, confusion, hallucinations, anxiety	Shortened systole, ↓automaticity, hypertension, arrhythmias	Nausea, vomiting, pancreatitis, ulcers	Renal stones, ↑urinary frequency, bone pain
Magnesium				
Hypomagnesemia	Tetany, weakness, hyperreflexia, muscle spasticity, apathy, depression, delirium, personality changes	Elevated vascular tone, impaired contractility, ischemia, Torsade de Pointes	Nausea, vomiting, decreased appetite	Hypokalemia, hypocalcemia
Hypermagnesemia	Weakness, facial paralysis, ↓deep tendon reflexes, lethargy, confusion	Hypotension, bradycardia, atriovenctricular block	Paralytic ileus	Impaired breathing and apnea, bladder paralysis, cutenous flushing, hypocalcemia

dangerous arrhythmias (Table 1.5). The symptoms of sodium imbalance are mainly neurological, resulting in some form of brain dysfunction. In many situations, hypo- and hypernatremia induce altered states of consciousness, such as stupor and coma. Potassium and calcium imbalances impair cardiac and muscular contractility, leading to muscle weakness and paralysis, including that of the smooth muscle in the lungs, stomach, and intestines. Abnormal [Ca^{2+}] induces tetany and circumoral paresthesia, whereas [K^+] mostly affects the cardiac function, engendering arrhythmias. Magnesium imbalance primarily affects deep tendon reflexes, muscular tone and spasticity, and ion transport between cell membranes, frequently causing blood [K^+] and [Ca^{2+}] abnormalities. In addition to Na^+, Ca^{2+} and Mg^{2+} imbalances can precipitate hemodynamic and BP disturbances.

Many symptoms of each dyselectrolytemia overlap with the ones of other conditions, hampering the ability to recognize electrolyte derangements at an early stage. Patients with mild—and even moderate—dyselectrolytemia are often asymptomatic

unless they are critically ill, or blood electrolyte levels are severely deranged or changed too rapidly (sudden onset), leading to an acute dyselectrolytemia episode. The clinical manifestations of electrolyte imbalance depend on four factors:

1. Severity level, i.e., the degree of deviation from the homeostatic range. Extreme deviations in either direction always represent a medical emergency, with patients manifesting evident signs of sickness.

2. The pace of imbalance onset. Sudden onset or acute dyselectrolytemia episodes are more likely to manifest prominent clinical signs (even at mild levels) than those that develop gradually or are chronic.

3. The presence of concomitant electrolyte or acid-base imbalance. Patients with more than one electrolyte derangement tend to display more evident symptoms than those with isolated imbalances, regardless of severity. The exception is when the concomitant imbalance is of two antagonists electrolytes, where one countervails the adverse physiological effects of the other, e.g., K^+ and Ca^{2+}. Even at the same $[K^+]$ and $[Ca^{2+}]$ levels, patients with hyperkalemia and hypercalcemia are less predisposed to show signs of dyselectrolytemia than those with isolated $[K^+]$ and $[Ca^{2+}]$ abnormalities.

4. The health status and pre-existent cardiovascular disease. Critically ill patients or those with cardiac structural, hemodynamic, or conduction disturbances are more susceptible to the physiological consequences of electrolyte imbalance and, thereby, more likely to manifest symptoms even at mild levels.

Treatment of dyselectrolytemia

Alongside the severity level, the patient's health status and their cardiovascular and renal capacity dictate the best treatment for dyselectrolytemia. Moderate to severe dyselectrolytemia requires treatment in a healthcare facility, while mild abnormalities can be corrected at home. However, dyselectrolytemia must always be treated under the supervision of healthcare professionals for patients with renal or cardiovascular disease, independently of its severity level.

Replacement of electrolytes is necessary to rectify low electrolyte levels and minimize further losses. Oral supplementation over a few days to weeks usually corrects mild hypoelectrolytemia, but moderate to severe imbalance entails the administration of intravenous electrolyte solutions. Hyperelectrolytemia warrants rectification by excretion and cessation of any exogenous electrolyte sources (diet or medication). Promoting excretion via diuresis is the preferable treatment for mild and moderate imbalance in patients with adequate renal function. Dialysis is the necessary course of action for those with renal disease or with severe imbalance.

1.3.3. Comorbidities and risk factors

Patients most susceptible to dyselectrolytemia are those that display renal dysfunction [5]. Without adequate functioning of the body's primary fluid and electrolyte regulator, homeostasis inevitably becomes compromised, and the likelihood of developing dyselectrolytemia increases. Renal dysfunction naturally stems from kidney degeneration or failure, as seen in *chronic kidney disease* (CKD) or *acute kidney injury*, with *end-stage renal disease* (ESRD) patients having an exacerbated risk of dyselectrolytemia [77]. Higher degrees of renal failure represent a higher risk of electrolyte imbalance.

However, other factors that dysregulate the homeostatic extrinsic control systems of the kidney function can also engender renal dysfunction. For instance, endocrine dysregulation of the hormones listed in Sec. 1.2.1, such as aldosterone, alters electrolyte reabsorption at the tubules, which results in renal dysfunction even if the kidney tissue itself is healthy. Thus, patients with endocrine disorders in the secretion sites of such hormones are also at risk of dyselectrolytemia [68].

Since the heart and the kidneys work in tandem to regulate BP, *cardiovascular disease* (CVD), namely, hypertension and HF, is another substantial risk factor for dyselectrolytemia [5, 14, 26, 76]. If the kidney function is not yet fully compromised, electrolyte derangements in CVD arise primarily due to therapeutical drugs that instigate renal dysfunction similar to endocrine dysregulation. Antihypertensive drugs (ACE inhibitors, diuretics) and β-adrenergic blockers to treat angina and arrhythmias predispose patients to electrolyte imbalance. Other medications that affect electrolyte homeostasis are β-agonists prescribed for rheumatological or pulmonary diseases (e.g., asthma), antibiotics, corticosteroids, chemotherapy, and psychiatric drugs.

Alongside kidney and heart diseases, liver disease (e.g., cirrhosis) and alcoholism, metabolic disorders (e.g., diabetes) [80], and malignancy (i.e., cancer) [81] are long-term conditions with a high risk of abnormal electrolyte levels. Comparatively to CKD, the incidence of dyselectrolytemia usually increases with the clinical progression of such diseases, mainly because of maladaptive homeostatic compensations that deteriorate kidney function.

Other risk factors are age, severe burns, prolonged fever, eating disorders, malnutrition (including intoxication) [78], and excessive diarrhea or vomiting. Critically ill patients, such as those with sepsis, grave infections, severe trauma, or any condition requiring treatment in the intensive care unit (ICU), frequently display several electrolyte and fluid disorders [76].

1.3.4. Epidemiology

The epidemiology of dyselectrolytemia varies for each electrolyte and level (hypo- or hyper) in different populations. Although the worldwide incidence of dyselectrolytemia in the general population is underestimated due to the lack of routine blood electrolyte monitoring, recent studies reported that 15% of community people above 55 years have at least one electrolyte disorder [5]. Most are ascribed to the usage of diuretics. The epidemiology for each electrolyte imbalance is summarized below.

Sodium

Hyponatremia is the most frequently encountered dyselectrolytemia in clinical practice, often as a complication of chronic diseases. It is found in 7.7% of the general population [5], 27% of CVD [26], 26% of CKD [12], and 22.5% of cancer patients [82]. Nearly half (44%) of hospitalized [83] and 38% of ICU [76] patients have hyponatremia.

Hypernatremia mainly emerges in the elderly and children, affecting 3.4% of community subjects [5]. About 4% of hospitalized patients display high [Na^+] [84]. This number is up to 9% in the ICU, but it has been reported as high as 26% [76].

Potassium

Hypokalemia occurs in 14% of the general population [18], in 4.6–19.7% of outpatients with eating disorders [85], but only in 1–2.7% of healthy individuals [5]. More than 20% of hospitalized patients develop hypokalemia during their hospital stay, primarily due to diuretic therapy [19]. In the ICU, 50–60% of trauma patients develop hypokalemia after injury resolution [76]. Low blood [K^+] is common in those receiving diuretics, with up to 80% of patients on non-potassium-sparing diuretic therapy displaying recurrent hypokalemia episodes [14]. Up to 14.9% of cancer patients also present hypokalemia [K^+] [82].

Hyperkalemia is present in 1.5–5% of the general population and is most frequent in CKD patients [86]. Its incidence depends on CKD progression but is reported in 5.9% of early-stage CKD patients and 11% in ESRD [12]. It is observed in up to 19% of hypertensive patients on potassium-sparing diuretics [18].

Calcium

Hypocalcemia incidence is difficult to determine, but it is present mainly in CKD (14.2–25.1% depending on the CKD stage) [87], vitamin D or Mg^{2+} deficiency settings, and acute pancreatitis. Low [Ca^{2+}] is frequent in hospitalized (27.2%) [76], ICU (90%) [76], and cancer (27.8%) [82] patients.

Hypercalcemia is relatively common and often mild but chronic. About 90% of cases are caused by hyperparathyroidism or malignancy [88], with incidence rates

ranging from 2.8% [82] to 30% [89] among cancer patients. In the ICU, 15% exhibit high blood [Ca^{2+}] [76].

Magnesium

Hypomagnesemia is found in less than 2% of the general population, but it occurs in 20% of hospitalized and 50% of ICU patients, 25% of diabetic outpatients, and 30–80% of persons suffering from alcoholism [5, 90]. Low [Mg^{2+}] is more frequent in patients with hematologic/oncological disorders. Hypomagnesemia is associated with hypokalemia and hypocalcemia.

Hypermagnesemia is rare, occurring only in critically ill patients with renal failure (15%) [86] and malignancy (10%) [82]. Some other risk factors include lithium therapy, hypothyroidism, and Addison's disease.

Bicarbonate

Metabolic acidosis is prevalent in 17.3% of CKD [77] and 12.8% of cancer patients [82]. *Metabolic alkalosis* is seen in 22.1% of malignancy cases [82], 51% of hospitalized patients, and 37% of CVD patients in advanced stages [26].

1.3.5. Clinical consequences of electrolyte imbalance

Dyselectrolytemia is associated with a risk of adverse events, including morbidity, mortality, and healthcare economic burden [5, 6, 91]. The clinical consequences of electrolyte imbalance depend on the severity level, patient health status, and episode duration, i.e., whether it is acute or chronic. Extreme deviations in the homeostatic range in either direction of any electrolyte lead to death, while moderate deviations engender sickness and limit the quality of life [2]. Thus, electrolyte imbalance can have health ramifications both in the short and long term.

Implications in short-term health

The most worrisome short-term consequence of dyselectrolytemia is arrhythmias with the potential to instigate SCD [7–9]. While derangements of any electrolyte can contribute to arrhythmogenesis in individuals with fragile hearts, potassium imbalance (i.e., dyskalemia) is the first and foremost pro-arrhythmogenic [7, 91]. Both acute and chronic hypo- and hyperkalemia can trigger fatal arrhythmias and are known major death causes in people with hypertension, diabetes, HF, and CKD [91], hence making timely correction of blood potassium derangements of utmost importance.

It is well-recognized that hyperkalemia is a common complication that warrants regular monitoring among CVD and CKD patients, especially those under maintenance hemodialysis (HD) [79, 92]. However, the effects of chronic or recurrent hypokalemia

episodes on the long-term health of those treated with β-blockers and RAAS inhibitors (RAASi) are less appreciated, despite current research [91]. For instance, hypokalemia in patients with early-stage CKD has recently been associated with increased mortality risk and faster progression to ESRD [93]. A U-shaped relationship between blood [K^+] on hospitalization and 90-day mortality has been reported in many populations, even those without CKD [94]. Alarmingly, only 52.8% of hypokalemic and 49% of hyperkalemic hospitalized patients are normokalemic at discharge [20]. While none of these studies have established a causal link between dyskalemia and death, they still point to the necessity of regularly monitoring blood potassium levels [91].

Implications in long-term health

Recent studies also speculate that recurrent mild dyselectrolytemia episodes induced by suboptimal dosages of RAASi, diuretics, and other therapeutical drugs for CVD can have long-lasting health ramifications [5]. Albeit not yet proven, these recurrent episodes may be involved in the genesis of *cardiorenal syndrome* (CRS) due to a maladaptive cascade of compensatory responses that the body activates to restore homeostasis, as so frequently seen in congestive HF [26]. For example, mild dyskalemia can cause abnormal (but not necessarily fatal) heart rhythms, which can lead to structural and electrical remodeling of the heart and, subsequently, decreased cardiac output. This cardiac output insufficiency alters renal blood flow and perfusion, which may damage the kidneys, further impairing renal [K^+] excretion [95]. The body then continuously activates the RAAS, the SNS, and other neurohormonal factors to promote blood [K^+] correction, which, in turn, prompts vasoconstriction and other hemodynamic disturbances in BP that can put additional strain on the heart. When patients still display sufficient renal and cardiac function, these compensatory mechanisms restore homeostasis. However, if activated for prolonged periods or recurrently, these compensatory mechanisms lead to a vicious cycle of cardiac and renal dysfunction, ultimately resulting in kidney and heart deterioration and failure [24]. Consequently, the clinical progression of the initial chronic disease is accelerated, and patients become susceptible to developing CVD, CKD, and even ESRD.

While clinicians tend to watch out for possible asymptomatic dyskalemia to avert unfavorable events, they frequently disregard other electrolyte imbalances unless they are severe. Still, mild episodes of other dyselectrolytemias can affect general health and cardiovascular function in the long term. Chronic mild episodes of sodium imbalance predispose hypertensive patients to syncope and falls [5], whereas those with chronic calcium imbalance can develop dermatological and bone complications (e.g., osteoporosis), kidney stones, ulcers, and pancreatitis [96]. In a recent cross-sectional and longitudinal study, high blood calcium was found to be a strong predictor of future hypertension and linked to a higher risk of developing diabetes, hypertension,

and metabolic syndrome [97]. Both calcium and magnesium imbalances are linked to a higher risk of atrial fibrillation [98]. In addition to frequently causing blood K^+ and Ca^{2+} abnormalities [7], magnesium imbalance precipitates hemodynamic and BP disturbances, and anomalous aldosterone production [99]. For instance, magnesium deficiency is known to cause hypertension and an increase in aldosterone production.

Considering the potential lifelong effects of electrolyte imbalance on the renal and cardiovascular functions, regular blood electrolyte monitoring is warranted in high-risk populations, such as those with CVD, CKD, diabetes, and hypertension. Besides enabling a prompt correction of electrolyte derangements before the onset of SCD-triggering arrhythmias [39], regular monitoring could facilitate drug titration, helping clinicians to continually adjust the dosage of life-saving medications for the maximum benefits without adverse effects [25]. In those at risk of drug-induced dyselectrolytemia, regular monitoring could delay—or even prevent—the development of CRS and the disease progression, thus promoting general long-term health.

1.4. Conclusions of the Chapter

1. Electrolytes (i.e., ions) are one of the many variables that must be kept within pre-defined limits in the blood to maintain homeostasis. They play a vital role in various physiological processes, including generating and conducting action potentials and balancing blood volume and pH. The most important electrolytes for cellular processes are Na^+, K^+, Ca^{2+}, Mg^{2+}, and HCO_3^-.

2. Optimal cell functioning depends on the ECF (i.e., blood) and ICF compartments having different ionic profiles. Na^+, Ca^{2+}, and HCO_3^- are more abundant in the ECF, whereas K^+, and Mg^{2+} are more concentrated in the ICF. Na^+ is essential for fluid balance, BP regulation, and transmission of electrical impulses in the nervous system. K^+ is pivotal in establishing the adequate resting membrane potential to spur action potentials and elicit proper contractility of both skeletal and cardiac myocytes. Ca^{2+} is essential for bone strength, muscular contraction, and the release of neurotransmitters and hormones. Mg^{2+} is involved in energy-production metabolism and neurotransmitter release, and also in the regulation of ion transport in cell membranes. HCO_3^- acts as a buffer of acidic metabolic waste products to maintain an adequate blood pH.

3. Homeostatic regulation of blood electrolytes and fluids falls primarily—but not exclusively—under the responsibility of the kidneys, mediated by RAAS, ADH, natriuretic peptides, PTH, and the SNS. Insulin, vitamin D, and calcitonin are other hormones that regulate blood electrolyte levels.

4. Electrolyte imbalance, or dyselectrolytemia, occurs when blood electrolyte levels fall outside their homeostatic range. It emerges primarily from inadequate in-

take, dysregulated excretion, and transcellular shifts in the case of ICF ions. Dysregulated excretion is the most frequent etiology of electrolyte imbalance, and it is typically caused by renal dysfunction due to direct damage/failure of the kidneys or dysregulation of their hormonal control centers (e.g., RAAS overactivation). Endocrine diseases and medications, namely antihypertensive drugs, engender this hormonal dysregulation.

5. The symptomatology of electrolyte imbalance is broad and usually nonspecific, varying from symptomless to general fatigue and malaise to neuromuscular paralysis and dangerous arrhythmias. The likelihood of clinical manifestations of dyselectrolytemia depends on their severity level, the pace of imbalance onset (i.e., whether the episode is chronic or sudden-onset), concomitant electrolyte or acid-based imbalance, and pre-existent CVD. Dyselectrolytemia is diagnosed with a blood test, and moderate-to-severe episodes require treatment in a healthcare facility.

6. Risk factors of dyselectrolytemia are CKD, CVD, metabolic disorders, such as diabetes, and the usage of certain medications, such as antihypertensive drugs (diuretics and RAASi), β-adrenergic blockers or β-agnostic, corticosteroids, chemotherapy drugs, and psychiatric drugs. Age, cancer, liver disease, and eating disorders also increase the risk of dyselectrolytemia.

7. Dyselectrolytemia has consequences for short- and long-term health. Electrolyte imbalance, particularly that of potassium, can precipitate fatal arrhythmias. In patients with chronic diseases, mild and recurrent dyselectrolytemia episodes induced by suboptimal dosages of antihypertensive and other essential drugs can initiate a vicious cycle of compensatory mechanisms, resulting in the deterioration of the cardiac and renal functions. This deterioration threatens long-term health. Thus, regular blood electrolyte monitoring is essential, not only for preventing fatal arrhythmias in the short term, but also for maintaining homeostasis and promoting general health in the long term.

2. OVERVIEW OF EXISTING APPROACHES FOR ASSESSING BLOOD ELECTROLYTE LEVELS

2.1. Electrolytes and the Heart: Theoretical Framework behind Noninvasive Monitoring of Blood Electrolyte Levels

2.1.1. The heart and its electrical conduction system

The heart is a muscular organ located in the center of the thoracic cavity responsible for pumping nutrient- and oxygen-rich blood through the circulatory system. Anatomically, the heart consists of four chambers, two on each of the left and right sides (Fig. 2.1): the atria (upper chambers) and the ventricles (lower chambers) [100]. These four chambers contract synchronously to pump blood into the lungs (*pulmonary circulation*) and throughout the body (*systemic circulation*). The heart wall is composed of three layers: endocardium (inner), myocardium (middle), and epicardium (outer) [100]. The myocardium is mainly composed of involuntary striated muscle cells known as *cardiomyocytes*, which are the contractile force of the heart [62]. A specialized group of cardiomyocytes with weak contractile properties, called the *pacemaker cells*, is located primarily in the sinoatrial (SA) node on the right atrium wall near the junction of the superior vena cava [62]. Pacemaker cells spontaneously generate the electrical impulses that orchestrate the contraction and relaxation of cardiomyocytes across the myocardium during each heartbeat.

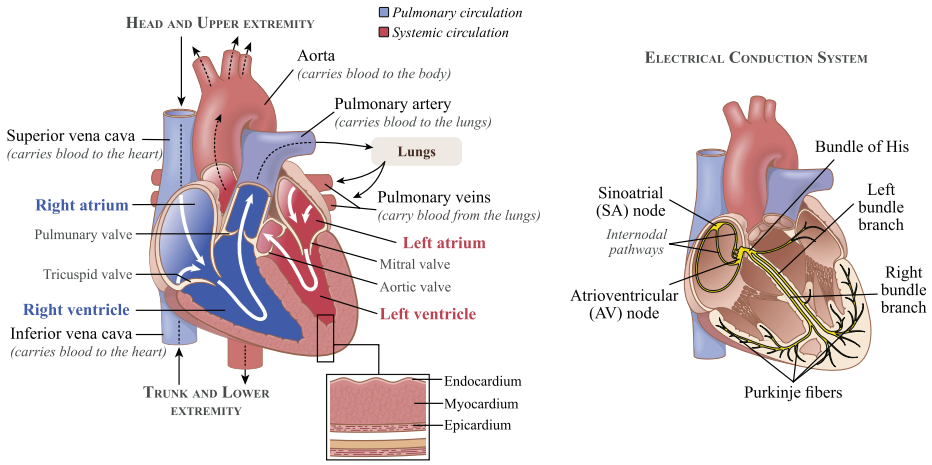

Fig. 2.1. Anatomy (**left**) of the heart and its electrical conduction system (**right**). Adapted from: [2].

One heartbeat, or *cardiac cycle*, is the period from the beginning of one contraction to the onset of the next [2]. Each cycle comprises two phases: *diastole*, during which the heart muscle relaxes and refills with blood, and the subsequent contraction to pump the blood, known as *systole*. In a healthy heart, the cardiac cycle begins in

the SA node with the genesis of electrical impulses by the pacemaker cells [62]. The wave of the generated impulses then propagates through the cardiac conduction system (Fig. 2.1) to activate cardiomyocytes [101]. The atrial myocytes are activated first, starting at the right atrium. The right atrial myocytes are triggered slightly earlier than the left ones and complete their cycle just before left atrial activation [62, 101]. The impulse wave next travels throughout the atrioventricular (AV) node, where conduction is delayed momentarily to allow optimal filling of the ventricles with the blood flowing from the atria. Once the impulse wave passes through the AV node, it spreads swiftly through the His bundle and the right and left bundles, activating the ventricles rapidly and almost simultaneously via a branching network of specialized conducting cells known as the Purkinje system [62, 101].

The atria and ventricles are separated by an electrically inert structure of dense connective tissue designated as *anuli fibrosi*, or the cardiac skeleton. This anatomical framework, along with the electrical delay within the AV node, ensures that the atria and ventricles beat in a synchronized fashion, minimizing the chance of electrical feedback between the chambers [62].

2.1.2. Principles of cardiac electrophysiology

Like any other excitable cells, the contractile forces of cardiomyocytes are activated by oscillations in the cell membrane potential (or voltage), an electrophysiological phenomenon known as an *action potential*. Action potentials (APs) arise from the sequential opening and closing of voltage-gated ion channels embedded in the cell membrane [62]. At different times during the cardiac cycle, the permeability of the cell membrane to specific ions varies, allowing those ions to flow between the intra- and extracellular mediums for a brief moment. This flow of ions creates an electrochemical gradient that alters the membrane potential ($\mathcal{V}_m$) at that given time, triggering the actin-myosin cycling that results in cardiomyocyte contraction [63].

The electrochemical gradient of ions that catalyzes an action potential stems from the potential energy created by the non-equilibrium of ICF and ECF ions. As described in Sec. 1.1.1, the ionic profile between the two fluids is different, which is maintained by cell membranes. Na^+, Ca^{2+}, and HCO_3^- are more abundant in the ECF, whereas the concentration of K^+, Mg^{2+}, and large anionic proteins are higher inside the cells [2]. Two main forces drive ions across the membrane [102]:

- *Chemical*: the ion moves down its concentration gradient from high to low;
- *Electrical*: the ion moves away from molecules of identical charge.

In the resting state of a cell, membranes are impermeable to Na^+ and Ca^{2+}, while K^+ can travel 'freely' via the open channels I_{K_1}. K^+ is at equilibrium, as the outward flow down the K^+ concentration gradient is balanced by an inward flow of K^+ created by the electrical forces exerted by the anionic proteins that cannot cross the membrane. How-

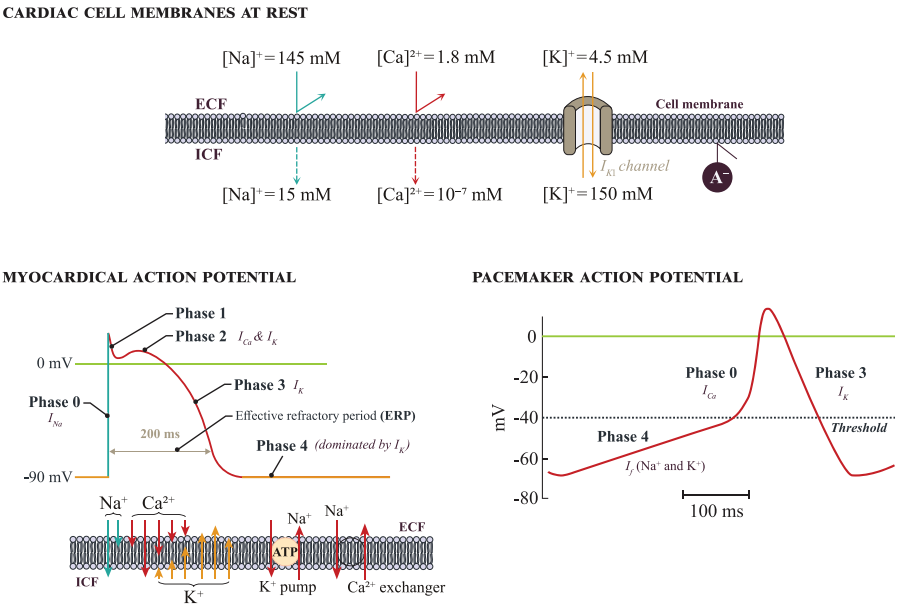

Fig. 2.2. Ionic profile (**top**) of a cardiac cell membrane at rest, and cardiomyocytes action potentials (**bottom**) of non-pacemaker cells in the myocardium (**left**) and pacemaker (**right**) cells in the SA node. Adapted from: [62] and [74].

ever, Na^+ and Ca^{2+} are not at equilibrium and represent potential energy [62]. When ion-selective channels open, Na^+ and Ca^{2+} can flow from the extracellular space, causing $\mathcal{V}_m$ to rise from its negative resting membrane potential ($\mathcal{V}_{rest}$). This sharp rise in $\mathcal{V}_m$ is known as *depolarization*. After reaching its peak potential, the cell membrane undergoes *repolarization*, during which the membrane returns to its static $\mathcal{V}_{rest}$.

Cardiac action potentials

Two AP types can be distinguished in cardiomyocytes: *fast response action potentials*, characterized by their rapid depolarization and prolonged plateau phase, observed in atrial and ventricular myocytes; and *slow response action potentials* found in pacemaker cells that exhibit a slow depolarization and no plateau phase [62]. Both types differ considerably from the APs of other excitable cells: an AP lasts for about 1 ms in neurons, 2–5 ms in skeletal muscle cells, and 200–400 ms in cardiomyocytes [103]. The influx of Ca^{2+} prolongs the AP duration in cardiomyocytes, producing a distinctive plateau phase that other types of excitable cells do not display.

Myocardial action potential

The myocardial AP, also referred to as *fast response action potential*, comprises five phases. It begins and ends with Phase 4 [103], as illustrated in Fig. 2.2. Briefly, each phase is depicted by the following events:

• **Phase 4** denotes the resting state of a cardiomyocyte. The cell membrane is impermeable to most positive ions, including Na^+ and Ca^{2+}, while K^+ is at equilibrium, yielding a resting potential of $\mathcal{V}_{rest} \approx -90\,\text{mV}$.

• **Phase 0** is the rapid depolarization phase triggered by a neighboring cardiomyocyte. The permeability to K^+ drops abruptly as K^+ channels close, and fast Na^+ channels begin to open, slowly leaking Na^+ into the cell. Once $\mathcal{V}_m$ rises to the threshold voltage of $\approx -70\,\text{mV}$, the Na^+ voltage-gated channels open and allow a precipitous inflow of Na^+ until $\mathcal{V}_m \approx 10\,\text{mV}$. These fast Na^+ channels close a fraction of a second after opening, and L-type Ca^{2+} channels open once $\mathcal{V}_m > -40\,\text{mV}$, resulting in a small but steady inflow of Ca^{2+}.

• **Phase 1** represents a partial repolarization due to a decrease in Na^+ permeability. Transient K^+ channels open briefly, and K^+ flows to the outside of the cell, lowering $\mathcal{V}_m$ to about $0\,\text{mV}$.

• **Phase 2** marks the plateau phase, during which the membrane permeability to Ca^{2+} increases, maintaining depolarization and prolonging the action potential. An efflux of K^+ co-occurs with the influx of Ca^{2+} in an electrically balanced countercurrent, and $\mathcal{V}_m$ is maintained slightly below $0\,\text{mV}$ throughout this phase. The constant inward current of Ca^{2+} activates several physiological mechanisms in the excitation-contraction coupling process, eliciting muscular contraction [2, 103].

• **Phase** 3 is the cell membrane repolarization that gradually inactivates Ca^{2+} channels. The persistent outflow of K^+ eventually exceeds the Ca^{2+} inflow and brings the $\mathcal{V}_m$ back towards its $\mathcal{V}_{rest} \approx -90\,\text{mV}$, so the cell is ready for a new cycle of depolarization. Several pumps (e.g., Na^+/K^+-ATPase) return the Na^+ and Ca^{2+} ions to the ECF in exchange for K^+, restoring the cardiomyocyte electrochemical potential. These ionic movements are against the electrochemical gradient and require cellular metabolism energy [42].

Phase 4, also termed the recovery phase, occurs in diastole, whereas depolarization and repolarization (Phases 0–3) occur during systole [42]. The period between the start of depolarization and the activation of the Na^+/K^+–ATPase pumps is known as the *absolute refractory period*, during which the cell is incapable of generating another AP. As more Na^+ channels start to recover, the cell enters its *relative refractory period* during Phase 3. The cell is not yet fully repolarized, but it can generate another AP with more inward Na^+ current.

Pacemaker action potential

Pacemaker APs, or *slow response action potential*, are characteristic of pacemaker cells in the SA and AV nodes. These cells display automaticity and are thus capable of self-initializing depolarization in a rhythmic fashion, in which the cell with

the highest inherent depolarization rate takes over as the primary pacemaker and determines the heart rate [103]. The autonomic nervous system controls the frequency of AP firing: the sympathetic accelerates, whereas the parasympathetic slows the heart rate.

Pacemaker cells have fewer inward I_{K_1} channels than the other cardiomyocytes, so their baseline potential is never lower than $-60\,\text{mV}$. Since fast Na^+ channels need $\mathcal{V}_{rest} \approx -90\,\text{mV}$ to reconfigure into an active state, these channels are permanently deactivated in pacemaker cells, and no rapid depolarization can occur [103]. The pacemaker AP comprises three phases (4, 0, and 3):

- **Phase 4** represents the gradual and initial depolarization of pacemaker cells. The spontaneous inward flow of Na^+ through slow Na^+ channels depolarizes the membrane from $-60\,\text{mV}$ to less than $-55\,\text{mV}$. This small current is known as *funny current*. At $\mathcal{V}_m \approx -55\,\text{mV}$, T-type Ca^{2+} channels open and continue slow depolarization. The slope of Phase 4 dictates the heart rate and varies for pacemaker cells in different regions.
- **Phase 0** is the 'true' depolarization phase, and it starts once $\mathcal{V}_m \geq -40\,\text{mV}$. L-type Ca^{2+} channels open to enable an influx of Ca^{2+} ions, depolarizing the membrane to $\mathcal{V}_m \approx 10\,\text{mV}$. Because Ca^{2+} channels are slower than Na^+ channels, the upstroke is not as steep as Phase 0 of cardiomyocytes.
- **Phase 3** marks the repolarization stage. K^+ channels open to counteract the inward Ca^{2+} flow for a brief plateau phase and then return $\mathcal{V}_{rest} \approx -60\,\text{mV}$.

Heterogeneity of ventricular repolarization

Myocardial repolarization is vastly different from depolarization [62]. For instance, repolarization occurs more gradually than depolarization. For ventricular activation, depolarization arises from the sudden opening of Na^+ channels. In contrast, repolarization occurs with a gradual decrease in Na^+ and Ca^{2+} permeability while more K^+ ions progressively flow inside the cell to restore $\mathcal{V}_{rest}$ [62]. Under normal conditions, when the depolarization wave that originated in the SA node reaches the ventricular myocardium, the His-Purkinje system helps to germinate the electrical impulse throughout all ventricular cells, depolarizing all cardiomyocytes almost simultaneously. However, there is significant ventricular repolarization heterogeneity observed within cell populations of different myocardium regions, each presenting distinct AP duration, morphology, and activation times [48]. Therefore, cardiac repolarization varies not only between cells of different heart chambers (i.e., atria vs. ventricles), but also between cell populations within different regions of the ventricular wall [48, 62].

Anatomically, the ventricular depolarization wave moves from the apex to the base and the endocardium to the epicardium, whereas the repolarization wave moves in the opposite direction, from the epicardium to the endocardium [2]. Thus, cardiomy-

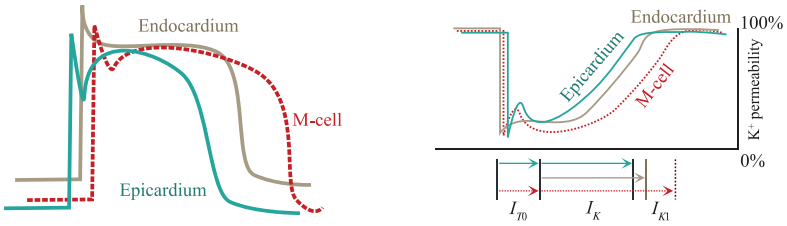

Fig. 2.3. Differences in the action potential morphology and duration (**left**) and K^+ permeability (**right**) after Phase 0 in cell populations within different regions of the ventricular wall. Endocardial cells do not have an I_{t_0} current. Epicardial cells have the shortest action potential duration due to I_{t_0} and I_k currents (increased K^+ permeability). M-cells have a smaller I_{t_0} current than epicardial cells and slower activation of I_k. Adapted from: [62].

ocytes near the epicardium depolarize last but repolarize first. This repolarization heterogeneity stems from dissimilarities in ion channels within each cell population [62], making some cells more permeable to K^+ than others (Fig. 2.3). Epicardial cells, for example, have two K^+ currents (I_{t_0} and I_k) and an increased K^+ permeability, displaying shorter APs than endocardium cells, which present only one current (I_k) [62]. In addition, a specialized group of cells in the 'mid-myocardium' called *M-cells* have slower activation of I_k currents, displaying longer APs, particularly at slower heart rates [62].

Ventricular repolarization heterogeneity is crucial for efficient cardiac contractility and pumping in a normal heart. However, exceeding the physiologically reasonable level of heterogeneity can precipitate life-threatening ventricular arrhythmias [48]. The intrinsic heterogeneity property of ventricular myocytes is the primary reason repolarization is more sensitive than depolarization to changes in the internal environment, such as temperature and electrolyte fluctuations [48]. Thus, abnormal blood electrolyte fluctuations can elicit pathological dispersion of ventricular repolarization, which may have dire consequences.

2.1.3. Physics of electrocardiography

When the depolarization and repolarization waves move throughout the heart, a differential voltage between depolarized cells and adjacent areas still at rest is generated [2]. Since a small portion of this generated electrical current travels all the way to the surface of the body, these differential voltages can be recorded by placing electrodes at strategic points on the skin [62]. The recorded signal is known as the *electrocardiogram* (ECG). The ECG depicts the electrical activity of cardiomyocytes in time across the heart. ECGs are typically displayed in millivolts (mV) and seconds (s) and show a series of peaks and waveforms, each reflecting a specific stage of the cardiac cycle.

An ECG is essentially the sum of all electrical signals produced by depolarization and repolarization, that is, the APs of various cells [62]. As illustrated in Fig. 2.4a, a positive signal is recorded when a wave of depolarization approaches the positive

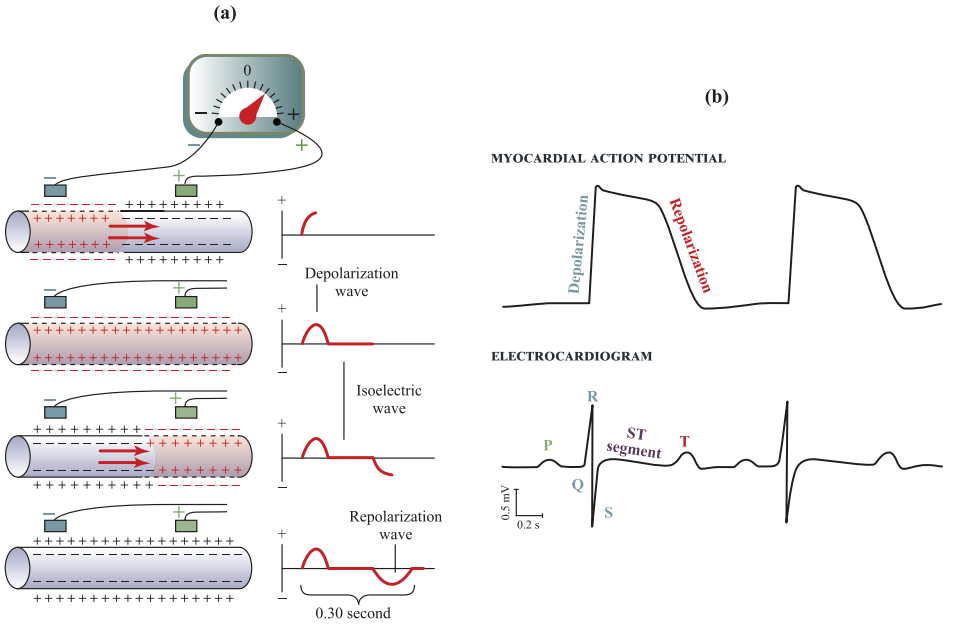

Fig. 2.4. Recording of a depolarization, isoelectric, and repolarization wave (**a**) from a cardiomyocyte and simultaneous recording (**b**) of a myocardial AP and the ECG. Adapted from: [2].

electrode of a recording device. Conversely, a negative signal is registered when the wave moves away from the positive electrode. Isoelectric signals are registered when cells have similar voltages. The amplitude of the recorded signal depends on three variables: *(i)* the amount of depolarized tissue, *(ii)* the direction of depolarization, and *(iii)* the presence of counteracting forces [62]. A wave moving directly toward the positive electrode in a large volume of tissue without any other wave simultaneously traveling away from the same positive electrode will have the largest amplitude.

ECG waveforms

A heartbeat is primarily composed of three waveforms (Fig. 2.4b): the *P-wave*, the *QRS complex*, and the *T-wave*, and one segment: the *ST segment*. The *P-wave* depicts the coordinated depolarization of the right and left atria and the onset of atrial contraction. The *QRS complex* reflects the ventricular depolarization after the activation of the His-Purkinje system and is followed by the *ST segment*, which indicates the period of ventricular contraction. After depolarization, the ventricles begin repolarizing, which is depicted by the *T-wave*.

In a healthy heart, an *isoelectric line* usually follows these waveforms. This line is the baseline of an ECG tracing and denotes the resting membrane potentials (the plateau phase). Occasionally, ECG tracings can display a *U-wave* ensuing the T-wave. U-waves are of small amplitude and are thought to represent delayed repolarization of the Purkinje fibers, although their exact source is unclear.

Other three regions of clinical importance in the ECG waveform are the *RR interval*, the *PR interval*, and the *QT interval*. The *RR interval* is measured between two successive R-waves and indicates the length of a ventricular cardiac cycle, i.e., the heart rate (HR). The *PR interval* is measured from the P-wave onset to the QRS onset and indicates the time required for an AP to travel through the atria. The *QT interval* measures the time between the QRS onset and the T-wave end, i.e., the duration of ventricular depolarization and repolarization. A more thorough description of each waveform and its relationship to the cardiomyocyte AP is outlined in Sec. 2.1.4.

Lead systems and anatomical planes

An ECG waveform is the differential recording between two points on the body, and each differential recording is termed a *lead* [104]. In clinical practice, *lead configurations* with standardized electrode positions are used to assess the electrical activity in the heart from various planes [62], with the standard 12-lead ECG being the most widely used configuration. The selection of a particular lead configuration depends on the type of desired clinical information. For instance, 12-lead ECGs are necessary to evaluate the whole heart structure, but two-to-three leads suffice to assess heart rate and rhythm disorders [104]. For ambulatory monitoring, the patient's comfort throughout the recording period is another factor to be considered when selecting a lead configuration. A higher number of leads permits more accurate diagnoses but requires more electrodes to be placed on the skin. It is discomforting and inconvenient for patients to wear several electrodes for prolonged periods and can result in premature self-termination of the recording in long-term monitoring scenarios.

The standard 12-lead system

The standard 12-lead ECG is the most popular lead configuration used in routine care as it provides a three-dimensional (3D) representation of the electrical activity of the heart [62]. Six *frontal leads* record the cardiac electrical activity in the frontal (vertical) plane (Fig. 2.5). In contrast, the other six *precordial leads* (Fig. 2.5) explore the flow of depolarization and repolarization in the transverse (horizontal) plane [104].

Frontal leads

The frontal leads are divided into two groups of three: the *standard limb* leads $\{I, II, III\}$, and the *augmented voltage* leads $\{aVR, aVF, aVL\}$. Since these leads are mathematically interdependent, registration of only leads I and II suffices to derive the remaining frontal leads [2]. According to Einthoven's law:

$$\text{Lead } II = \text{Lead } I + \text{Lead } III. \tag{2.1}$$

Lead I, positioned at 0°, is the reference lead and shows the electric impulse con-

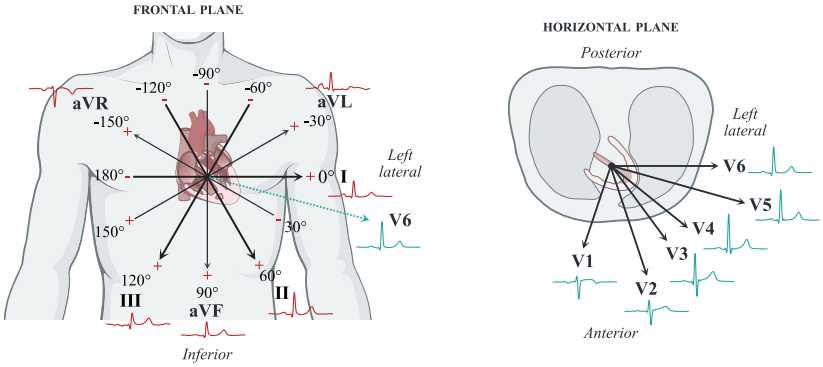

Fig. 2.5. Standard 12-lead ECG in the frontal (**left**) and horizontal (**right**) planes.

duction from a subject's left-hand side. Leads *II* and *III* look at the heart at respective angles of 60° and 120° clockwise from lead *I*. *aVL* shows the heart from the left (L stands for left) and is placed at 30° anticlockwise from lead *I*. By convention, anticlockwise movement is negative. *aVR* is positioned at −150° from lead *I*, is orthogonal to lead *III*, and looks at the from the right side (R is for right). Both *aVL* and *aVR* are set at 30° off the horizontal plane. *aVF* is perpendicular to lead *I* clockwise and looks at the heart straight up from the feet (F stands for feet) [104]. Leads *I*, *aVL*, and *−aVR* are often designated as *lateral leads*, and leads *II*, *aVF*, and *III* as known as the *inferior leads* [62].

Precordial leads

The *precordial leads*, *V1–V6*, are placed anteriorly on the surface chest wall in an arc. *V1* and *V2* are the *septal leads* and are placed in the fourth intercostal space to the right and left of the sternum, respectively. *V1–V2* primarily observe the ventricular septum. *V3*, positioned diagonally between *V2* and *V4*, and *V4*, placed between the fifth and the sixth ribs in the midclavicular line, are the *anterior leads* and examine the anterior wall of the left ventricle. *V5* and *V6* are the *anterolateral leads* and observe the lateral wall of the left ventricle. *V5–V6* are positioned on the same level as *V4*, with *V5* in the anterior axillary and *V6* in the midaxillary lines.

Since the *precordial leads* only examine the electrical activity of the left ventricle, supplementary right chest leads *V3R–V6R* can be placed on the anatomical locations of the left-sided counterparts if there is suspicion of right ventricular infarction [62, 104].

The orthogonal-lead system

An orthogonal-lead system reflects the electrical activity of the heart in three orthogonal planes [104, 105]: *frontal* (*XY*), *transverse* (*XZ*), and *sagittal* (*YZ*). Lead *X* examines the heart in the right-left axis, lead *Y* explores the head-to-feet axis, and lead

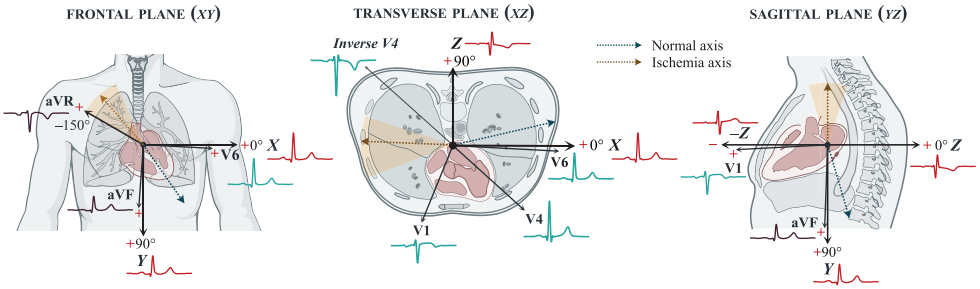

Fig. 2.6. Electrical activity of the heart in the frontal, transverse, and sagittal planes of an orthogonal-lead system. Dashed arrows represent the mean electrical axis of a normal and an ischemic heart. Adapted from: [106].

Z investigates the front-back axis (Fig. 2.6 and Fig. 2.7). Leads *XYZ* are used to obtain a vectocardiogram (VCG) which depicts the trajectory of the conduction vector of the depolarization and repolarization waves during the cardiac cycle. The ECG waveforms are represented as loops in the VCG.

The conduction vector changes rapidly in length and direction as the electrical impulse spreads through the heart [2]. It increases and decreases in magnitude (length) as the voltage of the vector varies and changes direction according to the average direction of the electrical potential from the heart. As depicted in Fig. 2.7, the vector ($\vec{v}_1$) extends downward toward the apex when the septum first becomes depolarized. This initial vector is relatively weak and denotes the first portion of the ventricular VCG. As more of the ventricular muscle depolarizes, the vector becomes stronger ($\vec{v}_2$ to $\vec{v}_4$), changing in direction as the depolarization wave spreads through the myocardium. Once the ventricles have become fully depolarized, the vector becomes zero ($\vec{v}_5$) since there is no electrical potential [2]. The figure generated by the positive ends of the vector renders the VCG loop.

The most recognized orthogonal-lead system is the Frank lead system [107], which is derived as linear combinations of seven electrodes on the chest, back, neck, and left foot (Fig. 2.7). However, leads *XYZ* are not routinely used in clinical practice, and orthogonalization methods [108, 109] are typically applied to 12-lead ECGs to reconstruct leads *XYZ* when orthogonal leads are required.

Cardiac electrical axis

During most of the ventricular depolarization cycle, the direction of the conduction vector is from the base of the ventricles toward the apex. This preponderant direction is known as the *mean electrical axis* of the ventricles (Fig. 2.8), and it provides clinically important information about their musculature and structure [2]. In a normal heart, the mean electrical axis averages at about 59°, although it can swing from 20° to 100°. Axis deviations beyond the normal range are associated with various

heart conditions, depending on which ventricle they affect. For instance, a *left axis deviation* (–30° to –90°) is present in left ventricular hypertrophy (LVH), hypertension, and hyperkalemia. Conversely, a *right axis deviation* (90° to 180°) is observed in right ventricular hypertrophy, right bundle branch block, and ventricular ectopic rhythms. Extreme deviations (180° and –90°) rarely occur in clinical practice.

Although the electrical axis should be determined in orthogonal-lead systems, the standard limb leads are usually used as an alternative [2]. If the QRS wave is biphasic, the electrical axis is directed to the front or back in the transverse plane and cannot be determined without lead *Z*.

2.1.4. Influence of blood electrolytes on ECG morphology

As outlined in Sec. 2.1.3, the ECG reflects the sum of all electrical signals of cardiomyocytes at a given time throughout their depolarization and repolarization cycle. The cycles (i.e., APs) require blood electrolyte levels to be maintained within specific values to preserve the normal $\mathcal{V}_{rest}$. Alterations in $\mathcal{V}_{rest}$ interfere with the normal flow of ions across cell membranes required to generate and conduct APs to elicit a healthy and synchronous heart contraction. When $\mathcal{V}_{rest}$ is altered, cells become either hyperpolarized (more negative $\mathcal{V}_{rest}$) or hyperexcitable (less negative $\mathcal{V}_{rest}$), and either of these issues can lead to an abnormal cardiac output, heart rate, and dangerous arrhythmias. *Hyperpolarization* can precipitate bradycardia since cells with a more negative $\mathcal{V}_{rest}$ require a higher voltage to be stimulated and initiate muscle contraction. Conversely, less negative $\mathcal{V}_{rest}$ in *hyperexcitability* translates into a perpetuating flow of ions and spontaneous AP generation, causing the heart to contract too fast and inefficiently [7, 62].

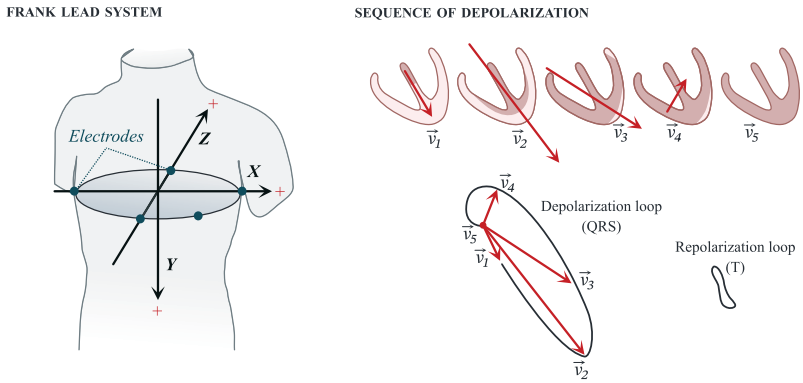

Fig. 2.7. Electrode placement (**left**) of Frank lead system for VCG registration. Changes in the magnitude and direction of the conduction vector (**right**) during the sequence of ventricular depolarization and its respective VCG loop. $\vec{v}_1$ is the vector at the start of depolarization in the septum. $\vec{v}_2$, $\vec{v}_3$ and $\vec{v}_4$ represent the state of depolarization 0.02 s, 0.04 s, and 0.05 s after $\vec{v}_1$. $\vec{v}_5$ marks the complete depolarization of ventricles. Adapted from: [2].

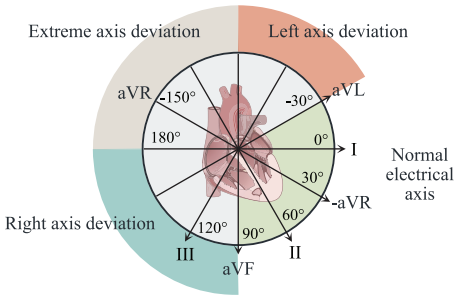

Fig. 2.8. Illustration of the ranges of normal, left, right, and extreme electrical axis of the heart.

Abnormal blood electrolyte levels derange the normal cycle of depolarization and repolarization by altering $\mathcal{V}_{rest}$, engendering either hyperpolarization or hyperexcitability. Since the ECG reflects the cardiomyocyte APs, morphology deviations from the typical ECG waveform can indicate electrolyte imbalance [42,62]. Thus, ECGs can be a tool for noninvasive blood electrolyte monitoring.

To properly grasp the association between ECG patterns and blood electrolytes, it is vital to understand the modulating relationship between a specific electrolyte and the AP shape and duration throughout the cardiac conduction system. This Section describes the influence of blood electrolytes on ECG morphology. The ECG patterns of homeostatic blood electrolyte levels, i.e., the patterns that relay a healthy generation and conduction of APs in the heart, are introduced first, and the patterns of electrolyte imbalance are presented afterwards.

ECG patterns of electrolyte balance

When blood electrolyte levels are within their homeostatic range, the cardiomyocyte AP, whether of a fast or slow response, unrolls as described in Sec. 2.1.2. Provided that no structural heart disease is present, the electrical impulse generated in the SA node travels through the cardiac electrical system, rendering an ECG waveform resembling the one illustrated in Fig. 2.9. The relationship of each ECG component with the cardiac AP is as follows.

Atrial depolarization—the P-wave

The P-wave reflects atrial depolarization of pacemaker cells, which initiates at the SA node. Since the right atrium depolarizes earlier than the left one, the first portion of the P-wave corresponds to right atrial depolarization, whereas the terminal portion reflects the left one [62]. Atrial depolarization (and hence P wave duration) generally lasts 0.1 s [103]. Atrial repolarization is not observable in the ECG [62].

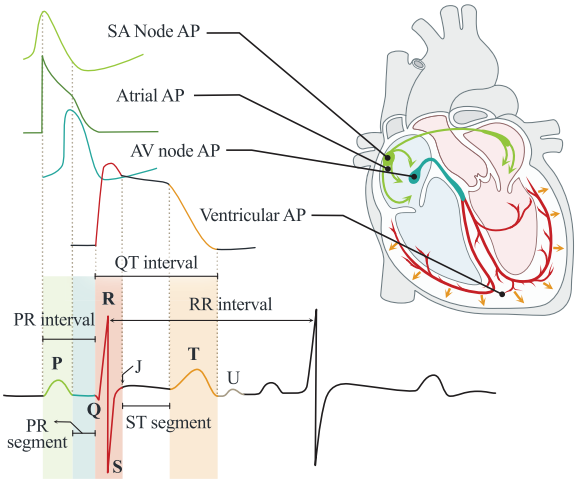

Fig. 2.9. Genesis of a normal ECG waveform in electrolyte balance. Adapated from: [74].

Atrioventricular conduction—the PR interval

The PR interval measures the time between the onsets of atrial and ventricular depolarization, usually ranging from 0.12–0.2 s [103]. The brief isoelectric period after the P-wave conveys the time the atria are fully depolarized, and the impulse travels within the AV node, where the conduction speed drops [103] due to the absence of Na^+ channels. The activation of the AV node begins at some point in the middle-terminal portion of the P-wave [62].

Ventricular depolarization—the QRS complex

The QRS complex typically comprises three waves: Q (negative deflection), R (large positive deflection), and S (negative deflection). It reflects ventricular depolarization after activation of the His-Purkinje system and is usually the largest amplitude waveform in the ECG (5–15mV) [62]. It lasts 0.06–0.1 s [103]. The sum of *Phases 0 and 1* of the ventricular AP, characterized mainly by the inflow of Na^+, yields the total duration and amplitude of the QRS complex [42]. Depolarization of the His-Purkinje system cannot be measured from the surface ECG as the total mass of the cardiac tissue is too small, unlike ventricular depolarization [62].

Beginning of ventricular contraction—the ST segment

The ST segment marks *Phase 2* (plateau) of the AP [42] in which an influx of Ca^{2+} occurs, and the ventricles begin to contract. It is generally isoelectric in healthy hearts, although some healthy individuals also display a non-pathological elevated ST segment [62].

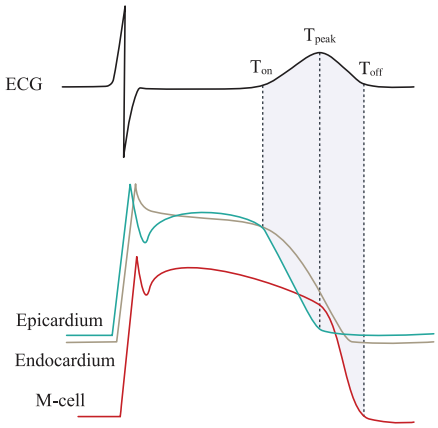

Fig. 2.10. Cellular explanations for T-wave genesis. In experimental preparations, the T-wave onset (T_{on}) coincides with the beginning of the separation of Phase 3 of the AP of epicardial and endocardial cells since repolarization starts earlier in the epicardium. The T-wave peak (T_{peak}) and offset (T_{off}) coincide with complete repolarization of the epicardial and M-cells, respectively. Adapted from: [62].

Ventricular repolarization—the T-wave

The T-wave reflects ventricular repolarization and is of comparable duration to that of *Phase 3* of the cardiomyocyte AP [42], in which an outward flux K^+ occurs to restore $\mathcal{V}_{rest}$. The slope of the terminal portion of the T-wave is analogous to the slope of Phase 3 [42]. In experimental studies, the T-wave onset seems to coincide with the separation of the repolarization phase of the epicardium from the endocardium and M-cells [62]. This gradual separation is why the accurate identification of the T-wave onset is often challenging. The T-wave peak matches the ending of epicardial repolarization, whereas the offset corresponds to the completion of M-cells repolarization (Fig. 2.10) and ventricular ejection [42].

T-waves are generally lower in amplitude than the QRS complex due to several factors. First, the repolarization rate is slower than depolarization as the opening of Na^+ channels involved in depolarization is sudden, whereas repolarization occurs with a gradual increase in K^+ permeability and ejection of Na^+ and Ca^{2+} to the ECF. Second, the His-Purkinje system facilitates simultaneous depolarization so that several cells initiate Phase 0 almost concurrently. In contrast, ventricular repolarization is heterogeneous as different cell populations repolarize at different times (Sec. 2.1.2).

Ventricular AP duration—the QT interval

The QT interval indicates the ventricular AP duration and is measured from the Q-wave onset to the T-wave offset. Its duration ranges from 0.2–0.4 s and depends on the heart rate. Higher heart rates entail fast contraction and, thus, shorter ventricular APs and QT intervals.

ECG patterns of electrolyte imbalance

Abnormal blood electrolyte levels predominantly affect the electrical activity of the ventricles, disturbing the shape and duration of the ventricular AP [42], in particular, that of repolarization. The intrinsic heterogeneity property of ventricular repolarization makes it much more vulnerable than depolarization to derangements in the internal environment, even in settings of only minor deviations from the homeostatic range [48]. Thus, the ECG patterns of dyselectrolytemia generally involve some form of morphological alterations in the post-depolarization ECG components—the *ST segment (Phase 2)* and the *T-wave (Phase 3)*.

Out of all ions playing a role in AP generation and propagation, Ca^{2+} and K^+, i.e., the central ions in Phase 2 and Phase 3, are the ones that exert the most prominent effects on the ventricular AP [62]. For this reason, potassium and calcium imbalances produce the most specific changes in the ventricular AP morphology and are the dyselectrolytemias with the most characteristic ECG patterns [42].

However, the electrocardiographic patterns of dyselectrolytemia vastly depend on the complete blood electrolyte profile. The ECG manifestations of isolated dyselectrolytemia (i.e., imbalance of only one electrolyte) do not always correlate with the anticipated patterns of the same dyselectrolytemia when concomitant with other electrolyte imbalances. Furthermore, the effects of the same dyselectrolytemia can differ within separate heart regions [7]. The mechanisms behind the ECG patterns of various dyselectrolytemias, their effects on the cardiac AP, and their interrelationship with other ions are elucidated below.

Potassium

The most determining ion of $\mathcal{V}_{rest}$ and repolarization is K^+. It exerts its electrophysiological effects directly on the membrane permeability to K^+ as the conductance of the I_{K_1} channels is proportional to the square root of blood $[K^+]$ [7]. Higher $[K^+]$ signifies that more ions flow into the cell until a less negative $\mathcal{V}_{rest}$ is reached [62], shortening the AP duration and increasing hyperexcitability. Conversely, low $[K^+]$ does not allow an adequate inward flow of K^+, resulting in hyperpolarization and subsequent longer AP [7]. Potassium imbalance disturbs Phase 3, leading to delayed (in the case of *hypokalemia*) or accelerated (in the case of *hyperkalemia*) repolarization rates that alter the T-wave morphology. Both hypo- and hyperkalemia decrease the AV conduction velocity and can exacerbate AV block [42].

Hyperkalemia

Cells become hyperexcitable when K^+ accumulates in the blood. Hyperkalemia produces three changes in the AP: *(i)* shortened duration, *(ii)* accelerated repolarization rate, reflected by a steeper curve of Phase 3, and *(iii)* a progressively less negative

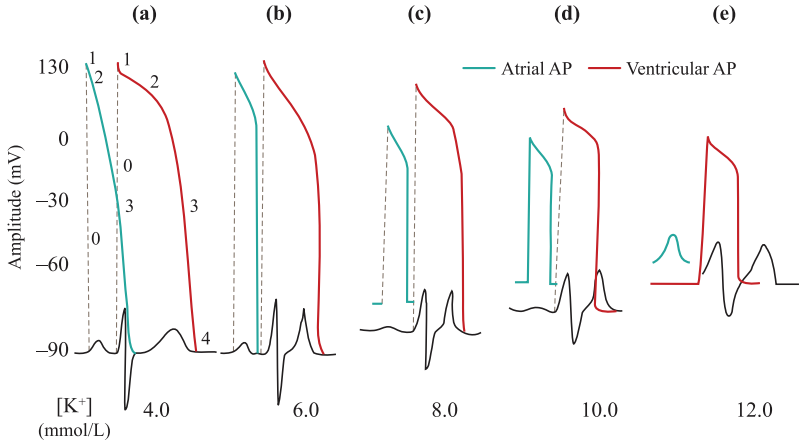

Fig. 2.11. Diagram of an atrial and ventricular AP superimposed on the ECG with different extracellular blood potassium concentrations: (**a**) potassium balance and (**b**) mild-to-moderate, (**c**) moderate-to-severe, (**d**) severe, and (**e**) life-threatening hyperkalemia. Adapted from: [7].

$\mathcal{V}_{rest}$ as $[K^+]$ rises, leading to partial membrane depolarization [42, 62]. Such partial depolarization reduces the number of Na^+ channels available to open in the resting state, thus impairing normal depolarization (Phase 0) of some cells [62]. Fig. 2.11 illustrates the ECG manifestations of hyperkalemia.

Hyperkalemia shortens the plateau phase of Purkinje fibers, decreasing the dispersion and heterogeneity of ventricular repolarization [7]. The atrial myocardium is the most vulnerable to high $[K^+]$, the ventricular myocardium is mildly vulnerable, and the specialized tissue (SA node and His bundle) is the least sensitive to hyperkalemia [7]. Thus, the excitability and conduction in the atria decrease at milder hyperkalemia levels than in other types of myocardial tissue [42].

ECG patterns of mild hyperkalemia. Prominent and narrow (i.e., peaked) T-waves are the earliest manifestation of hyperkalemia, occurring when $[K^+] \geq 5.5\,\text{mmol/L}$ and usually before any concomitant QRS changes [42]. Such peaked T-waves are typically visible in precordial leads [62]. If no cardiac structural abnormalities exist and the ST segment is regular, the QT interval is either normal or slightly decreased [42].

ECG patterns of moderate hyperkalemia. QRS changes usually become perceptible when $[K^+] \geq 6.5\,\text{mmol/L}$. The progressive lowering of $\mathcal{V}_{rest}$ slows intraventricular AP conduction, resulting in a less sharp Phase 0 and a uniform widening of the QRS [7, 42]. Widened initial and terminal portions characterize the QRS in hyperkalemia, differing from the one seen in bundle branch block, in which only one portion of the QRS widens. Such uniformly widened QRS is recognizable by deep S waves in leads *I* and *aVL* [62]. Despite the shortened AP duration, the QRS length roughly correlates with the degree of hyperkalemia [42].

ECG patterns of severe hyperkalemia. When $[K^+] \geq 7.0$ mmol/L, atrial excitability and AV conduction decrease, altering the P-wave amplitude (↓) and duration (↑) while prolonging the PR interval. At $[K^+] \geq 8.8$ mmol/L, the P-wave is usually invisible [7,42]. Low-amplitude or absent P-waves alongside wide QRS complexes help to distinguish hyperkalemia from intraventricular conduction disturbances of other origins [42].

ECG patterns of life-threatening hyperkalemia. Ventricular repolarization becomes extremely slow when $[K^+] \geq 10.0$ mmol/L, with large portions of the myocardium undergoing repolarization before depolarization is completed. At this stage, the delineation of the QRS complex is difficult or impossible [42]. If $[K^+]$ continues to rise, the QRS and T-waves merge into a 'sine wave', a preterminal rhythm almost identical to ventricular tachycardia or fibrillation [110].

Hypokalemia

Cells become hyperpolarized when blood $[K^+]$ drops below normal levels [7,42]. Hypokalemia produces three changes in the AP: *(i)* prolonged duration, *(ii)* delayed repolarization rate, marked by changes in the slope shape of Phase 3, and *(iii)* $\mathcal{V}_{rest}$ to below −90 mV. A more negative $\mathcal{V}_{rest}$ causes cells to be less excitable, and a greater-than-normal stimulus is required to spur depolarization. Without a sufficient inward flow of K^+, the repolarization rate is delayed, prolonging the AP. The repolarization slope of Phase 3 decelerates gradually with the progressive decrease in blood $[K^+]$, changing its morphology from convex to concave [42]. In contrast, the slope of Phase 2 steepens [42]. In the ECG, these changes in the AP shape and duration translate into broader and lower-amplitude T-waves, ST depression, and discernable U-waves (Fig. 2.12), which become progressively more pronounced with decreasing blood $[K^+]$ [42, 110].

Repolarization delays essentially slow down the conduction velocity in the heart, thus increasing the dispersion of ventricular repolarization. Hypokalemia decreases membrane excitability during diastole, particularly in Purkinje fibers, which can induce automaticity and potentially arrhythmogenic depolarizations in these cells [7].

ECG patterns of mild hypokalemia. Broader and lower-amplitude T-waves are the earliest ECG manifestation of mild hypokalemia ($3.0 \text{ mmol/L} \leq [K^+] < 3.5 \text{ mmol/L}$). However, such ECG patterns do not usually emerge until there is a moderate degree of hypokalemia.

ECG patterns of moderate hypokalemia. Once blood $[K^+] \leq 2.7$ mmol/L, the electrocardiographic patterns of hypokalemia become more prominent [42]. T-waves begin to broaden and flatten, P-waves increase in amplitude, and the PR interval elongates. In some patients, T-wave inversion is also observable. ST depression becomes noticeable alongside U-waves in leads *V2–V3*. These two leads usually show the most pronounced elevation of U-waves, which also become more negative in leads that al-

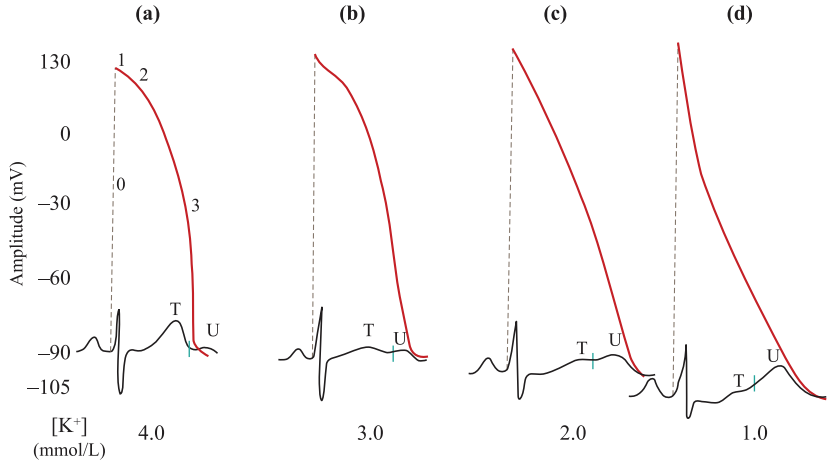

Fig. 2.12. Diagram of the ventricular AP superimposed on the ECG with different extracellular blood potassium concentrations: (**a**) potassium balance, and (**b**) mild-to-moderate, (**c**) moderate-to-severe and (**d**) severe-to-dangerous hypokalemia. Adapted from: [7].

ready display inverted U-waves under normal conditions, such as in the lead *aVR* [42]. The QRS complex also widens and increases in amplitude, albeit seldom by more than 0.02 s [42]. Patients can begin to develop ventricular extrasystoles [110].

ECG patterns of severe hypokalemia. The T- and U-waves fuse into one in more advanced stages of hypokalemia, making the QT interval appear longer [7, 42]. Nevertheless, as long as a notch separates the two waves, the QT interval remains unchanged [42]. The precise duration of the T-wave and the QT interval should be assessed in the lead with the lowest U-wave voltage, typically *aVL* [42].

ECG patterns of life-threatening hypokalemia. Isolated hypokalemia becomes dangerous once $[K^+] \leq 1.9$ mmol/L as patients develop ventricular fibrillation or supraventricular tachyarrhythmias that can result in cardiac arrest. Moderate hypokalemia with concomitant hypomagnesemia is also potentially fatal.

Some physicians suggest that the main ECG pattern of hypokalemia is a *bifid/notched T-wave* rather than the emergence of *U-waves*, in which the onset, the first and second peaks, and the offset of the T-wave (Fig. 2.13) correlate with the hypokalemia-induced repolarization delay of the various cell populations within the ventricular wall [62]. This rationale is grounded in the fact that the pattern of hypokalemia corresponds to a gradual shift of the primary repolarization wave from systole (T-wave, Phase 3) into diastole (U-wave, Phase 4) caused by the prolongation of ventricular repolarization [42]. Prominent ”U-waves” result from an almost complete split between the repolarization of the endocardium and myocardium cells [62] and can therefore be considered an extension of ventricular repolarization rather than a separate

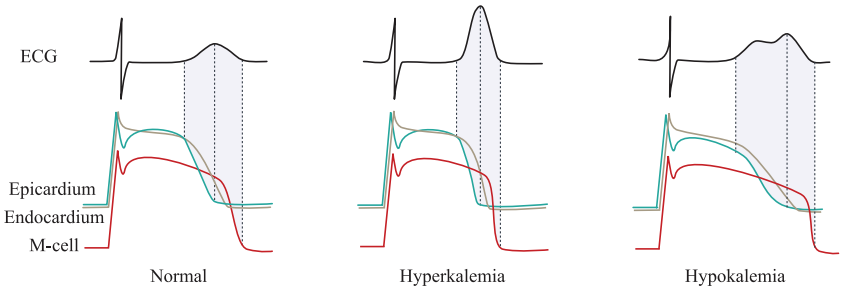

Fig. 2.13. Cellular explanations for the genesis of ECG patterns of hyper- and hypokalemia in different cell populations within the ventricular wall. In hyperkalemia, Phase 3 (repolarization) becomes steeper for all three cell types, and AP duration becomes similar, leading to a narrower and peaked T-wave. In hypokalemia, Phase 3 is less steep, and the differences in AP duration between the three cell types are magnified, resulting in a bifid/notched T-wave. The first peak coincides with the separation between endocardial and M-cell repolarization. The second peak occurs when the epicardium is fully repolarized. Adapted from: [62].

cardiac event. The nomenclature of U-waves in hypokalemia is, nonetheless, widely adopted in the literature and will continue to be employed throughout this thesis.

Calcium

While Ca^{2+} has no appreciable effect on $\mathcal{V}_{rest}$, abnormal blood $[Ca^{2+}]$ disrupts Phase 2 and, consequently, the AP duration—*hypocalcemia* prolongs Phase 2, whereas *hypercalcemia* shortens it. In the ECG, alterations in the ST segment morphology and length usually reflect Phase 2 disturbances induced by abnormal $[Ca^{2+}]$ (Fig. 2.14).

Generally, only severe calcium imbalances produce clinically significant electrophysiological effects in the heart if there is no concurrent imbalance of another electrolyte [7]. However, blood $[Ca^{2+}]$ can impair cardiac contractility and indirectly affect repolarization. Ca^{2+} controls the speed of time-dependent processes which eventually trigger repolarization and activate the conductance of K^+ channels during Phase 3 [111]. The higher is the plateau voltage, the earlier the cell repolarizes [111].

Mild-to-moderate calcium imbalances become particularly relevant in blood potassium abnormalities since Ca^{2+} and K^+ have antagonistic effects on the cardiac electrical activity. Increased $[Ca^{2+}]$ reverses the intra- and atrioventricular conduction disturbances induced by hyperkalemia, whereas, conversely, low $[Ca^{2+}]$ countervail the harmful effects of hypokalemia [42].

Hypercalcemia

Higher-than-normal blood $[Ca^{2+}]$ favors earlier repolarization, producing two changes in the AP: *(i)* shortened plateau and total AP durations [7]; and *(ii)* reconfigured ventricular AP shape to one resembling that of a normal atrial AP [42]. Shortening of Phase 2 is a counterintuitive electrophysiological consequence of hypercalcemia

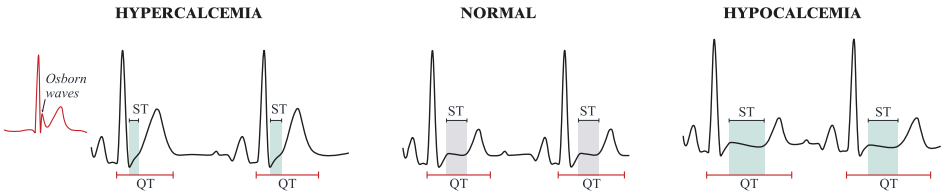

Fig. 2.14. ST segment and QT interval differences in calcium balance and hyper- and hypocalcemia.

given that higher blood [Ca^{2+}] would, presumptively, increase the inward flow of Ca^{2+} and prolong the AP plateau instead [112]. Animal studies suggest that a voltage decrease in the Na^{+}-Ca^{2+} exchange current and the earlier activation of the potassium I_{K_1} channels are the primary underlying mechanisms for the AP shortening and impaired cardiac contractility in hypercalcemia [7, 112].

In contrast to hyperkalemia, hypercalcemia leads to hyperpolarization. If cells are hyperexcitable due to a less negative $\mathcal{V}_{rest}$ as in hyperkalemia, elevated blood [Ca^{2+}] stabilizes the membrane by shifting the threshold potential to lower values. Thus, a higher magnitude of depolarization is required to elicit contraction [7].

ECG patterns of mild-to-moderate hypercalcemia. A shortened or absent ST segment is the characteristic ECG pattern of hypercalcemia [7, 112]. The ST segment shortening leads to a short QT interval of less than 0.4 s, often even shorter than 0.35 s. In moderate hypercalcemia ([Ca^{2+}] $\geq$ 2.0 mmol/L), T-waves begin immediately after the QRS complex. Occasionally, T-waves even emerge before the QRS returns to baseline, and no intervening ST segment exists, resulting in an ECG pattern mimicking the 'ST elevation' observed in myocardial infarction [62].

ECG patterns of severe hypercalcemia. When [Ca^{2+}] $\geq$ 2.5 mmol/L, changes in the T-wave polarity and amplitude can occur [112]. Patients typically display prominent J waves (*Osborn waves*) in precordial leads. These waves widen the QRS complex and lengthen the QT interval back to its typical duration [62].

Hypocalcemia

Low blood [Ca^{2+}] reduces the inward flow of Ca^{2+} ions during Phase 2 [112], prolonging the plateau and AP duration [112]. Hypocalcemia induces the opposite effect of hypercalcemia in the AP duration but does not disturb Phase 3 if no other concomitant electrolyte imbalances exist [42]. The ECG hallmark of hypocalcemia is QT interval prolongation secondary to a lengthened ST segment, while the T-wave duration remains unaltered [112]. No other metabolic abnormalities modify the ST segment without simultaneously altering the T-wave duration [42].

Hypocalcemia causes neuromuscular hyperexcitability, leading to involuntary muscle contraction and overly stimulated nerves. This hyperexcitability can counteract

the hyperpolarization induced by hypokalemia. Smaller ICF [Ca^{2+}] also compromise the excitation-extraction coupling mechanism and, consequently, cardiac and muscle contractility [112].

ECG patterns of mild-to-moderate hypocalcemia. When blood [Ca^{2+}] drops below its homeostatic limits, the QT interval elongates due to ST-segment lengthening while the T-wave duration is unaffected [112]. The severity of hypocalcemia correlates with the degree of QT prolongation [62], but the QT interval rarely exceeds 140% of its regular duration [42].

ECG patterns of severe hypocalcemia. In extreme cases of isolated hypocalcemia, the T-wave polarity can reverse. For instance, the T-wave may become flat or inverted (but never narrower or broader) in leads with an upright QRS complex, simulating the ECG pattern of myocardial ischemia [42, 62].

Magnesium

Although Mg^{2+} is not explicitly involved in any phase of the AP, blood [Mg^{2+}] abnormalities still affect cardiac function. Mg^{2+} is essential for stabilizing excitable membranes as it regulates ion channels and the inward flow of Ca^{2+}, acting as a natural Ca^{2+} antagonist [113]. Its effects emulate those of Ca^{2+}-channel blockers. In addition, Mg^{2+} contributes to an effective activation of the Na^{+}/K^{+}-ATPase pumps [113], which transport K^{+} into and Na^{+} out of cells during Phase 4. Thus, abnormal blood [Mg^{2+}] dysregulates the normal functioning of ion channels and pumps, affecting the transmembrane equilibrium of K^{+} [7, 114], which then encumbers repolarization and proper restitution of $\mathcal{V}_{rest}$.

The modulating relationship between Mg^{2+} and the other ions often results in Ca^{2+} or K^{+} imbalance alongside abnormal blood [Mg^{2+}]. Since isolated magnesium imbalance seldom occurs in clinical practice, and the knowledge of the influence of Mg^{2+} on the different phases of the cardiac AP is lacking [113], the ECG patterns of magnesium imbalance are nonspecific [7], not yet clearly defined [113], and often questioned. Nevertheless, the ECG patterns of magnesium imbalance reported thus far are described below.

Hypomagnesemia

Hypomagnesemia increases cardiac excitability, leading to a higher frequency of atrial and ventricular premature beats [7, 115]. However, failure to maintain intracellular K^{+} levels due to impaired activation of *Na^{+}/K^{+}–ATPase* is believed to be the primary cause of premature beat occurrence [115]. While low Mg^{2+} levels inhibit the slow inward current of Ca^{2+} channels, thus shortening Phase 2 [114], some studies indicate that magnesium deficiency had little effect on the AP in the presence of normal

blood [Ca^{2+}] [42]. Parallelly, hypomagnesemia exacerbates the effects of low blood [Ca^{2+}], further accentuating the ECG patterns of hypocalcemia [42].

Low blood [Mg^{2+}] is associated with frequent premature beats [7] and sinus tachycardia [114]. In a study performed in 2021, patients with isolated hypomagnesemia displayed prolonged P-waves, QT intervals, T peak-to-end intervals (Tpe), and a higher TPe/QT ratio [113], but other studies have not yet corroborated these ECG findings. Flattened [115] or biphasic [7] T waves have also been reported.

Hypermagnesemia

High blood [Mg^{2+}] depresses AV and intraventricular conduction [7] and prolongs the sinus recovery time. In the ECG, hypermagnesemia can manifest as a significantly prolonged PR interval, longer QT and JT intervals [116], peaked T-waves, and bradycardia [115]. Since Mg^{2+} exerts modulating effects on several K^+ currents and blocks Ca^{2+} channels, hypermagnesemia corrects the effects of hyperkalemia to some degree [7, 114].

Sodium

Na^+ is the primary determinant of the upstroke velocity and amplitude of Phase 0 of the AP [7]. Na^+ conductance increases rapidly with AP initiation, allowing the Na^+ gradient to dictate the first phase of the action potential and, consequently, its ultimate configuration [7]. Thus, hypernatremia increases and hyponatremia decreases Phase 0 by altering the transmembrane Na^+ gradient [7, 42].

When the intraventricular conduction velocity is delayed, high [Na^+] restores its normal velocity [42]. Accordingly, hypernatremia negates many of the electrophysiological consequences of hyperkalemia [7], shortening the wide hyperkalemia-induced QRS complex to its typical duration. Nevertheless, the effects of sodium on the electrophysiologic properties of cardiomyocytes are rarely of clinical importance, despite the high frequency of sodium imbalance in various populations [7]. In the absence of intraventricular conduction disturbances, whether instigated by additional electrolyte abnormalities or other causes, sodium imbalance does not appreciably affect the ECG pattern [42].

Bicarbonate

Metabolic acidosis and alkalosis induce transmembrane K^+ shifts, leading to hyperkalemia and hypokalemia [117], respectively, thus modifying the ECG patterns similarly to potassium imbalance [42]. Whether abnormal blood [HCO_3^-] or pH have a distinctive ECG pattern is difficult to determine, as patients regularly present concomitant potassium or calcium imbalance that can explain any visible ECG change [118].

ECG changes in *metabolic alkalosis* are thought to be primarily due to underlying

hypokalemia, with patients displaying decreased T wave amplitude, ST depression, and prominent U waves [118].

However, *metabolic acidosis* has been shown to affect AP configuration [119]. Low [HCO_3^-] impairs the L-type Ca^{2+} channels, and a decreased blood pH slows upstroke velocity and Phase 0 amplitude [119]. Moreover, acidosis affects the K^+ currents of Phases 3 and 4 [120], subsequently impacting repolarization. Isolated metabolic acidosis can instigate T-wave morphology changes resembling those of hyperkalemia [117] and changes in the PR interval identical to the third-degree AV block [121].

2.2. Existing Methods for Measuring Blood Electrolyte Levels

While blood tests are the only clinically valid method for assessing blood electrolyte levels, the ECG is a potential noninvasive diagnostic tool for dyselectrolytemia [122]. As explained in Sec. 2.1, blood electrolyte derangements alter the electrophysiological properties of cardiac cells, resulting in morphological changes in the ECG waveform.

The concept of using an ECG as a tool for capturing dyselectrolytemia has been discussed over the last few years in several studies. Many have evaluated the frequency of electrolyte-induced ECG changes in clinical practice [123–125], particularly that of the anticipated patterns of each dyselectrolytemia described in Sec 2.1.4. In a recent meta-analysis, clinicians reported a physiological association between blood electrolyte levels (K^+, Ca^{2+}, Na^+, Mg^{2+}) and ECG intervals (RR, QR, PR, JT) and the QRS duration [116]. Cardiac rhythm features, such as heart rate variability [7, 122] and markers of ventricular repolarization (QT interval [126]) and heterogeneity (QT dispersion [127]), have also been shown to be correlated with pre- and post-HD shifts in electrolyte levels of ESRD patients. Nevertheless, despite demonstrating that ECG-based monitoring of electrolyte balance is empirically conceivable, none of these studies sought to quantify blood electrolyte levels from the ECG. Thus, no concrete technological solutions were proposed.

Nearly no ECG-based solutions for the noninvasive quantification of blood electrolyte levels had been engineered before 2012. At the start of the research of this doctoral dissertation in 2017, only three methods for enabling bloodless [K^+] quantification had been described in the literature, while methods for measuring other electrolytes were not introduced until 2022. The state-of-the-art methods thus far can be divided into two categories: *semi-automatic and automatic*, and *machine-learning-based*, each summarized below in chronological order. A more in-depth review of the state-of-the-art in noninvasive blood electrolyte monitoring can be found in [122].

Semi-automatic and automatic methods

Frohnert *et al.* made one of the earliest attempts to estimate blood electrolyte levels from the ECG in 1970 by proposing a set of equations to derive [K^+] based on

T-wave morphology descriptors [128]. This method was not validated independently, and noninvasive blood electrolyte monitoring research quickly disappeared until the early 2000s.

Between 2009 and 2012, Corsi and Severi *et al.* introduced prototype methods to estimate blood [K^+] from 12-lead ECGs during HD sessions [129, 130], paving the way for other researchers to create different solutions for facilitating noninvasive blood electrolyte monitoring. Their final approach in 2017 relied on regression models and a T-wave slope-to-amplitude ratio (T_{SA}) descriptor to measure [K^+] with a mean absolute error of 0.46 ± 0.39 mmol/L from ECGs of 45 HD patients [43].

Mayo Clinic researchers further enhanced the descriptor for use in a single-lead ECG, first in precordial [44, 45], and later in lead *I* acquired from a handheld device [131]. Their solutions yielded a respective mean absolute error of 0.36 ± 0.34 and 0.38 ± 0.32 mmol/L, but the authors evaluated the performance only in ECGs registered during HD sessions.

Velagapudi *et al.* developed a computer-assisted image-processing model to detect hyperkalemia from 12-lead ECGs with a specificity of 84% and a sensitivity of 63% [132]. Most of the derived T-wave morphology descriptors were equivalent to those proposed by Frohnert *et al.* in 1970 [128]. An important finding was that the descending slope—but not the amplitude—of the T-wave was strongly correlated with hyperkalemia, corroborating the initial results of Corsi and Severi *et al.* [43]. Furthermore, the authors reported that QRS widths above 100 ms improved the model performance in predicting hyperkalemia.

In 2019, Krogager *et al.* quantified the degree of asymmetry, flatness, and notching of the T-wave with a descriptor called *Morphoplogy Combination Score* (MCS) and evaluated the relationship of MCS and six other ECG parameters with blood [K^+] in a cohort of 163 547 primary care patients [133]. MCS and other ECG parameters were derived from leads *II* and *V5*. The study reported a non-linear relationship between [K^+] and MCS, which was notably stronger in individuals displaying [K^+] ≤ 4.1 mmol/L.

Ambulatory monitoring of blood potassium levels

Investigation of ECG-based monitoring of blood [K^+] in ambulatory settings started in 2018 under the framework of the research project that funded this dissertation. The first study exploring the feasibility of capturing blood potassium fluctuations in ambulatory single-lead ECGs is part of this doctoral dissertation and is discussed further in Chapter 3.

Between 2019 and 2021, researchers at the University of Zaragoza examined the performance of time-warping-based descriptors of T-wave morphology in measuring [K^+] during and between HD sessions [52, 134]. Their proposed descriptors, previously found to be significant markers of ventricular repolarization dispersion in HF

patients [135], were strongly associated with [K^+] fluctuations. The team evaluated the performance in a database comprising of 12-lead ECG Holter recordings of 29 ESRD patients acquired during 48 h, starting at the beginning of one HD session until immediately before the next one. Blood samples were collected six times: five times during the first HD session and the sixth time right before the recording period ended. While their proposed descriptors outperformed the performance of T_{SA}, the researchers examined the responsiveness of the descriptors to blood [K^+] primarily throughout HD sessions since no blood samples were collected during the ambulatory recording period. Nevertheless, in 2021 and 2022, the same research team enhanced their T-wave morphology descriptors to be more robust to noise [136] and developed a polynomial model to measure the differences in [K^+] between two points (i.e., the rate of [K^+] change) [51]. Although precise during HD, the model displayed overfitting in estimating [K^+] fluctuations in ambulatory scenarios [52], despite using leads {*I*, *II*, *V1–V6*}.

Ambulatory monitoring of other electrolytes

To characterize ECG changes induced by blood [K^+] and [Ca^{2+}], the same team of researchers at the University of Zaragoza explored other descriptors to aid in the non-invasive monitoring of potassium and calcium imbalances in ESRD patients [137]. Their reported findings indicate that time-warping-based markers of T-wave morphology are more robust for characterizing electrolyte-induced repolarization changes since such markers account for the whole T-wave morphology instead of only local features [52, 53, 138]. The authors also suggested other QRS-based markers to predict [K^+] and [Ca^{2+}] with promising results during HD sessions but not so much in ambulatory settings [137]. While the authors recognized that the estimation errors may be due to the small number of blood samples taken outside of HD, they did not consider other variables that have been shown to affect the QRS morphology in intradialytic scenarios, such as rapid hemodynamic and fluid fluctuations [139].

Machine-learning-based methods

In 2003 and 2005, two proof-of-concept studies employed machine-learning techniques to classify hyperkalemic 12-lead ECGs. One of them proposed a two-stage neural network with an accuracy of 65.5%, a sensitivity of 60%, and a specificity of 65% in a cohort of 60 patients [140]. The other used a two-stage K-means classifier with a sensitivity of 85% and a specificity of 79% [141]. None of the authors tried improving their algorithms any further.

Recently, Galloway *et al.* tested a deep-learning model to detect hyperkalemia in two subsets of ECG leads: {*I*, *II*} and {*I*, *II*, *V3*, *V5*} [54]. While the accuracy, sensitivity, and specificity were above 75% for both subsets of ECG leads in their initial dataset, the performance of the developed model suffered a toll when the authors at-

tempted to detect hyperkalemia from ECGs of CKD patients (stage 3 and higher), with the highest accuracy and specificity below 70%. The sensitivity was, however, higher than 88.9%.

In 2020, Lin *et al.* introduced another deep-learning model named *ECG12Net* to detect potassium imbalances from 12-lead ECGs [142]. The model comprised 864 meta-features from 66 321 ECG recordings with a $[K^+]$ measurement taken one hour before and after the signal acquisition. Their model outperformed six cardiologists in detecting hypo- and hyperkalemia, showing a respective sensitivity of 96.7% and 83.3% and specificity of 93.3% and 97.8%. Nevertheless, the authors noted that the model showed a decreased sensitivity in detecting mild-to-moderate hypokalemia, which is the most commonly observed hypokalemic episode in clinical practice.

Equivalently to many other clinical problems, deep learning may offer attractive solutions for facilitating noninvasive blood electrolyte monitoring. The presented deep-learning-based solutions are recent, but more are expected to appear in the upcoming years. Nevertheless, the lack of large annotated datasets containing ECGs with simultaneous blood tests hinders the development of machine-learning approaches, thus limiting their clinical application [122].

2.3. Current Challenges and Opportunities

Although the influence of blood electrolytes on the cardiac AP has been unambiguously studied [7, 116], identifying dyselectrolytemia from an ECG is challenging [123, 124], especially if no baseline ECG is available for comparison [125]. The specific effects of electrolytes on the ECG morphology are vastly dependent on previous structural and conduction abnormalities in the heart, the pace of electrolyte fluctuations, and the levels of antagonistic electrolytes that stabilize the cardiac AP [42]. This multitude of factors that can mask or mimic many of the anticipated ECG changes of electrolyte imbalance profoundly contributes to the low ECG specificity [123] in detecting dyselectrolytemia, which is why most research focuses on developing new ventricular repolarization markers more specific to blood electrolyte levels.

While the methods mentioned in Sec. 2.2 demonstrate that ECG-based estimation of electrolyte levels is conceivable and worthy of further research, none has yet shed light on the feasibility of noninvasive blood electrolyte monitoring in ambulatory scenarios. All methods present at least one of the following limitations that can encumber ambulatory blood electrolyte monitoring:

1. They require standard 12-lead or precordial-lead ECGs, which cannot be registered with practical consumer healthcare devices designed for ambulatory monitoring.

2. They were developed and investigated in ECGs acquired throughout HD, where electrolyte levels fluctuate more rapidly than in everyday ambulatory scenarios.

Rapid fluctuations are known to induce noticeable ECG morphology changes [42], but it is unclear whether ECGs can capture gradual fluctuations. Furthermore, other variables, such as hemodynamic instability, ultrafiltration rate, dialysate composition, and fluid fluctuations, instigate electrophysiological disturbances similar to those attributed to electrolytes [139]. Thus, the causality of the changes reported by the previous studies needs deeper examination. For instance, the QRS-derived markers proposed in [137] were associated with $[K^+]$ and $[Ca^{2+}]$ fluctuations during—but not between—HD sessions.

3. They do not account for possible confounding factors that can affect the performance of the proposed markers, such as concomitant electrolyte imbalances [42, 125].

4. They entail precise delineation of low-amplitude waves, which can be challenging to achieve in noisy ambulatory signals.

The importance of reduced-lead ECGs for ambulatory monitoring

The fact that nearly all currently available methods or conventional approaches for deriving ventricular repolarization markers require 12-lead or several precordial-lead ECGs hinders the scientific-technological advancement of solutions for facilitating noninvasive ambulatory blood electrolyte monitoring. Standard 12-lead ECG systems are uncomfortable for long-term continuous monitoring applications, whereas most consumer healthcare devices designed to provide maximum comfort wear register only frontal-lead ECGs. Even the few devices that offer precordial lead ECG registration are limited to one-to-two precordial leads.

Intermittent monitoring of blood electrolyte levels could be a viable option to mitigate prolonged-wear discomfort. However, configuring eight-to-ten electrodes as specified by clinical Holter monitors is usually an intricate task for the ordinary patient, making it unfeasible to request patients to set up such devices at home. Conversely, consumer healthcare devices are designed to ameliorate patient discomfort and are compact, practical, and easy to configure, but, once again, they are constrained by the number of ECG leads they can register.

The lack of practical solutions for ambulatory monitoring scenarios is arguably the primary hurdle in the noninvasive blood electrolyte monitoring research pipeline. First, it complicates the performance evaluation of existing methods in realistic everyday scenarios where electrolyte levels fluctuate gradually. In addition, the lack of practical methods discourages the development of other potential solutions that could harness the value of some of the well-established ventricular repolarization markers, such as the spatial QRS-T angle, as blood electrolyte surrogates. Importantly, patient adherence would be low without comfortable ECG recording systems.

The tradeoffs of reduced-lead ECGs

Admittedly, reducing the number of leads to the ones that consumer healthcare devices can register comes with tradeoffs. The availability of multiple ECG leads can improve $[K^+]$ estimation [52] and enable the estimation of other multi-lead ventricular repolarization markers. Furthermore, many of the anticipated ECG changes of mild dyselectrolytemia are typically visible in precordial leads (*V5–V6*) [42, 62, 133]. Nevertheless, $[K^+]$ estimation from single-lead ECGs acquired before and after HD is possible [131], suggesting that consumer healthcare devices may suffice for noninvasive ambulatory blood electrolyte monitoring.

Requirements for ambulatory monitoring

In addition to being restricted to reduced-lead ECGs, methods for facilitating noninvasive blood electrolyte monitoring must face the other challenge shared by any technological ECG-based solution for ambulatory applications—noise. Ambulatory signals are prone to noise and artifacts that can negatively affect the performance of these potential ECG-derived markers of blood electrolyte levels. Thus, to be suitable for ambulatory applications, ECG-based descriptors must be capable of capturing gradual blood electrolyte fluctuations, robust to noise, and preferably estimated from reduced-lead ECGs.

2.4. Conclusions of the Chapter

1. Abnormal blood electrolyte levels alter the electrophysiological properties of cardiac cells, changing the shape and morphology of their AP, which can result in morphological changes in the ECG waveform. Thus, ECGs are an appealing solution for noninvasive blood electrolyte monitoring.

2. Because ventricular repolarization displays heterogeneity, it is more sensitive than depolarization to blood electrolyte derangements. The ECG patterns of dyselectrolytemia, therefore, generally involve some form of morphological alterations in the post-depolarization ECG components: the ST segment (influenced by $[Ca^{2+}]$) and T-wave (influenced by $[K^+]$).

3. Dyskalemias are the electrolyte disorders that most strongly correlate with noticeable ECG changes. Hyperkalemia is characterized by peaked T-waves, especially in precordial leads. As blood $[K^+]$ increases, the QRS widens uniformly, the P-wave decreases in amplitude, and the PR interval lengthens. In contrast, broad and flat T-waves are visible in hypokalemia, and U-waves become prominent in leads *V2–V3*, alongside ST depression. Some clinicians consider the bifid/notched T-waves rather than the emergence of U-waves as the main ECG pattern of hypokalemia.

4. Calcium abnormalities affect the duration of the ST segment: hypercalcemia

increases it, whereas hypocalcemia lengthens it. The T-wave duration is not altered in hypocalcemia.

5. Identifying dyselectrolytemia from an ECG is challenging because many factors mask or mimic the anticipated ECG patterns of electrolyte imbalance. The specific effects on the ECG morphology depend on pre-existent CVD, concomitant electrolyte abnormalities, and the pace of electrolyte fluctuations.

6. Recently, novel T-wave morphology descriptors have been proposed to estimate blood $[K^+]$. Albeit with promising results, the performance of such methods was investigated exclusively during HD sessions, where electrolytes fluctuate much more rapidly than in everyday ambulatory settings. Furthermore, the described methods require 12-lead or precordial-lead ECG systems impractical for ambulatory applications. Consequently, the feasibility of noninvasive blood electrolyte monitoring in out-of-hospital scenarios remains unexplored.

3. QUANTIFICATION OF T-WAVE MORPHOLOGY CHANGES IN SINGLE-LEAD ECGS VIA MODEL-BASED PARAMETERIZATION

3.1. Rationale and Conceptual Framework

As explained in Sec. 2.1.4, ventricular repolarization is rather more sensitive than depolarization to changes in blood electrolyte levels due to its heterogeneity [48]. Since K^+ is the central ion in repolarization, it is unsurprising that dyskalemia is a significant catalyst of SCD-triggering arrhythmias [143], making adequate blood potassium management a priority for clinicians treating chronic diseases.

One of the most vulnerable populations to dyskalemia is HD patients, who have little to no renal function and rely exclusively on intermittent K^+ clearance provided by HD to maintain the homeostatic blood electrolyte profile [144]. HD is typically programmed at three weekly sessions (e.g., Monday-Wednesday-Friday), separated by two 2-day- and one 3-day-long hiatus, known as the *short* and *long interdialytic intervals*. Between HD sessions, patients can excrete only small amounts of K^+ through the colon [145, 146], while most K^+ accumulates in the blood, often engendering hyperkalemia. The prevalence of hyperkalemia during the short interdialytic interval is already considerable at 16.3–16.8 events per 100 patient months but it is 2.0–2.4 times more likely to emerge during the long one [144]. Potassium fluctuations also precipitate more arrhythmogenic events throughout the long interdialytic interval [9, 10], further aggravating the odds of SCD during this period [92, 147].

Even the treatment of hyperkalemia is fraught with clinical challenges. For instance, increasing the K^+ clearance during HD is usually unavailing, often leading to post-HD hypokalemia in 40% of patients [148]. Both hyper- and hypokalemia are repeatedly linked to adverse events in HD patients [144, 148], thus further alluding to the clinical importance of regular blood $[K^+]$ monitoring in this population.

Given the high mortality risk and hyperkalemia prevalence in HD patients [92, 144], it is understandable that all current research on noninvasive blood electrolyte monitoring focuses on quantifying $[K^+]$ in this population, leveraging on the fact that hyperkalemia is more easily recognizable on the ECG than other dyselectrolytemias [149, 150]. Nearly all methods proposed in the literature use some form of T-wave morphology descriptor to measure $[K^+]$ [43–45, 51–53, 131, 138]. Albeit with encouraging results, the methods rely on descriptors derived from ECG leads unsuitable for ambulatory monitoring and were investigated exclusively during HD sessions, where electrolyte levels fluctuate much more rapidly than in everyday scenarios. Therefore, the feasibility of noninvasive ambulatory blood potassium monitoring of blood is still unexplored.

Research design

The study presented in this Chapter explores the feasibility of capturing blood potassium fluctuations during activities of daily living from a single-lead ECG. It examines two of the four research questions underlined earlier in the dissertation:

- Can reduced-lead ECGs capture gradual blood electrolyte fluctuations in ambulatory settings?
- What possible confounding factors can affect the performance of potential ECG-derived markers of blood electrolyte levels in ambulatory settings?

Since T-wave morphology descriptors can capture $[K^+]$ during HD sessions, the feasibility of ECG-based blood electrolyte monitoring in ambulatory scenarios—and hence the answer to the two previous questions—can be investigated by examining the responsiveness of T-wave morphology descriptors to gradual K^+ fluctuations during interdialytic settings. To conduct this feasibility study, a database of single-lead ECGs and blood samples was collected using a consumer healthcare device during the long interdialytic interval. In contrast to other studies, this database includes ECGs of HD patients with several cardiac diseases recorded in free-living conditions as a realistic representation of the HD population. Information about external variables affecting electrolyte levels, such as medications and meals, is also incorporated.

The response of patient-specific T-wave morphology changes to $[K^+]$ is evaluated with two descriptors: *(i)* θ_δ, a descriptor developed to account for the overall T-wave morphology changes, and *(ii)* T_{SA}, the only available descriptor sensitive to $[K^+]$ in single-lead ECGs during HD sessions. Given that the artifactual nature of ambulatory signals warrants for noise-robust descriptors, θ_δ is derived via *model-based parameterization*. The performance of θ_δ and T_{SA} is evaluated case-by-case to identify possible confounding factors and gain insights into what is necessary to address in the future research on noninvasive blood electrolyte monitoring.

The concept of the proposed method

The proposed descriptor θ_δ quantifies ventricular repolarization changes in single-lead ECGs via model-based parameterization of the T-wave morphology. θ_δ combines two parameters: an angle (θ) and a temporal displacement (δ) yielded by the T-wave model. These two parameters act as surrogates for electrophysiological traits of abnormal blood $[K^+]$ that cannot be straightforwardly determined—the T-wave peakedness (θ) and elongation (δ), as explained in Sec. 2.1.4. Conceptually, as $[K^+]$ rises, the T-wave becomes more peaked ($\downarrow\theta$) and shortens in duration ($\downarrow\delta$).

This Chapter presents the methodology applied to derive θ_δ and the results of the first study attempting to monitor gradual potassium fluctuations in ambulatory settings using single-lead ECGs. Parts of Sections 3.2–3.6 are quoted verbatim from the previously published article: [59].

3.2. Methods

The proposed descriptor θ_δ is derived from signal-averaged heartbeats of single-lead ECGs. The pipeline consists of three stages: ECG preprocessing (Sec. 3.2.1), T-wave parameterization (Sec. 3.2.2), and T-wave feature estimation (Sec. 3.2.3), each described below.

3.2.1. ECG preprocessing

Single-lead ECGs are first preprocessed to obtain a signal-averaged heartbeat representative of a predefined short period. The preprocessing stage consists of filtering, signal quality assessment, heart-rate-based correction of T-wave duration, beat averaging, and T-wave rectification (Fig. 3.1).

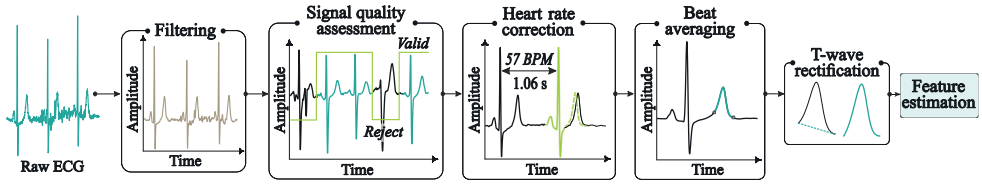

Fig. 3.1. Preprocessing of a single-lead ECG.

Filtering. Baseline wandering and high-frequency noise are suppressed using high- and low-pass finite impulse response (FIR) filters of high order with respective cutoff frequencies of $f_c = 0.6$ Hz and $f_c = 40$ Hz. Although less computationally expensive filters (e.g., zero-phase Butterworth) are generally employed to filter ECGs, FIR filters are selected instead to avoid instigating distortions in the ST-T segment and T-wave.

Signal quality assessment. The signal quality index (SQI) criteria proposed in [151] is applied to filtered ECGs to eliminate the beats of distinct morphology, such as ectopic beats or those corrupted by noise. Long-term ECGs should be segmented into predefined short periods with a few-second-long overlap. In the study presented in this dissertation, a 90 s-long sliding window with a 10 s overlap was employed to salvage as many heartbeats as possible throughout the whole recording[1]. Segments with more than 50% poor-quality beats are considered unanalyzable.

Heart rate correction. Since the T-wave morphology is sensitive to heart rate oscillations, the ST-T complex is resampled to fit the current RR interval according to Fridericia's formula [153]. Resampling of the ST-T complex rectifies morphological

[1] It should be noted that the 90 s window length is necessary to rigorously examine in detail the response of T-wave morphology changes to gradual electrolyte changes throughout the long interdialytic interval. However, in future ambulatory monitoring applications, 20 s-long windows would realistically suffice to obtain a good signal-quality averaged heartbeat [152].

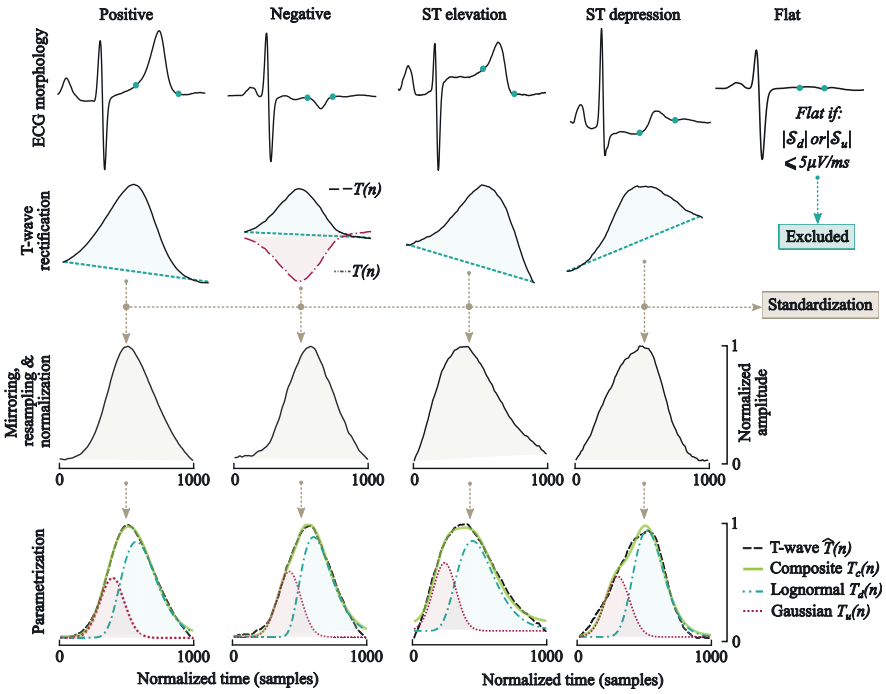

Fig. 3.2. T-wave rectification and parameterization for various ECG morphologies. After delineating the T-waves for every valid averaged heartbeat, the T-wave is rectified, mirrored, resampled, normalized, and subjected to parameterization.

alterations caused by heart rate to avoid misinterpreting them as alterations induced by electrolyte fluctuations. Although hyperpolarization or hyperexcitability of cardiomyocytes due to dyselectrolytemia can result in abnormal heart rhythms, its electrophysiological effects on the heart rate are considered clinically relevant only during episodes of arrhythmias [7, 42], which are not analyzed in this study.

Beat averaging. The high-quality resampled heartbeats are aligned and averaged, resulting in a single signal-averaged heartbeat representative of each ECG segment. The onset and offset of the QRS and T waves are delineated with the PQRST delineation algorithm included in the *ECGDeli* [154] toolbox. The proposed descriptor θ_δ is then estimated from the delineated T-waves of each averaged heartbeat.

T-wave rectification. Each delineated T-wave, $T(n)$, undergoes a series of steps to transform different waveforms as closely as possible into a positive T-wave (Fig. 3.2). Accordingly, negative T-waves are inverted, $T(n) = -T(n)$. The T-wave onset (t_{T_o}) and offset (t_{T_e}) are amended to their local minimum amplitude point in waveforms with ST-segment abnormalities. The T-wave baseline, estimated by linear interpolation between the amended onset and offset, is then subtracted from $T(n)$ so that $T(n)$ begins and ends at zero amplitude. Finally, $T(n)$ is standardized to counteract amplitude dis-

crepancies caused by body position changes or pre-existent cardiac diseases:

$$T^z(n) = \frac{T(n) - \bar{x}}{S}, \forall n, \tag{3.1}$$

where $T^z(n)$ denotes the standardized T-wave, $\bar{x}$, and S are the mean and standard deviation of $T(n)$. From this point onwards, $T^z(n)$ denotes the standardized T-wave, whereas $T(n)$ is the baseline-removed T-wave.

Although hypocalcemia can cause negative T-waves [42] and, therefore, inversion of the T-wave polarity may hold meaningful value for noninvasive blood electrolyte monitoring, the T-wave rectification stage is implemented to enable the inclusion of patients with a history of ischemia and myocardial infarction, which are usually excluded from studies due to displaying negative T-waves. Additionally, transforming different waveforms into positive T-waves allows investigating the responsiveness of T-wave morphology descriptors to blood [K^+] in circumstances of concurrent calcium imbalance that incurs T-wave polarity inversion.

3.2.2. T-wave model-based parameterization

The T-wave, composed of two asymmetrical slopes—upward and downward—is parameterized using a composite model of two functions to characterize each slope separately. The composite model, inspired by the models described in [155] and [156], and briefly described in [58], comprises one Gaussian and one lognormal function (Fig. 3.3). The Gaussian function construes the upward slope and is defined as:

$$T_u(n; \sigma_u, \mu_u) = \frac{1}{\sqrt{2\pi\sigma_u^2}} e^{-\left(\frac{(n-\mu_u)^2}{\sigma_u^2}\right)}, \tag{3.2}$$

where n is the sample number, μ_u and σ_u are the location and scale parameters. The lognormal function characterizes the downward slope and is expressed as:

$$T_d(n; \sigma_d, \mu_d, \gamma_d) = \frac{1}{(n - \gamma_d)\,\sigma_d\sqrt{2\pi}} e^{-\left(\frac{(\ln(n-\gamma_d) - \mu_d)^2}{2\sigma_d^2}\right)}, \tag{3.3}$$

where γ_d, μ_d, and σ_d are the respective location, scale, and shape parameters. Introducing the location parameter γ_d to the lognormal function allows for shifting $T_d(n)$ in time to always fit the downward slope without modifying the shape and scale parameters. This approach ensures that μ_d and σ_d react unambiguously to morphological but not temporal changes. $T(n)$ is then characterized by combining (3.2) and (3.3) as:

$$T_c(n) = w_u T_u(n) + w_d T_d(n) + h. \tag{3.4}$$

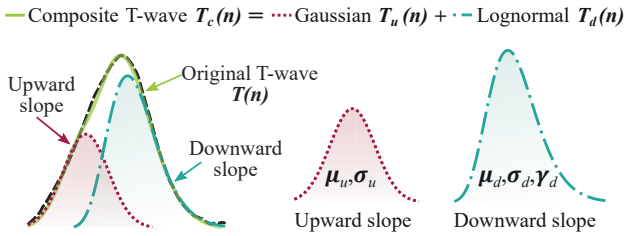

Fig. 3.3. T-wave composite model.

The subscript c denotes the fitted composite model, whereas u and d indicate the upward and downward slope parameters. Both functions are weighted by w_u and w_d and balanced with an offset h. All parameters are merged into the vector $\vec{\phi} = [\sigma_u, \sigma_d, \mu_u, \mu_d, \gamma_d, w_u, w_d, h]$ which is estimated using the trust-region reflective least-squares algorithm.

Similarly to all other curve-fitting algorithms, the trust-region-reflective least squares algorithm entails initializing the elements of $\vec{\phi}$ before starting the optimization process. The lower and upper limits of $\vec{\phi}$ also need to be specified prior to fitting. Bounding the elements of $\vec{\phi}$ aids in achieving computation efficiency by preventing unnecessary additional computations and guarantees that the model fits as expected. Instead of being determined empirically, as outlined in the published paper [59], the initial values and boundaries of $\vec{\phi}$ can be inferred from the physiological traits of the T-wave slopes, in particular, the duration and position in time of $T_u(n)$ and $T_d(n)$. The methodology for initializing and bounding $\vec{\phi}$ is presented below. The superscripts *0*, *L*, and *U* denote the initial, lower, and upper limits of $\vec{\phi}$ from this point onwards.

Parameter initialization

The preliminary values of the elements of $\vec{\phi}^0$ construct the pre-parameterization template $T_c^0(n)$. These values are dependent on the characteristics of $\widehat{T}(n)$ and are calibrated to ensure that $T_c^0(n)$ is below the peak of $\widehat{T}(n)$ and there is a clear separation (i.e., phase difference) between the initial functions $T_u^0(n)$ and $T_d^0(n)$, as illustrated in Fig. 3.4.

Since a Gaussian function construes the upward slope of the T-wave, μ_u controls the time location (i.e., the horizontal shift in the time axis) of $T_u^0(n)$, whereas σ_u indirectly regulates its duration. A larger σ_u indicates a wider 'spread' (scale) and ergo a more elongated $T_u^0(n)$. Thus, the initial parameters μ_u^0 and σ_u^0 can be straightforwardly determined using the peak of $\widehat{T}(n)$ as a reference point:

$$\mu_u^0 = 0.9\, n_{\widehat{T}_p} \text{ and } \sigma_u^0 = 0.01\,\text{s}, \text{ where } n_{\widehat{T}_p} = \arg\max_n \left(\widehat{T}(n)\right). \tag{3.5}$$

The assigned value of μ_u^0 situates $T_u^0(n)$ just before the peak of $\widehat{T}(n)$ and the arbitrary value of $\sigma_u^0 = 0.01$ second suffices to construe the initial function while ensuring that

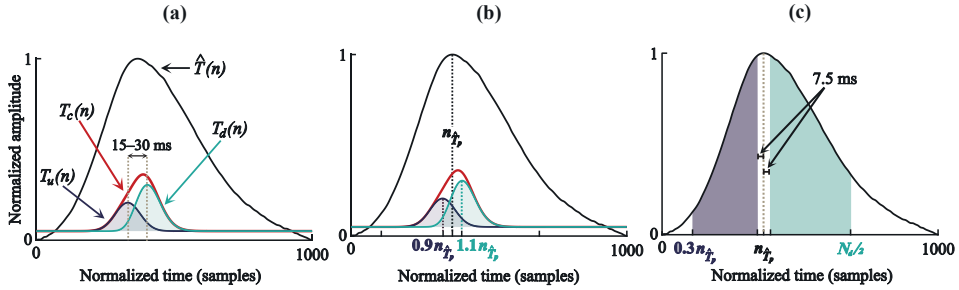

Fig. 3.4. Initialization of the T-wave template $T_c(n)$. Note the phase shift (**a**) between $T_u(n)$ and $T_d(n)$ and the initial values (**b**) of μ_u^0 and μ_x^0 and their lower and upper boundaries (**c**) in relation to $n_{\hat{T}_p}$.

$T_u^0(n)$ stays within the upward portion of $\widehat{T}(n)$. Since $\widehat{T}(n)$ is the T-wave $T(n)$ resampled at 1000 samples, σ_u^0 needs to be converted to samples by multiplying it with $\mathcal{F}$:

$$\mathcal{F} = \frac{f_s}{b}, \quad \text{where} \quad b = \frac{N}{1000}, \tag{3.6}$$

where f_s is the sampling frequency, and N is the number of samples in $T(n)$.

A similar rationale is applied to initialize μ_d^0 and σ_d^0 of the downward slope. While the parameters of a lognormal function cannot be stipulated directly as those of a Gaussian function, μ_d^0 and σ_d^0 can be derived from their Gaussian counterparts:

$$\mu_d^0 = \ln\left(\frac{\mu_x^2}{\sqrt{\mu_x^2 + \sigma_x^2}}\right) \quad \text{and} \quad \sigma_d^0 = \sqrt{\ln\left(1 + \frac{\sigma_x^2}{\mu_x^2}\right)}, \tag{3.7}$$

where μ_x and σ_x are the desired location and scale. Both parameters are selected analogously to μ_u^0 and σ_u^0: $\mu_x = 1.1\, n_{\hat{T}_p}$ to position $T_d(n)$ after the peak of $\widehat{T}(n)$ and $\sigma_x = \sigma_u^0 = 0.01$ s so that $T_d(n)$ stays underneath the downward portion of $\widehat{T}(n)$.

For most T-waves, the initial location parameter of $T_d(n)$ can be set to $\gamma_d^0 = 0$, as the described initialization of the μ and σ parameters usually suffices to obtain the necessary separation between $T_u^0(n)$ and $T_d^0(n)$. However, in T-waves of exceptionally short (or long) duration, $T_u^0(n)$ and $T_d^0(n)$ can overlap (if short) or be too far apart (if long). To mitigate such cases, γ_d^0 can be determined iteratively until the phase difference between the peaks of $T_u^0(n)$ and $T_d^0(n)$ is within 15–30 ms apart (see Algorithm 1). Confining the phase difference of $T_u^0(n)$ and $T_d^0(n)$ to a specific time frame standardizes the preliminary template $T_c^0(n)$ without adjusting any of the other initial μ and σ parameters, which are more reactive to morphological differences and, therefore, more difficult to define a priori. This constriction enables $T_c^0(n)$ to adjust for a variety of T-wave morphologies in an automated manner. The phase difference of [15–30] ms was ascertained empirically.

The weight parameters w_u and w_d manipulate the amplitude of each function without changing the location, scale, or shape parameters. Since empirical experi-

ments demonstrated that initializing $T_d^0(n)$ with a higher amplitude than $T_u^0(n)$ yields better results from the curve-fitting algorithm, $T_d^0(n)$ is set to have twice the maximum amplitude of $T_u^0(n)$. If $w_u^0 = 1$, then:

$$w_d^0 = 2\,\frac{\max\left(T_u^0(n)\right)}{\max\left(T_d^0(n)\right)}. \tag{3.8}$$

Lastly, the offset h is set to the arbitrary value of $h^0 = 0.05$ to shift $T_c^0(n)$ above the baseline.

Algorithm 1: Initialization of γ_d^0

Input: $T_u^0(n)$, $T_d^0(n)$, μ_u^0, σ_u^0, μ_d^0, σ_d^0
Output: γ_d^0

```
search ← true
γ_d^0 ← 0
while search do
    n_d ← arg max_n (T_d^0(n; σ_d^0, μ_d^0, γ_d^0))
    n_u ← arg max_n (T_u^0(n; σ_u^0, μ_u^0))
    Δ_n ← |n_d − n_u|
    if Δ_n > 30 ms then
        γ_d^0 ← γ_d^0 − 5 ms
    else if Δ_n < 15 ms then
        γ_d^0 ← γ_d^0 + 5 ms
    else
        search ← false
    end if
end while
```

Lower and upper limits

The lower and upper boundaries of $\vec{\phi}$ constrain each function to their respective slope. The boundaries of the location, shape, and scale parameters are set according to physiological constraints, and their rationale is clarified below. Table 3.1 discloses the boundaries for each element of $\vec{\phi}$.

Since the T-wave duration is typically not less than 100 ms, the lower boundaries of the scale parameters σ_u^L and σ_d^L must reflect this physiological constraint, i.e., σ_u^L and σ_d^L must ensure that $T_c(n)$ has a minimum duration of 0.10 s. According to the *empirical rule*, 99.7% of all observations of a Gaussian probability distribution $\mathcal{P}$ lie within three standard deviations of the mean:

$$\mathcal{P}\left(\mu - 3\sigma \leq \mathcal{X}_i \leq \mu + 3\sigma\right) \approx 0.997, \tag{3.9}$$

where $\mathcal{X}_i$ is an observation from a normally distributed random variable. Here, $\mathcal{X}_i$ is an instance in time. If the model was comprised of a single Gaussian function, σ could

Table 3.1. Initial values and lower and upper boundaries.

	$T_u(n)$			$T_d(n)$				
Elements of $\vec{\phi}$	μ_u	σ_u	w_u	μ_x †	σ_x †	γ_d	w_d	h
Initial values	$0.9\,n_{\widehat{T}_p}$	10‡	1.0	$1.1\,n_{\widehat{T}_p}$	10‡	Alg.1[a]		0.05
Lower boundaries	$0.3\,n_{\widehat{T}_p}$	70‡	1.0	$n_{\widehat{T}_p}+7.5$ ‡	70‡	$-n_{\widehat{T}_p}$	Eq. (3.8)	–2.0
Upper boundaries	$n_{\widehat{T}_p}-7.5$‡	$0.35\,n_{\widehat{T}_p}$	500	$N_d/2$*	$0.55\,N_d$*	$n_{\widehat{T}_p}$		3.0

† Convert to its Lognormal counterpart using Equation (3.7).
‡ In milliseconds. Transform to samples with Equation (3.6).
* $N_d = 1000 - n_{\widehat{T}_p}$.
[a] See Algorithm 1.

be estimated by manipulating Equation 3.9:

$$-(\mu - 3\sigma) + (\mu + 3\sigma) \approx 0.997\mathcal{X} \iff \sigma \approx \frac{0.997}{6}\mathcal{X}, \tag{3.10}$$

where $\mathcal{X}$ is the total number of observations. In this case, $\mathcal{X}$ would equal the T-wave minimum duration ($\mathcal{X} = 100$ ms). However, because $T_c(n)$ is a composite model of $T_u(n)$ and $T_d(n)$ with a minimum phase difference of 15 ms, σ_u^L and σ_d^L need to guarantee that $T_c(n)$ is not longer than 100 ms when $T_u(n)$ and $T_d(n)$ are separated by this minimum phase shift. Thus, the total number of observations $\mathcal{X}$ for $T_u(n)$ and $T_d(n)$ is $\mathcal{X} = 100 - 2 \times 15 = 70$ ms. σ_u^L is then obtained using Equation (3.10) with $\mathcal{X} = 70$ ms. σ_d^L is estimated from σ_x^L using Equation (3.7), and $\sigma_x^L = \sigma_u^L$. Both σ_u^L and σ_d^L are converted to samples using Equation (3.6).

The upper boundaries of σ_u^U and σ_d^U are defined as 35% and 55% of the length of their respective slopes (Fig. 3.4).

The lower and upper boundaries of the μ parameters position each function underneath their respective slope. Thus, $\mu_u^L = 0.3 n_{\widehat{T}_p}$ and $\mu_u^U = \widehat{T}_p - 7.5$ ms. Conversely, $\mu_x^L = \widehat{T}_p + 7.5$ ms to ensure the minimum phase of 15 ms separation between $T_u(n)$ and $T_d(n)$, and μ_x^U is set at the midpoint ($N_d/2$) of the downward slope (Fig. 3.4). μ_x^L and μ_x^U are then employed in Equation (3.7) to derive μ_d^L and μ_d^U.

Since the model is devised to account for morphological—but not temporal—T-wave changes, the location parameter γ is allowed to shift around the peak of $\widehat{T}(n)$: $\gamma_d^L = -n_{\widehat{T}_p}$ and $\gamma_d^U = n_{\widehat{T}_p}$.

The lower limits of the weight parameters w_u and w_d are the same as their initial values. As for the upper limits, $w_u^U = 500$, and w_d^U is calculated from Equation (3.8). Lastly, the offset boundaries are defined as $h^L = -2.0$ and $h^U = 3.0$. These limits were determined empirically.

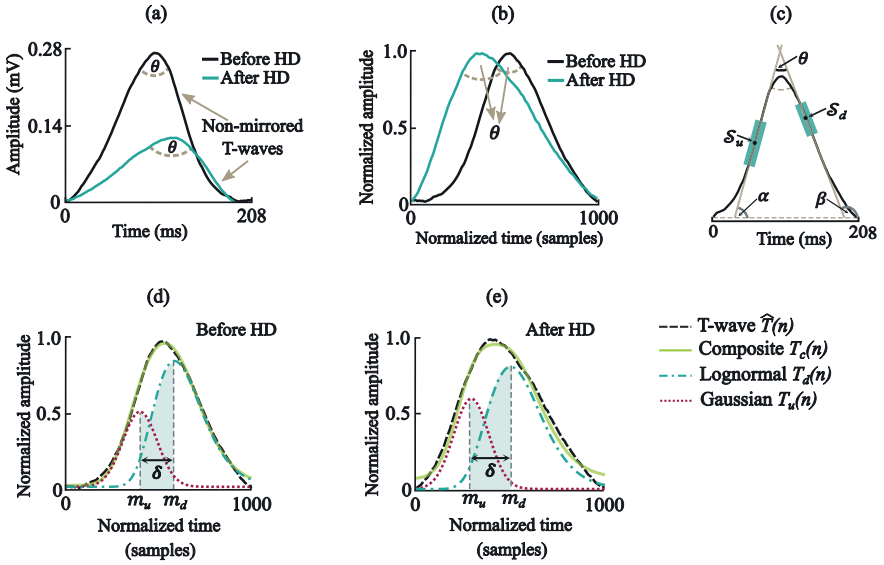

Fig. 3.5. T-wave feature estimation: (**a**) T-waves at different blood [K^+] without normalization; (**b**) variation of θ in normalized T-waves; (**c**) finding of $\mathcal{S}_u$, $\mathcal{S}_d$ and θ. The change in δ at different blood [K^+] levels: (**d**) [K^+] = 5.5mmol L^{-1} and (**e**) [K^+] = 3.2mmol L^{-1}.

3.2.3. T-wave feature estimation

When blood [K^+] rises above normal levels, the T-wave becomes more peaked and decreases in duration [7,42]. Variations in T-wave peakedness can be quantified with the angle θ between the upward and downward slopes: peaked T-waves render smaller θ values, while a higher θ equates to a flatter wave, as illustrated in Fig. 3.5a–b. Assuming that each slope is defined as a line with gradient $\mathcal{S}$, θ can be calculated as:

$$\theta = \beta - \alpha \equiv \arctan(\mathcal{S}_d) - \arctan(\mathcal{S}_u), \tag{3.11}$$

where β and α are the angles between the temporal axis and the downward and upward slope, and $\mathcal{S}_u$ and $\mathcal{S}_d$ are the gradients of the correspondent slopes (Fig. 3.5c). $\mathcal{S}_u$ and $\mathcal{S}_d$ are estimated from $T^z(n)$ in a similar way as in [157]: two lines are computed in an 8 ms window centered at the maximum gradient between T-onset and T-peak, and at the minimum gradient between T-peak and T-offset (Fig. 3.5c). $\mathcal{S}_u$ and $\mathcal{S}_d$ are the gradients obtained from the fitted lines in a.u./s.

As the duration of repolarization shortens, the T-wave becomes less elongated. Given that each function from the composite model depicts a slope, changes in T-wave elongation can be characterized by a temporal displacement, δ, between the points of global maximum of $T_d(n)$ and $T_u(n)$ functions (Fig. 3.5d–e). Considering that the point of global maximum of a probability distribution is its mode, δ is given by:

$$\widehat{\delta} = m_d - m_u, \tag{3.12}$$

where m_d and m_u are the modes of lognormal and Gaussian functions. The mode of a Gaussian function is μ_u, whereas, for the three-parameter lognormal function, it is calculated as follows:

$$m_d = \gamma_d + e^{(\mu_d - \sigma_d^2)}. \tag{3.13}$$

Given that $\widehat{\delta}$ is derived from the resampled $\widehat{T}(n)$, δ has to be amended to the original time scale:

$$\delta = \widehat{\delta}\frac{N}{1000}, \tag{3.14}$$

where N is the number of samples in $T(n)$. Conceptually, as blood $[K^+]$ starts to rise slowly, the T-wave becomes narrower and more peaked, translating into lower values of δ (s) and θ (°). Since θ and δ vary concordantly with each other, both decreasing when $[K^+]$ increases, the descriptor θ_δ is proposed to amplify their response to blood $[K^+]$ fluctuations:

$$\theta_\delta = -\log_{10}(\theta \cdot \delta). \tag{3.15}$$

The logarithm expands the dynamic range and ensures that θ_δ is positively correlated with $[K^+]$ levels.

3.3. Data

Single-lead ECGs were collected from 17 HD patients (9 females, age 57.4±14.6 years), hospitalized and ambulatory, during the long interdialytic interval using Bittium Faros (Bittium Corporation, Oulu, Finland) ambulatory recorder at a sampling rate of 500 Hz. The database contains a total of ~1078 hours of lead-I ECG signals, roughly 71 h per patient.

Data collection

Data acquisition started before the last HD of the week and ended after the following HD (Fig. 3.6). From this point onwards, Friday HD refers to the last HD of the week, whereas Monday HD denotes the following HD. Hospitalized patients were not bedridden and were free to move inside the hospital facilities.

Blood samples were drawn twice (at the start and end) during each HD procedure from hospitalized patients and thrice (at the start, mid, and end) from ambulatory patients to assess blood $[K^+]$, [Ca], $[Mg^{2+}]$, and $[HCO_3^-]$ levels. At least one additional blood sample between HD sessions was collected from hospitalized patients at a predetermined time instant, as decided by the physician on call. All patients were also asked to register the time of meals and medication intake.

Table 3.2. Patient and recording characteristics.

	Patient characteristics			Recording characteristics		
	# / Type[1]	*Sex*[2]*/ Age*	*Comorbidities*[3]	*Electrolyte imbalance*[4]	*Total duration / High quality*	*Other notes*[3]
Group I	#1/A	F/69	Hypertension History of AF Diabetes	Hyperkalemia Hypermagnesemia	73.2 h / 92.6%	Frequent PVCs
	#2/A	F/68	Hypertension Ischemic heart disease: stable angina pectoris	Hyperkalemia Hypocalcemia (severe)	73.4 h / 93.2%	Frequent PVCs
	#3/H	F/52	Hypertension LVH Hyperparathyroidism	Hyperkalemia Hypocalcemia (mild)	75.6,h / 95.3%	
	#4/A	M/32	History of AF LVH	Metabolic acidosis Hypermagnesemia	73.7 h / 56.8%	
	#5/H	F/70	Hypertension Severe anemia	Hypocalcemia (severe) Metabolic acidosis	55.8 h / 77.2%	IV iron infusions Blood transfusion Urgent start of HD
	#6/A	M/50	Hypertension LVH Ischemic heart disease Diabetes	Hypocalcemia (mild) Hypermagnesemia	74.7 h / 92.0%	
	#7/H	F/65	Hypertension Ischemic heart disease: stable angina pectoris LVH Severe anemia	Hypocalcemia (mild)	73.8 h / 73.1%	Blood transfusion before Friday HD
Group II	#8/H	F/69	Hypertension	Hyperkalemia Hypocalcemia (mild)	73.4 h / 65.1%	Paroxysmal AF
	#9/H	F/78	Ischemic heart disease	Hyperkalemia Hypocalcemia (mild)	69.8 h / 79.7%	PACs; Tachycardia Use of *Sorbisterit*
	#10/H	M/29	Hypertension LVH	Hyperkalemia Hypocalcemia (mild) Metabolic acidosis	77.6 h / 44.9%	Tachycardia Use of *Sorbisterit*
	#11/H	M/51	Hypertension	Hyperkalemia Hypocalcemia (severe) Metabolic acidosis	75.2 h / 97.2%	Use of *Sorbisterit*
	#12/H	M/64	Hypertension Diabetes	Hypocalcemia (severe) Hypomagnesemia	75.9 h / 79.8%	
	#13/H	M/47	Hypertension Stroke	Hyperkalemia Hypocalcemia (mild) Metabolic acidosis	75.8 h / 94.9%	Concomitant electrolyte imbalance during the whole recording
	#14/H	F/54	None	Hypocalcemia (mild) Hypomagnesemia	54.7 h / 41.0%	Thrombosis during Friday HD Taken to minor surgery Tachycardia Urgent start of HD
	#15/A	M/79	Hypertension Chronic heart failure Ischemic heart disease LVH Diabetes	Metabolic alkalosis Hypermagnesemia	75.6 h / 96.2%	

[1] A: ambulatory; H: hospitalized.
[2] F: female; M: male.
[3] AF: atrial fibrillation; LVH: left ventricular hypertrophy; PVCs: premature ventricular contractions; PACs: premature atrial contractions; IV: intravenous; *Sorbisterit* (calcium polystyrene sulphonate) is a potassium-lowering medication.
[4] Imbalances displayed at the start of Monday HD. Hyperkalemia: $[K^+] \geq 5.5$ mmol L^{-1}; Hypocalcemia (severe): $[Ca] \leq 1.9$ mmol/L; Hypocalcemia (mild): $1.9 < [Ca] < 2.23$mmol L^{-1}; Hypermagnesemia: $[Mg^{2+}] \geq 1.03$ mmol L^{-1}; Hypomagnesemia: $[Mg^{2+}] \leq 0.74$ mmol L^{-1}; Metabolic acidosis: $[HCO_3^-] < 22$ mmol L^{-1}; Metabolic alkalosis: $[HCO_3^-] \geq 26$ mmol L^{-1}.

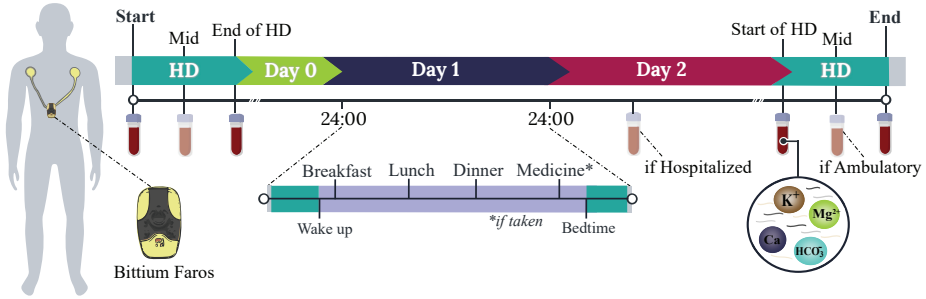

Fig. 3.6. Data acquisition protocol. Lead-I ECG signals of hospitalized and ambulatory patients were acquired throughout the long interdialytic interval using an ambulatory recorder. Blood samples of hospitalized patients were collected twice during each HD (at the start and end) and at least once during the long interdialytic interval. Blood samples of ambulatory patients were collected only through the course of each HD (at the start, mid, and end).

Patient and recording characteristics

Out of 17 patients, two were excluded from the analysis. One patient presented ventricular tachycardia episodes during the recording and was taken to the ICU, while the other terminated recording just a few hours after Friday HD due to discomfort. Two hospitalized patients required urgent HD one day earlier. The patients were divided into two groups: *Group I* comprises patients with regular sinus rhythm and high signal quality over the whole recording period, whereas *Group II* includes patients whose recordings were noisy, or affected by arrhythmia or ingestion of potassium-lowering medication (*Sorbisterit*). Patients in both groups manifested concomitant electrolyte imbalances. Table 3.2 provides the patient and recording characteristics.

Each ECG was divided into three days: *Day 0*, covering the remaining hours of the same day after Friday HD (until 22:00), *Day 1*, and *Day 2* as the ensuing and last days of the long interdialytic interval, respectively. Since lying positions can considerably alter the ECG morphology [158], *Day 1* and *Day 2* range from 07:00 till 22:00 as patients were usually awake within this period, and the likelihood of encountering a lying position was reasonably low. ECG segments within episodes of arrhythmogenic events were excluded from the analysis.

3.4. Experiments and Performance Evaluation

The performance of θ_δ is compared to the descriptor, T_{SA} introduced in [44, 45, 131]. Thus far, T_{SA} is the only available descriptor of blood [K^+] that has been evaluated in single-lead ECGs. T_{SA} is estimated as:

$$T_{SA} = \frac{\mathcal{S}_d}{\sqrt{T_A}}, \tag{3.16}$$

where $\mathcal{S}_d$ (in a.u./s) is the downward slope and T_A is the peak-to-peak amplitude between the T-wave peak and offset. $\mathcal{S}_d$ and T_A were computed from the non-mirrored $T(n)$, normalized by the signal energy of its correspondent QRS-wave, as described in [45]. It should be noted that T_{SA} is not applicable for negative T-waves [45]. Despite being often used by clinicians to identify potassium abnormalities, the T-wave amplitude was not included for comparison since it shows an inferior performance to that of T_{SA} [44]. Statistical descriptors of the T-wave morphology, such as skewness and kurtosis, were outperformed by other asymmetry metrics [132,133] and, therefore, not included for comparison.

Evaluation of potassium-induced T-wave morphology changes

The daily variation of θ_δ and T_{SA} relative to the [K^+] reference values of each individual is examined with distributions of $\theta_\delta - \theta_{\delta_{t0}}$ and $T_{SA} - T_{SA_{t0}}$ obtained using kernel density estimations. The reference values are calculated at t_0 by finding the mean during the first 30 min following Friday HD termination. Within this 30 min period, [K^+] remains nearly unchanged as none of the patients had a meal, thus avoiding insulin spikes that drive blood [K^+] into the intracellular space [159].

The overlapping index η [160] is used to quantify similarities between the daily distributions of θ_δ and T_{SA}. The index η can take values between zero and one, where η=1 indicates that two distributions are identical. Intuitively, it is expected that higher [K^+] fluctuations will translate into smaller η values. The relationship between η and Δ[K^+] is assessed with the Pearson's correlation coefficient (r), where Δ[K^+] is expected to be negatively correlated with η. The index η is calculated between the days with assessed [K^+], which, for the majority of patients, is solely between *Day 0* and *Day 2*. Since blood was collected at the start of Monday HD, the distribution of *Day 2* includes 2 h preceding Monday HD as well. The subscript of η specifies the days between which η is evaluated, whereas Δ[K^+] denotes the difference of [K^+] between two days.

Evaluation of noise robustness

The robustness to noise of θ_δ and T_{SA} is investigated by comparing the coefficient of variation c_v of each descriptor within periods during which [K^+] remains nearly unchanged, but the signal quality was expected to vary. c_v is estimated for each patient as follows:

$$c_v = \frac{s_x}{\bar{x}}, \tag{3.17}$$

where s_x and $\bar{x}$ are the standard deviation and mean of either θ_δ or T_{SA} within a given period. Lower c_v values within periods of low signal quality indicate a higher descriptor stability and, therefore, more robustness to noise. The rationale behind using c_v as a noise robustness metric is as follows. Periods of low signal quality render more

noisy averaged heartbeats, which can influence the estimation of T-wave descriptors. If the descriptors are noise-robust, they will display little to no variation (i.e., $\downarrow c_v$) within periods during which the T-wave morphology will not be expectedly affected by physiological conditions such as electrolyte fluctuations, body position changes, or heart rate, despite the low signal quality. Conversely, a high variability ($\uparrow c_v$) in such periods indicates that the descriptor reacts to noise rather than physiological causes.

Since ambulatory signals are recorded in an unsupervised fashion, c_v is measured in two different periods: t_1 = [21:00–22:00] of *Day 1* and t_2 = [00:00–01:00] of *Day 2*. During t_1, patients were still awake, and the ECGs are expected to be of a lower quality due to movement (e.g., walking around the house). Conversely, during t_2, patients were asleep, and their physical activity was minimal, thereby increasing the quality. This was confirmed through accelerometer signals recorded synchronously with the ECGs. The periods t_1 and t_2 are chosen for two reasons:

- Intra- and intercellular K^+ shifts are likely more stable during *Day 1* and *Day 2*, unlike during the same day after HD [161].
- The circadian variability of blood [K^+] in patients with impaired renal function indicates that [K^+] levels between 21:00 till 01:00 increase, on average, only by $0.06\,\mathrm{mmol\,L^{-1}}$ [162], which is minimal.

Although the circadian variability of blood [K^+] in HD patients has not been studied, it was observed that θ_δ responded similarly to the findings in [162] (see Fig. 3.10), thus implying that the circadian rhythm is maintained.

3.5. Results

3.5.1. T-wave morphology responsiveness to potassium fluctuations

Figure 3.7 depicts the variation of θ_δ and T_{SA} in the patients of *Group I*. As expected, θ_δ and T_{SA} rise with the increase of [K^+]. Note the low trendline steepness for patient #6, which corresponds well with little change in [K^+]. Interestingly, T_{SA} varies in the opposite direction in patient #4, who displayed positive and negative T-waves and occasional ST depression. The proposed descriptor θ_δ appears to better deal with alternating T-wave morphologies than T_{SA}.

Figure 3.8 shows the variation of θ_δ and T_{SA} in the patients of *Group II* of problematic recordings. Unsurprisingly, θ_δ and T_{SA} show trends discordant with [K^+] in patients with: atrial fibrillation (#8), premature atrial contractions (#9), and tachycardia (#9, #10, #14). Nevertheless, in periods of sinus rhythm, during which the T-wave morphology stabilizes, both descriptors vary agreeably with [K^+].

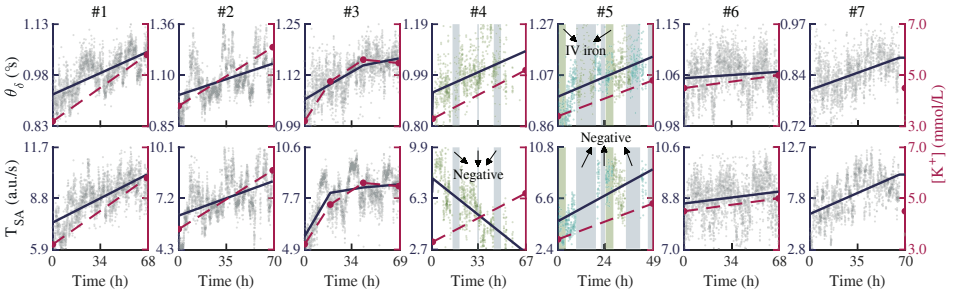

Fig. 3.7. Variation of θ_δ (top row) and T_{SA} (bottom row) together with the estimated linear trend (solid blue line) and [K$^+$] values (red dots, dashed line) for individual patients of *Group I*. The linear trends are estimated using the best-fit linear polynomial between the consecutive time instances of [K$^+$] assessments. Grey patches depict periods of negative T-waves, during which θ_δ is computed without any correspondent T_{SA} values. Yellow patches depict periods of intravenous (IV) iron infusion which may affect the T-wave morphology. Patient #5 was taken to HD one day earlier, and thus no blood was taken between HD sessions. The blood samples from Friday HD of patient #7 were misplaced; hence the absent trendline. Dots of different colors highlight patients with metabolic acidosis (yellow) or severe hypocalcemia and metabolic acidosis (blue and yellow).

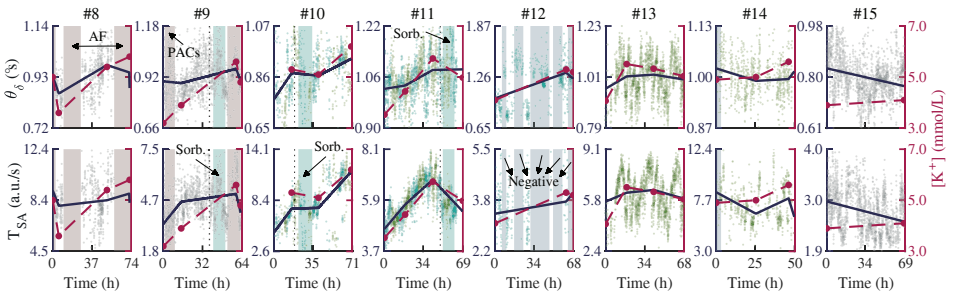

Fig. 3.8. Variation of θ_δ (top row) and T_{SA} (bottom row) together with the estimated linear trend (solid blue line) and [K$^+$] values (red dots, dashed line) for individual patients of *Group II*. The linear trends are estimated using the best-fit linear polynomial between the consecutive time instances of [K$^+$] assessments. Grey patches depict periods of negative T-waves, during which θ_δ is computed without any correspondent T_{SA} values. Red patches depict periods of arrhythmias: atrial fibrillation (AF) and premature atrial contractions (PACs). Patient #14 was taken to HD one day earlier. The blood sample at the end of Friday HD of patient #10 was misplaced. The dashed vertical line denotes the time of *Sorbisterit* (Sorb) intake, whereas blue patches depict the duration of the *Sorbisterit* effect. Dots of different colors highlight the patients who displayed metabolic acidosis (yellow), severe hypocalcemia (blue), or both.

Impact of concomitant electrolyte imbalance on T-wave morphology

Flat or negative T-waves prevailed in patients #5 and #12, who manifested severe isolated hypocalcemia. T_{SA} could only be computed during the short time intervals in which the T-wave was positive. Curiously, both patients displayed discrepantly high θ_δ values despite the absence of hyperkalemia, likely due to T-wave narrowing during ST-T complex resampling used for the correction of heart-rate induced T-wave changes.

In patients with hyperkalemia concomitant with metabolic acidosis (#10, #11,

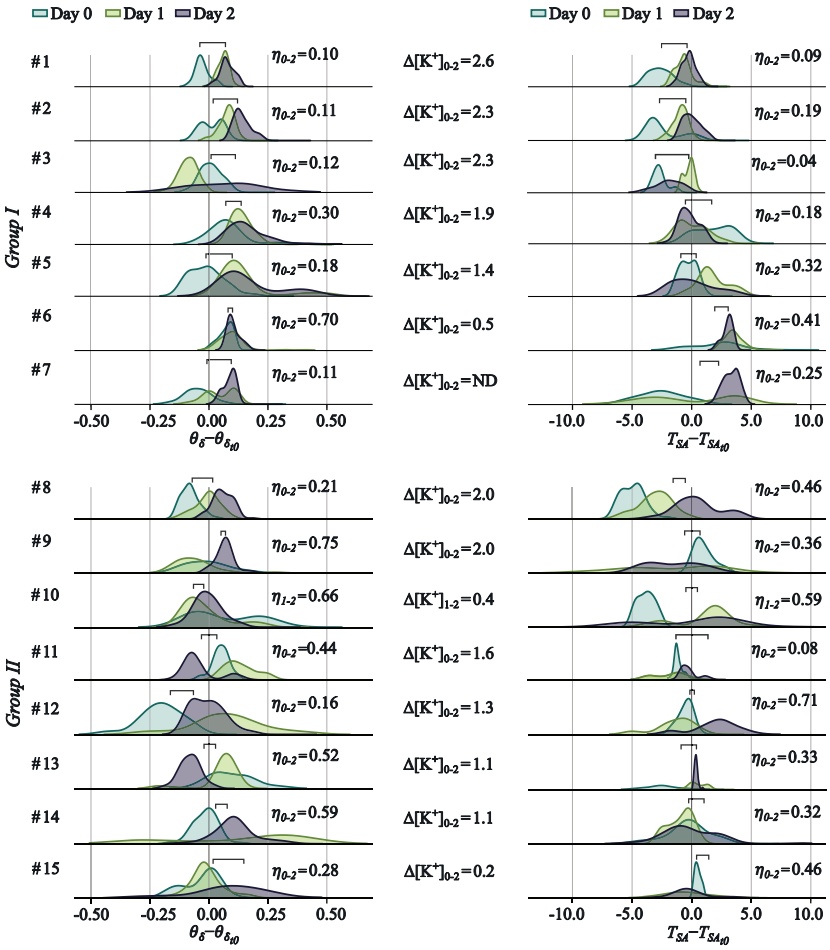

Fig. 3.9. Distribution of $\theta_\delta - \theta_{\delta_{t0}}$ (**left**) and $T_{SA} - T_{SA_{t0}}$ (**right**) of *Group I* and *Group II* during the long interdialytic interval. η_{0-2} is the overlapping index between the distributions of *Day 0* and *Day 2*, whereas $[K^+]_{0-2}$ is the increment of $[K^+]$ between the end of Friday HD and the start of Monday HD. The number of intervals during *Day 2* is small in patients #5 and #14 who were taken to HD one day earlier. The blood samples from Friday HD of patients #7 and #10 were misplaced (ND stands for *no data*). For patient #10, blood was collected on *Day 1*.

#13), T_{SA} showed a more prominent trendline steepness, possibly due to the overlaying effects of both electrolytes on the T-wave downward slope.

Daily variation of T-wave morphology

The daily distributions of $\theta_\delta - \theta_{\delta_{t0}}$ and $T_{SA} - T_{SA_{t0}}$ are given in Fig. 3.9. As anticipated, η responds inversely to $[K^+]$ variations, i.e., lower η values (patients #1–4, #8, and #12) indicate a higher increase in $[K^+]$ and, thus, a smaller overlap of distributions, and vice versa (patients #6, #10). The Pearson's correlation coefficient shows that both descriptors are moderately correlated with the changes in $[K^+]$, being $r=-0.56$ ($p<0.01$)

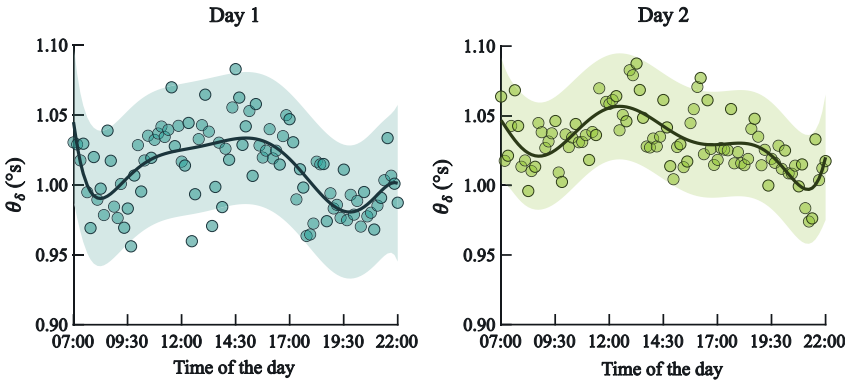

Fig. 3.10. Mean of θ_δ (dots) across all patients in non-overlapping 10 min intervals from 07:00 till 22:00 during *Day 1* and *Day 2*. The solid line is a fitted 7^{th} order polynomial to show a smoothened variation of θ_δ. The upper and lower boundaries represent the standard deviation of the fitted polynomial.

for θ_δ and r=−0.57 (p<0.01) for T_{SA}.

When calculated for each group separately, the correlation is much stronger in *Group I* with r=−0.81 (p>0.01) for θ_δ and r=−0.79 (p>0.01) for T_{SA}, with *Group II* showing a weaker correlation of r=−0.45 (p>0.01) for θ_δ and r=−0.44 (p>0.1) for T_{SA}. It appears that θ_δ is more stable than T_{SA} except for #9, #14, and #15, for whom η_{0-2} shows unexpected values compared to $\Delta[K^+]_{0-2}$. In those patients who displayed both metabolic acidosis and hyperkalemia (#10, #11, and #13), T_{SA} shows lower η_{0-2} values for $\Delta[K^+]_{0-2}$.

Broader distributions are observed in patients #4, #5, #9, #12, and #15, who exhibited T-wave morphologies across the long interdialytic interval different from those used to estimate $\theta_{\delta_{t0}}$ and $T_{SA_{t0}}$. A decrease of θ_δ and T_{SA} during *Day 0* is visible in the majority of patients, possibly due to insulin spikes during meals which can drive $[K^+]$ inside the cells.

Circadian variability of T-wave morphology descriptors

Figure 3.10 shows the mean of θ_δ from 07:00 till 22:00. During *Day 1* and *Day 2*, θ_δ shows higher values in the morning, peaks around lunchtime ([12:00–14:00]), and decreases across the afternoon until the evening. Also, θ_δ increases during the night as θ_δ is higher at 07:00 of *Day 2* compared to 22:00 of *Day 1*.

3.5.2. Impact of signal quality on performance

Figure 3.11 shows the dispersion of c_v for θ_δ and T_{SA} within the periods of low (t_1) and high (t_2) signal quality. Both θ_δ and T_{SA} show higher c_v during t_1. However, θ_δ displays lower c_v during t_1, which suggests a greater stability in noisy conditions than T_{SA}. While the median difference of T_{SA} is minimal between t_1 and t_2, T_{SA} exhibits a

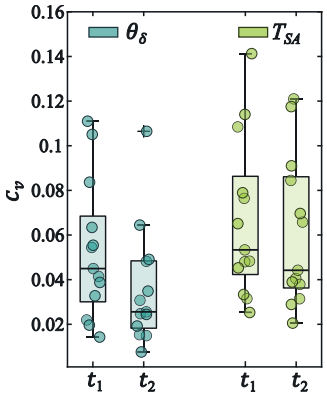

Fig. 3.11. Boxplot of coefficient of variation c_v computed for each patient during two different signal quality periods: t_1 = [21:00–22:00] of *Day 1* (lower signal quality) and t_2 = [00:00–01:00] of *Day 2* (higher signal quality).

large dispersion during t_2. In contrast, θ_δ seems more constant in less noisy conditions. Patients #8 and #12 were excluded from this analysis as #12 displayed T-wave inversion (for which T_{SA} cannot be estimated), and #8 displayed atrial fibrillation during t_1 and t_2.

3.6. Discussion

Gradual electrolyte-induced T-wave morphology changes were quantified using model-based parameterization. The yielded parameters of such models can act as surrogates of important physiological traits that cannot be straightforwardly determined (e.g., T-wave duration) [163]. Additionally, model-based parameterization enables a global evaluation of the T-wave morphology and may increase robustness to noise [164].

T-wave responsiveness to gradual blood potassium fluctuations

Changes in the T-wave morphology were tracked using two descriptors: θ_δ and T_{SA}. The progression of θ_δ and T_{SA} during the long interdialytic interval is promising, with both showing an appealing potential to become estimators of blood [K^+]. Even in a group of patients with various underlying cardiac diseases, θ_δ and T_{SA} are responsive to [K^+] fluctuations, indicating that long-term monitoring of such fluctuations is feasible. Furthermore, θ_δ exhibited a higher stability during noisy periods than T_{SA}, which is advantageous for ambulatory monitoring.

Interestingly, the descriptors showed an increased variability during *Day 0* compared to *Day 1* or *Day 2*. Such variability is plausible since the effects of HD-induced hemodynamic stress could presumably be felt for hours after HD, thus affecting the T-wave morphology. The existence of such a brief period, during which the T-wave morphology can differ from the one manifested during the long interdialytic interval,

may have substantial implications on [K^+] estimation. One approach for ECG-based estimation of [K^+] levels can be the use of a reference T-wave of each individual at a known [K^+] level. Indeed, previous studies have shown a decrease in the error of [K^+] estimation after patient-specific calibration [43, 45]. However, these studies focused on assessing [K^+] levels during HD exclusively, where the same T-wave morphology—similar to that used to estimate the reference values—persists throughout HD. Using T-waves acquired during or immediately after HD as a reference may result in [K^+] estimation errors when the morphology alters. Thus, days between HD sessions should preferably be used for reference T-wave assessment.

Another finding is the apparent circadian periodicity of θ_δ, suggesting that [K^+] naturally fluctuates during the day in HD patients similarly to healthy subjects [162]. Although there is a lack of studies examining the circadian rhythm of blood [K^+] levels in HD patients, such circadian variability in these patients is still plausible. With little to no renal function left, as an attempt to maintain homeostasis, HD patients heavily rely on aldosterone-regulated colonic K^+ secretion [145, 146]. While the circadian rhythm of aldosterone is well understood in healthy subjects [165], it is unclear whether HD patients maintain such circadian rhythm.

Both θ_δ and T_{SA} started to decrease 2 h after the intake of potassium-lowering medication (*Sorbisterit*), which is compatible with its onset of action. The decrease of θ_δ and T_{SA} lasted about 10 h, which is within the expected range of the *Sorbisterit* effect duration. This observation needs to be considered to understand how *Sorbisterit*, or other standard medications prescribed to HD patients, alter(s) the T-wave morphology.

Evaluation of blood potassium with concomitant calcium imbalance

Compared to T_{SA}, the range of θ_δ values is narrower and more consistent across the dataset, except for patients with isolated severe hypocalcemia (#5 and #12), both free from any pre-existent cardiac issues. Intriguingly, these patients exhibited high θ_δ values without hyperkalemia. Atypically low values of δ were found in these patients, which indicates T-wave narrowing as, conceptually, δ mostly depends on the T-wave duration. Considering that the T-wave duration is not affected by calcium imbalance with normal [K^+] levels [42], δ should not have reacted in this manner. Resampling of the ST-T complex, which is distinctively prolonged in hypocalcemia [42], may have affected the T-wave duration.

While flattened or negative T-waves can be prominent in isolated calcium abnormalities [42, 166], particularly in severe levels, changes in the ST-segment duration are the most discernible marker of [Ca] levels [42]. Although this study did not analyze the effects of [Ca] on the ECG in detail, a prolonged ST segment was observed in three patients who displayed severe hypocalcemia. However, ambulatory estimation of the ST-segment duration is challenging, particularly in pathological conditions

of ST-segment deviations, as frequently encountered in HD patients. For instance, in patient #10, with ST-elevation characteristic of left ventricular hypertrophy (LVH), the ST-elongation was not as blatant in lead-I as in patients #5 and #12, both without ST-deviations. In cases of ST-segment deviations, perhaps relying on other ECG leads can mitigate this problem.

Recognizing abnormal calcium levels may improve the detection of dangerous blood [K^+] levels for twofold reasons. Firstly, isolated calcium imbalance can alter the T-wave morphology [42], thus interfering with the assessment of potassium-induced T-wave changes. Secondly, [Ca] and [K^+] have a complex relationship, which affects the intra- and atrioventricular conduction within the heart [42], meaning that the harmfulness of [K^+] levels, either in hypo- or hyperkalemia, is tightly dependent on [Ca] levels [7]. For instance, hypercalcemia antagonizes, whereas hypocalcemia exacerbates the consequences of hyperkalemia [47]. Determining the presence of calcium imbalance can aid in ascertaining whether the measured [K^+] level is alarming.

Evaluation of blood potassium with concomitant acid-base imbalance

Along with concurrent calcium imbalance, the detection of [K^+] fluctuations can be hampered by an acid-base disturbance. When acidosis emerges, the electrophysiological effects of hyperkalemia are, expectedly, aggravated [47]. Consequently, one would anticipate θ_δ and T_{SA} to respond with higher values in such conditions, which was not entirely the case in patients with hyperkalemia and acidosis. Though rare, severe hyperkalemia with minimal T-wave changes has been reported in patients with concomitant acidosis [167]. Although noisy recordings or LVH could justify such an unexpected variation of θ_δ and T_{SA}, the impact of acidosis in [K^+] estimation should not be neglected. Acidosis can instigate T-wave morphology changes resembling those of hyperkalemia [117]. The use of solely T-wave-derived features to evaluate [K^+] levels when acidosis arises may either under- or overestimate [K^+] levels.

A compelling case to mention is patient #15 whose values of θ_δ and T_{SA} decreased during the long interdialytic interval. Besides being the patient with the most complicated medical history, including chronic heart failure (HF), LVH, and ischemic heart disease, he was the only patient who experienced metabolic alkalosis. Even though alkalosis does not usually cause hypokalemia in HD patients [168], it is peculiar to see that θ_δ and T_{SA} decreased. Such a behavior of θ_δ and T_{SA} is something we would expect in the case of [K^+] depletion as in hypokalemia. Since alkalosis-related ECG changes resemble those of hypokalemia [169], one must ask whether this unusual descriptor variation is an inherent result of the HF condition or a consequence of alkalosis.

While blood pH imbalance is seldom life-threatening in itself if not in severe levels [67], identifying acid-base disturbances may not only improve [K^+] monitoring, but

also aid in assessing the arrhythmogenic potential of [K^+]. In addition to being vastly prevalent in HD patients, acid-base imbalances can encourage the onset of arrhythmias by *(i)* impairing vascular and myocardial function [79], and *(ii)* influencing the levels of various electrolytes, including [K^+], [Na], and [Ca] [67, 117]. For instance, metabolic acidosis induces [K^+] shifts from the intracellular to the extracellular space, potentially leading to hyperkalemia [67]. Thus, the identification of [HCO_3^-] levels could enable a better management of blood [K^+]. Nevertheless, with [K^+] and [HCO_3^-] compounding their effects on the T-wave morphology, the feasibility of utilizing a single-lead ECG to monitor [K^+] fluctuations in the presence of abnormal [HCO_3^-] levels is, at the very least, contentious. Future studies should address the confounding potential of [HCO_3^-] by exploring other descriptors of [HCO_3^-] levels.

Evaluation of blood potassium in alternating T-wave morphologies

In addition to concomitant calcium and bicarbonate imbalances, the performance of the T-wave morphology descriptors for estimating blood [K^+] can be affected by alternating T-wave morphologies. Independently of whether different physiological conditions instigate morphology variations, the disparity in the observed T-wave morphologies, even in the same patient, further demonstrates the importance of dealing with various T-wave morphologies. With previous studies having used exclusively intradialytic T-waves to seed models for the quantification of blood [K^+], the performance of such models is, arguably, affected by different interdialytic morphologies. While estimating [K^+] levels from T-waves identical to the patient-specific reference is ideal, it may not always be attainable to do so during activities of daily living. The availability of multiple ECG leads and lead-reduction techniques could ameliorate the problem of alternating T-wave morphologies [170]; however, 12-lead ECG recorders are often uncomfortable to wear and are hence unsuitable for long-term monitoring. Handling various ECG morphologies is thus indispensable for the noninvasive monitoring of electrolyte fluctuations. Indeed, in a highly susceptible group of HD patients, the discrepancy in T-wave morphologies can stem from many sources, either psychological stress [171], changes in body position [158], physical activity [172], other electrolyte imbalances [42], or due to some pre-existent cardiac comorbidities. Understanding the causes of morphology changes in HD patients is pivotal to avoiding the misclassification of other pathologies and electrolyte imbalance.

Limitations and future directions

Despite the encouraging results, deriving θ_δ and T_{SA} in ambulatory conditions still poses some obstacles that must be tackled, with one of them being the innate complexity of determining T-wave boundaries in noisy conditions. When tachycardia or an episode of premature atrial contractions (PACs) occurs, the P-wave can partially

hide within the preceding T-wave, resulting in either a disturbed T-wave morphology or a misguided delineation of the T-wave. The accuracy of most PQRST delineators, including the one used in this study, is hindered during tachycardia or PAC episodes. Even though an SQI detector should have disregarded ECG segments with premature heartbeats, the SQI applied in this work failed to identify PAC episodes, eliminating exclusively ventricular ectopic beats and noisy segments. Premature heartbeats, atrial or ventricular, must be detected for two reasons: *(i)* to avoid delineation errors of the T-wave; and *(ii)* blood $[K^+]$ and $[Mg^{2+}]$ imbalance can trigger ectopy and, consequently, arrhythmias [143]. The frequency of ectopy occurrence might, therefore, indicate abnormal electrolyte fluctuations.

The small number of patients included in this study, albeit a realistic representation of the HD population, certainly restricts the generalization of the outlined findings, especially to other populations susceptible to potassium imbalance. Furthermore, the lack of patients with severe hypo- or hyperkalemia encumbers the evaluation of the performance of θ_δ and T_{SA} in extreme cases with distinctive ECG morphologies.

The exploration of additional electrolyte markers is needed. Having markers of blood $[K^+]$, [Ca], and $[HCO_3^-]$ can facilitate routine electrolyte monitoring, aid in ascertaining the harmfulness of $[K^+]$ levels, and possibly avert life-threatening conditions. Thus, future studies should focus on developing descriptors of [Ca] and $[HCO_3^-]$ levels and optimize $[K^+]$ estimation under concomitant electrolyte imbalance. Future studies should also strive to collect blood samples on days between HD sessions and extend the research to other populations susceptible to $[K^+]$ imbalance (e.g., HF patients).

3.7. Conclusions of the Chapter

1. Noninvasive ambulatory monitoring of blood electrolytes using single-lead ECGs is feasible even in complicated HD patients with comorbid heart disease.

2. Patient-specific T-wave morphology changes are responsive to blood potassium fluctuations during the long-interdialytic interval. The relationship between T-wave morphology changes and blood potassium fluctuations was examined using two descriptors: *(i)* θ_δ, a model-based parameterization descriptor developed to account for the overall T-wave morphology changes, and *(ii)* T_{SA}, the only available descriptor sensitive to $[K^+]$ in single-lead ECGs during HD sessions.

3. θ_δ and T_{SA} responded concordantly with $[K^+]$ fluctuations in a database of 15 ECGs and blood samples acquired over the long interdialytic interval (~3 days). Both descriptors also reacted to potassium-lowering medications and insulin spikes after meals. The overlapping indexes of the daily distribution (η) of θ_δ and T_{SA} are moderately correlated with the changes in $[K^+]$ ($r = -0.56$ and $r = -0.57$, respectively). θ_δ exhibited a daily variability similar to the circadian variation of blood $[K^+]$ in healthy

subjects, peaking amidst morning and decreasing until evening.

4. Although both θ_δ and T_{SA} can be estimated from ECGs registered with consumer healthcare devices, θ_δ is less affected than T_{SA} by motion-induced noise, which is preferable for ambulatory monitoring.

5. *Concomitant electrolyte imbalance*, namely that of calcium and bicarbonate, and *alternating T-wave morphologies* were two confounding factors that affected the performance of θ_δ and T_{SA}. Since the curve-fitting algorithm standardizes the T-wave template prior to parameterization, θ_δ performed better than T_{SA} in alternating T-wave morphologies. Nonetheless, future research must find technological solutions to handle alternating T-wave morphologies.

6. Given the preponderance of alternating T-wave morphologies that can differ from those exhibited during HD, reference T-waves should preferably be assessed in conditions that mimic the everyday monitoring scenario, i.e., in interdialytic settings. Future studies should strive to collect blood samples in such scenarios (and not just during HD) and extend to other patient populations susceptible to potassium imbalance.

4. DEEP-LEARNING-BASED ESTIMATION OF THE SPATIAL QRS-T ANGLE FROM REDUCED-LEAD ECGS

4.1. Rationale and Conceptual Framework

Ventricular repolarization and electrical conduction disturbances are well-documented consequences of electrolyte imbalance [48, 116]. One clinically significant aspect of ventricular repolarization is its *heterogeneity*. As pointed out in Sec. 2.1.2, the distribution of repolarization currents across the ventricular myocardium is heterogeneous, with cells in distinct ventricular regions having different activation times and AP durations [48, 62]. While a certain level of repolarization heterogeneity is crucial to ensure adequate cardiac function, exceeding the physiologically reasonable level of heterogeneity can precipitate SCD-triggering ventricular arrhythmias [143, 173]. Abnormal electrolyte levels amplify this repolarization heterogeneity, resulting in a pathological dispersion of ventricular repolarization [48]. Thus, assessing repolarization heterogeneity in the ECG could add value to noninvasive blood electrolyte monitoring.

One of the most well-established markers of repolarization heterogeneity is the spatial QRS-T angle [49]. The QRS-T angle measures the similarity between the direction of depolarization (QRS) and repolarization (T-wave). It is defined as the angle between the QRS- and T-vectors in the 3D space [57] and is deemed one of the most promising markers for SCD risk stratification in various patient populations, including the general population [50]. While the link between the spatial QRS-T angle and blood electrolyte levels has not yet been investigated, it is plausible to hypothesize that daily QRS-T angle variations could be related to repolarization disturbances caused by electrolyte fluctuations. Therefore, the spatial QRS-T angle may be a potential marker of blood electrolyte levels.

Unfortunately, spatial QRS-T angle estimation is restricted to clinical settings. The conventional approach for estimating the angle requires orthogonal signals, either the VCG from the Frank lead system [57], or orthogonalized 12-lead ECGs that resemble the VCG [174]. The registration of 12-lead ECGs, or even Frank VCG, requires patients to use eight or ten electrodes [108], causing considerable discomfort for ambulatory or long-term monitoring applications. Consumer healthcare devices are practical, comfortable, and hence suitable for out-of-hospital monitoring applications and could be a viable option for noninvasive blood electrolyte monitoring. However, the sets of ECG leads registered by these devices are insufficient to reconstruct the VCG, thus precluding the estimation of the spatial QRS-T angle in such ambulatory scenarios. Methods for estimating the spatial QRS-T angle from reduced-lead ECGs could be deployed in consumer healthcare devices and facilitate out-of-hospital QRS-T angle monitoring.

Research design

The lack of methods for estimating the spatial QRS-T angle suitable for ambulatory applications hinders the scientific investigation of the relationship between the QRS-T angle and blood electrolytes. For instance, the number of ECG-leads registered in the database (Sec. 3.3) collected for examining the feasibility of noninvasive blood electrolyte monitoring in Chapter 3 is insufficient to estimate the QRS-T angle using the conventional (i.e., gold standard) approach. Therefore, the first step toward examining the clinical value of the spatial QRS-T angle as a potential blood electrolyte surrogate is to develop technological solutions to derive the angle from sets of ECG leads that can be conveniently recorded with consumer healthcare devices. Thus far, no other solutions have been proposed to estimate the spatial QRS-T angle from reduced-lead ECGs, ergo raising the following question:

- Can well-established ventricular repolarization markers, such as the spatial QRS-T angle, be derived from reduced-lead ECGs with sufficient accuracy to be prospective solutions for ambulatory noninvasive blood electrolyte monitoring?

Deep neural networks have demonstrated tremendous capabilities to extract key data insights from sets of reduced-lead ECGs [175]. For instance, 1D convolutional neural networks (CNNs) can detect arrhythmias in clinical [176] and ambulatory [177, 178] single-lead ECGs, and even sleep apnea with up to 97.1% accuracy [179] with just one lead ECG. CNNs have also reconstructed the standard 12-lead ECG from a few measured leads [180, 181]. The ostensible potential of CNNs opens the hypothesis of whether the spatial QRS-T angle can be estimated from a set of reduced-lead ECGs. Accordingly, this dissertation proposes a 1D convolutional neural network (CNN1D) for estimating the QRS-T angle from reduced-lead ECGs to tackle the aforementioned research question.

The concept of the proposed method

The premise behind the proposed deep-learning-based approach is simple. With 12-lead ECGs, a model can be trained to predict the reference (i.e., VCG-derived) QRS and T vectors (output) from a specific subset of ECG leads (input) that consumer healthcare devices can register. The angle between the estimated vectors yields the spatial QRS-T angle, and the reference vectors are computed using the 12-lead-based conventional approach. Since the spatial location of QRS and T vectors is vastly dependent on the cardiac conduction axis (Sec. 2.1.3), the model is designed to return the coordinates of both vectors as the output, using an original composite loss comprised of the Euclidean distance and absolute mean error between the vectors and the angle. This loss function guides the model throughout the 3D space to locate the vectors in the X, Y, and Z axes.

This Chapter presents a CNN1D model for estimating the spatial QRS-T angle α from reduced-lead ECGs. A gradual reduction of ECG leads from the largest publicly available dataset of clinical 12-lead ECGs (*PTB-XL* [182]) was used for training and validation to find the best subset of ECG leads for deriving α. While the relationship between the spatial QRS-T angle and blood electrolyte levels was not evaluated, the results presented in this dissertation examine whether the deep-learning model can estimate the spatial QRS-T angle with sufficient accuracy to be a prospective solution for noninvasive ambulatory monitoring of blood electrolyte levels. The presented method is the first proposed for deriving the angle without requiring 12-lead ECGs.

Parts of Sections 4.2–4.7 and the paragraphs above are quoted verbatim from the previously published article: [60].

4.2. Conventional Approach for QRS-T Angle Estimation

The spatial QRS-T angle is estimated from a set of three orthogonal leads, obtained either by applying orthogonalization methods to 12-lead ECGs [174, 183], or, conventionally, the VCG (see Sec. 2.1.3). The VCG, composed of leads *XYZ*, reflects the electrical activity of the heart in the orthogonal planes [105]: frontal (*XY*), transverse (*XZ*), and sagittal (*YZ*). In essence, the VCG depicts heartbeats as a trajectory of *XYZ* leads over time:

$$\vec{v}(t) = [x(t), y(t), z(t)], \tag{4.1}$$

in which the depolarization (QRS) and repolarization (T) phases of a heartbeat are represented as two loops:

$$\vec{v}_{QRS}(t) = \vec{v}(t) - \vec{v}_0, \text{ with } t \in \{t_{QRS_o}, \dots, t_{QRS_e}\}, \tag{4.2}$$

$$\vec{v}_T(t) = \vec{v}(t) - \vec{v}_0, \text{ with } t \in \{t_{T_o}, \dots, t_{T_e}\}, \tag{4.3}$$

where t_{QRS_o}, t_{T_o}, t_{QRS_e}, and t_{T_e} are the onset and offset of the QRS and T loops. Following the guidelines of [184], the origin of both loops $\vec{v}_0$ is estimated as:

$$\vec{v}_0 = \underset{t}{\text{median}}\,(\vec{v}(t)), \text{ where } t \in \{t_{QRS_o} - \tau_0, \dots, t_{QRS_o}\} \text{ and } \tau_0 = 25\,\text{ms}. \tag{4.4}$$

Since inaccuracies in heartbeat delineation can generate significant errors in the estimation of the QRS-T angle, the onsets t_{QRS_o}, t_{T_o}, and offsets t_{QRS_e}, t_{T_e} are adjusted as instructed in [184].

The spatial QRS-T angle measures the dissimilarity between the orientation of the QRS and T loops in the XYZ space and is calculated as:

$$\alpha = \arctan\left(\frac{\left\|\vec{u}_{QRS} \times \vec{u}_T\right\|}{\vec{u}_{QRS} \cdot \vec{u}_T}\right), \tag{4.5}$$

where $\vec{u}_{QRS}$ and $\vec{u}_T$ are vectors that depict the dominant orientation of the QRS and T loops, respectively. The loop orientation is most commonly defined in the time instance $t = t_{max}$ where the maximum magnitude [57] of $\vec{v}_{QRS}(t)$ or $\vec{v}_T(t)$ is verified:

$$\vec{u}_{QRS} = \vec{v}_{QRS}(t_{QRS_{max}}), \text{ where } t_{QRS_{max}} = \arg\max_t \left(\left\|\vec{v}_{QRS}(t)\right\|\right), \tag{4.6}$$

$$\vec{u}_T = \vec{v}_T(t_{T_{max}}), \text{ where } t_{T_{max}} = \arg\max_t \left(\left\|\vec{v}_T(t)\right\|\right). \tag{4.7}$$

Although intuitive, defining the loop spatial orientation as the vector having the maximal magnitude at a single-time instance is an oversimplification, as it assumes that the morphology of the QRS and T loops is unambiguous enough to have a well-defined spatial orientation. In abnormal ECGs, the spatial orientation of the loops (particularly the one of the QRS loop) is too complex to be represented by a vector in a single instance in time. In fact, the estimation of the QRS-T angle using $\vec{v}_{QRS}(t_{QRS_{max}})$ and $\vec{v}_T(t_{T_{max}})$ has been associated with higher errors and poorer reproducibility [185], namely in unhealthy ECGs.

One strategy to tackle the problem of defining the underlying spatial orientation of the QRS loop is the *total cosine R-to-T* (TCRT) [174] method. The TCRT defines the QRS-T angle as the average cosine of all angles between $\vec{v}_T(t_{T_{max}})$ and every vector within the QRS loop that exceeds 70% of the maximum vector magnitude $\vec{v}_{QRS}(t_{QRS_{max}})$ [186]. However, the computation of an averaged angle can become problematic in sets of reduced-lead ECGs, which do not carry the same amount of spatial information as the VCG. Thus, a strategy similar to TCRT is adopted. Instead of deriving the average cosine, $\vec{u}_{QRS}$ and $\vec{u}_T$ are defined as the average of all vectors exceeding 70% of the maximum vector magnitude within the corresponding loops:

$$\vec{u}_{QRS} = \underset{t}{\text{mean}}\left(\vec{v}_{QRS}(t)\right) \text{ where } t \in \left\{t \mid \left\|\vec{v}_{QRS}(t)\right\| \geq 0.7\left\|\vec{v}_{QRS}(t_{QRS_{max}})\right\|\right\}, \tag{4.8}$$

$$\vec{u}_T = \underset{t}{\text{mean}}\left(\vec{v}_T(t)\right) \text{ where } t \in \left\{t \mid \left\|\vec{v}_T(t)\right\| \geq 0.7\left\|\vec{v}_T(t_{T_{max}})\right\|\right\}. \tag{4.9}$$

By defining $\vec{u}_{QRS}$ and $\vec{u}_T$ with Equations (4.8) and (4.9), the spatial QRS-T angle α is then calculated as the angle between $\vec{u}_{QRS}$ and $\vec{u}_T$ using Equation (4.5).

4.3. Deep-learning-based Approach for QRS-T Angle Estimation

A deep-learning model is proposed to estimate the spatial QRS-T angle from reduced-lead ECGs. The model takes the signal-averaged beats from a set of leads as the input and produces the three coordinates of $\vec{u}_{QRS}$ and $\vec{u}_T$, i.e., $\vec{u}_{QRS} = (x_{QRS}, y_{QRS}, z_{QRS})$ and $\vec{u}_T = (x_T, y_T, z_T)$, as the output. The subset of the input leads varies in different experiments, as discussed in Sec. 4.5.

When using 12-lead ECGs, the reference (*target*) VCG vectors $\vec{u}_{QRS}$ and $\vec{u}_T$

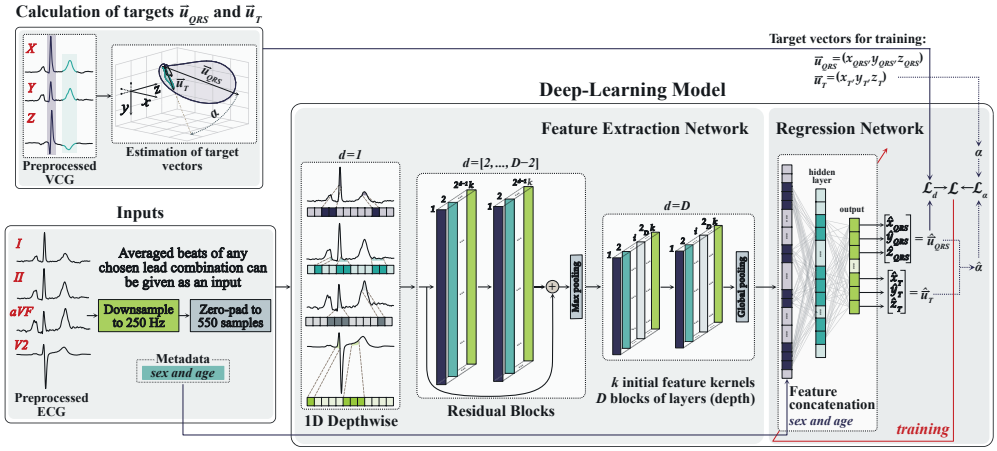

Fig. 4.1. Overview of the proposed deep learning model for estimating the QRS-T angle from reduced-lead ECGs. The model is composed of two parts: feature extraction and regression. The target vectors $\vec{u}_{QRS}$ and $\vec{u}_T$ and the spatial QRS-T angle α are computed from VCGs.

can be computed using the conventional approach described in Sec. 4.2, and train the model to produce the *estimates* $\widehat{\vec{u}}_{QRS}$ and $\widehat{\vec{u}}_T$ of the targets from specific subsets of ECG leads. The estimated QRS-T angle can then be calculated as the angle between the estimated vectors $\widehat{\vec{u}}_{QRS}$ and $\widehat{\vec{u}}_T$ using Equation (4.5). The model is purposely designed to produce the vectors instead of the angle to harness the available spatial information during model training (see Sec. 4.3.2). Figure 4.1 illustrates an overview of the proposed deep-learning-based approach.

From this point onwards, the circumflex symbol denotes variables estimated by the model: $\widehat{\vec{u}}_{QRS}$, $\widehat{\vec{u}}_T$, and the QRS-T angle $\hat{\alpha}$ between them; whereas $\vec{u}_{QRS}$ and $\vec{u}_T$ are the VCG target vectors, and α is the angle between them.

4.3.1. Model architecture

A 1D convolutional neural network (CNN1D) with a regression output is the baseline architecture for the proposed deep-learning model. The model is trained end-to-end using error backpropagation and gradient descent. It can conceptually be divided into two main networks: *feature extraction* and *regression*.

Since distinct subsets of ECG leads may entail different configurations, this Sec. solely describes the baseline architecture of the model. Hyperparameter tuning is detailed in Sec. 4.5.

Feature extraction network

The feature extraction network is composed of D blocks of layers connected sequentially. Each block consists of two 'layer structures', except for the first block, which includes only one. Each layer structure is a sequence of a full 1D convolutional

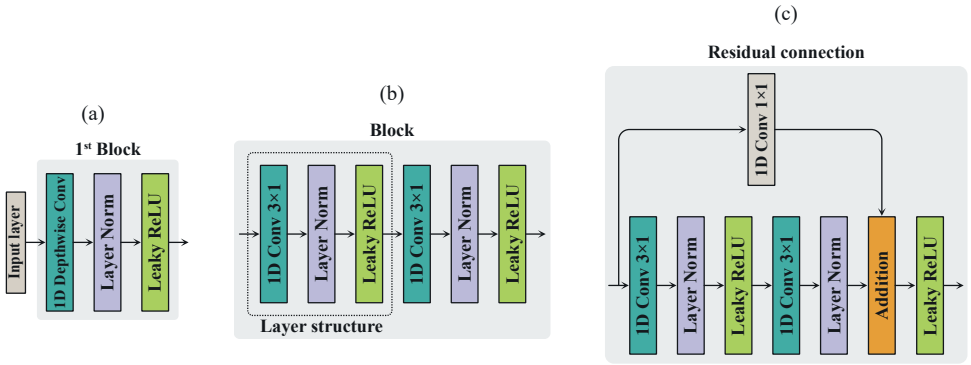

Fig. 4.2. Detailed representation of the three types of blocks employed in the feature extraction network: **(a)** first block, **(b)** last block, and **(c)** blocks with residual connections.

layer with k feature kernels of size 3×1 and a stride of 1, followed by layer normalization and an activation function (Fig. 4.2b). The layer normalization balances the intermediate features to have a mean close to 0.0 and a standard deviation close to 1.0 using trainable scale and shift parameters for each feature map. *Leaky Rectified Linear Unit* (Leaky ReLU) with the negative slope coefficient of 0.1 is the chosen activation function.

A depthwise convolutional layer is employed in the first block instead of a full convolution (Fig. 4.2a). A depthwise convolution allows the model to learn lead-specific features separately, as each lead can carry relevant information on the position of each coordinate of $\vec{u}_{QRS}$ and $\vec{u}_{T}$. Because depthwise convolution layers generate feature maps for each lead, the initial number of kernels k is distributed across all leads, giving $k/j-1$ each, where j is the number of input leads. This avoids having a larger feature map in the first layer than in the second one.

Residual connections (Fig. 4.2c) are introduced from the second block $d = 2$ to the block number $d = D - 1$ to maintain the data flow throughout the network and avoid gradient degradation during training. Prior to addition, a 1×1 convolution is used on the residual connection to equalize the number of feature maps between the layers. The number of filters increases by a factor of 2 in every subsequent residual block. Abstraction of the most significant features is performed with *max pooling* at the end of blocks $d = [2 : D - 1]$, whereas *global average pooling* is implemented to finalize the last block $d = D$ of the feature extraction network. To avoid overfitting, *dropout* with a probability of 0.25 is applied after feature extraction.

Regression network

The resultant feature map is connected to the fully-connected layers (*regression*), which learns to associate the abstracted features with the six neurons in its output: one for each of the three coordinates of $\widehat{\vec{u}}_{QRS} = (\hat{x}_{QRS}, \hat{y}_{QRS}, \hat{z}_{QRS})$ and $\widehat{\vec{u}}_{T} = (\hat{x}_{T}, \hat{y}_{T}, \hat{z}_{T})$.

The regression network consists of three dense layers, the first two followed by layer normalization and Leaky ReLU activation function. The output layer consisting of six neurons is followed by linear activation. Since ECGs can exhibit sex- and age-related dissimilarities in morphology [187] that can affect QRS-T angle estimation [188,189], metadata about sex (*0* for males, or *1* for females) and age (scaled from 0.0 to 1.0) is concatenated to the first layer of the regression network. Providing hints to the model about a possible association between ECGs and the metadata may be valuable when the available spatial information in the input leads is reduced.

4.3.2. Loss function

Since the end goal is to determine the QRS-T angle, the most straightforward approach would be to train the model to estimate the VCG-derived α directly instead of $\vec{u}_{QRS}$ and $\vec{u}_{T}$, optimizing it with the mean absolute error loss between the target α and the estimated $\widehat{\alpha}$:

$$\mathcal{L}_{\alpha}\left(\alpha, \widehat{\alpha}\right) = \frac{1}{n}\sum_{i=1}^{n}\left(\left|\alpha_i - \widehat{\alpha}_i\right|\right), \tag{4.10}$$

where $0^{\circ} \leq \mathcal{L}_{\alpha} \leq 180^{\circ}$ and n is the batch size.

Direct estimation of the QRS-T angle, albeit intuitive and straightforward, overlooks crucial information about the spatial orientation and position of the QRS and T loops, trivializing the problem of QRS-T angle estimation as explained in Sec. 4.2. In sets of reduced-lead ECGs that only carry fragments of all spatial information contained in the VCG, this approach can produce errors in ECGs with visible differences in morphology but similar QRS-T angles. Morphologically different ECGs with QRS-T angles of an equivalent range can occur in patients in which the electrical activity of the heart is not conducted in the same direction—that is, the cardiac conduction axis is nonidentical. In two patients with distinct cardiac conduction axes but similar QRS-T angles, the corresponding vectors $\vec{u}_{QRS}$ and $\vec{u}_{T}$ of each patient are located in different planes (*octants*) in the 3D space, but the angle between them is still alike (Fig. 4.3a).

To address these scenarios, the model is designed to locate the coordinates of $\vec{u}_{QRS}$ and $\vec{u}_{T}$ instead of α directly, allowing the model to harness any spatial information available in the input leads. The model is guided throughout the 3D space using the Euclidean distance as the parameter to be minimized in the backpropagation algorithm. The 3D Euclidean distance (d) between $\vec{u}$ and $\widehat{\vec{u}}$ is computed as:

$$\mathcal{L}_{d}\left(\vec{u}, \widehat{\vec{u}}\right) = \frac{1}{n}\sum_{i=1}^{n}\sqrt{(x_i - \widehat{x_i})^2 + (y_i - \widehat{y_i})^2 + (z_i - \widehat{z_i})^2}, \tag{4.11}$$

where $0 \leq \mathcal{L}_{d} \leq 2$ if $\vec{u}$ and $\widehat{\vec{u}}$ have a magnitude of 1 (i.e., unit vectors)[1].

[1]Two unit vectors $\vec{a}$ and $\vec{b}$ with opposite directions are circumscribed by an angle of 180°, thus

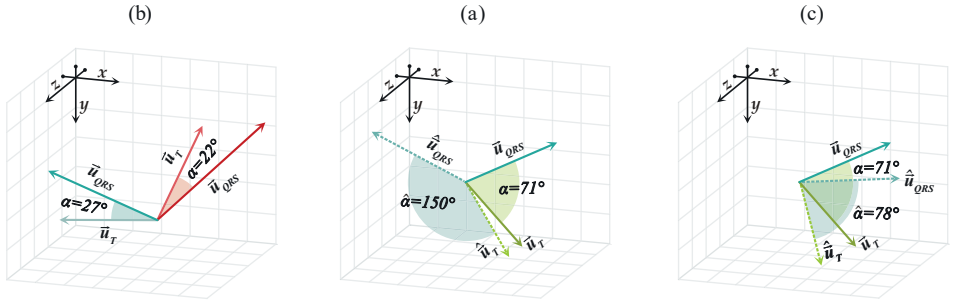

Fig. 4.3. Case scenarios of: (**a**) similar QRS-T angles α of two $\vec{u}_{QRS}$ and $\vec{u}_T$ located in two different planes; (**b**) correct location of one vector ($\vec{u}_T$) but not the other ($\vec{u}_{QRS}$), yielding large errors in the estimated QRS-T angle $\hat{\alpha}$; (**c**) compromise between minor errors in the location of both $\vec{u}_{QRS}$ and $\vec{u}_T$ to achieve a more accurate QRS-T angle estimation.

For $\hat{\alpha}$ to be equal to α, only the direction—but not the magnitude—of the estimated $\hat{\vec{u}}$ has to match the target $\vec{u}$. Given that the Euclidean distance between two vectors also accounts for differences in magnitude, which is undesirable in this case, $\vec{u}$ and $\hat{\vec{u}}$ are transformed to unit vectors prior to calculating $\mathcal{L}_d$. Calculating the Euclidean distance between unit vectors avoids the wrongful calculation of a high loss in cases of two vectors with the same direction but discrepant magnitudes, which should be zero in this application. The principle is similar to the *cosine similarity*. However, the Euclidean distance is preferable for this case scenario as it permits navigating throughout each axis in the *XYZ* plane, whereas the *cosine similarity* only discerns one axis[2].

Another problem left to address during the training process is the cases in which one of the vectors is less complicated to determine than the other (Fig. 4.3b), i.e., the model properly locates one vector but not the other (e.g., $\mathcal{L}_d(\vec{u}_T, \hat{\vec{u}}_T) \cong 0$ and $\mathcal{L}_d(\vec{u}_{QRS}, \hat{\vec{u}}_{QRS}) \cong 1.2$). Significant errors in estimating one vector will inherently affect the accuracy of the QRS-T angle. Since the angle between $\hat{\vec{u}}_{QRS}$ and $\hat{\vec{u}}_T$ needs to be equivalent to α, such cases are mitigated by confining the model's search grid to preserve the angle $\hat{\alpha}$ between $\hat{\vec{u}}_{QRS}$ and $\hat{\vec{u}}_T$ as close as possible to α. Thus, the overall loss is defined as a composite function of Equations (4.10) and (4.11):

$$\mathcal{L} = w_1\left(\mathcal{L}_d(\vec{u}_{QRS}, \hat{\vec{u}}_{QRS}) + \mathcal{L}_d(\vec{u}_T, \hat{\vec{u}}_T)\right) + w_2\,\mathcal{L}_\alpha(\alpha, \hat{\alpha}), \tag{4.12}$$

where w_1 and w_2 are hyperparameters which weigh the penalization factor of $\mathcal{L}_d$ and $\mathcal{L}_\alpha$. The proposed composite loss function safeguards the overall accuracy of the model by avoiding cases in which $\mathcal{L}_d$ of one vector is substantially higher than $\mathcal{L}_d$ of the other, with the tradeoff of allowing minor errors in the location of both vectors (i.e., $\mathcal{L}_d \cong 0.1$

translating into a Euclidean distance equal to the sum of their magnitudes: $\|\vec{a}\| + \|\vec{b}\| = 1 + 1 = 2$.

[2]In the 2D space, the cosine can distinguish quadrant *I* from *II*, or *IV* from *III*, but not *I* from *IV* or *II* from *III*.

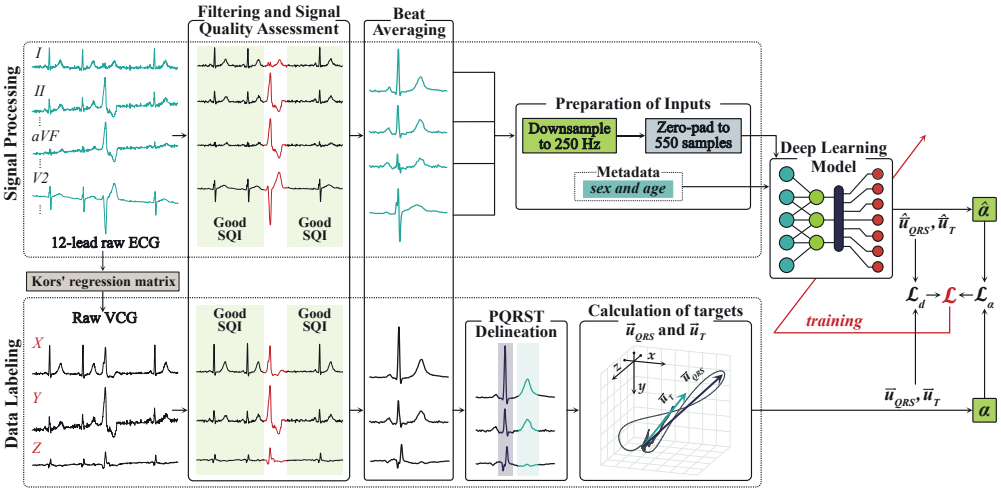

Fig. 4.4. Data preparation and labeling. Signals undergo preprocessing comprised of filtering and signal quality assessment to generate the input signal-averaged beats.

instead of $\mathcal{L}_d \approxeq 0$), as long as the angle $\widehat{\alpha}$ between them is close to α (see Fig. 4.3c). To equalize the scales of $\mathcal{L}_d$ and $\mathcal{L}_\alpha$, $\mathcal{L}_\alpha(\alpha, \widehat{\alpha})$ is estimated in radians rather than degrees.

4.4. Data

The deep-learning model was developed and validated on the Physionet [190] *PTB-XL* dataset [182], the currently largest publicly available dataset of 12-lead ECG recordings. *PTB-XL* comprises 21,837 clinical recordings of 10 s-long ECGs, upsampled to 500 Hz, from 18,885 patients (48% females) with ages ranging from 0 to 95 years. Information on the diagnosis, form, rhythm, and signal quality is provided for all recordings. As to diagnosis, the ECGs are categorized into five different superclasses: Normal (*NORM*), Myocardial Infarction (*MI*), Conduction Disturbance (*CD*), ST/T change (*STTC*), and Hypertrophy (*HYP*). The superclasses are branched into several subclasses, apart from *NORM*.

4.4.1. Data preparation and labeling

Leads X, Y, and Z (VCG) are derived from raw ECGs by applying the Kors regression matrix [109], the mathematical transformation that more accurately reconstructs Frank's VCG from an ECG [108]. The generated 15-lead signals undergo preprocessing comprised of filtering, signal quality assessment, and beat averaging, resulting in a signal-averaged heartbeat representative of each lead. The target vectors $\vec{u}_{QRS}$ and $\vec{u}_T$ are finally computed from the generated signal-averaged VCG leads to label the data. Figure 4.4 illustrates the data preparation process.

Signal preprocessing

The pipeline of signal preprocessing is simple and similar to the one described in Sec. 3.2.1: ECGs are firstly filtered to remove noise, and then undergo signal quality assessment. Lastly, the beats deemed analyzable are signal-averaged.

Filtering. High-frequency noise and baseline wandering are filtered with zero-phase low- and high-pass Butterworth filters with cut-off frequencies of 45 Hz and 0.5 Hz to match the filtering protocol of other studies which derived the QRS-T angle using the conventional methodology [174, 184].

Signal quality assessment. The SQI criterion proposed in [151] is applied to each lead individually to eliminate beats of dissimilar morphology, such as ectopic beats, or those corrupted by noise. Recordings with at least one lead that contains more than 50% poor-quality beats within the 10 s ECG are considered unanalyzable and discarded. ECGs with discernible rhythm disturbances, such as atrial or ventricular flutter or fibrillation, are also excluded from the analysis, given their greater predisposition to PQRST delineation errors, which can affect the reliability of $\vec{u}_{QRS}$ and $\vec{u}_{T}$ [184]. In the case of rhythm disturbances, such as bradycardia, tachycardia, or sinus arrhythmia, PQRST delineation can be less problematic when signals are of a high quality; thus, such ECGs are still considered analyzable if 70% of all beats satisfy the SQI criteria. Annotations regarding rhythm are provided in the *PTB-XL* dataset.

Beat averaging. High-quality beats are aligned using the R-peak as the reference point and averaged, resulting in a single-averaged heartbeat representative of each chosen lead.

Data labeling

The *training labels*, i.e., the target VCG vectors $\vec{u}_{QRS}$ and $\vec{u}_{T}$, are computed from the three averaged beats of leads *XYZ* using the conventional approach described in Sec. 4.2. The QRS and T loops onset and offset, t_{QRS_o}, t_{T_o}, t_{QRS_e}, and t_{T_e}, and R-peaks are identified with the multilead PQRST delineation algorithm available in the *ECGDeli* [154] toolbox[3]. The onset and offset of the loops are adjusted as instructed in [184].

Lastly, the averaged beats are downsampled to 250 Hz and zero-padded to 550 samples to equalize their length, as deep-learning models require inputs of an identical size. Since the standard clinical ECG bandwidth is 0.05 Hz to 100 Hz [191], downsampling the average beats to 250 Hz reduces the computational complexity of the model and the resources necessary for training (e.g., RAM) without compromising crucial

[3]Note that robust PQRST delineation algorithms are critical for computing reliable *training labels* to develop the model but are not necessary for future applications in which only averaged heartbeats and metadata are required as input.

signal information. Patient metadata is also added to the *training labels*: information about the sex is specified as *0* for males and *1* for females, and the age is scaled from 0.0 (0 years) to 1.0 (100 years).

Of 21 837 clinical recordings, 18,618 are eligible for labeling and analysis. In addition to poor-quality ECGs or complicated rhythm disturbances, recordings in which the assigned subclass is underrepresented in the dataset, having less than 100 recordings that meet the SQI criteria, are excluded. ECGs of rare subclasses have such unusual morphologies that errors can be accidentally introduced into the model due to the scarcity of recordings.

4.4.2. Exploratory data analysis

Exploratory data analysis is performed on the labeled recordings before splitting the data between the training and validation sets. The goal is to eliminate any statistical bias by ensuring that both sets preserve the same distribution of sex, morphological classes, and the spatial QRS-T angle in the ranges of $\alpha = [0{:}5{:}180]^\circ$, as in the original dataset. The exploratory data analysis (and the subsequent splitting) is centered around these three attributes due to the following:

- Sex-related morphological differences in the ECG may influence the decision of the regression network (see Sec. 4.3.1); thus, the training set must be proportioned in terms of sex.
- Each of the morphological classes is characterized by distinctive morphological traits. Since contrastive ECG morphologies can still exhibit QRS-T angles of a comparable range, the training set must include a diversity of morphologies to prevent the model from associating a specific range of QRS-T angles with just one subset of particular morphological traits.
- Randomly splitting the data without considering the uneven distribution of α within specific ranges could result in a disproportionate depiction of specific ranges in the training set, which would lead to higher estimation errors in other ranges.

Recordings are divided into six morphological classes: the same five diagnostic superclasses stipulated in the *PTB-XL* dataset, *NORM*, *MI*, *CD*, *STTC*, *HYP*, and low magnitude T-waves (*LOWM*). A recording is deemed *LOWM* if the ratio between $\|\vec{u}_T\|$ and $\|\vec{u}_{QRS}\| < 0.1$. Although signals with low magnitude T-waves seem to have a higher propensity to QRS-T angle errors [184] and are often discarded [184, 192], it is reasonable to incorporate them into this study, given that low magnitude T-waves are routinely found in clinical practice.

Figure 4.5 shows the distribution of α across the ranges of $\alpha = [0{:}5{:}180]^\circ$ according to sex and the morphological class. The dataset has a median of 52.9° (in-

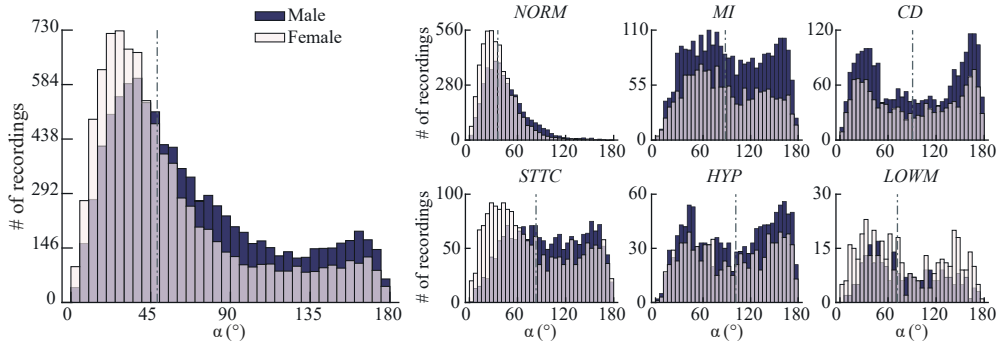

Fig. 4.5. Distribution of spatial QRS-T angle across the ranges of $\alpha = [0{:}5{:}180]^\circ$ according to sex (overlapped) for all eligible recordings in the dataset (**left**) and for each morphological class (**right**). α is the angle between the VCG vectors $\vec{u}_{QRS}$ and $\vec{u}_{T}$. The dashed line is the median α for each class.

terquartile range of 63.3°). The distribution of α, albeit balanced between males and females, varies considerably for each morphological class. Although spatial QRS-T angles $15^\circ \leq \alpha \leq 90^\circ$ comprise the vast majority of the eligible recordings, all other ranges of α are represented by at least 100 recordings, which may be sufficient for deep-learning-based estimation of the QRS-T angle with an acceptable error.

4.4.3. Training and validation sets

The data is split separately for females and males in each morphological class to ensure an appropriate data allocation between the training and validation sets. The split is performed as follows. For any given morphological class, 80% of female ECGs and 80% of male ECGs with $\alpha = [i{:}i + 5[$ for every $i = [0{:}5{:}175]^\circ$, are randomly assigned to the training set. Given the propensity of *LOWM* signals to display larger α errors, the 50:50 partition ratio is used for this class instead of 80:20. A smaller partition of the *LOWM* class still enables the class to be adequately represented in the training set without excessively misleading the model. Figure 4.6 shows that both the training and validation sets preserve the original distribution of α.

It should be noted that the data split described above was performed once, and no *k-folds* cross-validation was employed, meaning that no single recording of the validation dataset was used during training. Thus, the validation dataset is essentially a testing dataset comprised of only 'unseen' data. Since the results presented in the dissertation are the ones yielded by the best combination of hyperparameters for each subset of leads, the term *'validation dataset'* is preferable.

4.5. Experiments and Performance Evaluation

The model is written in *Python* (v3.8.10) using the Keras abstraction layer on *Tensorflow* 2.8.0 backend. Training and validation are performed on a desktop com-

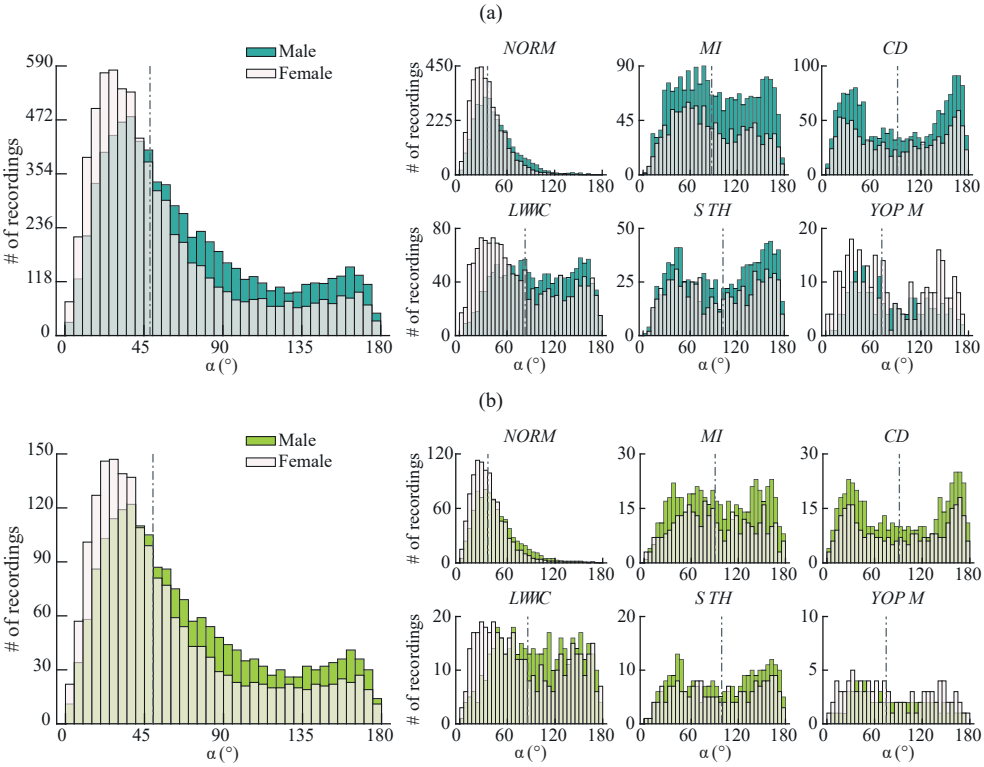

Fig. 4.6. Distribution of spatial QRS-T angle across the ranges of $\alpha = [0{:}5{:}180]^{\circ}$ according to sex (overlapped) for all recordings suitable for analysis (**left**) and for each morphological class (**right**) in the (**a**) training and (**b**) validation sets. The dashed line is the median α for each class.

puter under a *Windows 10* environment with the following hardware specifications: Intel® Core® i7-8700k 3.70 GHz CPU with six cores (12-threads), 32 GB of RAM, and NVIDIA® GeForce® GTX 1080Ti.

Tuning of hyperparameters

Several experiments are conducted to find the best architecture for each of the tested subsets of leads according to the hyperparameters w_1 and w_2 (Sec. 4.3.2), depth D, and the initial number of kernels k (Sec. 4.3.1). The hyperparameters are chosen among the following options:

- $D = \{2, 3, 4, 5\}$;
- $k = \{8, 16\}$;
- $w_1 = \{0.5, 0.8, 1.0, 1.2, 1.5\} \wedge w_2 = |1 - w_1|$;
- $w_2 = \{0.5, 0.8, 1.0, 1.2, 1.5\} \wedge w_1 = |1 - w_2|$.

The hyperparameters D and k are constrained to the above values due to the following. First, complex CNNs employed for image-based applications are likely an overengineered solution for 1D signals. Second, smaller CNN architectures enhanced

with residual connections and case-specific loss functions can outperform architectures based on regular convolutional blocks [193, 194]. Third, lightweight and low-complexity models are preferable for deployment in devices with hardware and computational constraints, such as consumer healthcare devices.

Training is performed with a batch size of $n = 8$ at an initial learning rate of 0.001 for 100 epochs. After every 20 epochs, the learning rate is reduced by half. Although the model was always trained for 100 epochs, the final weights are the ones that yielded the lowest loss and not those rendered at the end of the training process.

Selection of subsets of ECG leads

The performance of the deep learning model to estimate the spatial QRS-T angle is investigated in various subsets of ECG leads. The goal is to identify how many leads suffice to estimate the QRS-T angle with acceptable accuracy without sacrificing the patient comfort. The baseline architecture of the model is first configured using the leads that contain all the 3D spatial information, *XYZ*, from which the target $\vec{u}_{QRS}$ and $\vec{u}_{T}$ are derived. Next, the number of precordial leads carrying insights about the spatial position of $\vec{u}_{QRS}$ and $\vec{u}_{T}$ in each of the *X*, *Y*, and *Z* axes are progressively trimmed. The baseline model architecture is optimized for sets of reduced-lead ECGs that incorporate a minimum of one lead shown to reflect each orthogonal axis: $X \subseteq \{I, V5, V6\}$; $Y \subseteq \{II, III, aVF\}$; and $Z \subseteq \{V1, V2, V3\}$ [195].

Since the ultimate goal is to develop a method to facilitate QRS-T angle monitoring in free-living conditions, only sets of reduced-lead ECGs that can be acquired from commercialized consumer healthcare devices are tested. The registration of frontal leads is straightforward: all six frontal leads ($\{I, II, III, aVL, aVR, aVF\}$) can be derived from any device with two-frontal channels. However, most consumer healthcare devices equipped for frontal and precordial lead registration offer no more than two precordial leads: *V2* and *V6*. Thus, the experiments are limited to the subsets of leads $S \subseteq \{I, II, III, aVL, aVR, aVF, V2, V6\}$.

While a decline in performance is anticipated as the number of precordial leads decreases, the ability of the proposed model to estimate the spatial QRS-T angle from subsets of exclusively frontal leads is also explored as a proof-of-concept. Section 4.6 presents the results of the best subset of leads: first *XYZ*, then few-frontal-and-two-precordial leads, few-frontal-and-one-precordial leads, and, lastly, exclusively frontal leads.

Performance metrics

The accuracy of the proposed model is evaluated with four performance metrics: the absolute mean ($\bar{\epsilon}$) and median ($\tilde{\epsilon}$) estimation errors, the root-mean-squared-error (*RMSE*), and the Spearman's rank correlation coefficient (ρ) between the target α and

the estimated $\widehat{\alpha}$ angles. The absolute estimation error between an observation i is quantified as: $\epsilon_i = |\widehat{\alpha}_i - \alpha_i|$, whereas $\bar{\epsilon}$, $\tilde{\epsilon}$, and $RMSE$ as:

$$\bar{\epsilon} = \frac{1}{r}\sum_{i=1}^{r}\epsilon_i\,; \quad \tilde{\epsilon} = \text{median}(\epsilon_1, \ldots, \epsilon_r); \quad RMSE = \sqrt{\frac{1}{r}\sum_{i=1}^{r}(\widehat{\alpha}_i - \alpha_i)^2}, \tag{4.13}$$

and r is the number of recordings (3,873) in the validation dataset.

Since the Kolmogorov-Smirnov test shows a non-normal distribution of ϵ, $\bar{\epsilon}$ and $\tilde{\epsilon}$ are computed with the nonparametric *bootstrap* method [196] with resampling of 5,000 times. Other metrics shown in the diagrams displayed in the next two subsections are also approximated with *bootstrap*: the 95% confidence intervals of $\bar{\epsilon}$ estimated with the bias-corrected percentile method [197], and the bias and interquartile ranges (iqr) to define the limits-of-agreement ($1.45\,iqr$) in the Bland-Altman plots.

4.6. Results

All the presented results are obtained from the validation dataset. Sec. 4.6.1 discloses the influence of various hyperparameters on the model performance, whereas Sec. 4.6.2 displays the performance of the best model configuration for each set of leads. The presented subsets of leads are the ones with the lowest error $\tilde{\epsilon}$. The recordings in the validation dataset are divided into *healthy* (class *NORM*) and *cardiac disease* (classes *MI*, *CD*, *STTC*, *HYP*, and *LOWM*).

4.6.1. Assessment of the best model configuration

Figures 4.7 and 4.8 display the model's performance in estimating α from leads *XYZ* when trained with various combinations of w_1 and w_2. An initial number of kernels $k = 8$ suffices to obtain a satisfactory accuracy from leads *XYZ*. Only the depth at which the lowest median error $\tilde{\epsilon}$ was obtained for each combination of w_1 and w_2 is shown.

Although the lowest $\tilde{\epsilon}$ was reached with $\{w_1 = 1.2, w_2 = 0.2\}$ at $D = 3$ ($\tilde{\epsilon} = 3.1°$), the model trained with $\{w_1 = 0.8, w_2 = 0.2\}$ at $D = 4$ ($\tilde{\epsilon} = 3.3°$) achieved the narrowest interquartile range (4.6° vs. 5.1°, see Fig. 4.7) and the best overall results throughout all ranges of α. In particular, this configuration outperformed the others for $\alpha \geq 90°$, showing lower absolute mean errors $\bar{\epsilon}$ (Fig. 4.8) despite the smaller number of recordings (samples) in the training dataset for such ranges.

As hypothesized, prioritizing the Euclidean distance ($w_1\mathcal{L}_d$) over the QRS-T angle ($w_2\mathcal{L}_\alpha$) as the predominant penalization factor (i.e., $w_1 > w_2$) results in smaller errors. The combination of the the Euclidean distance and the angle in the loss function yields better results than the use of each metric alone ($\{w_1 = 1.0,\ w_2 = 0.0\}$ and vice versa).

The model trained with the same hyperparameters $\{w_1 = 0.8,\ w_2 = 0.2\}$ achieved the lowest $\tilde{\epsilon}$ at a smaller depth ($D = 3$) for all investigated sets of reduced-lead ECGs,

Table 4.1. Performance of the deep-learning model on estimating the spatial QRS-T angle α from various subsets of leads in the whole validation dataset and ECGs with healthy (*NORM*) and diseased cardiac function.

		Subset of Leads											
		XYZ			***{I, aVF, V2, V6}***			***{I, II, aVF, V2}***			***{I, II, aVL, aVR}***		
Recordings	**Ranges of α**	***RMSE***	$\bar{\epsilon}$	$\tilde{\epsilon}$	***RMSE***	$\bar{\epsilon}$	$\tilde{\epsilon}$	***RMSE***	$\bar{\epsilon}$	$\tilde{\epsilon}$	***RMSE***	$\bar{\epsilon}$	$\tilde{\epsilon}$
All val. dataset	$0° \le \alpha \le 180°$	12.2°	5.8°	3.3°	17.2°	10.3°	6.4°	18.4°	11.4°	7.3°	25.4°	17.9°	12.7°
	$5° \le \alpha < 115°$ [1]	9.2°	4.7°	2.9°	15.4°	9.8°	6.3°	16.0°	10.5°	7.1°	22.8°	16.6°	12.2°
NORM	$0° \le \alpha \le 180°$	6.1°	3.4°	2.5°	13.5°	8.3°	5.5°	14.1°	9.0°	6.1°	21.0°	14.9°	11.1°
	$5° \le \alpha < 70°$ [1]	4.6°	3.0°	2.4°	11.0°	7.2°	5.1°	11.1°	7.6°	5.7°	15.2°	11.7°	9.8°
Cardiac disease	$0° \le \alpha \le 180°$	16.8°	8.7°	4.9°	20.5°	12.2°	7.3°	21.8°	13.7°	8.7°	29.1°	20.7°	14.3°
	$15° \le \alpha < 115°$ [1]	12.8°	7.2°	4.2°	18.4°	12.1°	8.1°	19.6°	13.3°	9.5°	27.7°	20.6°	15.0°

[1] Ranges of α adequately represented in the training dataset (>200 samples).

but required more initial kernels ($k = 16$).

Concatenating metadata (sex and age) resulted in a lower $\tilde{\epsilon}$, especially for subsets of reduced-lead ECGs, but the improvement in performance was not significant ($\le 1.5°$).

4.6.2. Performance assessment in various subsets of ECG leads

Figures 4.9–4.11 detail the performance of the best model configuration in estimating α when using leads *XYZ* and various subsets of reduced-lead ECGs: two precordial leads $\{I, aVF, V2, V6\}$, one precordial lead $\{I, II, aVF, V2\}$, and solely frontal leads $\{I, II, aVL, aVR\}$. Table 4.1 discloses the obtained performance evaluation metrics for each investigated set of leads in the validation dataset.

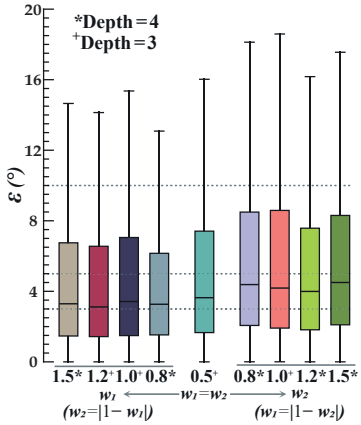

Fig. 4.7. Boxplot of the obtained absolute error ϵ (outliers not shown) of various model configurations tuned with different combinations of hyperparameters w_1 and w_2. w_1 increases to the left side, whereas w_2 to the right. The other hyperparameter value is obtained as $|1 - w|$ on each side.

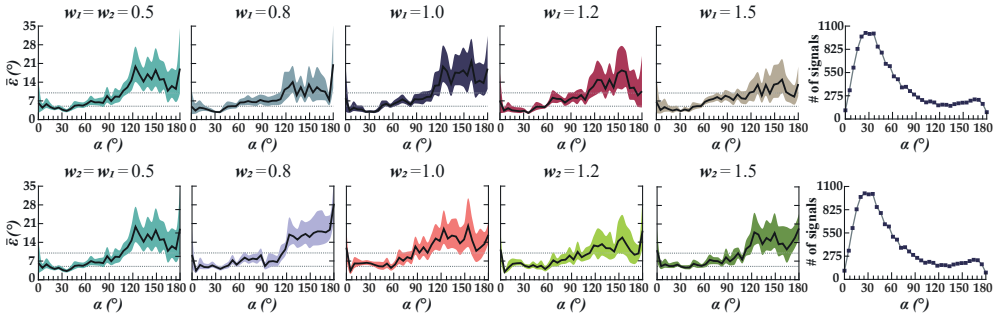

Fig. 4.8. Performance of various model configurations tuned with different combinations of hyperparameters w_1 and w_2 in estimating the spatial QRS-T angle α from leads *XYZ* in the validation dataset. The mean absolute error $\bar{\epsilon}$ and the respective 95% confidence interval are shown across the ranges of $\alpha = [0:5:180]^\circ$ for increasing w_1 (**top row**) and w_2 (**bottom row**). The rightmost column displays the number of training samples for each range of α.

Estimation errors across all ranges of α

Figure 4.9 shows the agreement between the estimated $\widehat{\alpha}$ and the target α. Even though the estimation errors naturally increase with the reduction of the spatial information available in the input leads, the results indicate that reduced-lead estimation of the QRS-T angle is achievable. In the whole validation dataset, the correlation between $\widehat{\alpha}$ and α, albeit strong, decreased from $\rho = 0.96$ for leads *XYZ* which contain all spatial information, to $\rho = 0.91$ for leads $\{I, aVF, V2, V6\}$ (two precordial), $\rho = 0.9$ for $\{I, II, aVF, V2\}$ (one precordial), and $\rho = 0.77$ for $\{I, II, aVL, aVR\}$ (solely frontal).

Despite *RMSE*, $\bar{\epsilon}$, and $\tilde{\epsilon}$ always being higher in ECGs with cardiac disease than the healthy ones, regardless of the subset of leads, $\widehat{\alpha}$ and α are more strongly correlated in all morphological classes with cardiac disease than *NORM* for sets of reduced-lead ECGs. The agreement between $\widehat{\alpha}$ and α decreases from $\rho = 0.86$ (*NORM*) vs. $\rho = 0.91$ (cardiac disease) for $\{I, aVF, V2, V6\}$; to $\rho = 0.85$ (*NORM*) vs. $\rho = 0.9$ (cardiac disease) for $\{I, II, aVF, V2\}$; and even smaller for $\{I, II, aVL, aVF\}$ with $\rho = 0.55$ (*NORM*) vs. $\rho = 0.81$ (cardiac disease). Since $\bar{\epsilon}$ is much lower in the ranges of $5^\circ \leq \alpha < 70^\circ$ which are substantially more represented in the training dataset (Fig. 4.10), this correlation decline may be ascribed to higher errors in the underrepresented ranges of α. In leads *XYZ*, $\rho = 0.98$ for *NORM* recordings, and $\rho = 0.95$ for cardiac disease.

Estimation errors across different ranges of α

Figure 4.10 displays the variation of $\bar{\epsilon}$ in the various sets of leads. The model exhibited markedly higher estimation errors in the ranges of α underrepresented in the training dataset (< 200 recordings): $\alpha < 5^\circ$ and $\alpha \geq 70^\circ$ for healthy (*NORM*) ECGs; and $\alpha < 15^\circ$ and $\alpha \geq 115^\circ$ for ECGs with cardiac disease. The downsizing of input precordial leads exacerbated the drop in accuracy, with the set $\{I, II, aVL, aVR\}$ showing the highest susceptibility to estimation errors in the underrepresented ranges of α. The

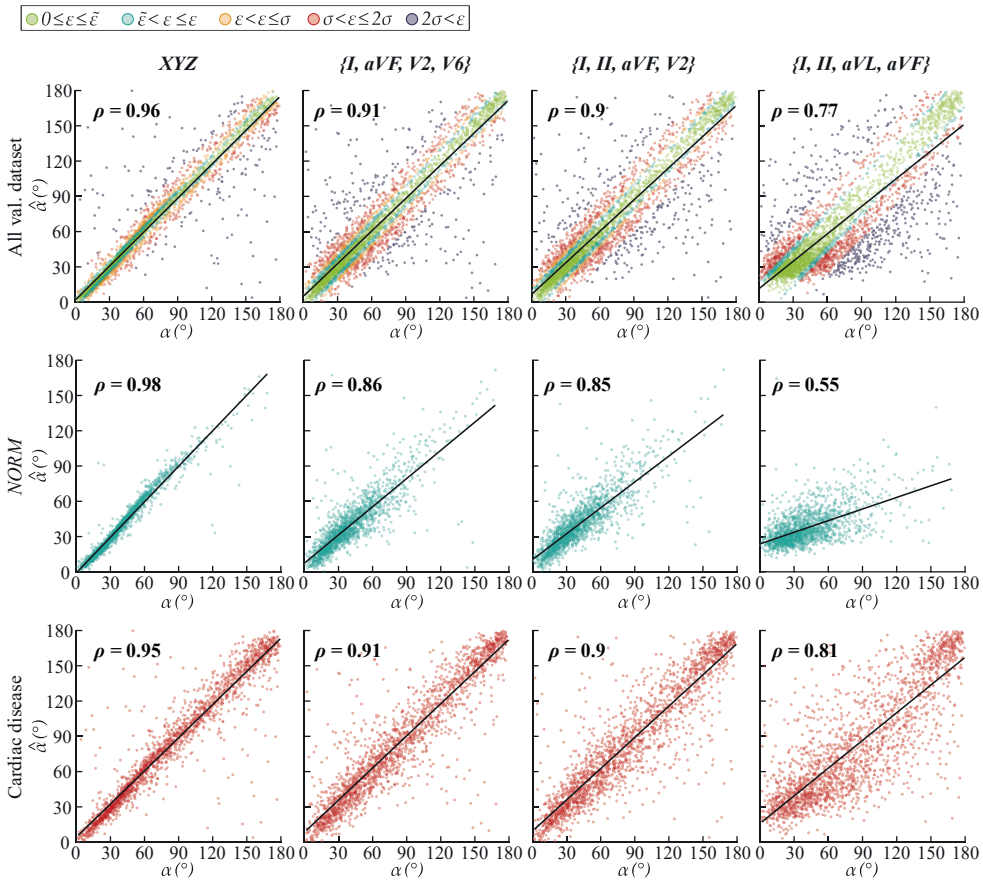

Fig. 4.9. Scatter plot diagrams of the deep-learning-estimated $\widehat{\alpha}$ vs. target α from various sets of leads for (top row) all recordings, and ECGs with normal (middle row) *NORM* and (bottom row) cardiac disease in the validation dataset. The estimation error ϵ of every $\widehat{\alpha}$ in the first row is color-grouped based on the absolute median ($\tilde{\epsilon}$), mean ($\bar{\epsilon}$), and standard deviation (σ_ϵ) error.

error $\bar{\epsilon}$ is significantly lower in the ranges of α containing more than 200 samples in the training dataset (see Table 4.1). Nevertheless, $\bar{\epsilon}$ rises as anticipated with the reduction of the available spatial information in the input leads.

Interestingly, in ECGS with cardiac disease, leads *XYZ*, as opposed to any subset of reduced-lead ECGs, displayed the highest estimation errors in the ranges of $\alpha > 115°$. The loss of crucial diagnostic information in diseased ECGs caused by the VCG reconstruction method might explain such an unexpected result.

The Bland-Altman diagrams in Fig. 4.11 corroborate the abovementioned results. The limits of agreement between $\widehat{\alpha} - \alpha$ and α are narrower in the leads *XYZ* and start to broaden as the number of precordial leads decreases, with recordings of the class *NORM* having less variability from the median bias than those with cardiac disease. In $\{I, II, aVL, aVF\}$, however, the model reveals an inversely proportional, yet homoscedastic

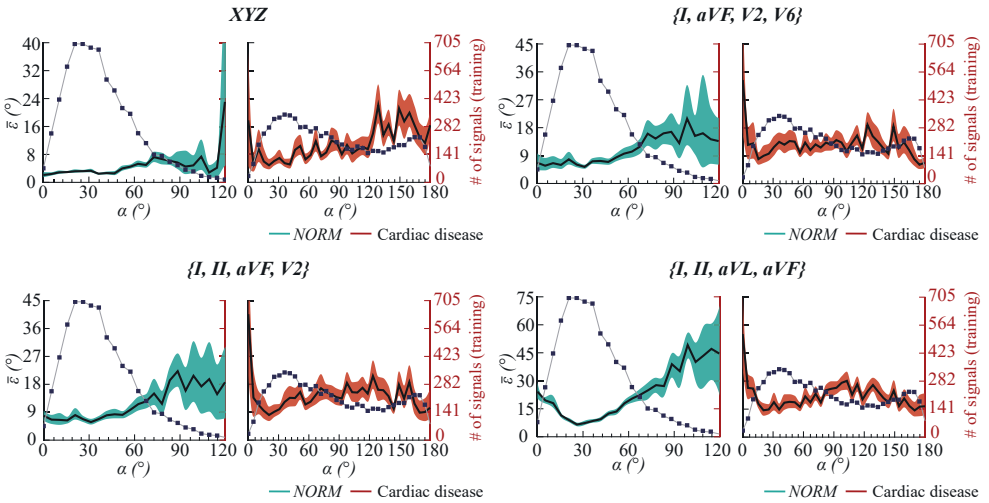

Fig. 4.10. Variation of the mean absolute error $\bar{\epsilon}$ and the respective 95% confidence interval across the ranges of $\alpha = [0{:}5{:}180]^\circ$ for ECGs with normal (*NORM*) and diseased cardiac function. The right axis indicates the number of training samples in each range of α. Since the number of *NORM* subjects with $\alpha > 120^\circ$ is negligible, $\bar{\epsilon}$ is not shown for these ranges of α.

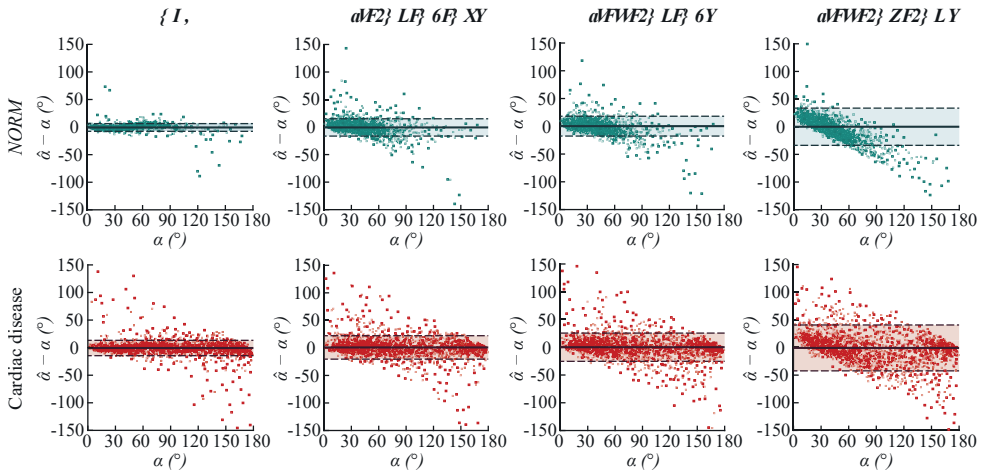

Fig. 4.11. Bland-Altman diagrams of deep-learning-based estimation of $\widehat{\alpha}$ from various sets of leads of ECGs with (**top**) normal (*NORM*) and (**bottom**) diseased cardiac function.

bias, i.e., the variance across different ranges of α is similar. Homoscedasticity is characteristic of models with a variable that has not been fully enclosed. In this case, the missing variable is the information on the electrical activity of the heart in sagittal (*YZ*) and transverse planes (*XZ*) that are provided by the front-back (*Z*) axis. Nevertheless, the inversely proportional bias is not favorable for cardiovascular health assessment. The model would underestimate the ranges of $\alpha > 110^\circ$ associated with an increased risk of dangerous cardiac events.

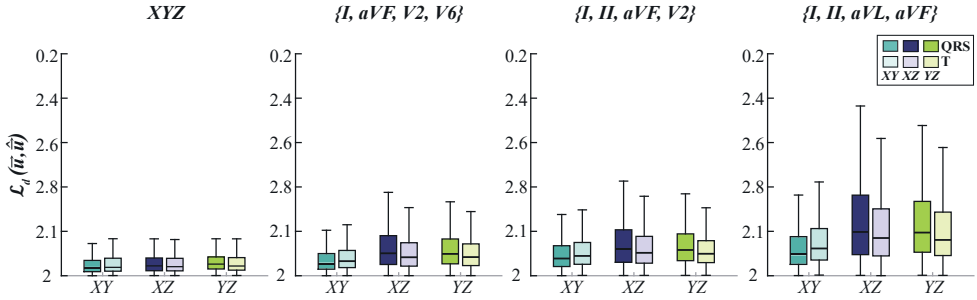

Fig. 4.12. Distribution of the Euclidean distance $\mathcal{L}_d(\vec{u}, \hat{\vec{u}})$ between $\vec{u}_{QRS}$ and $\hat{\vec{u}}_{QRS}$, and $\vec{u}_T$ and $\hat{\vec{u}}_T$ in each of the three planes: XY (frontal), XZ (transverse), and YZ (sagittal).

Estimation errors of the Euclidean distance across the anatomical body planes

Figure 4.12 displays the distribution of the Euclidean distance $\mathcal{L}_d(\vec{u}, \hat{\vec{u}})$ between $\vec{u}_{QRS}$ and $\hat{\vec{u}}_{QRS}$, and $\vec{u}_T$ and $\hat{\vec{u}}_T$ in each plane: XY (frontal), XZ (transverse), and YZ (sagittal). The distance is calculated as the projection of $\vec{u}$ and $\hat{\vec{u}}$ in the respective plane. $\mathcal{L}_d(\vec{u}, \hat{\vec{u}})$ gradually lengthens in every plane from the leads XYZ to $\{I, aVF, V2, V6\}$ and $\{I, II, aVF, V2\}$, but becomes discernibly higher in the XZ and YZ planes in the frontal leads $\{I, II, aVL, aVF\}$ which only carry information in the XY plane. Larger $\mathcal{L}_d(\vec{u}, \hat{\vec{u}})$ suggests that the model encountered extra obstacles to locate the vector's coordinates within the specified plane.

4.7. Discussion

Monitoring the spatial QRS-T angle, evidenced as one of the most propitious markers for risk assessment of SCD [50, 57], was presumed to be impracticable in out-of-hospital settings thus far. This doctoral dissertation introduces a deep-learning-based method to measure the spatial QRS-T angle using a set of reduced-lead ECGs that can conveniently be recorded with consumer healthcare devices. The proposed model, albeit prototypal, sparks scientific interest in engineering methods for ambulatory monitoring of the spatial QRS-T angle, which can lead to substantial contributions toward harnessing the diagnostic value of the QRS-T angle for cardiovascular health assessment in free-living conditions.

Considerations on the model architecture

The baseline architecture of the proposed model is engineered to be accurate yet simple enough to be lightweight and have a sufficiently low computational power to be integrated into consumer healthcare devices. Compared to other CNN1Ds for ECG analysis, often comprised of 8-to-34 [176, 178, 179, 198] blocks of layers, the proposed baseline architecture of three-to-four blocks ($D = \{3, 4\}$) and $k = 16$ suffices to get satisfactory results. The model contains only 105,578 trainable parameters, nearly 12 times

less than the CNN1D developed for classifying single-lead ambulatory ECGs [178]. While popular due to their high accuracy, deeper neural networks also entail larger training datasets and computational resources that can hamper the deployment of the network in devices with hardware and computational constraints such as wearables. Furthermore, adopting deeper neural networks does not necessarily translate into significant improvements in accuracy to justify the tradeoffs in resources if the goal application is for out-of-hospital monitoring of the QRS-T angle.

Smaller networks, such as the one described in this research, or as in the one applied for automatic diagnosis of 12-lead ECGs [198], outperform their convolutional-blocks-only counterparts when enhanced with custom blocks, such as residual connections, squeeze-and-excitation, atrous spatial pooling, or case-specific loss functions [193, 194]. The strategy behind the proposed model involved residual blocks with a predominant focus on an original loss function. The described loss function (Sec. 4.3.2) combines two metrics, each with their penalization weight, to train the model: the Euclidean distance (w_1) and the QRS-T angle (w_2). Prioritizing the Euclidean distance over the QRS-T angle (i.e., $w_1 > w_2$) as the main penalization factor results in smaller errors, namely, in sets of reduced-leads ECGs. Optimization with the Euclidean distance combined with the QRS-T angle instead of the QRS-T angle alone allows the model to recognize that ECGs with visible differences in morphology can still have similar QRS-T angles, minimizing the chances of the model associating a specific morphology to a particular range of α. Morphologically different ECGs with similar QRS-T angles are often the case in patients with distinctive cardiac conduction axes in which the direction of the overall electrical activity of the heart is not the same. In a 3D space, this means that the vectors $\vec{u}_{QRS}$ and $\vec{u}_{T}$ of each patient are located in different planes (octants), but the angle between them does not necessarily differ. Searching for the coordinates of both target vectors helps the model leverage any available information to boost accuracy. Thus, adopting such metrics that guide the model in the 3D space is a favorable choice.

Considerations on the attained results

The model has demonstrated a propensity to higher estimation errors in ranges of QRS-T angle represented by less than 200 recordings (samples) per morphological class in the training data. This propensity is amplified as the number of input precordial leads decreases. Although an increase in estimation errors is anticipated with the reduction of the spatial information available in the input leads, the interconnection between higher errors and fewer training samples suggests that additional recordings may promote a more accurate QRS-T angle estimation from reduced-lead ECGs. When the complete spatial information is accessible in leads *XYZ*, the model can straightforwardly identify relevant data features from fewer recordings. Conversely, the relevant

data features may be less conspicuous and more challenging to detect in reduced-lead ECGs with limited spatial information. Thus, the model may necessitate more training samples to identify relevant data features.

Surprisingly, leads *XYZ*—but not subsets of reduced-lead ECGs—showed the highest estimation errors in ECGs with cardiac disease in the underrepresented ranges of $\alpha \geq 115°$. Such an unexpected result may be attributed to possible signal distortions caused during the VCG reconstruction process. In certain cardiac pathologies, the mathematical transformations to derive the VCG can camouflage (or even eliminate) distinctive data features [195,199], hindering the model's ability to recognize any feature patterns that point to the location of $\vec{u}_{QRS}$ and $\vec{u}_T$. In contrast, these distinctive data features are preserved in ECGs of cardiac pathology, even in frontal leads, hence impelling the model to locate the target vectors more correctly.

An analogous argument can also explain the accuracy drop in the estimated $\widehat{\alpha}$ from any subset of reduced-lead ECGs of class *NORM*, in which the estimation errors were substantially higher in the underrepresented ranges of $\alpha \geq 70°$. Since wider QRS-T angles are generally associated with severe cardiac diseases [50, 200], such a surprising result raises the question of whether large values of α can occur in healthy ECGs or are ascribed to label noise. However, label noise could only justify such a result if leads *XYZ* displayed the same discrepancy in estimation errors in the ranges of α observed in reduced-lead ECGs. A plausible explanation lies in the sagittal (*YZ*) plane, which may contain the most indicative data features of wider QRS-T angles in the absence of cardiac disease. With only fragments of sagittal information given in reduced-lead ECGs, the model struggles to identify data features characteristic of wide QRS-T angles in seemingly healthy ECGs if fewer training samples are provided.

The correct estimation of the location of $\vec{u}_{QRS}$ and $\vec{u}_T$ in any plane incorporating the orthogonal lead *Z* (sagittal and transverse) is challenging in reduced-lead ECGs regardless of the morphological class. Reducing the amount of spatial information in the input ECG-leads encumbers the search for the coordinates of $\vec{u}_{QRS}$ and $\vec{u}_T$, namely through the z-axis, as verified by an increase of the Euclidean distance between the target and the estimated vectors. In parallel with additional recordings, decomposing the Euclidean distance loss into each of the three planes could be a potential solution to enhance the location accuracy of the z-coordinate. Isolating the planes in the loss function enables tailoring the penalization factor to each plane, which may promote better estimation results.

Suitability for ECG consumer healthcare devices

While the investigation presented in this dissertation consisted only of non-ambulatory ECGs collected with clinical devices, the suitability of the proposed model for consumer healthcare devices is plausible and merits further discussion. Con-

ceptually, ambulatory estimation of the spatial QRS-T angle can be performed similarly to KardiaMobile® [201] for arrhythmia detection or the prototype technology developed to monitor electrolyte fluctuations in hemodialysis patients at home [152]. Preprocessing, heartbeat averaging, and the subsequent QRS-T angle computation is feasible offline with some delay for short intermittent ECG recordings (15-to-60 s), or through cloud processing for longer recordings. Cloud processing would also support the transmission of estimated QRS-T angles to health professionals for remote verification of potentially dangerous cardiac events.

An attractive attribute of the proposed deep-learning model is its simplicity. When looking at the computational demands of the whole algorithm, the QRS-T angle can be estimated swiftly, with the preprocessing stage exercising more computational time and resources than the deep-learning model itself. In recordings scenarios that assure that 10-to-15 s long ECGs are registered with sufficient quality to warrant low-complexity filtering in the preprocessing stage, the spatial QRS-T angle can be calculated in a few seconds with the advantage of not needing PQRST delineation, which is often problematic in ambulatory recordings due to noise.

The model measured the spatial QRS-T angle with reasonable accuracy from a set of three frontal and one precordial leads ($\{I, II, aVF, V2\}$) that can be registered with three electrodes instead of the eight required to derive the QRS-T angle when using the conventional approach. The requirement of one precordial lead evidently restricts the type of consumer healthcare devices suitable for deploying the deep learning model in future applications, precluding the use of devices that maximize comfort, such as wrist-worn wearables [202] which only register frontal-lead ECGs. Nevertheless, the market already offers a handful of practical devices that acquire frontal and one precordial lead ECGs with an acceptable degree of comfortableness [203], namely those patch-based (e.g., Bittium OmegaSnap™ [204]), or contact-based textile (e.g., Viscero ECG vest [205]) ECG electrodes. A downsize of eight to three electrodes is still a substantive improvement. Even if the comfort level of three electrodes is lower than that of other wearables, the existing patch- or textile-based ECG devices are durable, easy to configure, and may be adequate for intermittent monitoring of the QRS-T angle in free-living conditions. Recent advancements in the reconstruction of the standard 12-lead ECG from sets of reduced-lead ECGs have, however, demonstrated the possibility to derive lead *V2* from lead *II* [206] in healthy subjects. The encouraging preliminary results indicate an appealing solution for estimating the spatial QRS-T angle with comfortable wearable devices in the future.

Most commercialized ECG consumer healthcare devices have technical specifications analogous to the clinical recordings used to develop the model: *(i)* a minimum 16-bit precision at a resolution of 1 µV/LSB; *(ii)* ECG bandwidth of 0.05 Hz to at least 100 Hz; and *(iii)* sampling rates starting at 200 Hz. However, since the estimation of

the spatial QRS-T angles has been, to date, performed exclusively from clinical devices with higher signal resolution and sampling rates, the minimal technical specifications of devices suitable for ambulatory measurement still need to be defined. While the model estimated QRS-T angles from heartbeats downsampled to 250 Hz with satisfactory accuracy, the influence of different technical specifications on the estimation of the QRS-T angle was not investigated, nor, to the best of the knowledge of the author of this dissertation, do any studies exist that have examined this question. Although higher ECG bandwidths and sampling rates ≥ 500 Hz are pertinent for detecting arrhythmias [191], and in pediatric ECGs [207]—and are indeed often recommended for clinical ECGs [191]—deep-learning models can detect arrhythmias from ECGs with sampling rates of 300 Hz [177], 200 Hz [178], and even 100 Hz [208]. Thus, a minimum sampling rate of 200 Hz seems a reasonable compromise between adequate deep-learning-based analysis of ambulatory ECGs without increasing the hardware and computational complexity or draining the battery life of consumer healthcare devices [209].

Prospective of the spatial QRS-T angle as a blood electrolyte marker

Although the results presented in this dissertation do not examine the relationship between the spatial QRS-T angle and blood electrolyte levels, the proposed deep-learning model can be a prospective solution for facilitating noninvasive ambulatory monitoring of blood electrolyte levels. The model offers the first step toward examining the relationship between the spatial QRS-T angle and blood electrolyte levels in everyday ambulatory scenarios.

The spatial QRS-T angle, albeit not yet investigated as a potential marker of blood electrolyte balance, is a promising risk stratification index for SCD in various populations [50] and an indicator of blood levels of anti-inflammatory heat shock proteins [210] and troponin T[4] [211]. However, the effect of HD on the spatial QRS-T angle has been variable in different studies [139]. Some report little-to-no variation throughout the HD session, whereas one study documented an increase in the spatial QRS-T angle before and after HD. While these findings can suggest a lack of responsiveness of the spatial QRS-T angle to electrolyte fluctuations, the variability—or lack thereof—of ECG features observed during HD does not necessarily translate to the same ECG changes in interdialytic settings. As discussed in Sec. 3.6, many patients display ECG alterations during HD that are absent throughout the long interdialytic interval. In addition, multiple other hemodynamic and biochemical variables which can affect the cardiac function are rapidly changing during HD.

One plausible explanation for the lack of variability is the antagonist relationship between K^+, Ca^{2+}, and Mg^{2+}. Since the spatial QRS-T angle measures the similarity

[4]Increased troponin-T levels in the blood are associated with CVD and heart failure.

between depolarization and repolarization, the hyperpolarization/hyperexcitability effects of one ion may be counteracted by another, thereby stabilizing the cardiac APs and protecting the normal repolarization heterogeneity (Sec. 2.1.4). If that is the case, the spatial QRS-T angle may aid in ascertaining whether blood electrolyte levels measured by other ECG-derived descriptors are alarming, thus mitigating the confounding factors described in Sec. 3.6. Thus, the relationship between the QRS-T angle and blood electrolyte levels warrants investigation in out-of-hospital settings.

Limitations and future directions

When considering the ultimate application goal of this research, which is to facilitate ambulatory monitoring of the spatial QRS-T angle for cardiovascular health research, one must pose two central questions:

- What is the maximum acceptable estimation error?
- What is the clinical value of an 1° increase?

All medical research regarding the QRS-T angle focuses on its prognostic value for SCD, using observational studies [50, 57] with follow-up periods of 2-to-30 years that categorize the angle into subranges, most commonly as normal ($<110^\circ$) vs. dangerous ($\geq 110^\circ$) [50, 212]. While the optimal cut-off threshold for assessing the dangerousness level of the spatial QRS-T angle depends on sex [188], age [189], medical history [57], and even the methods to derive the $\vec{u}_{QRS}$ and $\vec{u}_{T}$ [185, 199], no studies have investigated thus far if day-to-day fluctuations of the QRS-T angle offer any clinical value. Populations susceptible to cardiac repolarization disturbances, such as CKD and HF patients, could benefit from daily monitoring of QRS-T angle fluctuations in which the angle variation would be more auspicious than the absolute value itself. For instance, QRS-T angle fluctuations may be related to abnormal repolarization heterogeneity induced by electrolyte imbalance. Higher estimation errors may be acceptable for such application scenarios, providing that the bias is constant. Oppositely, scenarios aiming to classify subranges of spatial QRS-T angles per clinical importance may require smaller estimation errors within the predefined cut-off ranges.

Unfortunately, the answer to the posed questions remains open and falls beyond the scope of this research. Nevertheless, considering that intra-subject inaccuracies up to 10° are to be expected [185] and that a 20° increase in the spatial QRS-T angle is associated with a 4% aggravated risk of mortality [213], the estimation errors obtained from the subset $\{I, II, aVF, V2\}$ may suffice for detecting abnormal QRS-T angles without compromising patient comfortability. Furthermore, measuring the spatial QRS-T angle from subsets of solely frontal leads looks plausible in the future with further refinements of the deep-learning prototype model.

A viable solution for boosting the estimation of the spatial QRS-T angle from reduced-lead ECGs could be the adoption of ensemble methods in a hierarchical or-

der. Ensemble methods could first classify ECGs into various subranges (classes) of QRS-T angles and subsequently assign different regression networks to each separate class. The designated classes could categorize ranges of spatial QRS-T angles by clinical significance: *narrow* ($0^\circ \leq \alpha < 30^\circ$), *healthy* ($30^\circ \leq \alpha < 70^\circ$), *borderline healthy* ($70^\circ \leq \alpha < 110^\circ$), *dangerous* ($110^\circ \leq \alpha < 135^\circ$), *life-threatening* ($135^\circ \leq \alpha \leq 180^\circ$). This strategy would narrow the scope of the angle to be measured, enabling the selection of regression networks (or loss functions) better fitted to handle specific challenges within each subrange of QRS-T angles. For instance, if the model struggles to locate the z-coordinate only in ranges of $\alpha \geq 70^\circ$, a higher penalization factor of the Euclidean distance or a deeper regression network could be appropriate options to train the model for such ranges of the QRS-T angle. Alternatively, other subranges of QRS-T angles could benefit from different regression algorithms, such as *ElasticNet*. Cascading the estimation of the QRS-T angle from reduced-lead ECGS is also a compelling solution to mitigate the shortage of training data in the given ranges of the QRS-T angle—in particular, in small ($\alpha < 15^\circ$) or wide ($\alpha > 135^\circ$) QRS-T angles. Accurate measurement of the actual value of the QRS-T angle from reduced-lead ECGS for such ranges may be unattainable if the number of recordings for training the model is low, but grouping the recordings into different classes may yield satisfactory classification results. Considering that spatial QRS-T angles starting from $\alpha = [110{:}135]^\circ$ are associated with an elevated risk of SCD [50], correctly categorizing the ECG as a life-threatening QRS-T angle ($\alpha > 135^\circ$) would provide a sufficient clinical value.

The lack of ambulatory long-term 12-lead ECG signals is a limitation of this research. The *PTB-XL* database, albeit comprehensive in terms of healthy controls and cardiac pathologies, includes only short 10 s long ECGs; therefore, it is unclear how noisy real-life ECG signals will impact the performance of the deep-learning-based method for spatial QRS-T angle estimation. The frontal QRS-T angle is also useful in predicting mortality [50] and ventricular arrhythmias [214]. Future studies should also investigate monitoring of the frontal—along with the spatial—QRS-T angle from a reduced ECG lead system.

Future research should also consider supplementing the training data with additional recordings, namely, those of the underrepresented ranges of $\alpha < 15^\circ$ and $\alpha \geq 115^\circ$, either by data augmentation techniques, or by inclusion of other datasets of 12-lead ECGs likely to display $\alpha \geq 115^\circ$ to complement the *PTB-XL* dataset.

4.8. Conclusions of the Chapter

1. A deep-learning model for deriving the spatial QRS-T angle from reduced-lead ECGs has been proposed. The model measures the spatial QRS-T angle α with reasonable accuracy ($\bar{\epsilon} = 11.4^\circ$ and $\tilde{\epsilon} = 7.3^\circ$) from three frontal and one precordial leads ($\{I, II, aVF, V2\}$) instead of the eight leads required to derive it when using the

conventional approach ($\{I, II, V1–V6\}$). The accuracy suffices for detecting abnormal angles without sacrificing the patient comfort.

2. A gradual reduction of ECG leads from the largest publicly available dataset of clinical 12-lead ECGs (*PTB-XL*) was used for training and finding the best subset ($\{I, II, aVF, V2\}$) of ECG leads to estimate α. Although the prototype model showed high estimation errors when using a subset of solely frontal ECG leads, measuring the spatial QRS-T angle from frontal-lead ECGs looks plausible in the future with further refinements to the model architecture.

3. The model locates the coordinates of $\vec{u}_{QRS}$ and $\vec{u}_{T}$ in the X, Y, and Z axes, using an original composite loss function comprised of the 3D Euclidean distance and the absolute mean error between the target and the estimated vectors and the QRS-T angle. Adopting metrics that guide the model through the 3D space enables the estimation of spatial ECG features even when the input leads provide limited spatial information. A similar strategy could propel the development of solutions for estimating other well-established 3D-based ventricular repolarization markers, such as the ventricular gradient.

4. The model architecture is lightweight and requires low computational power. It comprises $D = 4$ blocks of layers, $k = 16$ kernels, and 105,578 training parameters, making the model appealing to be deployed in consumer healthcare devices.

5. The proposed model will enable exploring the clinical value of the spatial QRS-T angle as a potential blood electrolyte surrogate in ambulatory scenarios. The ECG lead subset $\{I, II, aVF, V2\}$ can be registered with easy-to-use patch- or textile-based consumer healthcare devices already available in the market. Even though the requirement one precordial lead precludes the use of devices that would maximize comfort, such as wrist-worn wearables, devices that register leads $\{I, II, aVF, V2\}$ may still facilitate intermittent monitoring of the spatial QRS-T angle in out-of-hospital settings.

6. Future research can also validate the potential clinical benefits of this technology in populations at risk of SCD, such as CKD and CVD patients.

5. SYMBOLIC CLUSTERING ALGORITHM FOR FASTER HEARTBEAT ANALYSIS AND ANNOTATION IN LONG-TERM ECGS

5.1. Rationale and Conceptual Framework

Since the scientific research of noninvasive methods for monitoring blood electrolyte levels is still in its infancy, researchers require large amounts of long-term data to study how electrolyte fluctuations affect the physiological parameters of an ECG in everyday ambulatory scenarios. While researchers ought to infer electrolyte-induced ECG morphology changes from the cardiac electrophysiological principles, as noted throughout this dissertation, such anticipated ECG findings are not always apparent, easily identifiable, or even specific to dyselectrolytemia (see Sec. 2.3 and Sec. 3.6). This ambiguity of the emblematic electrolyte-related ECG features, coupled with other problematic variables that can also impact the ECG morphology in ambulatory monitoring (e.g., noise, physical activity, psychological stress, or body position changes), put the scientific development of technological solutions for noninvasive blood electrolyte monitoring at an impasse.

Large amounts of data can (evidently) provide valuable insights that would deepen the scientific knowledge of blood electrolytes and their relationship with the ECG morphology. By collecting long-term ECGs, researchers can perform descriptive and exploratory studies to identify what confounding factors are masking or mimicking the anticipated ECG features of electrolyte imbalance and even discover other unexpected morphological ECG changes related to blood electrolyte fluctuations. Performing such studies with large amounts of ambulatory data is paramount to: *(i)* propel research and development of new ECG-derived surrogates for electrolytes, *(ii)* identify the external causes of ECG morphology changes (i.e., confounding factors), *(iii)* devise and improve monitoring protocols, and ultimately *(iv)* perfect algorithms for an accurate assessment of blood electrolyte balance.

Unfortunately, sizeable amounts of long-term data add another challenging layer to the cardiovascular research pipeline—it requires manual analysis and annotation. Data annotation is arduous and time-consuming, and important details may be missed amidst the monotonousness of long-term signals. Machine-learning algorithms could expedite the research and analysis of long-term ECGs but also entail large annotated datasets and, in many cases, human supervision to develop and train such algorithms. Accordingly, a system that balances the benefits of automated algorithms with the attention of a human expert, in which the data is structured to be efficiently analyzed and annotated, could expedite the cardiovascular research pipeline and the scientific-technological development of methods for facilitating noninvasive blood electrolyte monitoring.

Such a system, for instance, would aid in overcoming two challenges encountered in the feasibility study described in Chapter 3: detecting and pinpointing the in-

stances in time when alternating T-wave morphologies and subtle ST-segment changes occurred throughout the long interdialytic interval (Sec. 3.6). Alternating T-wave morphologies impact the T-wave parameterization algorithm, whereas subtle ST-segment changes can be related to blood [Ca^{2+}] fluctuations. A fully annotated dataset would, therefore, help to assemble a complete picture of the electrophysiological changes happening in the heart during periods of gradual blood electrolyte fluctuations.

Research design

Various algorithms have been proposed for heartbeat clustering [215, 216]. The authors of [216] selected representative heartbeats from each generated cluster for labeling, decreasing the time needed for annotation. While thriving in relatively short ECG signals (up to 30 min long in [215] and 24 h long in [216]), the currently available heartbeat clustering algorithms analyze every individual beat in the signal, thus consuming many computational resources, making them inefficient for long-term signals. The lack of heartbeat clustering algorithms suitable for analyzing long-term ECGs raises the following question:

- How can the efficiency of heartbeat annotation algorithms be improved so that cardiovascular research of noninvasive blood electrolyte markers in long-term ECGs can be expedited?

One strategy to lessen the computational resources of unsupervised clustering algorithms is to decrease the number of heartbeats to be analyzed. One way to do so is to reduce data dimensionality through *data discretization* techniques. Data discretization is frequently employed to improve the accuracy and processing time of *motif discovery algorithms* in time-series data mining problems which aim to find repeating patterns (i.e., motifs) in data. In essence, such techniques simplify data description by discretizing the values of continuous time-series features into small intervals, where each interval is mapped to a discrete symbol. Given that the goal is to identify morphological ECG patterns, data discretization techniques employed in motif discovery algorithms may enhance the efficiency of heartbeat annotations in long-term ECGs recordings.

The concept of the proposed method

Since ECGs are essentially time series with periodic patterns (heartbeats), a similar principle to data discretization in motif discovery algorithms can be applied to cluster heartbeats in long-term ECGs. Heartbeats can be compressed into symbols by using data discretization and subsequently grouped into same-symbol pre-clusters. Here, the classic discretization technique described in [217] transforms heartbeats into short strings. Instead of every individual heartbeat, hierarchical clustering is performed only between heartbeats representative of each generated pre-cluster, thus lessening computational demands by reducing the number of beats to be analyzed. Clusters can then

be conveniently analyzed and annotated by the researcher.

This Chapter proposes a symbolic clustering algorithm for facilitating heartbeat annotation in long-term ECGs, free from fatigue-caused errors or exorbitantly long computations. As a proof-of-concept of its efficiency, the algorithm is applied to annotate ambulatory 3-day-long ECGs of HD patients (Sec. 3.3). The algorithm's accuracy is tested on the Physionet *MIT-BIH* database [218] with 13 manually labeled classes. Parts of Sec. 5.2–5.5 and the paragraphs above are quoted verbatim from the previously published conference paper: [61].

5.2. Methods

The pipeline of the symbolic clustering algorithm comprises five stages: preprocessing, symbolic conversion, pre-clustering, hierarchical clustering, and manual investigation and annotation, as illustrated in Fig. 5.1.

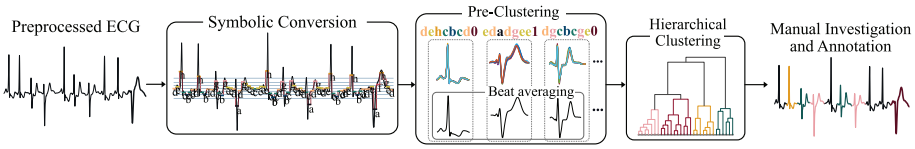

Fig. 5.1. An overview of the symbolic-clustering-based approach for annotating heartbeats in long-term ECG signals.

5.2.1. ECG preprocessing

Long-term ECGs undergo preprocessing, consisting of four stages: filtering, detrending, standardization, and heartbeat delineation. Each stage is detailed below.

Filtering. High-frequency noise and baseline wandering are removed using low- and high-pass FIR filters, with respective cut-off frequencies of 40 Hz and 0.6 Hz.

Detrending. Since data discretization techniques are amplitude-dependent, ECGs must be detrended and demodulated to remove any trace of baseline wandering and noise artifacts. A centered moving average is computed and subtracted from the filtered ECGs to detrend the signals. Demodulation is performed similarly to the strategy described in [219]. Periods contaminated with large amplitude deviations, such as motion artifacts, are discarded.

Standardization. Long-term ECGs have to be segmented into periods of comparable amplitude to minimize errors in the symbolic conversion stage (Sec. 5.2.2). The segmentation window length w_{len} is arbitrary but should not be limited to a single fixed value, i.e., the algorithm should not segment the whole ECG recording only into

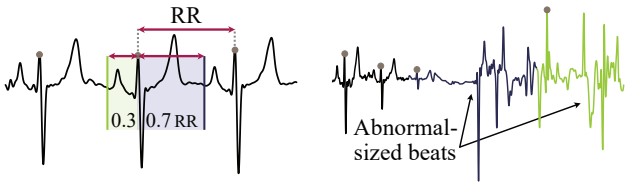

Fig. 5.2. RR-based beat delineation (**left**): a beat is outlined at 30% and 70% of its RR interval. Abnormal-length beats are categorized as noise (**right**). Such beats usually emerge from incorrect R-peak detection fails in noisy ECG periods.

one-hour-long periods. Instead, w_{len} should depend on the signal amplitude trend to ensure that all heartbeats within each segmented period have a homogeneous amplitude. $w_{len} = 30\,\text{min}$ is usually enough, providing that no motion artifacts are present. Each ECG segment $\mathcal{Y}(n)$ is then standardized in amplitude (*z-score*):

$$\mathcal{Y}^z(n) = \frac{\mathcal{Y}(n) - \bar{x}}{S}, \ \forall n, \ n \in \{t_o, \dots, t_e\}, \tag{5.1}$$

where $\mathcal{Y}^z(n)$ denotes the standardized ECG segment, $\bar{x}$ and S are the mean and standard deviation of $f(n)$, and t_o and t_e are the starting and end points of each ECG segment.

Heartbeat delineation. Beats are roughly delineated based on their respective RR-interval (Fig. 5.2) since the symbolic clustering algorithm does not entail precise and computationally expensive PQRST detectors. Good-quality beats are aligned using R-peak as a reference point and zero-padded to equalize their length.

5.2.2. Symbolic conversion

Heartbeats are individually compressed to short strings using the classical data discretization technique, *Symbolic Aggregation approXimation* (SAX) [217]. SAX converts a time series into a set of equiprobable symbols (strings) that approximate the original time series. SAX embodies two parts: discretization via *Piecewise Aggregate Approximation* (PAA) [217], followed by symbol assignment (Fig. 5.3). PAA reduces the dimensionality of a time series $\mathcal{T}$ of length n by splitting it into w segments of equal size z. Each i-th segment $\mathcal{T}_i$ is calculated as:

$$\mathcal{T}_i = \frac{w}{n} \left(\sum_{j=\frac{n}{w}(i-1)+1}^{\frac{n}{w}i} \mathcal{T}_j \right). \tag{5.2}$$

In other words, $\mathcal{T}_i$ is the mean value of the data contained within the segment.

The PAA-transformed time series is divided into a equiprobable symbols, where a is an arbitrary alphabet size of $2 \leq a \leq 20$ [217]. Since normalized time series have a Gaussian distribution [217], the Gaussian curve can be split into equal-size regions, $\beta = \{\beta_1, \dots, \beta_{a-1}\}$, such that the area under the curve between β_i and β_{i+1} is $1/a$. β are

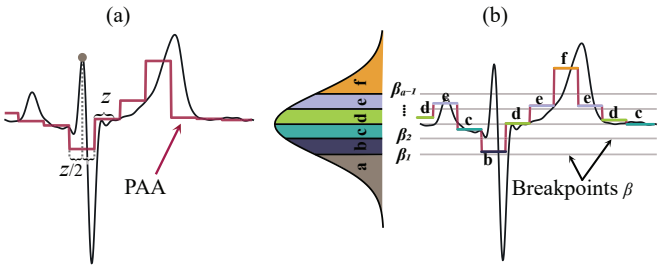

Fig. 5.3. SAX Conversion: **(a)** PAA transformation of a heartbeat. PAA coefficients are calculated starting at $z/2$ samples centered at the R-peak; **(b)** Symbol assignment. PAA coefficients are mapped out according to the breakpoints β as follows. The symbol *'**a**'* is ascribed to the coefficients below β_1; *'**b**'* to the ones above β_1 ($\geq \beta_1$) but below β_2 ($< \beta_2$), and so forth.

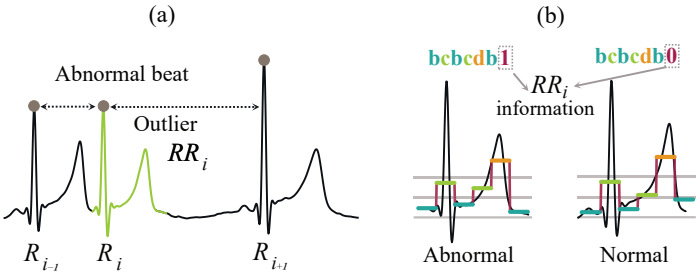

Fig. 5.4. (**a**) RR_i of an abnormal beat (APB). (**b**) Addition of RR_i information to distinguish strings of APB from normal beats. The symbol *'**1**'* is added to beats whose RR_i is an outlier, and *'**0**'* otherwise.

the breakpoints for assigning the symbols and are provided by a statistical table.

5.2.3. Pre-clustering

SAX-based data series motif-discovery algorithms aim to find motif pairs, i.e., pairs of the most similar subsequences of a given length L using a distance function. When using a sliding window approach, the algorithms typically search for motif pairs of variable-length subsequences $[L_{min}, \ldots, L_{max}]$ in the time series, thus computing the distance function $n - m + 1$ times for each $m = [L_{min}, \ldots, L_{max}]$. For each m, however, the algorithm measures the similarity only between subsequences represented by different strings instead of comparing every possible subsequence of length L. In data mining applications, this approach helps identify 'discords', i.e., isolated subsequences far from the rest of the data.

Since ECGs are periodical, the subsequences (i.e., heartbeats) to be analyzed are of fixed length L; thus, SAX can be applied to each heartbeat directly instead of trying to find the optimal length L which better identifies all motifs in the data. Heartbeats are compressed into strings using R-peaks as reference points: the PAA coefficients are calculated starting at $z/2$ samples centered at the R-peak and then mapped out according

to the breakpoints β (Fig. 5.3). Every unique string then becomes a pre-cluster of all beats the string represents.

The morphology of certain abnormal beats, such as premature atrial contractions (PACs), resembles normal beats, except in the low-amplitude components (e.g., P-waves), which SAX can envelop. Enveloping such components causes abnormal beats to be represented by matching strings as beats of a different class (Fig. 5.4) and thereby be wrongly pre-clustered. To minimize pre-clustering errors, for every i-th beat, an extra symbol is added. This extra symbol represents the RR information of two neighboring beats: $RR_i = RR_{(i,i-1)}/RR_{(i+1,i)}$. The symbol *'**1**'* is added to beats whose RR_n is an outlier, and *'**0**'* otherwise.

The number of pre-clusters depends on the chosen a and z parameters. Incrementing either a or z lowers the compression rate but at the trade-off of a higher number of pre-clusters, thus increasing the computational demands. Since ambulatory ECGs are generally noisy, beats within the same pre-cluster are signal-averaged to enhance the signal quality.

5.2.4. Hierarchical clustering

Hierarchical clustering is employed to cluster the signal-average beats representative of each pre-cluster. In contrast to other heartbeat-clustering algorithms, the dissimilarity matrix D_m is calculated by combining dissimilarity matrices of various heartbeat components:

$$D_m = D'_{PQ} + D'_{QRS} + D_b^{0.5}. \tag{5.3}$$

D'_{PQ} and D'_{QRS} measure the *Spearman* distance between the gradient of the PQ-interval and the QRS-complex, and D_b is the *complexity-invariant* distance [220] of the whole heartbeat. The combination of various dissimilarity matrices enables the clustering algorithm to account for low-amplitude components of the ECG that could otherwise be disregarded. Hyperparameter tuning of the symbolic clustering algorithm is detailed in Sec. 5.3.

5.3. Data and Performance Evaluation

The performance of the proposed symbolic clustering algorithm is evaluated according to its *accuracy* and *efficiency* in two separate databases. To evaluate efficiency, the algorithm is applied to annotate long-term ambulatory ECG recordings (2-to-3 days long, see Sec. 3.3). Accuracy is tested on the Physionet *MIT-BIH* [190, 218] database with 13 manually labeled classes.

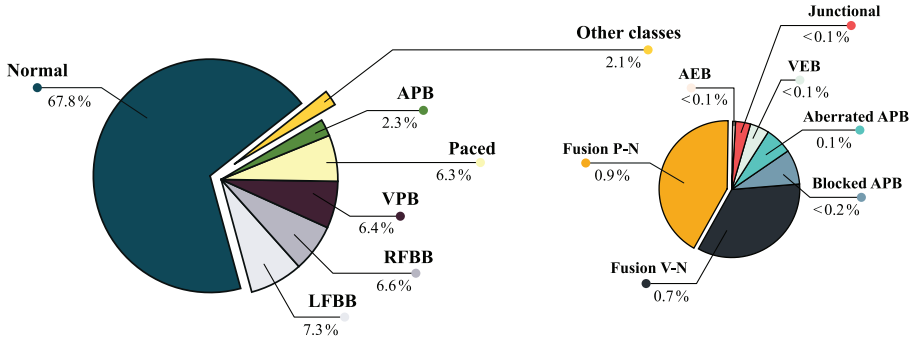

Fig. 5.5. Graphical summary of the MIT-BIH database in terms of percentage of annotated beats in each of the 13 classes. The pie chart on the right is a magnified view of the seven classes that together comprise 2.1% of all heartbeats. Acronyms: LFBB and RLBB—left and right bundle branch block; VPB and APB—ventricular and atrial premature beat; Fusion P-N—fusion of paced and normal beat; Fusion V-N—fusion of ventricular and normal beat; VEB and AEB—ventricular and atrial escape beat.

MIT-BIH database

Since labeled ECGs are necessary for accuracy assessment and as no databases of labeled long-term ECGs are currently available, the algorithm is developed and tested on the *MIT-BIH* database. This database comprises 48 annotated ambulatory 30-minute-long ECG recordings and includes manual annotations of all heartbeats. Each heartbeat is labeled according to 13 possible morphological classes (Fig. 5.5). Recordings have 2307±437 beats on average, tallying 110,740 labeled beats in the database. Every ECG contains at least two heartbeat classes (a median of four per recording) with a maximum of nine.

Performance evaluation metrics

Five performance metrics are employed to evaluate the accuracy: misclassification, recall, precision, Fowlkes-Mallows (FM) index, and Matthews Correlation Coefficient (MCC). Misclassification is the % of beats that end up in clusters where the dominant class is a different one. The recall (i.e., sensitivity) and the precision range are in $[0, 1]$ and are calculated as follows:

$$\text{recall} = \frac{TP}{TP + FN}; \quad \text{precision} = \frac{TP}{TP + FP}. \tag{5.4}$$

The similarity between two clusters is defined by the FM index, which combines the previous two metrics:

$$\text{FM} = \sqrt{\text{recall} \cdot \text{precision}}, \quad \text{and} \quad \text{FM} = [0, 1]. \tag{5.5}$$

FM = 0 states that the model misclassified all the elements, whereas FM = 1 corresponds to a perfect classification. The MCC is obtained as:

$$\text{MCC} = \frac{(TP \times TN) - (FP \times FN)}{\sqrt{(TP + FP)\,(TP + FN)\,(TN + FP)\,(TP + FN)}}, \tag{5.6}$$

and ranges in $[-1, 1]$. MCC = 1 indicates a perfect prediction, MCC = 0 a random prediction, and MCC = −1 corresponds to a total disagreement between the prediction and the labels. The true positives (TP), true negatives (TN), false positives (FP), and false negatives (FN) are the number (#) of pairs of beats with:

- TP: the same class and cluster;
- TN: different classes and clusters;
- FP: different classes, but the same cluster;
- FN: the same class, but different clusters.

Note that although the *MIT-BIH* database only has 13 labeled classes, the clustering algorithm can find as many relevant classes as it deems fit. The total # of classes found by the algorithm is not a meaningful metric, and the human expert is tasked to decide the final # of classes across all clusters by, for example, grouping two clusters into the same class. Instead, the algorithm is deemed accurate if all beats within the same cluster belong to the same class.

Tuning of the clustering hyperparameters

In supervised multi-class classification problems, accuracy is traditionally defined by the number of elements correctly classified by the machine-learning model, as the total number of classes is known a priori. However, the number of heartbeat classes within a long-term ECG recording is not inferable beforehand. Thus, the algorithm must cluster heartbeats in an unsupervised fashion, and the optimal number of clusters ($\mathcal{K}_m$) needs to be estimated based on the internal information of the clustering result. Internal clustering validation indices (CVIs) provide a quantitative measure of the quality of a clustering result, enabling the choice of the appropriate $\mathcal{K}_m$ according to the compactness and separation of the clusters. Three internal CVIs are evaluated in this research: *Calinski-Harabasz*, *Davies-Bouldin*, and *silhouette* [221].

Another element of hierarchical clustering which requires investigation is the *linkage* method, i.e., the method that specifies how the distance between two clusters is calculated. This research examines three linkage types: *complete*, *weighted*, and *average*. Each of the three internal CVIs is evaluated with all three linkage types, rendering six possible combinations of hyperparameters to be tuned. The optimal hyperparameters are chosen according to their accuracy performance in the *MIT-BIH* database.

The SAX parameters a and z (Sec. 5.2.3) are set to $a = 4$ and $z = 0.1$ s. While devising this algorithm, these parameters were found to be adequate for most case

scenarios without escalating the computational complexity.

5.4. Results

5.4.1. Accuracy assessment in labeled ECGs

The compression rate for the *MIT-BIH* database was 26.2%, yielding on average 556.4±318.9 unique strings per recording. Recordings have an average of 2,258.6±440 heartbeats. Beat misclassification was 0.97±1.51% after SAX, with junctional and escape beats being the most susceptible to being improperly pre-clustered.

Figure 5.6 shows boxplots of the performance evaluation metrics on the *MIT-BIH* database. The results reveal a large variability of MCC for all combinations of linkage and internal validation indexes, despite high precision and FM index, with a few MCC values reaching near or below 0, likely caused by an increase in FNs (Fig. 5.7). Since the symbolic clustering algorithm aims to facilitate heartbeat annotation, FNs are not problematic, but rather the incidence of FPs. Thus, a low MCC does not indicate poor clustering results if allied with a high FM index and a low rate of FPs.

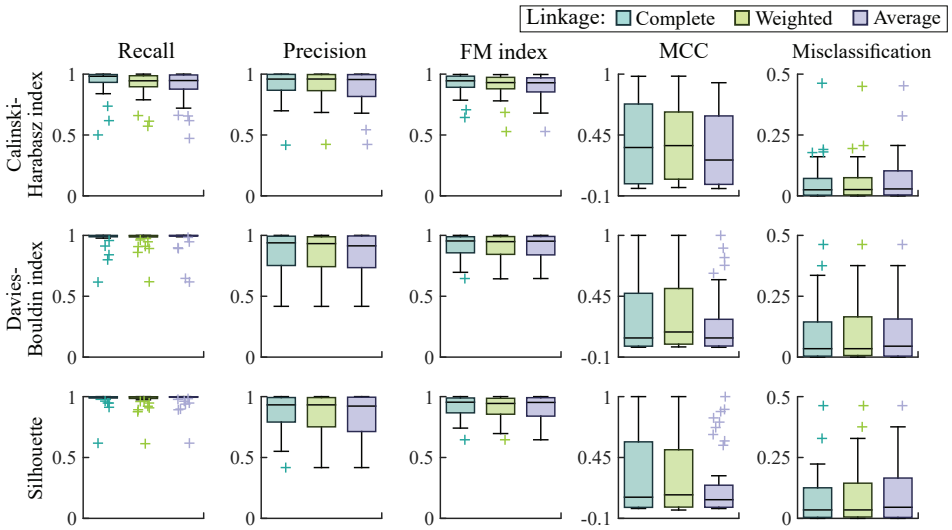

Fig. 5.6. Boxplots of the performance metrics obtained by the proposed algorithm in the *MIT-BIH* database using various linkage and internal clustering validation indexes.

Combining the complete or weighted linkage with the Calinski-Harabasz index produces the best precision, FM index, MCC, and misclassification results, with a respective mean of 0.91, 0.91, 0.37, and 5.6%. This combination results in the lowest misclassification and the highest FM index, indicating that, despite producing many clusters for the same class (low MCC), the chances of wrongly annotating beats decrease. On average, beat misclassification was <2% over 13 labeled classes for each

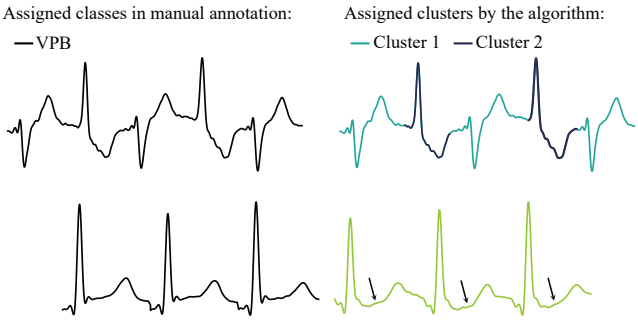

Fig. 5.7. Examples of clustering results. Five beats labeled with the same class of ventricular premature beats (VPB) from the *MIT-BIH* database are assigned to two different clusters by the proposed algorithm (**top**). This is a case of *FNs* that is not fundamentally undesirable for manual annotation. Normal beats from two distinct periods with subtle ST-changes from long-term ECG recordings (**bottom**).

combination above, respectively. In contrast, the large variance of the FM index, MCC, and misclassification indicate that the Silhouette index is an inadequate CVI despite having the best recall.

5.4.2. Efficiency assessment in long-term ECGs

As for efficiency, in one 3-days-long recording, more than 480,000 beats were reduced to less than 30,000 unique strings, and further to 30 clusters, which were then annotated as three classes plus noise. Heartbeats with subtle changes in the ST-T segment morphology were grouped into different clusters, as displayed in Fig. 5.7. The computations took less than an hour on an AMD Ryzen™5 3.6 GHz CPU with six cores (12-threads) and 16 GB of RAM.

5.5. Discussion

This dissertation proposes a symbolic clustering algorithm for facilitating heartbeat annotation in long-term ECG signals. Beats are compressed to short strings using SAX and pre-clustered before performing hierarchical clustering of the generated pre-clusters. A human expert then annotates the generated clusters.

A similar annotation strategy was adopted in [216], in which only selective heartbeats representative of each cluster are labeled. Albeit precise, the clustering algorithm is computationally demanding as it examines all beats within the recording. In contrast, the proposed algorithm pre-clusters equal-string beats, performing hierarchical clustering only to signal-averaged beats of every pre-cluster. Moreover, signal-averaging may also boost clustering results. It enables the inclusion of various low-amplitude components, such as P-waves and ST-segments, into the dissimilarity matrix that would otherwise be occluded by noise.

The symbolic clustering algorithm is promising. While low MCC values tend to suggest poor clustering results, it is not always the case, especially when paired with high-precision values. MCC decreases when the # of *FNs* or *FPs* increases. An increase in *FNs*, i.e., same-class beats categorized into different clusters, is not fundamentally undesirable for manual annotation. The algorithm categorized beats labeled with the same class into various clusters if differences in beat morphology exist (see Fig. 5.7). Categorizing same-class beats into various clusters allows researchers to explore how heartbeats fall into various classes naturally and even study the existence of unexpected sub-classes. In ambulatory cardiovascular research, even modest changes in the ECG morphology can hold meaningful value. For instance, as discussed in Sec. 3.6, detecting variations in the ST-T morphology is pivotal for investigating non-invasive markers of electrolyte fluctuations in out-of-hospital settings. Changes in the ST-T segment can indicate calcium imbalance and therefore aid in developing blood [Ca^{2+}] markers. However, as observed in the feasibility study in Chapter 3, changes in the ST-T segment (and alternating T-wave morphologies) are recurrent in ambulatory signals. Since these changes can stem from many other sources (e.g., body position changes) besides electrolyte imbalance, categorizing same-class beats into various clusters if differences in morphology exist enables researchers to identify the causes of such morphological variations and avoid misclassifying them as electrolyte imbalance. Another scenario of low MCC is ECGs with minimal abnormal beats (e.g., five APBs occur amidst 2000 regular beats). Misclassifying one or two heartbeats in such recordings increases *FPs* but is unlikely to compromise cardiovascular research.

Albeit beneficial for annotating long-term ECG recordings, pre-clustering using SAX can increase the incidence of *FPs* by enveloping beats of different classes into the same pre-cluster. Misclassification is higher in beats whose distinctive morphological feature lies in subtle low-amplitude components, such as APBs, escape, or junctional beats. Higher a and z values (see Sec. 5.2.3) could ameliorate beat misclassification by allowing such components to be discernible by SAX but at the expense of higher computational cost without necessarily producing better clustering results. Finding the best compromise between a and z parameters, computational demands, and accuracy is a subject of future research. Future studies should also explore other dissimilarity metrics to improve precision and evaluate the most propitious combination of the parameters of SAX.

5.6. Conclusions of the Chapter

1. A symbolic clustering algorithm has been proposed to enhance the efficiency of heartbeat annotation and analysis in long-term ECGs. The algorithm compresses heartbeats into short strings (symbols) using SAX, which is a classical data discretization technique for time-series analysis and data mining. Every unique string becomes

a pre-cluster of all beats represented by this string.

2. Instead of every individual heartbeat, the human expert is presented with the hierarchical clustering results of the generated pre-clusters for manual investigation and annotation. This strategy significantly reduces the computational demands of hierarchical clustering. In a 3-day-long ECG, more than 480,000 beats were reduced to 30,000 unique strings and to 30 clusters, and then annotated as three classes plus noise. Computations and labeling took less than one hour.

3. Accuracy was tested in a labeled database (*MIT-BIH*). The combination of complete or weighted linkage with the Calinski-Harabasz index produced the best precision (0.91), FM index (0.91), MCC (0.37), and misclassification results (5.6%). The algorithm misclassified 0.97±1.51% beats after SAX and displayed a compression rate of 26.2% in the *MIT-BIH* database.

4. While low MCC values tend to suggest poor clustering results, the high precision values show that this is not the case. The algorithm categorized beats labeled with the same class but with different morphological traits into several clusters (i.e., an increased number of FNs). This feature is not fundamentally undesirable as it allows researchers to explore how heartbeats naturally fall into other classes and even identify unexpected sub-classes for further study.

5. Although future research should explore other dissimilarity metrics to improve precision, the symbolic clustering algorithm can expedite the cardiovascular research pipeline and aid the scientific investigation of new ECG markers of blood electrolytes.

6. CONCLUSIONS

1. Regular blood electrolyte monitoring in chronic disease patients is essential for their short- and long-term health. While severe dyselectrolytemia episodes can precipitate life-threatening arrhythmias and are thus dangerous in the short term, mild—yet recurring—episodes can have long-lasting detrimental effects. Despite not posing an imminent threat to the patients, such mild and recurring episodes can deteriorate the cardiac and renal functions, which hastens disease progression and jeopardizes long-term health. These episodes commonly result from suboptimal dosages of standard medications for chronic disease treatment, such as antihypertensive drugs. Therefore, the timely detection and correction of dyselectrolytemia enabled by regular blood electrolyte monitoring could avert dangerous arrhythmias and help clinicians titrate life-saving medications for maintaining homeostasis and promoting general long-term health.

2. Ambulatory monitoring of blood electrolyte levels using single-lead ECGs is feasible for HD patients with comorbid heart diseases. Two T-wave morphology descriptors, θ_δ and T_{SA}, responded to gradual potassium fluctuations during the long interdialytic interval and are moderately correlated with changes in $[K^+]$ ($r = -0.56$ and $r = -0.57$, respectively). θ_δ and T_{SA} also reacted to potassium-lowering medications and insulin spikes after meals which drive K^+ inside the cells. The daily variability of θ_δ is similar to the circadian variation of blood $[K^+]$ in healthy subjects. Compared to T_{SA}, the proposed model-based parameterization descriptor θ_δ is less affected by motion-induced noise, making it preferable for ambulatory applications. Nevertheless, confounding factors, such as concomitant electrolyte imbalances, particularly calcium and bicarbonate, and alternating T-wave morphologies, can affect the performance of both descriptors.

3. A deep-learning model can accurately measure the spatial QRS-T angle α from the reduced-lead ECG subset $\{I, II, aVF, V2\}$, with absolute mean and median errors of 11.4° and 7.3°. The model locates the 3D coordinates of the QRS and T vectors (output) necessary for computing α from signal-averaged heartbeats (input) of each lead within the subset $\{I, II, aVF, V2\}$. This subset can be registered with easy-to-configure consumer healthcare devices already available on the market. An original composite loss function which uses the angle and the 3D Euclidean distance between the vectors was employed to train the model to estimate α even when the input ECG leads provided limited spatial information. The model architecture is lightweight enough to be deployed in consumer healthcare devices. It is a promising solution for ambulatory QRS-T angle monitoring and investigating its interrelationship with blood electrolyte levels.

4. The proposed symbolic clustering algorithm can enhance the efficiency of

heartbeat annotation and analysis in long-term ECGs. Compressing heartbeats into short strings (symbols) enables grouping them into same-symbol pre-clusters to reduce the computational demands of hierarchical clustering. E.g., in a 3-day-long ECG, more than 480,000 beats were reduced to 30,000 unique strings and then to 30 clusters that researchers can conveniently analyze and annotate. The combination of complete or weighted linkage with the Calinski-Harabasz index produced the best precision (0.91), FM index (0.91), MCC (0.37), and misclassification results (5.6%). The low MCC values and the high precision indicate that the algorithm categorized beats labeled with the same class but with different morphological traits into various clusters. This feature allows researchers to explore how heartbeats naturally fall into different classes and even identify unexpected sub-classes for further study.

SANTRAUKA

ĮVADAS

Mokslinių tyrimų svarba

Elektrolitų pusiausvyros sutrikimas, arba diselektrolitemija, pasireiškia, kai elektrolitų kiekis kraujyje nukrenta už homeostazės ribų ir yra susijęs su padidėjusiu sergamumu, mirtingumu dėl visų priežasčių ir staigia širdies mirtimi (SŠM) įvairiose populiacijose [3–6]. Pagrindiniai dielektrolitemijos rizikos veiksniai yra amžius, lėtinės ligos, tokios kaip lėtinė inkstų liga (LIL), medžiagų apykaitos sutrikimai (cukrinis diabetas), širdies ir kraujagyslių ligos (ŠKL), ir standartinių vaistų šioms ligoms gydyti, t. y. antihipertenzinių vaistų, β-adrenerginių blokatorių arba agnostikų ir kortikosteroidų, vartojimas [14, 26, 76, 77].

Daugeliui žmonių visame pasaulyje gresia elektrolitų pusiausvyros sutrikimas, nes LIL, hipertenzija ir ŠKL yra pasaulinės epidemijos. LIL serga daugiau kaip 10% pasaulio gyventojų [27], o hipertenzija serga beveik 32% moterų ir 34% vyrų [28] ir apie 60% vyresnių nei 60 metų žmonių [17]. Beveik pusei jų taikomas antihipertenzinis gydymas [28]. Maždaug 8,8% pasaulio gyventojų serga cukriniu diabetu [29], o 70–80% jų ir gretutine hipertenzija [30]. JAV ir Jungtinėje Karalystėje nuo 5,5% [31] iki 21,3% [32] suaugusiųjų serga ŠKL, ir tai jau yra 32% visų pasaulio mirčių priežastis [33], o nuo ŠKL kasmet miršta apie 5–10 mln. žmonių [34]. Prognozuojama, kad iki 2030 m. sergamumas šiomis lėtinėmis ligomis, taigi ir pavojingos dielektrolitemijos atvejų skaičius, dar labiau padidės dėl senėjančios visuomenės [27, 34].

Be padidėjusios mirtingumo dėl visų priežasčių rizikos, elektrolitų pusiausvyros sutrikimas yra ekonominė našta [35]. Dielektrolitemijos gydymas padidina ir taip dideles sveikatos priežiūros išlaidas, susijusias su ŠKL ir LIL, ypač sunkiais epizodais, dėl kurių reikia hospitalizuoti [36]. LIL sergantiems pacientams kiekvienas sunkus dielektrolitemijos atvejis JAV kainuoja iki 31 212 JAV dolerių, o lengvam atvejui gydyti pakanka tik 1782 JAV dolerių [35]. Apskaičiuota, kad hospitalizavimas dėl dielektrolitemijos sukelia papildomą sveikatos priežiūros išlaidų naštą, kuri vidutiniškai sudaro 7–39% [37], o, JAV duomenimis, 2009 m. vien natrio disbalansui gydyti išleista 1,6–3,6 mlrd. JAV dolerių [38].

Reguliarus elektrolitų kiekio kraujyje stebėjimas gali padėti išvengti nepalankių trumpalaikių ir ilgalaikių padarinių sveikatai. Reguliari stebėsena ne tik leistų greitai koreguoti elektrolitų sutrikimus prieš prasidedant SŠM sukeliančioms aritmijoms [39], bet ir palengvintų vaistų titravimą, padėdama gydytojams nuolat koreguoti gyvybę gelbstinčių vaistų dozę, kad būtų pasiekta kuo didesnė nauda be nepageidaujamo poveikio [25]. Ankstyvosios stadijos ŠKL pacientams laiku koreguojant dielektrolitemiją galima atitolinti ligos progresavimą iki galutinės stadijos inkstų ligos (GSIL) [93], kai pacientams, norint, kad išgyventų, kas dvi ar tris dienas reikia atlikti hemodializes

(HD), arba net užkirsti kelią ligos progresavimui [94]. Be to, reguliari kraujo elektrolitų stebėsena taip pat galėtų sumažinti ekonominę lėtinių ligų naštą. Pavyzdžiui, laiku nustačius lengvą dielektrolitemiją, galima išvengti bent 22 proc. vyresnio amžiaus pacientų hospitalizacijų [40], o, sustabdžius LIL progresavimą iki GSIL, LIL išlaidos gali sumažėti šešis kartus [41]. Vidutinės metinės GSIL išlaidos vienam pacientui yra 100 593 JAV doleriai, o JAV LIL gydyti pakanka 16 112 JAV dolerių [41].

Nepaisant to, kad reguliari stebėsena gali išgelbėti gyvybę ir yra rekomenduotina pažeidžiamiems pacientams, klinikinėje praktikoje ji mažai taikoma, visų pirma dėl to, kad nėra praktinių metodų elektrolitų kiekiui kraujyje įvertinti. Kraujo tyrimai yra vienintelis kliniškai pagrįstas metodas elektrolitų pusiausvyros sutrikimui nustatyti, tačiau kraujo tyrimai gali būti brangūs, o jų reguliarus atlikimas sveikatos priežiūros įstaigoms gali būti logistiškai sudėtingas. Be to, kraujo tyrimai yra neįmanomi neklinikinėje aplinkoje, todėl ambulatorinis elektrolitų kiekio kraujyje stebėjimas yra neįmanomas. Nebrangios, o geriausia – neinvazinės, technologijos elektrolitų kiekiui kraujyje įvertinti galėtų palengvinti reguliarų tiek stacionare, tiek ambulatoriškai gydomų pacientų stebėjimą, todėl būtų kliniškai svarbios [25, 39].

Mokslinė ir technologinė problema

Dėl nehomeostatinio elektrolitų kiekio kraujyje sutrinka širdies ląstelių veikimo potencialas [7], todėl atsiranda skilvelių repoliarizacijos sutrikimų, kurie gali atsispindėti elektrokardiogramoje (EKG) [42]. Pavyzdžiui, pakitusi T bangos morfologija yra gerai žinomas kalio sukeltų repoliarizacijos sutrikimų požymis [42]. Taigi EKG skilvelių repoliarizacijos žymenys gali būti panaudoti kraujo elektrolitų lygiui netiesiogiai vertinti.

Pastaraisiais metais buvo sukurti nauji elektrokardiogramos T bangų morfologijos parametrai, leidžiantys kiekybiškai įvertinti kalio kiekį kraujyje [43–45]. Nors šių parametrų rezultatai daug žadantys, jie buvo tiriami tik GSIL pacientams HD seansų metu, kai elektrolitų kiekis kinta daug greičiau nei kasdienėje ambulatorinėje aplinkoje. Nors yra žinoma, kad greiti elektrolitų svyravimai sukelia pastebimus T bangos morfologijos pokyčius [46, 47], vis dar neištirta, ar EKG gali užfiksuoti laipsniškus elektrolitų svyravimus, kurių galima tikėtis kasdienėje aplinkoje.

Be T bangos morfologijos, kaip skilvelių repoliarizacijos žymenys plačiai tyrinėti ir kiti EKG požymiai, pavyzdžiui, erdvinis QRS-T kampas [48–50]. Nors jų ryšys su kraujo elektrolitais dar neaiškus, kai kurie iš šių žymenų yra stiprūs ląstelių elektrinio aktyvumo indikatoriai [48], todėl skatina mokslininkų susidomėjimą kaip perspektyvūs neinvazinės kraujo elektrolitų stebėsenos sprendimai. Tačiau beveik visi esami T bangomis pagrįsti parametrai [43, 45, 51–56] ir kiti skilvelių repoliarizacijos žymenys [48, 57] apskaičiuojami tik iš 12-os derivacijų arba krūtinės EKG derivacijų sistemų, todėl juos sieja ta pati *pagrindinė technologinė problema* – jie nepraktiški

ilgalaikiam ambulatoriniam naudojimui. Todėl reikalingi metodai, leidžiantys įvertinti skilvelių repoliarizacijos žymenis iš sumažintų EKG derivacijų rinkinio. Tokie metodai galėtų būti taikomi vartotojų sveikatos priežiūros prietaisuose ir palengvintų neinvazinę elektrolitų kiekio kraujyje stebėseną.

Tyrimo problema: praktinių metodų, skirtų skilvelių žymenims repoliarizacijos ambulatorinėje aplinkoje įvertinti, trūkumas trukdo mokslinei ir technologinei neinvazinės elektrolitų lygio stebėsenos sprendimų pažangai. Tai trukdo: *(i)* esamų sprendimų veiksmingumo tyrimui kasdienėje ambulatorinėje aplinkoje; *(ii)* kitų galimų sprendimų, kuriuos būtų galima panaudoti vertinant kai kuriuos gerai žinomus skilvelio repoliarizacijos žymenis, pavyzdžiui, erdvinį QRS-T kampą, kūrimui.

Tyrimo klausimai

Kadangi nėra tinkamų technologinių sprendimų, skirtų ambulatorinėms įstaigoms, neinvazinės elektrolitų kiekio kraujyje stebėsenos galimybės kasdienėje ne ligoninės aplinkoje yra sudėtingos, todėl kyla šie pagrindiniai klausimai:

1. Ar gali sumažinto derivacijų skaičiaus EKG užfiksuoti laipsniškus kraujo elektrolitų svyravimus ambulatorinėmis sąlygomis?
2. Kokie galimi klaidinantys veiksniai gali turėti įtakos elektrolitų kiekio kraujyje žymenims, vertinamiems pagal iš EKG, ambulatorinėmis sąlygomis?
3. Ar gerai žinomi skilvelių repoliarizacijos žymenys, tokie kaip erdvinis QRS ir T kampas, gali būti pakankamai tikslai įvertinti iš sumažinto skaičiaus EKG derivacijų ir būti perspektyviais sprendimais neinvaziniam ambulatoriniam elektrolitų kiekio kraujyje stebėjimui?
4. Kaip pagerinti širdies ritmo anotavimo algoritmų efektyvumą, kad būtų galima paspartinti širdies ir kraujagyslių tyrimus, atliekamus naudojant ilgalaikes EKG?

Darbo hipotezė

Skilvelių repoliarizacijos žymenys gali būti pakankamai tiksliai įvertinti net ir naudojant sumažintą, tačiau ilgalaikei stebėsenai tinkamą EKG derivacijų skaičių tuo tikslu taikant modeliais pagrįstus parametrizavimo ir mašininio mokymosi metodus, leidžiančius ilgalaikę potencialių kraujo elektrolitų kiekio netiesioginių įverčių stebėseną.

Tyrimo tikslas

Šios daktaro disertacijos tikslas – ištirti ir sukurti metodus, palengvinančius neinvazinį ambulatorinį elektrolitų kiekio kraujyje stebėjimą.

Tyrimo objektas

Tyrimuose daugiausia dėmesio skiriama signalų apdorojimo algoritmų, skirtų skilvelių repoliarizacijos pokyčiams užfiksuoti iš sumažintų derivacijų EKG, kūrimui.

Tyrimo tikslai

1. Išanalizuoti elektrolitų pusiausvyros reikšmę sveikatai ir aptarti reguliaraus elektrolitų kiekio kraujyje stebėjimo klinikinę vertę ilgalaikiams sveikatos rezultatams.

2. Pasiūlyti T bangų morfologijos deskriptorius, kuriuos galima įvertinti iš vienos derivacijos EKG ir kurie būtų tinkami ambulatoriniam stebėjimui. Tokie deskriptoriai būtini norint ištirti galimybę fiksuoti laipsniškus kalio koncentracijos pokyčių sukeltus repoliarizacijos sutrikimus ne ligoninėje ir taip nustatyti galimus klaidinančius veiksnius, kurie gali turėti įtakos neinvaziniam kraujo elektrolitų stebėjimui.

3. Sukurti algoritmus, leidžiančius iš sumažinto derivacijų skaičiaus EKG įvertinti žinomus skilvelių repoliarizacijos žymenis, tokius kaip erdvinis QRS-T kampas. Tokie metodai gali padėti išnaudoti šių žymenų klinikinę vertę ir paskatinti naujų technologinių sprendimų, skirtų neinvaziniam kraujo elektrolitų stebėjimui, mokslinius tyrimus.

4. Sukurti metodus, skirtus ilgalaikių EKG signalų analizei ir anotavimui pagreitinti. Tokie metodai pagreitintų naujų EKG elektrolitų kiekio kraujyje žymenų mokslinius tyrimus.

Mokslinis naujumas

Šioje daktaro disertacijoje išsamiai apžvelgiamos klinikinės elektrolitų disbalanso pasekmės ilgalaikei sveikatai, nagrinėjant pasikartojančių lengvos dielektrolitemijos atvejų poveikį širdies ir inkstų funkcijoms bei homeostazei. Priešingai nei ankstesniuose neinvazinės elektrolitų kiekio kraujyje stebėsenos tyrimuose, šioje disertacijoje kontekstualizuojama reguliarios elektrolitų kiekio kraujyje stebėsenos svarba, neapsiribojant tik poreikiu fiksuoti elektrolitų sutrikimus SŠM prevencijos tikslais. Šioje disertacijoje teigiama, kad tikėtina, jog pasikartojantys lengvi dielektrolitemijos epizodai gali turėti ilgalaikių pasekmių sveikatai, o tai dar labiau sustiprina poreikį plėsti mokslinius ir technologinius tyrimus bei kurti metodus, kurie palengvintų neinvazinį ambulatorinį elektrolitų kiekio kraujyje stebėjimą.

Šioje daktaro disertacijoje siūlomi du metodai skilvelių repoliarizacijos žymenims gauti iš sumažintų derivacijų EKG. Abu metodus sudaro algoritmai, sukurti taip, kad palengvintų ambulatorinį elektrolitų kiekio kraujyje stebėjimą. Pirmajame metode naudojamas modeliu pagrįstas parametrizavimo metodas T bangos morfologijos parametrui įvertinti iš vienos derivacijos EKG. Skirtingai nuo kitų T bangų parametrų, pasiūlytame deskriptoriuje atsižvelgiama į bendrąją T bangos morfologiją, o ne tik į lokalias T bangos savybes. Be to, deskriptorius yra atsparesnis triukšmui, o tai palanku

ambulatorinėje sveikatos stebėsenoje.

Antrasis metodas naudoja giliuoju mokymusi pagrįstą algoritmą vertinant erdvinį QRS-T kampą iš sumažinto EKG derivacijų skaičiaus rinkinių. Kadangi QRS-T kampas atspindi kampą tarp QRS ir T vektorių trimatėje (3D) erdvėje, modelis buvo sukurtas taip, kad kaip išvestį būtų galima gauti kiekvieno vektoriaus koordinates. Buvo pasiūlyta originali sudėtinė algoritmo mokymo nuostolių funkcija, kuri sujungia QRS-T kampą ir Euklido atstumą, kad būtų galima vadovautis modeliu visoje 3D erdvėje. Šioje disertacijoje ne tik pasiūlytas pirmasis erdvinio QRS-T kampo įvertinimo iš sumažintų derivacijų EKG metodas, bet ir ištirta galimybė įvertinti kampą tik iš priekinių krūtininių derivacijų EKG.

Šioje daktaro disertacijoje taip pat pateikiamas pirmasis tyrimas, kuriame nagrinėjama galimybė fiksuoti laipsniškus kalio kiekio kraujyje svyravimus ambulatorinėje aplinkoje naudojant vienos derivacijos EKG. Jokiame kitame tyrime dar nebuvo tirta galimybė neinvaziniu būdu stebėti elektrolitų kiekį ne HD seansų metu. Kalio fluktuacijų sukeltiems skilvelių repoliarizacijos pokyčiams kiekybiškai įvertinti buvo naudojami du T bangų morfologijos deskriptoriai: pasiūlytas modeliu pagrįstas deskriptorius ir vienintelis šiuo metu prieinamas vienos derivacijos EKG deskriptorius, jautrus kalio kiekiui kraujyje HD seansų metu. Pateiktame tyrime nustatyta, kokie galimi klaidinantys veiksniai gali turėti įtakos potencialių EKG išvestinių kalio kiekio kraujyje žymenų veikimui, atskleidžiant neinvazinio elektrolitų kiekio kraujyje stebėjimo iššūkius. Kadangi neinvazinės kraujo elektrolitų stebėsenos moksliniai tyrimai dar tik įsibėgėja, tokie galimybių tyrimai suteikia vertingų įžvalgų būsimiems plataus masto tyrimams, todėl yra būtini siekiant pagilinti mokslines žinias ir paskatinti tolesnę tyrimų srities plėtrą.

Galiausiai, paskutiniame disertacijos skyriuje pateikiamas simboliniu klasterizavimu pagrįstas algoritmas, skirtas spartesniam pusiau automatiniam širdies dūžių anotavimui ilgalaikėse EKG. Algoritmas sukoncentruoja širdies dūžius į trumpas sekas, naudodamas klasikinį diskretizacijos metodą, taikomą sprendžiant daugelį laiko sekų duomenų gavybos problemų. Vienodomis sekomis atvaizduoti dūžiai grupuojami į tuos pačius klasterius siekiant sumažinti skaičiavimo reikalavimus. Vietoj kiekvieno atskiro širdies dūžio ekspertui pateikiami hierarchinio klasterizavimo rezultatai, gauti iš sukurtų išankstinių klasterių, kuriuos jis turi ištirti ir anotuoti rankiniu būdu. Algoritmas, klasterizuodamas širdies dūžius nekontroliuojamu būdu, leidžia tyrėjams atrasti netikėtų morfologinių EKG pokyčių, kurie gali būti susiję su kraujo elektrolitų svyravimais.

Praktinė reikšmė

1. Metodai, leidžiantys tiksliai įvertinti elektrolitų profilį ambulatorinėmis sąlygomis, gali:

(a) Laiku nustatyti sunkią dielektrolitemiją prieš prasidedant SŠM sukeliančioms aritmijoms.

(b) Padėti titruojant ir individualiai parenkant vaistus pacientams, kuriems gresia vaistų sukelta dielektrolitemija.

(c) Padėti išsiaiškinti priežastinį ryšį tarp elektrolitų svyravimų ir aritmijos atsiradimo bei progresavimo.

(d) Padėti tiriant širdies ir inkstų funkcijos, homeostazės, kraujo elektrolitų ir jų ilgalaikių pasekmių sveikatai sąsajas.

2. Šioje disertacijoje sukurti algoritmai ir metodai gali būti naudojami šiose srityse:

(a) Siūlomas T bangos morfologijos deskriptorius gali palengvinti technologinių sprendimų, skirtų kiekybiniam kalio kiekio kraujyje nustatymui ambulatorinėmis sąlygomis, kūrimą.

(b) Kadangi siūlomam T bangų morfologijos deskriptoriui gauti pakanka vienos derivacijos EKG, ilgalaikiams duomenims rinkti vietoj Holterio prietaisų galima naudoti patogius vartotojų sveikatos priežiūros prietaisus. Ilgalaikių EKG ir sinchroninių kraujo mėginių duomenų bazės vis dar iš esmės neprieinamos, o jos yra labai svarbios neinvazinės kraujo elektrolitų svyravimų stebėsenos mokslinių tyrimų srityje.

(c) Galima ištirti erdvinio QRS-T kampo ir elektrolitų kiekio kraujyje ryšį, nes siūlomas giliuoju mokymusi pagrįstas metodas įvertina kampą iš sumažintų derivacijų EKG rinkinių. Erdvinis QRS-T kampas galėtų būti potencialus neinvazinės kraujo elektrolitų stebėsenos sprendimas.

(d) Erdvinio QRS-T kampo įvertinimas iš sumažintų derivacijų EKG atkarpų atveria galimybę panaudoti gerai žinomą jo diagnostinę vertę SŠM rizikos vertinimui ir ankstyvam pavojingų širdies įvykių aptikimui pažeidžiamose populiacijose, pavyzdžiui, sergantiesiems LIL ir ŠKL.

(e) Panašiai į siūlomą giliojo mokymosi modelį galėtų būti sukurti ir kiti algoritmai, pagrįsti 3D repoliarizacijos analize, pavyzdžiui, skilveliniam gradientui išvesti.

(f) Simbolinis klasterizavimo algoritmas leidžia tyrėjams daug greičiau anotuoti ilgalaikius biosignalus. Didelės anotuotos duomenų bazės gali palengvinti mašininio mokymosi modelių, skirtų EKG signalams interpretuoti, kūrimą.

(g) Simbolinis klasterizavimo algoritmas gali padėti tyrėjams atrasti netikėtus morfologinius EKG pokyčius, susijusius su kraujo elektrolitų svyravimais.

3. Galimybių tyrimo rezultatai suteikia vertingų įžvalgų, padėsiančių tobulinti

tolesnius neinvazinio elektrolitų kiekio kraujyje stebėjimo tyrimus, t. y. apie klaidinančius veiksnius, galinčius turėti įtakos galimų EKG nustatomų kraujo elektrolitų žymenų veikimui.

4. Šiame darbe aprašyti algoritmai buvo sukurti įgyvendinant Europos regioninės plėtros fondo kartu su Lietuvos mokslo taryba (LMTLT) 2018–2022 m. finansuojamą projektą „*Personalizuotos dėvimos technologijos gyvybei pavojingoms sveikatos būsenoms įvertinti lėtine inkstų liga sergantiems pacientams – KidneyLife*“, projekto Nr. 01.2.2-LMT-K-718-01-0030.

Rezultatų patvirtinimas

Daktaro disertacija grindžiama dviem pagrindiniais straipsniais, paskelbtais tarptautiniuose mokslo žurnaluose, kurių citavimo indeksas nurodytas „*Clarivate Analytics Web of Science*“ duomenų bazėje. Pagrindiniai rezultatai buvo pristatyti keturiose tarptautinėse konferencijose, pripažintose visame pasaulyje: 2017 m. IEEE Biomedicininių grandinių ir sistemų konferencijoje (*BioCAS*), 45-oje ir 48-oje „Computing in Cardiology“ (*CinC*) konferencijose ir 15-oje tarptautinėje konferencijoje „Bio-inspired Systems ir Signal Processing, Biosignals“ (*BIOSTEC 2022*).

Tyrimas buvo įvertintas tiek tarptautiniu mastu, tiek Lietuvoje. 2018 m. Kauno technologijos universitetas apdovanojo kaip vieną aktyviausių Elektros ir elektronikos inžinerijos krypties doktorantų. Konferencijoje „45th Computing in Cardiology“ moksliniai tyrimai buvo apdovanoti *Gary ir Bill Sanders Poster Award*. 2021 m. tyrimui skirta Lietuvos mokslo tarybos skatinamoji stipendija už akademinius rezultatus.

Ginamieji teiginiai

1. Klinikinės elektrolitų pusiausvyros sutrikimo pasekmės yra ne tik pavojingos aritmijos. Lėtinėmis ligomis sergantiems pacientams net trumpi ir pasikartojantys dielektrolitemijos epizodai gali sukelti neadaptyvių kompensacinių mechanizmų kaskadą, dėl kurios pablogėja širdies ir inkstų funkcijos. Šis pablogėjimas galiausiai gali sukelti grėsmę ilgalaikei sveikatai ir pagreitinti ligos progresavimą. Todėl reguliarus elektrolitų kiekio kraujyje stebėjimas yra labai svarbus ne tik siekiant išvengti staigios širdies mirties trumpuoju laikotarpiu, bet ir siekiant palaikyti homeostazę bei skatinti bendrą sveikatą ilguoju laikotarpiu.

2. T bangų morfologijos deskriptoriai gali užfiksuoti skilvelių repoliarizacijos sutrikimus, kuriuos sukelia laipsniški kalio kiekio kraujyje svyravimai ambulatorinėse vienos derivacijos EKG. Tačiau ambulatoriniai įrašai yra jautrūs triukšmui, todėl EKG parametrams įvertinti būtina atlikti modeliais pagrįstą parametrizavimą. Nepaisant to, tuo pat metu vykstantis elektrolitų disbalansas ir kintanti T bangų morfologija yra klaidinantys veiksniai, kurie gali turėti įtakos galimų EKG kalio kiekio kraujyje žymenų veiksmingumui.

3. Pasitelkus giliojo mokymosi dirbtinius neuroninius tinklus galima pakankamai patikimai įvertinti erdvinį QRS-T kampą, naudojant sumažinto skaičiaus derivacijų EKG rinkinį. Pritaikius metrikas, kuriomis modelis vadovaujasi 3D erdvėje, pagerėja modelio veikimas, todėl galima įvertinti erdvinius skilvelių repoliarizacijos žymenis net ir tada, kai įvesties EKG derivacijose pateikiama ribota erdvinė informacija. Šis metodas yra perspektyvus sprendimas ambulatorinei QRS-T kampo stebėsenai.

4. Simboliniai klasterizavimo algoritmai gali padidinti širdies dūžių anotavimo ir analizės efektyvumą ilgalaikėse EKG. Šie algoritmai gerokai sumažina įvairių mašininio mokymosi klasterizavimo metodų skaičiavimo reikalavimus. Be to, simbolinis klasterizavimas leidžia tyrėjams ištirti, kaip širdies dūžiai natūraliai patenka į skirtingas klases, ir netgi nustatyti netikėtus poklasius, kuriuos būtų galima toliau tirti.

1. KLINIKINIS ELEKTROLITŲ FIZIOLOGIJOS IR HOMEOSTAZĖS PAGRINDIMAS

Elektrolitai – tai kraujyje ir organizmo skysčiuose ištirpę elektringi mineralai, būtini homeostazei palaikyti [1]. Elektrolitai dalyvauja įvairiuose fiziologiniuose procesuose, įskaitant veikimo potencialo susidarymą, užtikrinantį tinkamą nervų laidumą ir širdies raumens susitraukimą [2]. Kaip ir daugelis kitų gyvybiškai svarbių žmogaus biologinės sistemos kintamųjų, elektrolitų kiekis kraujyje turi būti griežtai reguliuojamas pagal iš anksto nustatytas ribas, kad ląstelės galėtų normaliai funkcionuoti [2]. Kai elektrolitų kiekis nukrypsta nuo idealaus intervalo, gali smarkiai sutrikti neurologinės ir širdies bei kraujagyslių funkcijos, todėl gali sutrikti homeostazė, o tai gali turėti pasekmių visam gyvenimui ar net baigtis mirtimi [1, 2].

Gyvosios sistemos pasisavina daug elektrolitų, tačiau vieni svarbiausių ląstelių procesams yra natris (Na^+), kalis (K^+), kalcis (Ca^{2+}), magnis (Mg^{2+}) ir bikarbonatas (HCO_3^-). Šių elektrolitų koncentracija vidiniuose ir tarpląsteliniuose skysčiuose skiriasi (1.1 pav.), o optimalus ląstelių funkcionavimas labai priklauso nuo to, ar abiejų skysčių joninis profilis skiriasi. Patikimi homeostazės mechanizmai griežtai reguliuoja elektrolitų kiekį ekstraląsteliniame skystyje (t. y. kraujyje), pirmiausia inkstai ir renino-angiotenzino-aldosterono sistema (RAAS).

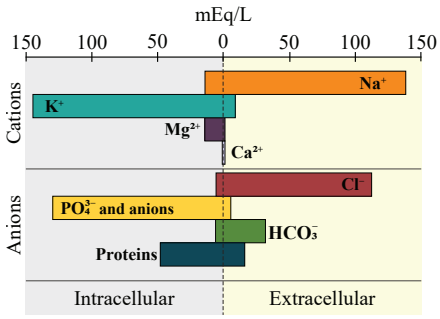

1.1 pav. Pagrindiniai vidinių ir išorinių ląstelių skysčių katijonai ir anijonai. Parengta pagal [2]

Elektrolitų pusiausvyros sutrikimas – sutrikusios homeostazės šalutinis produktas

Diselektrolitemija atsiranda dėl dviejų ar trijų etiologijų (1.2 pav.). Dažniausiai diselektrolitemija yra šalutinis patologijos, kuri dėl inkstų funkcijos sutrikimo sutrikdo homeostatinius elektrolitų reguliavimo mechanizmus, produktas. Todėl pacientai, kurių inkstų funkcija sutrikusi, yra jautriausi diselektrolitemijai. Inkstų pažeidimas, pasireiškiantis LIL, akivaizdžiai apsunkina inkstų funkciją, todėl LIL sergantys pacientai yra ypač pažeidžiami SŠM sukeliančių elektrolitų sutrikimų [6, 12]. Beveik 39,5–74,2 proc. pacientų pasireiškia bent viena diselektrolitemija [13], nors sergamumo dažnis skiriasi esant kiekvienai konkrečiai elektrolitų ir LIL stadijai [12]. Inkstų

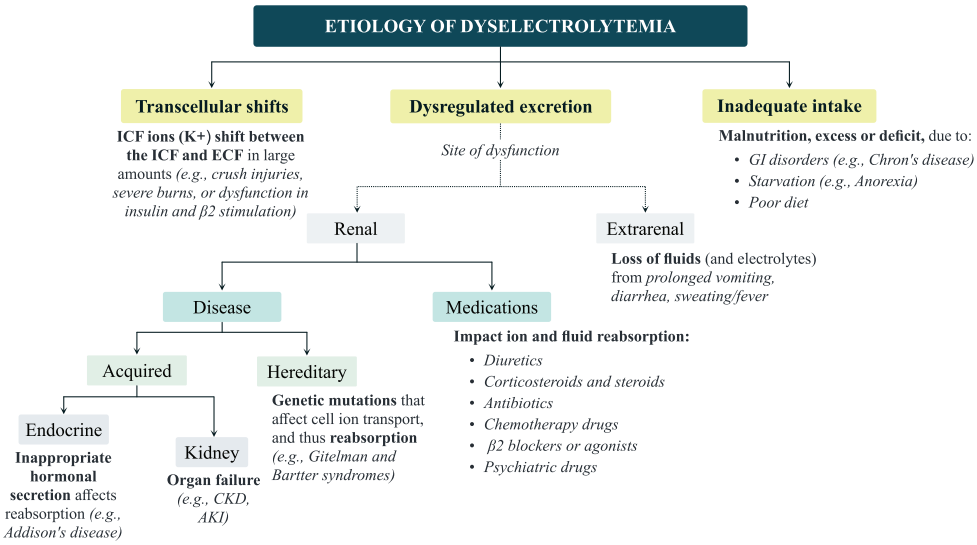

1.2 pav. Grafinė trijų elektrolitų disbalanso etiologijų apžvalga

pažeidimo laipsnis dar labiau padidina polinkį į elektrolitų pusiausvyros sutrikimus, o GSIL sergantiems pacientams yra didžiausia rizika [77].

Tačiau kasdienėje klinikinėje praktikoje dažniausiai pasitaikanti dielektrolitemijos priežastis yra terapiniai vaistai [14, 15]. Daugelis įprastinių terapijų, skirtų įvairioms lėtinėms ligoms gydyti, sukelia inkstų funkcijos sutrikimus, net jei inkstų audinys yra sveikas [16]. Vienas ryškus pavyzdys – antihipertenziniai vaistai ir kiti nuo ŠKL skiriami vaistai, pavyzdžiui, diuretikai ir β-blokatoriai. Maždaug 10% pacientų per metus nuo hipertenzijos gydymo pradžios pasireiškia vienas dielektrolitemijos epizodas [14], o 26,8% pacientų natrio pusiausvyros sutrikimas pasireiškia pakartotinai [17]. Lengvas kalio nuokrypis būna 19% [18] ir net 80% [14] diuretikų vartojančių pacientų, priklausomai nuo paskirtų diuretikų klasės. Taip pat manoma, kad panašūs gydymo būdai skatina dielektrolitemiją 20–48% pacientų hospitalizavimo metu, nors tik 3–8% iš jų priėmimo į ligoninę metu buvo nustatytas nenormalus diuramino kiekis [19, 20].

Klinikinės elektrolitų pusiausvyros sutrikimo pasekmės

Viena iš labiausiai nerimą keliančių elektrolitų , ypač kalio, disbalanso [7] pasekmių yra aritmijos, galinčios sukelti SŠM [8, 9]. Deja, tokios pavojingos aritmijos paprastai atsiranda be jokių akivaizdžių elektrolitų disbalanso požymių, kurie galėtų įspėti pacientus, kad jie kreiptųsi dėl prevencinio medicininio gydymo [10]. Ankstyvosios (ir lengvos) dielektrolitemijos simptomatika yra plati ir dažnai nespecifinė – nuo besimptomės iki bendro nuovargio ir blogos savijautos bei įprastų virškinimo problemų [11]. Taigi, neatlikus kraujo tyrimo, lengvos dielektrolitemijos praktiškai neį-

manoma nustatyti. Kai pacientams pasireiškia ryškesni klinikiniai požymiai, kraujo elektrolitai jau būna pasiekę gyvybei pavojingą lygį, todėl būtina skubi pagalba.

Nors pavieniai nedidelės dielektrolitemijos epizodai paprastai nekelia tiesioginės grėsmės pacientui, naujausi tyrimai rodo, kad pasikartojantys epizodai gali turėti ilgalaikių pasekmių sveikatai [5]. Lėtinė lengva diselektrolitemija lemia hipertenzija sergančių pacientų polinkį į sinkopę ir kritimus [5], o hospitalizuotų pacientų, išrašytų iš ligoninės esant nekoreguotam lengvam elektrolitų disbalansui, pakartotinės hospitalizacijos ir 60 dienų [21], 90 dienų [22] bei vienų metų [23] mirtingumo rodikliai yra didesni. Nors dar neįrodyta, šie pasikartojantys lengvos dielektrolitemijos epizodai gali būti susiję su *kardiorenalinio sindromo* (KRS), kuriam, kaip rodo jo pavadinimas, būdingas širdies ir inkstų funkcijų pablogėjimas, atsiradimu. Šis sindromas blogina ilgalaikę sveikatą ne tik dėl to, kad pagreitina jau esamos lėtinės ligos klinikinį progresavimą, bet ir dėl to, kad sudaro prielaidas pacientams susirgti ŠKL, LIL ir net GSIL [24]. Be to, lengva diselektrolitemija gali padidinti mirtinos baigties tikimybę labiau progresavusiose lėtinės ligos stadijose, ypač jei ji pasireiškia kartu su gretutine ŠKL [21]. Taigi, norint išvengti nepalankių pasekmių, labai svarbu skubiai koreguoti nenormalų elektrolitų kiekį.

Kai kurie gydytojai tokius lengvus epizodus laiko nekenksmingais – dažnai jų nepastebi, kol jie neperauga į sunkius, o daugelis kitų gydytojų, bijodami nepageidaujamų poveikių, skiria per mažai arba per mažą nepakeičiamų vaistų dozę [25]. Tačiau ilgainiui nepakankamas vaistų skyrimas tampa „dviašmeniu kardu“, dar labiau apsunkinančiu lėtinių ligų valdymą. Be tinkamo vaistų vartojimo režimo organizmas negali palaikyti homeostazės ir suaktyvina neadaptyvius kompensacinius mechanizmus, kurie galiausiai pažeidžia daugelį organų [2, 26], todėl atsiranda KRS ir blogėja sveikatos būklė [1].

2. ESAMŲ ELEKTROLITŲ KIEKIO KRAUJYJE VERTINIMO METODŲ APŽVALGA

Kol kas kraujo tyrimai yra vienintelis kliniškai pagrįstas metodas dielektrolitemijai nustatyti. Nepaisant to, pastaraisiais metais diskutuojama apie EKG panaudojimą elektrolitų pusiausvyros sutrikimams fiksuoti [122]. Jo koncepcija remiasi teoriniu pagrindu, kad nenormalus elektrolitų kiekis kraujyje keičia širdies ląstelių elektrofiziologines savybes [7], ypač repoliarizaciją [48], dėl ko atsiranda morfologiniai EKG bangos formos pokyčiai [42].

Elektrolitų kiekio kraujyje įtaka EKG morfologijai

Kai kraujo elektrolitų kiekis atitinka homeostazės ribas, elektros impulsas, kurį generuoja stimuliatoriaus ląstelės sinuatrialiniame mazge, keliauja per širdies elektrinę sistemą ir sukuria EKG bangos formą, panašią į pavaizduotą 2.1 pav. Kadangi skilvelių repoliarizacija yra jautresnė kraujo elektrolitų disfunkcijai, o ne depoliarizacijai, elektrolitų disbalanso EKG modeliai paprastai susiję su tam tikrais morfologiniais pokyčiais po depoliarizacijos EKG komponentuose: ST segmente (Ca^{2+}, žr. 2.3 pav.) ir T bangoje (K^+, žr. 2.2 pav.).

Dabartiniai neinvazinės kraujo elektrolitų stebėsenos iššūkiai

Keliuose medicininiuose tyrimuose buvo vertinamas elektrolitų sukeltų EKG pokyčių dažnumas klinikinėje praktikoje [116, 122, 124, 125]. Nors nė viename iš jų nesiekta kiekybiškai įvertinti kraujo elektrolitų kiekį pagal EKG, šie tyrimai rodo, kad

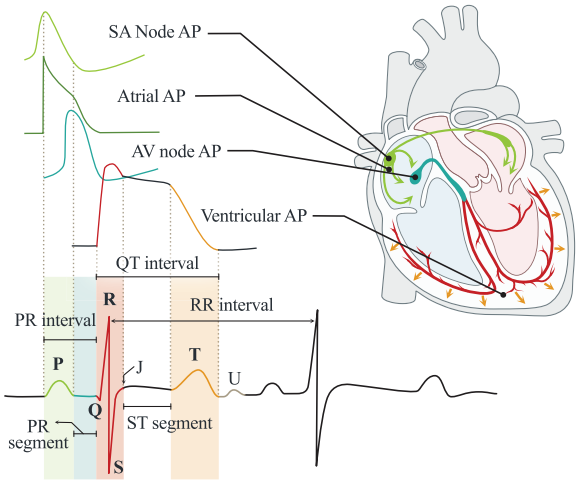

2.1 pav. Normalios EKG bangos genezė elektrolitų pusiausvyros požiūriu. QRS kompleksas atitinka skilvelio depoliarizaciją, kuriai daugiausia būdingas Na^+ įtekėjimas. ST segmentas atspindi Ca^{2+} antplūdį, kuris sukelia skilvelio susitraukimą. T banga atspindi skilvelio repoliarizaciją, kurios metu vyksta K^+ srautas į išorę, siekiant atkurti kardiomiocitų ramybės membranos potencialą. Parengta pagal: [74]

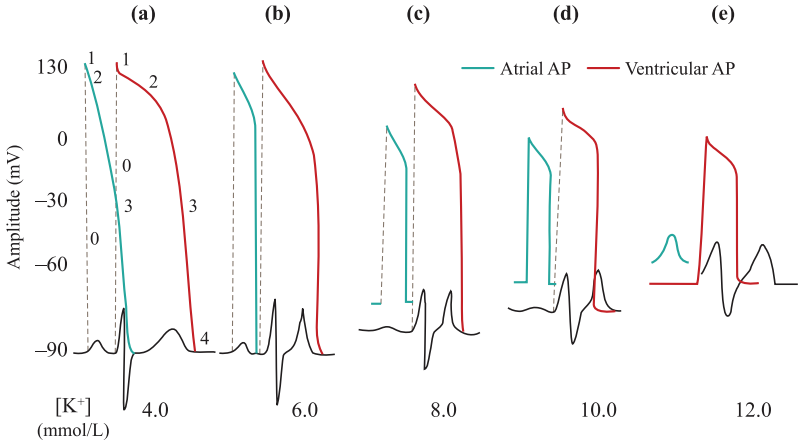

2.2 pav. Prieširdžių ir skilvelių veikimo potencialo diagrama, uždėta ant EKG, esant skirtingoms kraujo [K^+]: (a) normokalemijai; (b) lengvai ar vidutinio sunkumo; (c) vidutinio sunkumo ar sunkiai; (d) sunkiai; (e) gyvybei pavojingai hiperkalemijai. Parengta pagal [7]

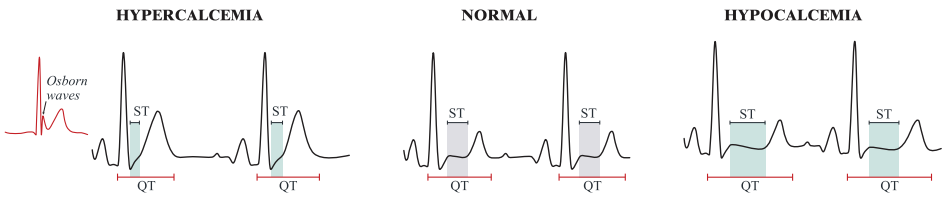

2.3 pav. ST segmento ir QT intervalo skirtumai esant kalcio balansui ir hiper- bei hipokalcemijai

elektrolitų balanso stebėjimas pagal EKG yra empiriškai įmanomas. Neseniai atliktoje metaanalizėje gydytojai pranešė apie fiziologinį ryšį tarp elektrolitų kiekio kraujyje, EKG intervalų ir skilvelių repoliarizacijos žymenų [116], taip patvirtindami daugelio EKG požymių, kaip perspektyvių bekraujų elektrolitų kiekio žymenų, neišnaudotą potencialą.

Nepaisant mokslinio susidomėjimo, EKG pagrįstos kraujo elektrolitų stebėsenos technologinių tyrimų sritis vis dar yra pradinės stadijos, nes iki 2012 m. nebuvo pasiūlyta beveik jokių konkrečių inžinerinių sprendimų [122]. Nuo 2016 m. ši sritis ėmė įgauti vis didesnį pagreitį, kai keliuose tyrimuose buvo pristatyti nauji T bangų morfologijos deskriptoriai, skirti kiekybiniam kraujo kalio [K^+] kiekiui nustatyti, ir gauti daug žadantys rezultatai [43–45, 52, 128, 131–133, 137]. Tačiau nė viename iš jų nebuvo atskleista neinvazinės kraujo elektrolitų stebėsenos ambulatorinėmis sąlygomis galimybė. Be to, visi siūlomi metodai turi bent vieną iš toliau išvardytų apribojimų, kurie gali apsunkinti ambulatorinę kraujo elektrolitų stebėseną:

1. Jiems reikia standartinių 12-os derivacijos elektrokardiogramų, kurios yra nepraktiškos naudoti ambulatoriškai.

2. Jie buvo tiriami tik HD metu, kai elektrolitų kiekis svyruoja greičiau nei kas-

dienėje ambulatorinėje aplinkoje.

3. Juose neatsižvelgiama į galimus klaidinančius veiksnius, kurie gali turėti įtakos siūlomų žymenų veikimui, pavyzdžiui, gretutines širdies ligas, vaistus ir gretutinius elektrolitų pusiausvyros sutrikimus [42, 125].

4. Jų metu reikia tiksliai išskirti mažos amplitudės bangas, o tai gali būti sudėtinga pasiekti triukšminguose ambulatoriniuose signaluose.

Pagrindinė neinvazinės kraujo elektrolitų stebėsenos mokslinių tyrimų kliūtis yra praktinių sprendimų ambulatorinės stebėsenos scenarijams trūkumas. Pirma, tai apsunkina esamų metodų veiksmingumo vertinimą pagal realius ambulatorinės stebėsenos scenarijus. Tai taip pat neskatina kurti kitų galimų sprendimų, kurie galėtų panaudoti kai kurių gerai žinomų skilvelio repoliarizacijos žymenų (pvz., erdvinio QRS-T kampo) vertę kaip perspektyvių kraujo elektrolitų pakaitalų. Svarbu ir tai, kad be tokių metodų pacientai menkai laikytųsi reikalavimų, nes EKG įrašymo prietaisus būtų per daug nepatogu nešiotis. Kad deskriptoriai būtų tinkami naudoti ambulatoriškai, jie turi gebėti fiksuoti laipsniškus kraujo elektrolitų svyravimus, būti atsparūs triukšmui ir, pageidautina, turi tenkintis sumažintu EKG derivacijų skaičiumi.

3. T BANGOS MORFOLOGIJOS POKYČIŲ KIEKYBINIS ĮVERTINIMAS VIENOS DERIVACIJOS EKG, TAIKANT MODELIU PAGRĮSTĄ PARAMETRIZAVIMĄ

Hemodializės (HD) pacientai yra jautrūs gyvybei pavojingoms aritmijoms, kurių dažnumas yra daug didesnis trijų dienų pertraukos tarp HD seansų metu, vadinamuoju ilguoju tarpdializiniu intervalu [9, 10, 147]. Manoma, kad elektrolitų, ypač kalio, svyravimai yra vieni iš pagrindinių šių pavojingų aritmijų sukėlėjų [9]. Todėl neinvazinis ambulatorinis kalio svyravimų stebėjimas tarp HD seansų yra kliniškai svarbus šiai populiacijai [39].

Naujausiuose tyrimuose buvo pasiūlyta įvairių T bangos morfologijos deskriptorių [K^+] kiekybiniam įvertinimui ir gauta daug žadančių rezultatų [43–45, 131]. Tačiau tokių deskriptorių efektyvumas buvo tiriamas tik HD metu, todėl EKG pagrįstos kraujo elektrolitų stebėsenos ambulatoriniais atvejais galimybės liko neištirtos. Šiame tyrime nagrinėjama galimybė fiksuoti kalio svyravimus per ilgą tarpdializinį intervalą.

3.1. Metodai

Kadangi kraujas [K^+] veikia ne tik vietines T bangos savybes, bet ir bendrą T bangos morfologiją [42], taikant *modeliu pagrįstą parametrizavimą* buvo sukurtas deskriptorius θ_δ, kuriuo atsižvelgiama į globalius T bangos morfologijos pokyčius. θ_δ efektyvumas lyginamas su T_{SA}. T_{SA} matuoja T bangos nuolydžio ir amplitudės santykį (vietiniai požymiai) ir yra vienintelis turimas deskriptorius, jautrus [K^+] pokyčiams HD metu vienos derivacijos EKG [131]. θ_δ ir T_{SA} išvedami iš iš anksto apdorotų signalo vidurkių širdies dūžių (3.1 pav.).

T bangos parametrų nustatymas ir požymių įvertinimas

T banga $T(n)$, sudaryta iš vieno didėjančio ($\mathcal{S}_u$) ir vieno mažėjančio ($\mathcal{S}_d$) nuolydžio, parametrizuojama naudojant sudėtinį modelį ($T_c(n)$), kurį sudaro viena Gauso ($T_u(n)$) ir viena lognormalinė ($T_d(n)$) funkcija, apibūdinanti kiekvieną nuolydį. θ_δ sujungia du parametrus, gaunamus pagal T bangos modelį: kampą θ (°) ir laiko poslinkį δ (s), t. y. fazės poslinkį tarp $T_d(n)$ ir $T_u(n)$ režimų (3.2 pav.). Šie du parametrai veikia kaip elektrofiziologinių nenormalaus kraujo [K^+] požymių, kurių negalima tiesiogiai

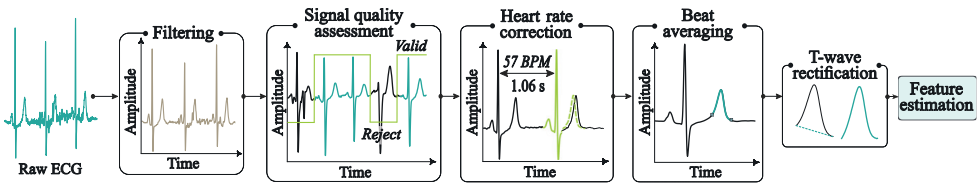

3.1 pav. Pirminis vienos derivacijos EKG apdorojimas. EKG segmentuoti buvo naudojamas 90 s slankiojantis langas su 10 s persidengimu

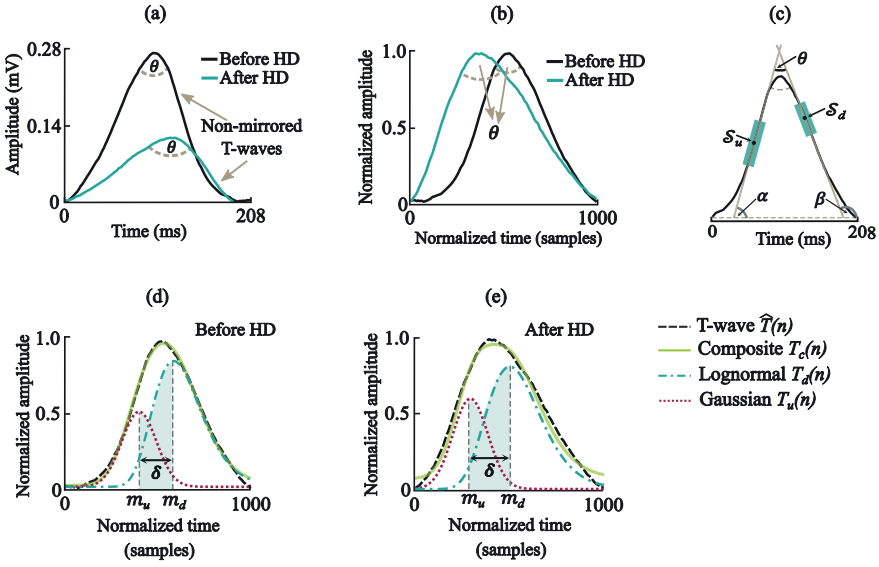

3.2 pav. T bangos požymių įvertinimas: (a) T bangos esant skirtingiems kraujo $[K^+]$ lygiams be normalizavimo; b) variacija θ normalizuotose T bangose; (c) $\mathcal{S}_u$, $\mathcal{S}_d$ ir θ radimas. δ pokytis esant skirtingiems kraujo $[K^+]$ lygiams: (d) $[K^+] = 5{,}5\text{mmol}\,L^{-1}$ ir (e) $[K^+] = 3{,}2\text{mmol}\,L^{-1}$

nustatyti, pakaitalai – T bangos smailumo (θ) ir pailgėjimo (δ) [42]. θ_δ principas yra toks: kai $[K^+]$ pakyla virš normos, T banga tampa statesnė ir aukštesnė ($\downarrow\theta$), taip pat sutrumpėja jos trukmė ($\downarrow\delta$). θ_δ sustiprina θ ir δ atsaką į kalio svyravimus ir apskaičiuojamas taip:

$$\theta_\delta = -\log_{10}(\theta \cdot \delta). \tag{3.1}$$

Logaritmas išplečia dinaminį diapazoną ir užtikrina teigiamą θ_δ koreliaciją su kalio svyravimais. Daugiau informacijos apie siūlomą metodą galima rasti straipsnyje: [59].

Duomenys

Per ilgą tarpdializinį intervalą (3.3 pav.) naudojant vartotojų sveikatos priežiūros prietaisą buvo surinkta 17 HD pacientų (9 moterys, amžius 57,4 ± 14,6 metų), sergančių gretutinėmis širdies ligomis, vienos derivacijos EKG ir kraujo mėginių duomenų bazė. Duomenų bazėje yra ~1078 valandų EKG I derivacijos signalų, maždaug 71 val. vienam pacientui iš ambulatorinių arba neguldomų hospitalizuotų pacientų. Taip pat įtraukta informacija apie išorinius kintamuosius, darančius įtaką elektrolitų kiekiui, pavyzdžiui, vaistus ir maistą. Pacientai, kuriems būdingas reguliarus sinusinis ritmas ir aukšta signalų kokybė, priskiriami *I grupei*, o pacientai, kurių įrašai buvo triukšmingi arba su aritmijomis, – *II grupei*. Du pacientai į analizę nebuvo įtraukti.

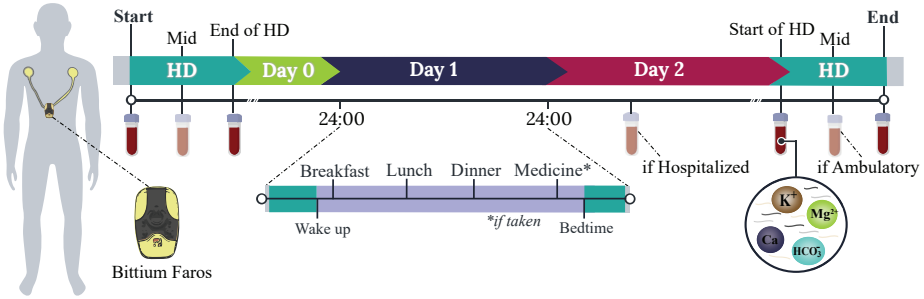

3.3 pav. Duomenų rinkimo protokolas. Hospitalizuotų ir ambulatorinių pacientų EKG I derivacijos signalai buvo gaunami per visą ilgą tarpdializinį intervalą naudojant ambulatorinį registratorių. Hospitalizuotų pacientų kraujo mėginiai buvo imami du kartus per kiekvieną HD (pradžioje ir pabaigoje) ir bent kartą per ilgąjį interdializinį intervalą. Ambulatorinių pacientų kraujo mėginiai buvo imami tik kiekvieno HD metu (pradžioje, viduryje ir pabaigoje)

3.2. Rezultatai ir aptarimas

Neinvazinis ambulatorinis kraujo elektrolitų stebėjimas naudojant vienos derivacijos EKG yra įmanomas net ir sudėtingų HD pacientų, sergančių gretutinėmis širdies ligomis, atveju. Paros θ_δ ir T_{SA} pasiskirstymai kiekvieno paciento $[K^+]$ etaloninių verčių atžvilgiu (3.5 pav.) rodo, kad abu deskriptoriai vidutiniškai koreliuoja su $[K^+]$ pokyčiais (atitinkamai $r = -0{,}56$ ir $r = -0{,}57$). Apskaičiavus kiekvienai grupei atskirai, koreliacija yra daug stipresnė *I grupėje* – $r = -0{,}81$ θ_δ ir $r = -0{,}79$ T_{SA}, o *II grupėje* – $r = -0{,}45$ θ_δ ir $r = -0{,}44$ T_{SA}. Tiek θ_δ, tiek T_{SA} taip pat reagavo į kalį mažinančius vaistus ir insulino šuolius po valgio. θ_δ paros kintamumas buvo panašus į sveikų žmonių cirkadinį kraujo $[K^+]$ kintamumą (3.4 pav.).

Nors tiek θ_δ, tiek T_{SA} galima įvertinti iš EKG, užregistruotų vartotojų sveikatos priežiūros prietaisais, θ_δ mažiau nei T_{SA} veikia judesių sukeltas triukšmas, o tai geriau

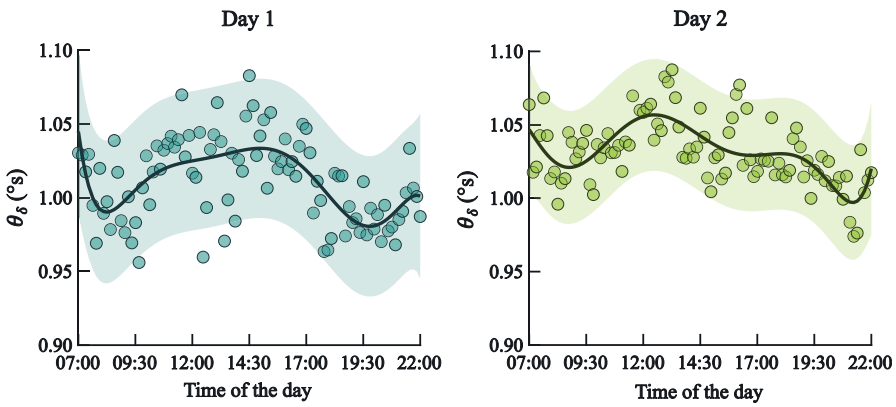

3.4 pav. Visų pacientų θ_δ (taškai) vidurkis nesikartojančiais 10 min. intervalais nuo 07.00 iki 22.00 val. *1* ir *2 dieną*. Ištisinė linija yra pritaikytas 7 eilės polinomas, rodantis tolygesnį θ_δ kitimą. Viršutinė ir apatinė ribos rodo pritaikyto polinomo standartinį nuokrypį

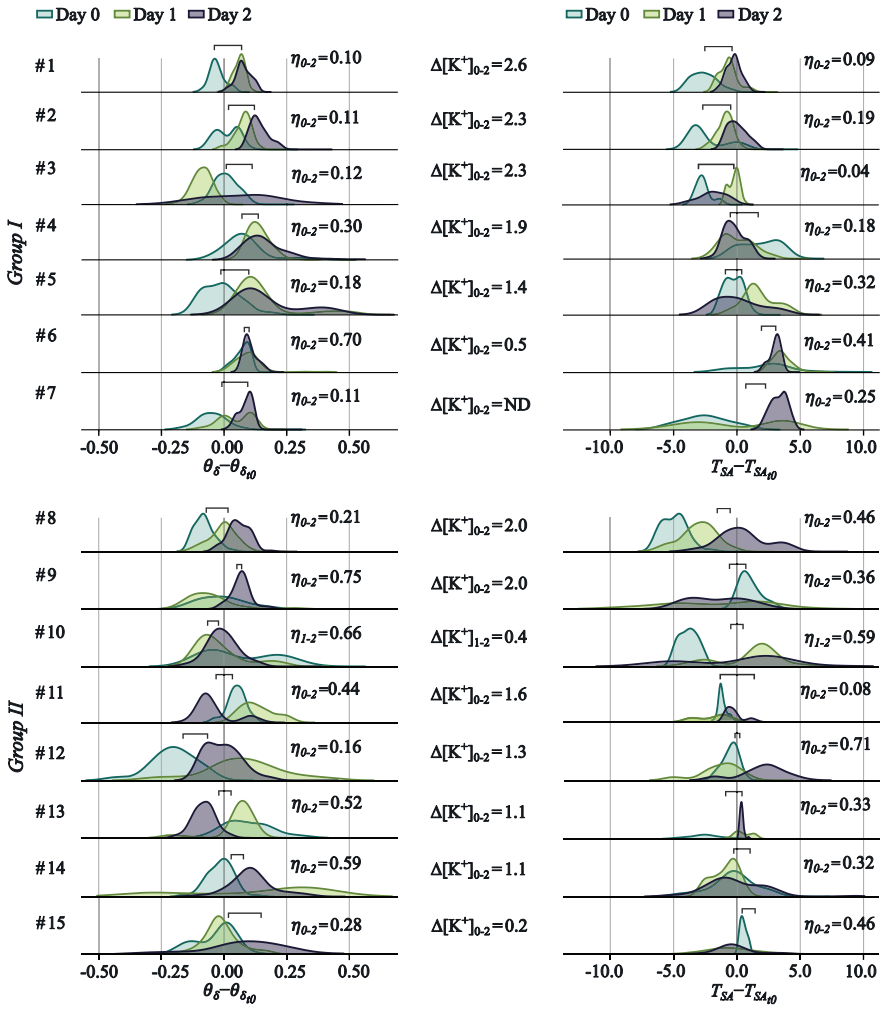

3.5 pav. Pasiskirstymas $\theta_\delta - \theta_{\delta_{t0}}$ (kairėje) ir $T_{SA} - T_{SA_{t0}}$ (dešinėje) *I grupės* (viršuje) ir *II grupės* (apačioje). Atskaitos vertės apskaičiuotos t_0. η_{0-2} – sutapimo indeksas [160] tarp *0* ir *2 dienos* pasiskirstymų, kadangi $[K^+]_{0-2}$ yra $[K^+]$ prieaugis tarp šių dviejų dienų. ND reiškia, kad duomenų nėra. 10 paciento kraujas buvo paimtas *1 dieną*

tinka ambulatorinei stebėsenai.

Du klaidinantys veiksniai turėjo įtakos θ_δ ir T_{SA}: gretutinis kalcio ir bikarbonato elektrolitų pusiausvyros sutrikimui bei kintančios T bangų morfologijos rodikliams. θ_δ rezultatai buvo patikimesni nei T_{SA}. T bangos morfologijos rodikliai turėtų būti vertinami tokiomis sąlygomis, kurios imituoja kasdienio stebėjimo scenarijų, vienoj eilutėj tarpdializinėse sesijose. Ateities tyrimuose turėtų būti stengiamasi rinkti kraujo mėginius tokiomis sąlygomis (ne tik HD metu) ir apimti kitas pacientų populiacijas, jautrias kalio disbalansui.

4. GILIUOJU MOKYMUSI PAGRĮSTAS ERDVINIO QRS-T KAMPO ĮVERTINIMAS IŠ SUMAŽINTO DERIVACIJŲ SKAIČIAUS EKG

Skilvelių repoliarizacijos ir elektrinio laidumo sutrikimai yra gerai dokumentuotos elektrolitų disbalanso pasekmės [48, 116]. Vienas iš kliniškai reikšmingų skilvelių repoliarizacijos aspektų yra jos heterogeniškumas, kuris gali sustiprėti virš fiziologiškai pagrįsto lygio dėl nenormalaus elektrolitų kiekio. Taigi gerai žinomi skilvelių repoliarizacijos heterogeniškumo žymenys, tokie kaip erdvinis QRS-T kampas, skatina mokslininkų susidomėjimą kaip perspektyvūs neinvazinės kraujo elektrolitų stebėsenos sprendimai. Tačiau QRS-T kampo vertinimas yra nepraktiškas ambulatoriniam stebėjimui, nes tam reikalingos nepatogios 12-os derivacijų EKG sistemos [57], o tai trukdo moksliškai tirti erdvinio QRS-T kampo ir elektrolitų ryšį. Todėl reikia metodų, leidžiančių išvesti QRS-T kampą iš sumažintų derivacijų EKG rinkinių, kuriuos galima įrašyti ambulatoriniam stebėjimui tinkamais prietaisais.

4.1. Metodai

Erdvinis QRS-T kampas α matuoja depoliarizacijos (QRS bangos) ir repoliarizacijos (T bangos) krypties panašumą ir apibrėžiamas kaip kampas tarp QRS ir T vektorių 3D erdvėje [57]. Jis apskaičiuojamas taip:

$$\alpha = \arctan\left(\frac{\left\|\vec{u}_{QRS} \times \vec{u}_{t}\right\|}{\vec{u}_{QRS} \cdot \vec{u}_{T}}\right), \tag{4.2}$$

čia $\vec{u}_{QRS}$ ir $\vec{u}_{T}$ yra vektoriai, vaizduojantys dominuojančią QRS ir T bangų orientaciją. $\vec{u}_{QRS}$ ir $\vec{u}_{T}$ paprastai apskaičiuojami iš vektokardiogramos (VCG), sudarytos iš *XYZ* derivacijų, paprastai gaunamos ortogonalizuojant standartinę 12 derivacijų EKG.

Giliuoju mokymusi pagrįstas QRS-T kampo įvertinimo metodas

Siūlomas 1D konvoliucinis neuroninis tinklas (CNN1D) su regresijos išvestimi, skirtas erdviniam QRS-T kampui įvertinti iš sumažintų derivacijų EKG. Modelis kaip įvestį ima signalo vidurkį iš kelių derivacijų rinkinio ir kaip išvestį pateikia tris $\vec{u}_{QRS}$ ir $\vec{u}_{T}$ koordinates, t. y. $\vec{u}_{QRS} = (x_{QRS}, y_{QRS}, z_{QRS})$ ir $\vec{u}_{T} = (x_{T}, y_{T}, z_{T})$, kaip *išvestis*.

Naudojant 12 EKG derivacijų, etaloninius (*tikslinių*) VGR vektorius $\vec{u}_{QRS}$ ir $\vec{u}_{T}$ galima apskaičiuoti taikant įprastinį metodą ir išmokyti modelį gauti *įverčius* $\widehat{\vec{u}}_{QRS}$ ir $\widehat{\vec{u}}_{T}$ iš konkrečių EKG derivacijų poaibių. Tada įvertintą QRS-T kampą $\hat{\alpha}$ galima apskaičiuoti kaip kampą tarp įvertintų vektorių $\widehat{\vec{u}}_{QRS}$ ir $\widehat{\vec{u}}_{T}$ taikant (4.2) lygtį. 4.1 pav. pavaizduota siūlomo giliuoju mokymusi pagrįsto metodo apžvalga. Daugiau informacijos apie modelio struktūrą pateikiama: [60].

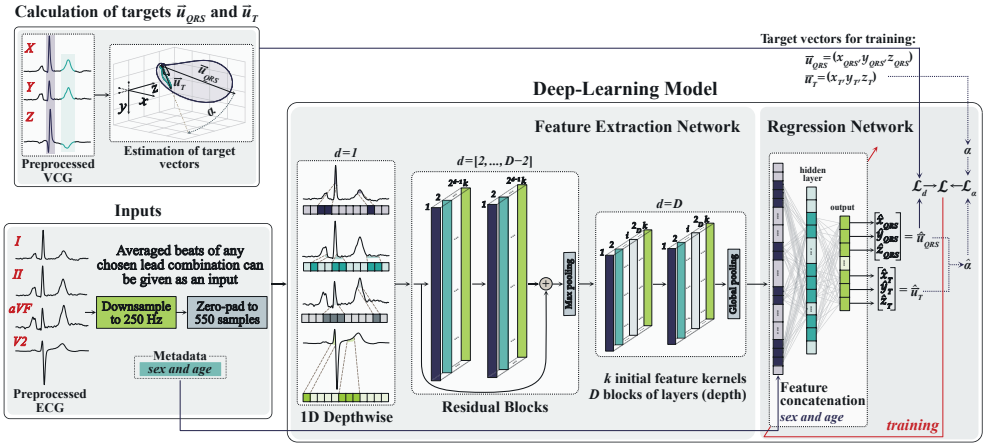

4.1 pav. Siūlomo gilaus mokymosi modelio, skirto erdviniam QRS-T kampui įvertinti iš sumažintų derivacijų EKG, apžvalga. Modelį sudaro dvi dalys: požymių išskyrimas ir regresija. Vektoriai $\vec{u}_{QRS}$ ir $\vec{u}_T$ bei erdvinis QRS-T kampas α apskaičiuojami iš EKG

Nuostolių funkcija

Modelis specialiai sukurtas taip, kad būtų galima tiesiogiai nustatyti ne α, o $\vec{u}_{QRS}$ ir $\vec{u}_T$ koordinates, kad būtų galima panaudoti bet kokią įvesties derivacijų erdvinę informaciją. Siūloma originali sudėtinė nuostolių funkcija $\mathcal{L}$, kuri modelio mokymo metu yra minimizuojama. $\mathcal{L}$ apima Euklido atstumą ($\mathcal{L}_d$) tarp $\vec{u}$ ir $\widehat{\vec{u}}$ koordinačių ir vidutinę absoliučiąją paklaidą ($\mathcal{L}_\alpha$) tarp α ir $\widehat{\alpha}$. Ji apibrėžiama taip:

$$\mathcal{L} = w_1\left(\mathcal{L}_d(\vec{u}_{QRS}, \widehat{\vec{u}}_{QRS}) + \mathcal{L}_d(\vec{u}_T, \widehat{\vec{u}}_T)\right) + w_2\,\mathcal{L}_\alpha(\alpha, \widehat{\alpha}), \tag{4.3}$$

čia w_1 ir w_2 yra svertiniai hiperparametrai, kurie nulemia nuostolių funkcijos komponentų $\mathcal{L}_d$ ir $\mathcal{L}_\alpha$ svarbą.

4.2. Duomenys

Modelis buvo sukurtas ir patikrintas naudojant „Physionet“ [190] *PTB-XL* duomenų rinkinį [182] – didžiausią šiuo metu viešai prieinamą 12-os EKG derivacijų duomenų rinkinį. *X*, *Y*, ir *Z* derivacijos (VCG) išvedamos iš neapdorotų EKG įrašų taikant Korso regresijos matricą [109]. 4.2 pav. pavaizduotas duomenų parengimo modeliui išmokyti procesas.

Duomenys padalijami į mokymo ir tikrinimo aibes taikant 80:20 padalijimo santykį. Abiejuose rinkiniuose išsaugomas pradinis α pasiskirstymas visame $\alpha = [0{:}5{:}180]^\circ$ intervale.

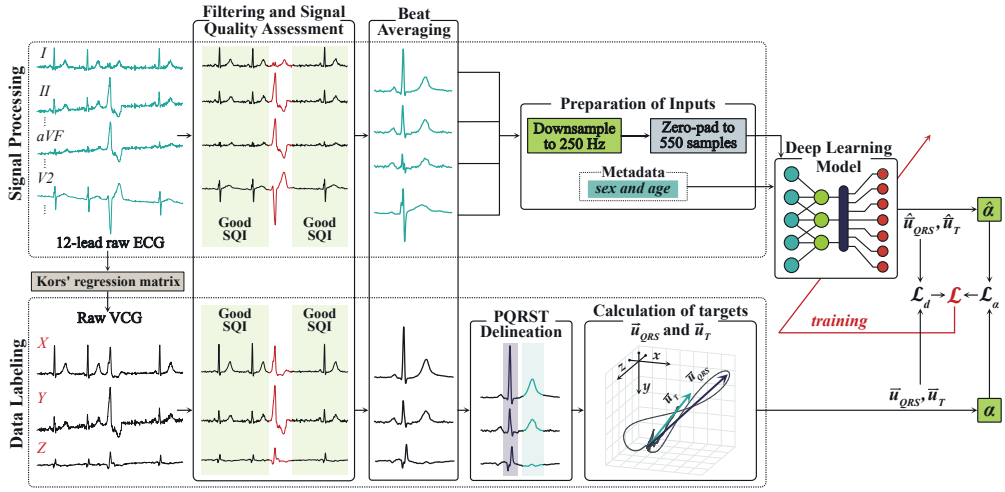

4.2 pav. Duomenų paruošimas ir ženklinimas. Atliekamas pirminis signalų apdorojimas, kurį sudaro filtravimas ir signalų kokybės vertinimas, kad būtų gauti įvesties signalų vidurkiai

4.3. Rezultatai ir aptarimas

Iki šiol buvo manoma, kad stebėti erdvinį QRS-T kampą, kuris yra vienas iš perspektyviausių SŠM rizikos vertinimo rodiklių [50, 57], ne ligoninės sąlygomis yra neįmanoma. Siūlomas modelis, nors ir prototipinis, skatina mokslinį susidomėjimą inžineriniais ambulatorinio erdvinio QRS-T kampo stebėsenos metodais, kurie gali labai prisidėti prie jo diagnostinės vertės panaudojimo ambulatoriniam širdies ir kraujagyslių sveikatos vertinimui ir kraujo elektrolitų stebėsenai.

Modelis gana tiksliai nustatė α ($\bar{\epsilon} = 11{,}4°$ ir $\bar{\epsilon} = 7{,}3°$) iš trijų frontalinių ir vienos krūtinės derivacijų ($\{I, II, aVF, V2\}$) vietoj standartinių 12, kurių reikalaujama taikant įprastinį metodą, kaip parodyta 4.3 pav. ir 4.4 pav. Modelis pasižymėjo pastebimai didesnėmis įvertinimo klaidomis α diapazonuose, kurie nepakankamai reprezentuojami mokymo duomenų rinkinyje (< 200 įrašų): $\alpha < 5°$ ir $\alpha \geq 70°$ sveikų (*NORM*) EKG; $\alpha < 15°$ ir $\alpha \geq 115°$ EKG su širdies ligomis. Nors įvertinimo paklaidos natūraliai didėja mažėjant įvesties derivacijų turimai erdvinei informacijai, rezultatai rodo, kad erdvinio QRS-T kampo įvertinimas sumažintu derivacijų rinkiniu yra įmanomas.

EKG derivacijų pogrupį $\{I, II, aVF, V2\}$ galima registruoti lengvai konfigūruojamais vartotojų sveikatos priežiūros prietaisais, kurie jau yra rinkoje. Nors reikalavimas turėti vieną prieširdinę derivaciją neleidžia naudoti prietaisų, kurie maksimaliai padidina patogumą, pavyzdžiui, ant riešo nešiojamų prietaisų, prietaisai, registruojantys $\{I, II, aVF, V2\}$, vis tiek gali palengvinti protarpinį α stebėjimą. Nepaisant to, α matavimas naudojant tik priekinių EKG derivacijų pogrupį ($\{I, II, aVL, aVF\}$) atrodo tikėtinas ateityje, toliau tobulinant modelio architektūrą.

Modelis nustato $\vec{u}_{QRS}$ ir $\vec{u}_T$ koordinates X, Y ir Z ašyse, naudodamas originalią sudėtinę nuostolių funkciją $\mathcal{L}$, kurios minimizavimas leidžia išmokyti neuroninį tinklą.

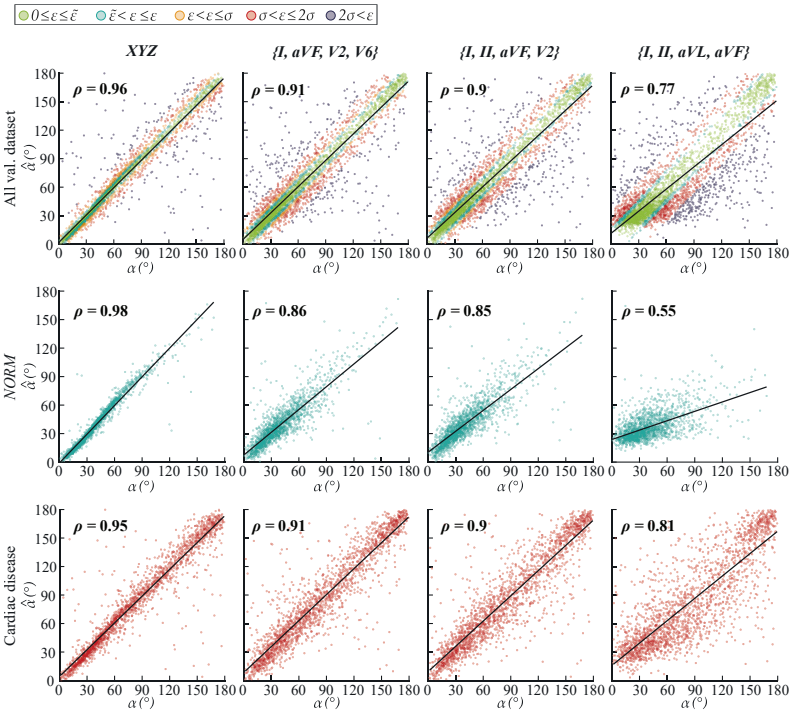

4.3 pav. $\widehat{\alpha}$ ir tikslo α sklaidos diagramos iš įvairių darinių rinkinių (viršutinė eilutė) visiems įrašams ir sveikiems EKG (vidurinė eilutė) bei EKG su širdies liga (apatinė eilutė) patvirtinimo duomenų rinkinyje. Kiekvieno $\widehat{\alpha}$ pirmoje eilutėje įvertinimo paklaida ϵ sugrupuota spalvomis pagal absoliučios medianos ($\tilde{\epsilon}$), vidurkio ($\bar{\epsilon}$) ir standartinio nuokrypio (σ_ϵ) paklaidą. ρ – Spirmano ranginės koreliacijos koeficientas

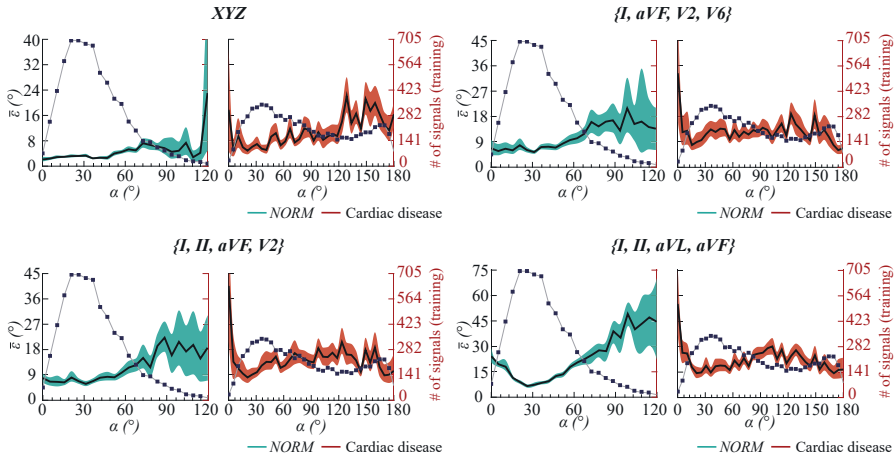

4.4 pav. Vidutinės absoliutinės paklaidos $\bar{\epsilon}$ tarp $\widehat{\alpha}$ ir α ir atitinkamo 95% pasikliautinojo intervalo kitimas $\alpha = [0{:}5{:}180]^\circ$ diapazonuose EKG su normalia (*NORM*) ir sutrikusia širdies funkcija. Dešinėje ašyje nurodytas mokymo pavyzdžių skaičius kiekviename α intervale, kadangi *NORM* tiriamųjų, kurių $\alpha > 120^\circ$, skaičius yra nereikšmingas, $\bar{\epsilon}$ šiems α intervalams nepateikiamas

Ši strategija leidžia įvertinti erdvinius EKG požymius net ir tada, kai įvesties derivacijos suteikia ribotą erdvinę informaciją.

Ateityje būtų galima ištirti erdvinio QRS-T kampo, kaip perspektyvinio kraujo elektrolitų žymens, klinikinę vertę ambulatoriniais atvejais, taip pat patvirtinti galimą šios technologijos naudą populiacijose, kurioms gresia SŠM.

5. SIMBOLINIS KLASTERIZAVIMO ALGORITMAS,SKIRTAS GREITESNEI ŠIRDIES RITMO ANALIZEI IR ANOTACIJAI ILGALAIKĖJE EKG

Kadangi neinvazinių elektrolitų kiekio kraujyje stebėjimo metodų moksliniai tyrimai dar tik pradedami, mokslininkams reikia didelio kiekio ilgalaikių duomenų, kad galėtų ištirti, kaip elektrolitų svyravimai veikia fiziologinius EKG parametrus kasdienėje ambulatorinėje aplinkoje. Deja, dideli ilgalaikių duomenų kiekiai širdies ir kraujagyslių tyrimų procesą papildo dar vienu sudėtingu sluoksniu – juos reikia analizuoti ir anotuoti rankiniu būdu. Rankinis duomenų anotavimas yra varginantis ir užima daug laiko, o monotoniškuose ilgalaikiuose signaluose gali būti praleistos svarbios detalės ir įvykiai. Mašininio mokymosi algoritmai galėtų pagreitinti ilgalaikių EKG tyrimus ir analizę, tačiau taip pat reikalauja didelių anotuotų duomenų rinkinių, o daugeliu atvejų tokių algoritmų kūrimui ir mokymui reikalinga žmogaus priežiūra. Todėl sistema, kurioje automatinių algoritmų privalumai derinami su žmogaus eksperto dėmesiu, o duomenys yra struktūrizuoti taip, kad juos būtų galima efektyviai analizuoti ir anotuoti, galėtų pagreitinti neinvazinės kraujo elektrolitų stebėsenos širdies ir kraujagyslių sistemos mokslinių tyrimų procesą.

5.1. Metodai

Siūlomas simbolinis klasterizavimo algoritmas, kuriuo siekiama padidinti širdies ritmo anotavimo ir analizės efektyvumą ilgalaikėse EKG. Algoritmą sudaro penki etapai, kaip parodyta 5.1 pav. Išsamesnės informacijos galima rasti: [61].

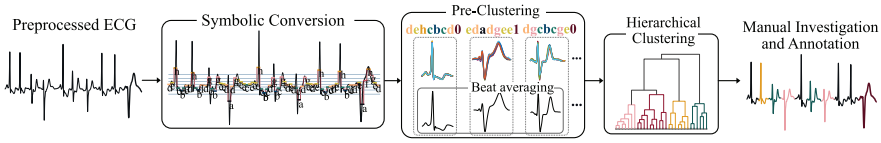

5.1 pav. Simboliniu klasterizavimu pagrįsto metodo, skirto širdies dūžiams anotuoti ilgalaikiuose EKG signaluose, apžvalga

Širdies dūžiai suspaudžiami į trumpas sekas (simbolius) naudojant *simbolinio agregavimo* metodą (SAX) [217] – diskretizavimo metodą, pagal kurį kiekviename laiko intervale sekų vidutinės vertės paverčiamos simboliais. SAX apima dvi dalis: dalinė agreguota aproksimacija (angl. *Piecewise Aggregate Approximation* (PAA)) [217] ir po jos vykstantis simbolių priskyrimas (5.2 pav.).

Kiekviena unikali seka tampa išankstiniu visų šia seka žymimų širdies dūžių klasteriu, todėl sumažėja dūžių, kurie bus klasterizuojami, skaičius. Ši strategija gerokai sumažina klasterizavimo algoritmų skaičiavimo reikalavimus. Kadangi SAX gali apgaubti mažos amplitudės EKG komponentus (pvz., P bangas), prie sekos pridedamas papildomas simbolis, žymintis dviejų kaimyninių dūžių RR informaciją, kad būtų su-

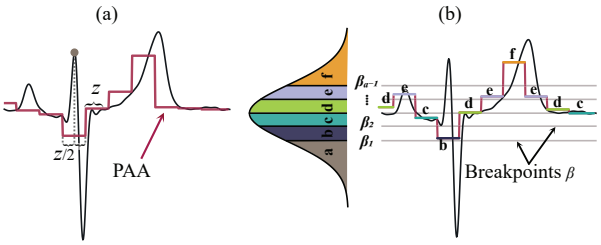

5.2 pav. SAX konversija: (a) PAA transformacija. PAA koeficientai skaičiuojami pradedant nuo $z/2$ mėginių, kurių centras yra R viršūnė; (b) simbolių priskyrimas. PAA koeficientai atvaizduojami pagal lūžio taškus β taip. "***a***" priskiriamas koeficientams, esantiems žemiau β_1; "***b***" – koeficientams, aukščiau β_1 ($\geq \beta_1$), bet žemiau β_2 ($< \beta_2$), ir t. t.

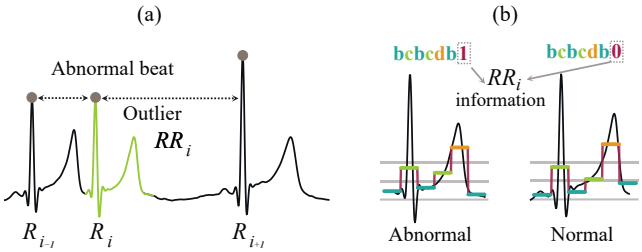

5.3 pav. (a) RR_i nenormalus ritmas (APB). (b) RR_i informacijos pridėjimas, siekiant atskirti APB eilutes nuo normalių ritmų. Kiekvienam ritmui $RR_i = RR_{(i,i-1)}/RR_{(i+1,i)}$. Simbolis "***1***" pridedamas prie ritmų, kurių RR yra nuokrypis, o kitu atveju – "***0***"

mažintos išankstinio klasterizavimo klaidos (5.3 pav.).

Toliau atliekamas hierarchinis kiekvieno išankstinio klasterio signalų vidurkių širdies dūžių klasterizavimas. Taip vietoj kiekvieno atskiro širdies dūžio ekspertui pateikiami hierarchinio klasterizavimo rezultatai, kuriuos jis gali ištirti ir anotuoti rankiniu būdu.

5.2. Rezultatai ir aptarimas

Siūlomo algoritmo efektyvumui ištirti naudojamos dvi atskiros duomenų bazės. Tikslumas tikrinamas „Physionet" *MIT-BIH* duomenų bazėje su 13 rankiniu būdu pažymėtų klasių [190, 218], o veiksmingumas – ambulatoriniuose ilgalaikiuose EKG įrašuose (žr. 3.1 skirsnį).

Svertinio susiejimo derinys su Calinski-Harabasz indeksu parodė geriausius tikslumo (0,91), Fowlkes-Mallows indekso (0,91), Matthews koreliacijos koeficiento (0,37) ir klaidingo klasifikavimo rezultatus (5,6%), kaip rodo 5.4 pav. Algoritmas po SAX klaidingai klasifikavo 0,97 ± 1,51% ritmų ir parodė 26,2% suspaudimo lygį *MIT-BIH* duomenų bazei. Klaidingas klasifikavimas apibrėžiamas kaip ritmų, patekusių į klasterius, kuriuose dominuojanti klasė yra kita, skaičius.

Nors mažos Matthewso koreliacijos koeficiento (MKK) reikšmės paprastai rodo

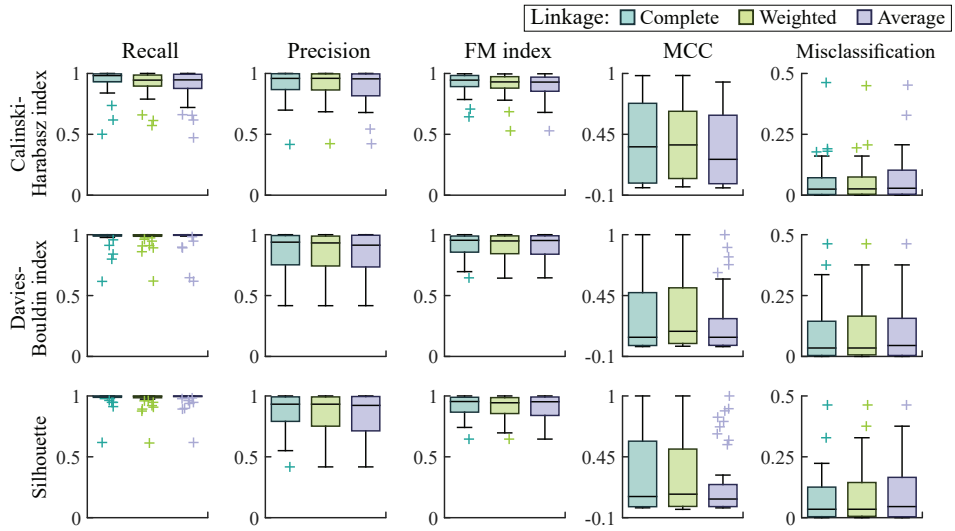

5.4 pav. Siūlomo algoritmo *MIT-BIH* duomenų bazėje gautų efektyvumo rodiklių, naudojant įvairius susiejimo ir vidinio klasterizavimo patvirtinimo indeksus, stačiakampės diagramos

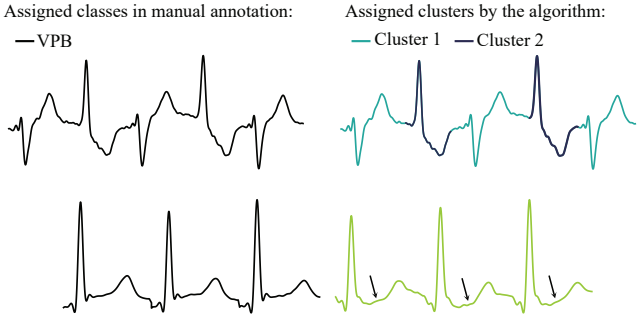

5.5 pav. Klasterizavimo rezultatų pavyzdžiai. Penki dūžiai, pažymėti ta pačia skilvelio priešlaikinių dūžių (VPB) klase iš *MIT-BIH* duomenų bazės, pagal pasiūlytą algoritmą priskiriami dviem skirtingiems klasteriams (viršuje). Tai atvejis, kuris nėra iš esmės nepageidautinas anotuojant rankiniu būdu. Normalūs dviejų skirtingų laikotarpių ritmai su nedideliais ST pokyčiais iš ilgalaikių EKG įrašų (apačioje)

prastus klasterizavimo rezultatus, didelės tikslumo reikšmės rodo, kad taip nėra. Algoritmas suskirstė širdies dūžius, pažymėtus ta pačia klase, bet pasižyminčius skirtingais morfologiniais požymiais, į įvairias grupes (5.5 pav.). Ši savybė nėra iš esmės nepageidautina, nes ji leidžia tyrėjams ištirti, kaip širdies dūžiai natūraliai patenka į kitas klases, ir netgi nustatyti netikėtus poklasius tolesniems tyrimams, o tai gali paspartinti naujų EKG elektrolitų kraujyje žymenų mokslinius tyrimus.

Efektyvumo požiūriu 3 dienas trukusiame EKG tyrime daugiau kaip 480 000 dūžių buvo redukuota į 30 000 unikalių sekų, o vėliau – į 30 klasterių ir anotuota kaip trys klasės ir triukšmas, o skaičiavimams ir anotavimui prireikė mažiau nei vienos valandos.

IŠVADOS

1. Lėtinėmis ligomis sergantiems pacientams būtina reguliariai stebėti elektrolitų kiekį kraujyje, kad būtų užtikrinta jų trumpalaikė ir ilgalaikė sveikata. Sunkūs dielektrolitemijos epizodai gali sukelti gyvybei pavojingas aritmijas, todėl yra pavojingi trumpuoju laikotarpiu, o lengvi, tačiau pasikartojantys epizodai gali turėti ilgalaikį žalingą poveikį. Nepaisant to, kad tokie lengvi ir pasikartojantys epizodai nekelia tiesioginės grėsmės pacientams, jie gali pabloginti širdies ir inkstų funkcijas, o tai pagreitina ligos progresavimą ir kelia pavojų ilgalaikei sveikatai. Šie epizodai dažniausiai atsiranda dėl neoptimalių standartinių vaistų, skirtų lėtinėms ligoms gydyti, pavyzdžiui, antihipertenzinių vaistų, dozių. Todėl, laiku nustačius ir ištaisius dielektrolitemiją, kurią galima nustatyti reguliariai stebint elektrolitų kiekį kraujyje, būtų galima išvengti pavojingų aritmijų ir padėti gydytojams titruoti gyvybę gelbstinčius vaistus homeostazei palaikyti ir bendrai ilgalaikei sveikatai stiprinti.

2. Ambulatorinis elektrolitų kiekio kraujyje stebėjimas naudojant vienos derivacijos EKG yra įmanomas HD pacientams, sergantiems gretutinėmis širdies ligomis. Du T bangos morfologijos deskriptoriai, θ_δ ir T_{SA}, reagavo į laipsniškus kalio svyravimus per ilgą tarpdializinį intervalą ir yra vidutiniškai susiję su [K^+] pokyčiais (koreliacijos koeficientai atitinkamai $r = -0,56$ ir $r = -0,57$). θ_δ ir T_{SA} taip pat reagavo į kalį mažinančius vaistus ir insulino šuolius po valgio, kurie skatina K^+ ląstelėse. θ_δ paros kintamumas panašus į sveikų žmonių cirkadinį kraujo [K^+] kintamumą. Palyginti su T_{SA}, pasiūlytam modeliu pagrįstam deskriptoriui θ_δ mažiau įtakos turi judesių sukeltas triukšmas, todėl jį geriau naudoti ambulatorinėse programose. Nepaisant to, abiejų deskriptorių veikimą gali paveikti tokie klaidinantys veiksniai, kaip kartu vykstantis elektrolitų, ypač kalcio ir bikarbonatų, disbalansas ir kintanti T bangų morfologija.

3. Gilaus mokymosi modelis gali patikimai įvertinti erdvinį QRS-T kampą α iš sumažinto EKG derivacijų skaičiaus $\{I, II, aVF, V2\}$, o absoliučios vidutinės ir vidutinės paklaidos yra 11.4° ir 7.3°. Modelis įvertina QRS ir T vektorių 3D koordinates (išvestis), reikalingas α kampui apskaičiuoti iš kiekvienos derivacijos signalų vidurkių (įvestis), esančių $\{I, II, aVF, V2\}$ poaibyje. Šį poaibį galima užregistruoti paprastai konfigūruojamuose vartotojų sveikatos priežiūros prietaisuose, kurių jau yra rinkoje. Modeliui išmokyti buvo pasiūlyta originali sudėtinė nuostolių funkcija, kurioje naudojamas kampas ir 3D Euklido atstumas tarp vektorių, kad jis įvertintų α net tada, kai įvesties EKG derivacijos teikia ribotą erdvinę informaciją. Modelio struktūra yra nesudėtinga, kad ją būtų galima įdiegti vartotojų sveikatos priežiūros prietaisuose. Tai perspektyvus sprendimas QRS-T kampą stebėti ambulatoriškai ir tirti jo sąsajas su elektrolitų kiekiu kraujyje.

4. Siūlomas simbolinis klasterizavimo algoritmas gali padidinti širdies dūžių anotavimo ir analizės efektyvumą ilgalaikėse EKG. Širdies dūžius suspaudus į trumpas

sekas (simbolius), juos galima grupuoti į vienodų simbolių klasterius ir taip sumažinti skaičiavimo reikalavimus hierarchiniam klasterizavimui. Pavyzdžiui, 3 dienų trukmės EKG daugiau kaip 480 000 dūžių buvo suglaudinta iki 30 000 unikalių sekų, o šios – iki 30 klasterių, kuriuos tyrėjai gali patogiai analizuoti ir anotuoti. Ši savybė leidžia tyrėjams ištirti, kaip širdies dūžiai natūraliai patenka į skirtingas klases, ir netgi nustatyti netikėtus poklasius tolesniems tyrimams.

REFERENCES

[1] WANG, S. and QIN, L. Homeostatic medicine: a strategy for exploring health and disease. *Current Medicine*. 2022, 1(1).

[2] HALL, J. E. and HALL, M. E. *Guyton and Hall textbook of medical physiology*. 14th ed. ser. Guyton Physiology. Elsevier, 2020.

[3] TAZMINI, K. and RANHOFF, A. H. Electrolyte outpatient clinic at a local hospital - experience from diagnostics, treatment and follow-up. *BMC Health Serv. Res.* 2020, 20(1), 154.

[4] TAZMINI, K., NYMO, S. H., LOUCH, W. E., RANHOFF, A. H., and ØIE, E. Electrolyte imbalances in an unselected population in an emergency department: A retrospective cohort study. *PLoS One*. 2019, 14(4), e0215673.

[5] LIAMIS, G., RODENBURG, E. M., HOFMAN, A., ZIETSE, R., STRICKER, B. H., and HOORN, E. J. Electrolyte disorders in community subjects: prevalence and risk factors. *Am. J. Med.* 2013, 126(3), 256–263.

[6] XIONG, J., HE, T., WANG, M., NIE, L., ZHANG, Y. *et al.* Serum magnesium, mortality, and cardiovascular disease in chronic kidney disease and end-stage renal disease patients: a systematic review and meta-analysis. *J. Nephrol.* 2019, 32(5), 791–802.

[7] EL-SHERIF, N. and TURITTO, G. Electrolyte disorders and arrhythmogenesis. *Cardiology Journal*. 2011, 18(3), 13.

[8] AL-KHATIB, S. M., STEVENSON, W. G., ACKERMAN, M. J., BRYANT, W. J., CALLANS, D. J. *et al.* 2017 AHA/ACC/HRS guideline for management of patients with ventricular arrhythmias and the prevention of sudden cardiac death. *Journal of the American College of Cardiology*. 2018, 72(14), e91–e220.

[9] GENOVESI, S., BORIANI, G., COVIC, A., VERNOOIJ, R. W. M., COMBE, C. *et al.* Sudden cardiac death in dialysis patients: different causes and management strategies. *Nephrology Dialysis Transplantation*. 2019.

[10] TURAKHIA, M. P., BLANKESTIJN, P. J., CARRERO, J.-J., CLASE, C. M., DEO, R. *et al.* Chronic kidney disease and arrhythmias: conclusions from a Kidney Disease: Improving Global Outcomes (KDIGO) Controversies Conference. *European Heart Journal*. 2018, 39(24), 2314–2325.

[11] WEISS-GUILLET, E.-M., TAKALA, J., and JAKOB, S. M. Diagnosis and management of electrolyte emergencies. *Best Practice & Research Clinical Endocrinology & Metabolism*. 2003, 17(4), 623–651.

[12] DHONDUP, T. and QIAN, Q. Acid-base and electrolyte disorders in patients with and without chronic kidney disease: An update. *Kidney Dis. (Basel)*. 2017, 3(4), 136–148.

[13] MEHMOOD, H. R., KHAN, Z., JAHANGIR, H. M. S., HUSSAIN, A., ELAHI, A., and ASKARI, S. M. H. Assessment of serum biochemical derangements and associated risk factors of chronic kidney disease. *Journal of Taibah University Medical Sciences*. 2022, 17(3), 376–383.

[14] LIAMIS, G., MILIONIS, H., and ELISAF, M. Blood pressure drug therapy and electrolyte disturbances. *Int. J. Clin. Pract.* 2008, 62(10), 1572–1580.

[15] ROSE, B. D. and POST, T. *Clinical physiology of acid-base and electrolyte disorders*. 5th ed. New York, NY: McGraw-Hill Medical, 2000.

[16] BRASS, E. P. and THOMPSON, W. L. Drug-induced electrolyte abnormalities. *Drugs*. 1982, 24(3), 207–228.

[17] FALHAMMAR, H., SKOV, J., CALISSENDORFF, J., NATHANSON, D., LINDH, J. D., and MANNHEIMER, B. Associations between antihypertensive medications and severe hyponatremia: A swedish population-based case-control study. *J. Clin. Endocrinol. Metab.* 2020, 105(10), e3696–e3705.

[18] KARDALAS, E., PASCHOU, S. A., ANAGNOSTIS, P., MUSCOGIURI, G., SIASOS, G., and VRYONIDOU, A. Hypokalemia: a clinical update. *Endocr. Connect.* 2018, 7(4), R135–R146.

[19] UNWIN, R. J., LUFT, F. C., and SHIRLEY, D. G. Pathophysiology and management of hypokalemia: a clinical perspective. *Nat. Rev. Nephrol.* 2011, 7(2), 75–84.

[20] ELIACIK, E., YILDIRIM, T., SAHIN, U., KIZILARSLANOGLU, C., TAPAN, U. *et al.* Potassium abnormalities in current clinical practice: frequency, causes, severity and management. *Med. Princ. Pract.* 2015, 24(3), 271–275.

[21] KLEIN, L., O'CONNOR, C. M., LEIMBERGER, J. D., GATTIS-STOUGH, W., PIÑA, I. L. *et al.* Lower serum sodium is associated with increased short-term mortality in hospitalized patients with worsening heart failure: results from the outcomes of a prospective trial of intravenous milrinone for exacerbations of chronic heart failure (OPTIME-CHF) study. *Circulation*. 2005, 111(19), 2454–2460.

[22] KROGAGER, M. L., EGGERS-KAAS, L., AASBJERG, K., MORTENSEN, R. N., KØBER, L. *et al.* Short-term mortality risk of serum potassium levels in

acute heart failure following myocardial infarction. *Eur. Heart J. Cardiovasc. Pharmacother.* 2015, 1(4), 245–251.

[23] THONGPRAYOON, C., CHEUNGPASITPORN, W., THIRUNAVUKKARASU, S., PETNAK, T., CHEWCHARAT, A. *et al.* Serum potassium levels at hospital discharge and one-year mortality among hospitalized patients. *Medicina (Kaunas)*. 2020, 56(5), 236.

[24] RONCO, C., BELLASI, A., and DI LULLO, L. Cardiorenal syndrome: An overview. *Adv. Chronic Kidney Dis.* 2018, 25(5), 382–390.

[25] ROSSIGNOL, P., COATS, A. J., CHIONCEL, O., SPOLETINI, I., and ROSANO, G. Renal function, electrolytes, and congestion monitoring in heart failure. *European Heart Journal Supplements*. 2019, 21(Supplement_M), M25–M31.

[26] URSO, C., BRUCCULERI, S., and CAIMI, G. Acid-base and electrolyte abnormalities in heart failure: pathophysiology and implications. *Heart Fail. Rev.* 2015, 20(4), 493–503.

[27] KOVESDY, C. P. Epidemiology of chronic kidney disease: an update 2022. *Kidney International Supplements*. 2022, 12(1), 7–11.

[28] NCD RISK FACTOR COLLABORATION (NCD-RISC). Worldwide trends in hypertension prevalence and progress in treatment and control from 1990 to 2019: a pooled analysis of 1201 population-representative studies with 104 million participants. *Lancet*. 2021, 398(10304), 957–980.

[29] EINARSON, T. R., ACS, A., LUDWIG, C., and PANTON, U. H. Prevalence of cardiovascular disease in type 2 diabetes: a systematic literature review of scientific evidence from across the world in 2007-2017. *Cardiovasc. Diabetol.* 2018, 17(1), 83.

[30] NAHA, S., GARDNER, M. J., KHANGURA, D., KURUKULASURIYA, L. R., and SOWERS, J. R. *Hypertension in Diabetes*. MDText.com, Inc., 2021. [Online]. Available: https://www.ncbi.nlm.nih.gov/books/NBK279027/

[31] Heart disease prevalence, health, united states, 2020–2021, 2022. [Online]. Available: https://www.cdc.gov/nchs/hus/topics/heart-disease-prevalence.htm

[32] HINTON, W., MCGOVERN, A., COYLE, R., HAN, T. S., SHARMA, P. *et al.* Incidence and prevalence of cardiovascular disease in english primary care: a cross-sectional and follow-up study of the royal college of general practitioners (RCGP) research and surveillance centre (RSC). *BMJ Open*. 2018, 8(8), e020282.

[33] CORONADO, F., MELVIN, S. C., BELL, R. A., and ZHAO, G. Global responses to prevent, manage, and control cardiovascular diseases. *Prev. Chronic Dis.* 2022, 19(220347), E84.

[34] LUYCKX, V. A., TONELLI, M., and STANIFER, J. W. The global burden of kidney disease and the sustainable development goals. *Bulletin of the World Health Organization*. 2018, 96(6), 414–422D.

[35] BETTS, K. A., WOOLLEY, J. M., MU, F., XIANG, C., TANG, W., and WU, E. Q. The cost of hyperkalemia in the united states. *Kidney Int. Rep.* 2018, 3(2), 385–393.

[36] ZORNIC, N., RADOJEVIC, D. J., JANKOVIC, S., DJURIC, D., VARJACIC, M. *et al.* Monitoring of drug-associated electrolyte disturbances in a hospital. *Pharmacoepidemiol. Drug Saf.* 2009, 18(11), 1026–1033.

[37] OKSEN, D., PETRUSKI-IVLEVA, N., EAPEN, S., ISAMAN, D., LEWIS, K., and EVERS, T. Healthcare resource utilization and costs associated with abnormal potassium levels among us patients with systolic and diastolic heart failure: A population-based cohort study. *Value Health*. 2019, 22, S126.

[38] BOSCOE, A., PARAMORE, C., and VERBALIS, J. G. Cost of illness of hyponatremia in the united states. *Cost Eff. Resour. Alloc.* 2006, 4(1), 10.

[39] KOOMAN, J. P., WIERINGA, F. P., HAN, M., CHAUDHURI, S., VAN DER SANDE, F. M. *et al.* Wearable health devices and personal area networks: can they improve outcomes in haemodialysis patients? *Nephrology Dialysis Transplantation*. 2020, 35(Supplement_2), 1143–1150.

[40] PICKENHAN, L., RUNGG, C., and SCHIEFERMEIER-MACH, N. Electrolyte imbalances in nursing home residents: A review of prevalence, management and considerations. *J. Nurs. Home Res. Sci.* 2020.

[41] BETTS, K. A., SONG, J., FAUST, E., YANG, K., DU, Y. *et al.* Medical costs for managing chronic kidney disease and related complications in patients with chronic kidney disease and type 2 diabetes. *Am. J. Manag. Care*. 2021, 27(20 Suppl), S369–S374.

[42] SURAWICZ, B. Relationship between electrocardiogram and electrolytes. *American Heart Journal*. 1967, 73(6), 814–834.

[43] CORSI, C., CORTESI, M., CALLISESI, G., DE BIE, J., NAPOLITANO, C. *et al.* Noninvasive quantification of blood potassium concentration from ECG in hemodialysis patients. *Sci Rep*. 2017, 7(1).

[44] DILLON, J. J., DESIMONE, C. V., SAPIR, Y., SOMERS, V. K., DUGAN, J. L. *et al.* Noninvasive potassium determination using a mathematically processed ECG: Proof of concept for a novel "blood-less, blood test". *Journal of Electrocardiology*. 2015, 48(1), 12–18.

[45] ATTIA, Z. I., DESIMONE, C. V., DILLON, J. J., SAPIR, Y., SOMERS, V. K. *et al.* Novel bloodless potassium determination using a signal-processed single-lead ECG. *Journal of the American Heart Association*. 2016, 5(1).

[46] SURAWICZ, B., CHLEBUS, H., and MAZZOLENI, A. Hemodynamic and electrocardiographic effects of hyperpotassemia. differences in response to slow and rapid increases in concentration of plasma k. *American Heart Journal*. 1967, 73(5), 647–664.

[47] WEISBERG, L. S. Management of severe hyperkalemia. *Critical Care Medicine*. 2008, 36(12), 3246–3251.

[48] ARTEYEVA, N. V. Dispersion of ventricular repolarization: Temporal and spatial. *World Journal of Cardiology*. 2020, 12(9), 437–449.

[49] SKAMPARDONI, S., GREEN, D., HNATKOVA, K., MALIK, M., KALRA, P. A., and POULIKAKOS, D. QRS-t angle predicts cardiac risk and correlates with global longitudinal strain in prevalent hemodialysis patients. *Frontiers in Physiology*. 2019, 10.

[50] ZHANG, X., ZHU, Q., ZHU, L., JIANG, H., XIE, J. *et al.* Spatial/Frontal QRS-T Angle Predicts All-Cause Mortality and Cardiac Mortality: A Meta-Analysis. *PloS one*. 2015, 10(8). [Online]. Available: https://pubmed.ncbi.nlm.nih.gov/26284799/

[51] PALMIERI, F., GOMIS, P., RUIZ, J. E., FERREIRA, D., MARTÍN-YEBRA, A. *et al.* ECG-based monitoring of blood potassium concentration: Periodic versus principal component as lead transformation for biomarker robustness. *Biomedical Signal Processing and Control*. 2021, 68, 102719.

[52] PALMIERI, F., GOMIS, P., FERREIRA, D., RUIZ, J. E., BERGASA, B. *et al.* Monitoring blood potassium concentration in hemodialysis patients by quantifying t-wave morphology dynamics. *Scientific Reports*. 2021, 11(1).

[53] BUKHARI, H. A., PALMIERI, F., RAMÍREZ, J., LAGUNA, P., RUIZ, J. E. *et al.* Characterization of t wave amplitude, duration and morphology changes during hemodialysis: Relationship with serum electrolyte levels and heart rate. *IEEE Transactions on Biomedical Engineering*. 2021, 68(8), 2467–2478.

[54] GALLOWAY, C. D., VALYS, A. V., SHREIBATI, J. B., TREIMAN, D. L., PETTERSON, F. L. *et al.* Development and validation of a deep-learning model to screen for hyperkalemia from the electrocardiogram. *JAMA Cardiol.* 2019, 4(5), 428–436.

[55] LIN, C., CHAU, T., LIN, C.-S., SHANG, H.-S., FANG, W.-H. *et al.* Point-of-care artificial intelligence-enabled ECG for dyskalemia: a retrospective cohort analysis for accuracy and outcome prediction. *NPJ Digit. Med.* 2022, 5(1), 8.

[56] KWON, J.-M., JUNG, M.-S., KIM, K.-H., JO, Y.-Y., SHIN, J.-H. *et al.* Artificial intelligence for detecting electrolyte imbalance using electrocardiography. *Ann. Noninvasive Electrocardiol.* 2021, 26(3), e12839.

[57] OEHLER, A., FELDMAN, T., HENRIKSON, C. A., and TERESHCHENKO, L. G. QRS-T Angle: A Review. *Annals of Noninvasive Electrocardiology*. 2014, 19(6), 534–542.

[58] RODRIGUES, A., PETRĖNAS, A., KUŠLEIKAITĖ-PERE, N., LAGUNA, P., and MAROZAS, V. ECG-based monitoring of electrolyte fluctuations during the long interdialytic interval. In *2018 Computing in Cardiology Conference (CinC)*. Computing in Cardiology, 2018.

[59] RODRIGUES, A. S., PETRĖNAS, A., PALIAKAITĖ, B., KUŠLEIKAITĖ-PERE, N., JARUŠEVIČIUS, G. *et al.* Noninvasive monitoring of potassium fluctuations during the long interdialytic interval. *IEEE Access*. 2020, 8, 188 488–188 502.

[60] RODRIGUES, A. S., AUGUSTAUSKAS, R., LUKOŠEVIČIUS, M., LAGUNA, P., and MAROZAS, V. Deep-learning-based estimation of the spatial QRS-t angle from reduced-lead ECGs. *Sensors*. 2022, 22(14), 5414.

[61] RODRIGUES, A. S., LUKOŠEVIČIUS, M., and MAROZAS, V. A fast algorithm for facilitating heartbeat annotation in long-term ecg signals. In *2021 Computing in Cardiology (CinC)*. 2021, 48, 1–4.

[62] KUSUMOTO, F. *ECG interpretation: From Pathophysiology to Clinical Application*. 2nd ed. Cham, Switzerland: Springer International Publishing, 2020.

[63] PINNELL, J., TURNER, S., and HOWELL, S. Cardiac muscle physiology. *Contin. Educ. Anaesth. Crit. Care Pain*. 2007, 7(3), 85–88.

[64] Part 10.1: Life-threatening electrolyte abnormalities. *Circulation*. 2005, 112(24_supplement), IV–121–IV–125.

[65] ON DIET, N. R. C. U. C. and HEALTH. *Diet and Health: Implications for Reducing Chronic Disease Risk*. Washington (DC): National Academies Press (US), 1989. https://www.ncbi.nlm.nih.gov/books/NBK218735(visited 2022-11-21).

[66] GREGER, R. F. Physiology and pathophysiology of calcium homeostasis. *Z. Kardiol.* 2000, 89(14), S004–S008.

[67] REILLY, R. F. and PERAZELLA, M. A. *Nephrology in 30 Days (In Thirty Days Series)*. 2nd ed. McGraw-Hill Education / Medical, 2013.

[68] SINGH, A. K. and WILLIAMS, G. H. *Textbook of Nephro-Endocrinology*. 2017.

[69] FOUNTAIN, J. H. and LAPPIN, S. L. *Physiology, Renin Angiotensin System*. [INTERNET], S., Ed. Treasure Island (FL): StatPearls Publishing, 2022. [Updated 2022 Jun 18]. [Online]. Available: https://www.ncbi.nlm.nih.gov/books/NBK470410/?report=classic

[70] OCSÉNYI, Z., TULASSAY, T., MILTÉNYI, M., and SZABÓ, A. Effects of insulin on renal electrolyte handling. *Child Nephrol. Urol.* 1988, 9(1-2), 16–20.

[71] PALMER, B. F. and CLEGG, D. J. Physiology and pathophysiology of potassium homeostasis. *Adv. Physiol. Educ.* 2016, 40(4), 480–490.

[72] SATA, Y., HEAD, G. A., DENTON, K., MAY, C. N., and SCHLAICH, M. P. Role of the sympathetic nervous system and its modulation in renal hypertension. *Frontiers in Medicine*. 2018, 5.

[73] BLAINE, J., CHONCHOL, M., and LEVI, M. Renal control of calcium, phosphate, and magnesium homeostasis. *Clinical Journal of the American Society of Nephrology*. 2015, 10(7), 1257–1272.

[74] LE, T. and BHUSHAN, V. *First aid for the USMLE step 1 2017*. 27th ed. McGraw-Hill Education/Medical, 2017.

[75] SWAMINATHAN, R. Magnesium metabolism and its disorders. *Clin. Biochem. Rev.* 2003, 24(2), 47–66.

[76] BUCKLEY, M. S., LEBLANC, J. M., and CAWLEY, M. J. Electrolyte disturbances associated with commonly prescribed medications in the intensive care unit. *Crit. Care Med.* 2010, 38(6 Suppl), S253–64.

[77] DHONDUP, T. and QIAN, Q. Electrolyte and acid-base disorders in chronic kidney disease and end-stage kidney failure. *Blood Purification*. 2017, 43(1-3), 179–188.

[78] MEHLER, P. S. and WALSH, K. Electrolyte and acid-base abnormalities associated with purging behaviors. *Int. J. Eat. Disord.* 2016, 49(3), 311–318.

[79] QIAN, Q. Acid-base alterations in ESRD and effects of hemodialysis. *Seminars in Dialysis*. 2017, 31(3), 226–235.

[80] PALMER, B. F. and CLEGG, D. J. Electrolyte and acid-base disturbances in patients with diabetes mellitus. *N. Engl. J. Med.* 2015, 373(6), 548–559.

[81] LIAMIS, G., FILIPPATOS, T. D., and ELISAF, M. S. Electrolyte disorders associated with the use of anticancer drugs. *European Journal of Pharmacology*. 2016, 777, 78–87.

[82] LI, Y., CHEN, X., SHEN, Z., WANG, Y., HU, J. *et al.* Electrolyte and acid-base disorders in cancer patients and its impact on clinical outcomes: evidence from a real-world study in china. *Renal Failure*. 2020, 42(1), 234–243.

[83] GIORDANO, M., CIARAMBINO, T., CASTELLINO, P., MALATINO, L., SOMMA, S. D. *et al.* Diseases associated with electrolyte imbalance in the ED: age-related differences. *The American Journal of Emergency Medicine*. 2016, 34(10), 1923–1926.

[84] ARZHAN, S., ROUMELIOTI, M.-E., LITVINOVICH, I., BOLOGA, C. G., MYERS, O. B., and UNRUH, M. L. Hypernatremia in hospitalized patients: A large population-based study. *Kidney360*. 2022, 3(7), 1144–1157.

[85] D, G., D, M., DM, Q., and P, R. Hypokalemia in outpatients with eating disorders. *American Journal of Psychiatry*. 1995, 152(1), 60–63.

[86] LINDNER, G., BURDMANN, E. A., CLASE, C. M., HEMMELGARN, B. R., HERZOG, C. A. *et al.* Acute hyperkalemia in the emergency department: a summary from a kidney disease: Improving global outcomes conference. *European Journal of Emergency Medicine*. 2020, 27(5), 329–337.

[87] VIKRANT, S. and PARASHAR, A. Prevalence and severity of disordered mineral metabolism in patients with chronic kidney disease: A study from a tertiary care hospital in india. *Indian Journal of Endocrinology and Metabolism*. 2016, 20(4), 460.

[88] A, V., C, A., and P, M. *Malignancy-Related Hypercalcemia*. StatPearls Publishing, 2022. [Online]. Available: https://www.ncbi.nlm.nih.gov/books/NBK482423/

[89] BOWMAN, B. T. Electrolyte disorders associated with cancer. *Journal of Onco-Nephrology*. 2017, 1(1), 30–35.

[90] AHMED, F. and MOHAMMED, A. Magnesium: The forgotten electrolyte—a review on hypomagnesemia. *Medical Sciences*. 2019, 7(4), 56.

[91] TOTO, R. D. Serum potassium and cardiovascular outcomes: The highs and the lows. *Clinical Journal of the American Society of Nephrology*. 2017, 12(2), 220–221.

[92] WONG, M. C., KALMAN, J. M., PEDAGOGOS, E., TOUSSAINT, N., VOHRA, J. K. *et al.* Temporal distribution of arrhythmic events in chronic kidney disease: Highest incidence in the long interdialytic period. *Heart Rhythm*. 2015, 12(10), 2047–2055.

[93] KORGAONKAR, S., TILEA, A., GILLESPIE, B. W., KISER, M., EISELE, G. *et al.* Serum potassium and outcomes in CKD. *Clinical Journal of the American Society of Nephrology*. 2010, 5(5), 762–769.

[94] KROGAGER, M. L., TORP-PEDERSEN, C., MORTENSEN, R. N., KØBER, L., GISLASON, G. *et al.* Short-term mortality risk of serum potassium levels in hypertension: a retrospective analysis of nationwide registry data. *European Heart Journal*. 2016, ehw129.

[95] WANG, A. Y.-M. Optimally managing hyperkalemia in patients with cardiorenal syndrome. *Nephrology Dialysis Transplantation*. 2019, 34(Supplement_3), iii36–iii44.

[96] WINTER, W. E. and HARRIS, N. S., Disorders of calcium metabolism, In *Handbook of Diagnostic Endocrinology*. Elsevier, 2021, 309–388.

[97] CHOU, C.-W., FANG, W.-H., CHEN, Y.-Y., WANG, C.-C., KAO, T.-W. *et al.* Association between serum calcium and risk of cardiometabolic disease among community-dwelling adults in taiwan. *Scientific Reports*. 2020, 10(1). [Online]. Available: https://doi.org/10.1038/s41598-020-60209-w

[98] LARSSON, S. C., DRCA, N., and MICHAËLSSON, K. Serum magnesium and calcium levels and risk of atrial fibrillation. *Circulation: Genomic and Precision Medicine*. 2019, 12(1).

[99] MICKE, O., VORMANN, J., KRAUS, A., and KISTERS, K. Serum magnesium: time for a standardized and evidence-based reference range. *Magnes. Res.* 2021, 34(2), 84–89.

[100] IAIZZO, P. A., Ed. *Handbook of cardiac anatomy, physiology, and devices*. 3rd ed. Cham, Switzerland: Springer International Publishing, 2015.

[101] ANDERSON, R. H., YANNI, J., BOYETT, M. R., CHANDLER, N. J., and DOBRZYNSKI, H. The anatomy of the cardiac conduction system. *Clin. Anat.* 2009, 22(1), 99–113.

[102] AMIN, A. S., TAN, H. L., and WILDE, A. A. M. Cardiac ion channels in health and disease. *Heart Rhythm*. 2010, 7(1), 117–126.

[103] KLABUNDE, R. E. *Cardiovascular Physiology Concepts*. 3rd ed. ser. Lippincott Connect. Baltimore, MD: Wolters Kluwer Health, 2021.

[104] SORNMO, L. and LAGUNA, P. *Bioelectrical signal processing in cardiac and neurological applications*. ser. Biomedical Engineering. San Diego, CA: Academic Press, 2005.

[105] MAN, S., MAAN, A. C., SCHALIJ, M. J., and SWENNE, C. A. Vectorcardiographic diagnostic & prognostic information derived from the 12-lead electrocardiogram: Historical review and clinical perspective. *J. Electrocardiol.* 2015, 48(4), 463–475.

[106] KASHOU, A. H., LOCOCO, S., ASIRVATHAM, S. J., MAY, A. M., and NOSEWORTHY, P. A. A lateral lead variant of the de winter pattern due to left main stenosis and left anterior descending artery occlusion. *Journal of Electrocardiology*. 2020, 61, 77–80.

[107] FRANK, E. An accurate, clinically practical system for spatial vectorcardiography. *Circulation*. 1956, 13(5), 737–749.

[108] JAROS, R., MARTINEK, R., and DANYS, L. Comparison of different electrocardiography with vectorcardiography transformations. *Sensors*. 2019, 19(14), 3072.

[109] KORS, J. A., VAN HERPEN, G., SITTIG, A. C., and VAN BEMMEL, J. H. Reconstruction of the frank vectorcardiogram from standard electrocardiographic leads: diagnostic comparison of different methods. *Eur. Heart J.* 1990, 11(12), 1083–1092.

[110] MORRIS, F., ELDHOUSE, J., BRADY, W. J., and CAMM, A. J. *ABC of Clinical Electrocardiography*. ELECTRONIC PRODUCTION, B., Ed. London: BMJ Books, 2003.

[111] KASS, R. S. and TSIEN, R. W. Control of action potential duration by calcium ions in cardiac purkinje fibers. *Journal of General Physiology*. 1976, 67(5), 599–617.

[112] CHORIN, E., ROSSO, R., and VISKIN, S. Electrocardiographic manifestations of calcium abnormalities. *Annals of Noninvasive Electrocardiology*. 2015, 21(1), 7–9.

[113] YANG, Y., CHEN, C., DUAN, P., THAPALIYA, S., GAO, L. *et al.* The ECG characteristics of patients with isolated hypomagnesemia. *Frontiers in Physiology*. 2021, 11.

[114] EFSTRATIADIS, G., SARIGIANNI, M., and GOUGOURELAS, I. Hypomagnesemia and cardiovascular system. *Hippokratia*. 2006, 10(4), 147–152.

[115] HINKLE, C. Electrolyte disorders in the cardiac patient. *Critical Care Nursing Clinics of North America*. 2011, 23(4), 635–643.

[116] NOORDAM, R., YOUNG, W. J., SALMAN, R., KANTERS, J. K., VAN DEN BERG, M. E. *et al.* Effects of calcium, magnesium, and potassium concentrations on ventricular repolarization in unselected individuals. *Journal of the American College of Cardiology*. 2019, 73(24), 3118–3131.

[117] DREYFUSS, D., JONDEAU, G., COUTURIER, R., RAHMANI, J., ASSAYAG, P., and COSTE, F. Tall T waves during metabolic acidosis without hyperkalemia. *Critical Care Medicine*. 1989, 17(5), 404–408.

[118] GLASS, G. F., SUDHIR, A., and PANDIT, A. A. K., The ECG and metabolic abnormalities, 307–313, 2020.

[119] SALAMEH, A., ZÖBISCH, H., SCHRÖDER, B., VIGELAHN, J., JAHN, M. *et al.* Effects of hypoxia and acidosis on cardiac electrophysiology and hemodynamics. is NHE-inhibition by cariporide still advantageous? *Frontiers in Physiology*. 2020, 11.

[120] DU, C. Y., ADENIRAN, I., CHENG, H., ZHANG, Y. H., HARCHI, A. E. *et al.* Acidosis impairs the protective role of hERG k+ channels against premature stimulation. *Journal of Cardiovascular Electrophysiology*. 2010, 21(10), 1160–1169.

[121] CHENG, H., SMITH, G. L., ORCHARD, C. H., and HANCOX, J. C. Acidosis inhibits spontaneous activity and membrane currents in myocytes isolated from the rabbit atrioventricular node. *Journal of Molecular and Cellular Cardiology*. 2009, 46(1), 75–85.

[122] PILIA, N., SEVERI, S., RAIMANN, J. G., GENOVESI, S., DÖSSEL, O. *et al.* Quantification and classification of potassium and calcium disorders with the electrocardiogram: What do clinical studies, modeling, and reconstruction tell us? *APL Bioengineering*. 2020, 4(4), 041501.

[123] WRENN, K. D., SLOVIS, C. M., and SLOVIS, B. S. The ability of physicians to predict hyperkalemia from the ecg. *Annals of Emergency Medicine*. 1991, 20(11), 1229–1232.

[124] MONTAGUE, B. T., OUELLETTE, J. R., and BULLER, G. K. Retrospective Review of the Frequency of ECG Changes in Hyperkalemia. *Clinical Journal American Society of Nephrology*. 2008, 3(2), 324–330.

[125] DURFEY, N., LEHNHOF, B., BERGESON, A., DURFEY, S., LEYTIN, V. *et al.* Severe hyperkalemia: Can the electrocardiogram risk stratify for short-term adverse events? *Western Journal of Emergency Medicine*. 2017, 18(5), 963–971.

[126] GENOVESI, S., BRACCHI, O., FABBRINI, P., LUISETTO, E., VIGANO, M. R. *et al.* Differences in heart rate variability during haemodialysis and haemofiltration. *Nephrology Dialysis Transplantation*. 2007, 22(8), 2256–2262.

[127] CUPISTI, A., GALETTA, F., CAPRIOLI, R., MORELLI, E., TINTORI, G. C. *et al.* Potassium removal increases the QTc interval dispersion during hemodialysis. *Nephron*. 1999, 82(2), 122–126.

[128] FROHNERT, P. P., GLULIANI, E. R., FRIEDBERG, M., JOHNSON, W. J., and TAUXE, W. N. Statistical investigation of correlations between serum potassium levels and electrocardiographic findings in patients on intermittent hemodialysis therapy. *Circulation*. 1970, 41(4), 667–676.

[129] SEVERI, S., CORSI, C., HAIGNEY, M., DEBIE, J., and MORTARA, D. Non-invasive potassium measurements from ecg analysis during hemodialysis sessions. In *2009 36th Annual Computers in Cardiology Conference (CinC)*. 2009, 821–824.

[130] CORSI, C., BIE, J. D., MORTARA, D., and SEVERI, S., Innovative solutions in health monitoring at home: The real-time assessment of serum potassium

concentration from ECG, In *Impact Analysis of Solutions for Chronic Disease Prevention and Management*. Springer Berlin Heidelberg, 2012, 116–123.

[131] YASIN, O. Z., ATTIA, Z., DILLON, J. J., DESIMONE, C. V., SAPIR, Y. *et al.* Noninvasive blood potassium measurement using signal-processed, single-lead ecg acquired from a handheld smartphone. *Journal of Electrocardiology*. 2017, 50(5), 620–625.

[132] VELAGAPUDI, V., O'HORO, J. C., VELLANKI, A., BAKER, S. P., PIDIKITI, R. *et al.* Computer-assisted image processing 12 lead ECG model to diagnose hyperkalemia. *Journal of Electrocardiology*. 2017, 50(1), 131–138.

[133] KROGAGER, M. L., KRAGHOLM, K., SKALS, R. K., MORTENSEN, R. N., POLCWIARTEK, C. *et al.* The relationship between serum potassium concentrations and electrocardiographic characteristics in 163, 547 individuals from primary care. *Journal of Electrocardiology*. 2019, 57, 104–111.

[134] PALMIERI, F., GOMIS, P., RUIZ, J. E., BERGASA, B., DINA, F. *et al.* T-wave morphology changes as surrogate for blood potassium concentration in hemodialysis patients. In *2019 Computing in Cardiology Conference (CinC)*. Computing in Cardiology, 2019.

[135] RAMÍREZ, J., ORINI, M., TUCKER, J. D., PUEYO, E., and LAGUNA, P. Variability of ventricular repolarization dispersion quantified by time-warping the morphology of the t-waves. *IEEE Transactions on Biomedical Engineering*. 2017, 64(7), 1619–1630.

[136] PALMIERI, F., GOMIS, P., RUIZ, J. E., FERREIRA, D., MARTÍN-YEBRA, A. *et al.* ECG-based monitoring of blood potassium concentration: Periodic versus principal component as lead transformation for biomarker robustness. *Biomedical Signal Processing and Control*. 2021, 68, 102719.

[137] BUKHARI, H. A., SÁNCHEZ, C., RUIZ, J. E., POTSE, M., LAGUNA, P., and PUEYO, E. Monitoring of serum potassium and calcium levels in end-stage renal disease patients by ECG depolarization morphology analysis. *Sensors*. 2022, 22(8), 2951.

[138] BUKHARI, H. A., SÁNCHEZ, C., SRINIVASAN, S., PALMIERI, F., POTSE, M. *et al.* Estimation of potassium levels in hemodialysis patients by t wave nonlinear dynamics and morphology markers. *Computers in Biology and Medicine*. 2022, 143, 105304.

[139] POULIKAKOS, D. and MALIK, M. Challenges of ECG monitoring and ECG interpretation in dialysis units. *Journal of Electrocardiology*. 2016, 49(6), 855–859.

[140] WU, M., CHIANG, J., YANG, Y., CHAO, I., SHIEH, S. *et al.* Predicting hyperkalemia by a two-staged artificial neural network. In *Computers in Cardiology, 2003*. 2003, 433–435.

[141] TZENG, W., CHAN, Y., and HSIEH, J. Predicting hyperkalemia by the use of a 12-lead temporal-spatial electrocardiograph: clinical evaluations and model simulations. In *Computers in Cardiology, 2005*. IEEE, 2005. [Online]. Available: https://doi.org/10.1109/cic.2005.1588075

[142] LIN, C.-S., LIN, C., FANG, W.-H., HSU, C.-J., CHEN, S.-J. *et al.* A deep-learning algorithm (ECG12Net) for detecting hypokalemia and hyperkalemia by electrocardiography: Algorithm development. *JMIR Med. Inform.* 2020, 8(3), e15931.

[143] WEISS, J. N., QU, Z., and SHIVKUMAR, K. Electrophysiology of Hypokalemia and Hyperkalemia. *Circ Arrhythm Electrophysiol*. 2017, 10(3).

[144] YUSUF, A. A., HU, Y., SINGH, B., MENOYO, J. A., and WETMORE, J. B. Serum potassium levels and mortality in hemodialysis patients: A retrospective cohort study. *American Journal of Nephrology*. 2016, 44(3), 179–186.

[145] SANDLE, G. I., GAIGER, E., TAPSTER, S., and GOODSHIP, T. H. J. Evidence for large intestinal control of potassium homoeostasis in uraemic patients undergoing long-term dialysis. *Clinical Science*. 1987, 73(3), 247–252.

[146] GIEBISCH, G., KRAPF, R., and WAGNER, C. Renal and extrarenal regulation of potassium. *Kidney International*. 2007, 72(4), 397–410.

[147] PERL, J. and CHAN, C. T. Timing of sudden death relative to the hemodialysis procedure. *Nat Rev Nephrol*. 2006, 2(12), 668–669.

[148] CORREA, S., SCOVNER, K. M., TUMLIN, J. A., ROY-CHAUDHURY, P., KOPLAN, B. A. *et al.* Electrolyte changes in contemporary hemodialysis: A secondary analysis of the monitoring in dialysis study. *Kidney360*. 2021, 2(4), 695–707.

[149] RAFFEE, L. A., ALAWNEH, K. Z., ABABNEH, M. J., HIJAZI, H. H., ABDI, R. M. A. *et al.* Clinical and electrocardiogram presentations of patients with high serum potassium concentrations within emergency settings: a prospective study. *International Journal of Emergency Medicine*. 2022, 15(1).

[150] DIERCKS, D. B., SHUMAIK, G. M., HARRIGAN, R. A., BRADY, W. J., and CHAN, T. C. Electrocardiographic manifestations: electrolyte abnormalities. *The Journal of Emergency Medicine*. 2004, 27(2), 153–160.

[151] ORPHANIDOU, C., BONNICI, T., CHARLTON, P., CLIFTON, D., VALLANCE, D., and TARASSENKO, L. Signal quality indices for the electrocardiogram and photoplethysmogram: Derivation and applications to wireless monitoring. *IEEE Journal of Biomedical and Health Informatics*. 2015, 19(3), 832–8.

[152] RODRIGUES., A. S., PALIAKAITĖ., B., DAUKANTAS., S., SOLOŠENKO., A., PETRĖNAS., A., and MAROZAS., V. Personalized evaluation of life-threatening conditions in chronic kidney disease patients: The concept of wearable technology and case analysis. In *Proceedings of the 15th International Joint Conference on Biomedical Engineering Systems and Technologies - BIOSIGNALS,*. INSTICC. SciTePress, 2022, 244–250.

[153] VANDENBERK, B., VANDAEL, E., ROBYNS, T., VANDENBERGHE, J., GARWEG, C. *et al.* Which QT correction formulae to use for QT monitoring? *Journal of the American Heart Association*. 2016, 5(6).

[154] PILIA, N., NAGEL, C., LENIS, G., BECKER, S., DÖSSEL, O., and LOEWE, A. ECGdeli - an open source ECG delineation toolbox for MATLAB. *SoftwareX*. 2021, 13, 100639.

[155] SOLOŠENKO, A., PETRĖNAS, A., MAROZAS, V., and SÖRNMO, L. Modeling of the photoplethysmogram during atrial fibrillation. *Computers in Biology and Medicine*. 2017, 81, 130–138.

[156] M. HUOTARI, K. M., A. VEHKAOJA and KOSTAMOVAARA, J. Photoplethysmography and its detailed pulse waveform analysis for arterial stiffness. *Journal of Structural Mechanics*. 2011, 22(4), 345–362.

[157] ROMERO, D., RINGBORN, M., LAGUNA, P., and PUEYO, E. Detection and quantification of acute myocardial ischemia by morphologic evaluation of QRS changes by an angle-based method. *Journal of Electrocardiology*. 2013, 46(3), 204–214.

[158] ADAMS, M. G. and DREW, B. J. Body position effects on the ECG. *Journal of Electrocardiology*. 1997, 30(4), 285–291.

[159] SCHAEFER, T. J. and WOLFORD, R. W. Disorders of potassium. *Emergency Medicine Clinics of North America*. 2005, 23(3), 723–747.

[160] PASTORE, M. and CALCAGNÌ, A. Measuring distribution similarities between samples: A distribution-free overlapping index. *Frontiers in Psychology*. 2019, 10.

[161] BLUMBERG, A., ROSER, H., ZEHNDER, C., and MULLER-BRAND, J. Plasma potassium in patients with terminal renal failure during and after haemodialysis; relationship with dialytic potassium removal and total body potassium. *Nephrology Dialysis Transplantation*. 1997, 12(8), 1629–1634.

[162] SCHMIDT, S. T., DITTING, T., DEUTSCH, B., SCHUTTE, R., FRIEDRICH, S. *et al.* Circadian rhythm and day to day variability of serum potassium concentration: a pilot study. *Journal of Nephrology*. 2014, 28(2), 165–172.

[163] BADILINI, F., VAGLIO, M., DUBOIS, R., ROUSSEL, P., SARAPA, N. *et al.* Automatic analysis of cardiac repolarization morphology using gaussian mesa function modeling. *Journal of Electrocardiology*. 2008, 41(6), 588–594.

[164] CANDY, J. V. *Model-Based Signal Processing*. 1st ed. New Jersey: John Wiley & Sons, Inc., Hoboken, New Jersey, 2006.

[165] WILLIAMS, G. H., CAIN, J. P., DLUHY, R. G., and UNDERWOOD, R. H. Studies of the control of plasma aldosterone concentration in normal man. *Journal of Clinical Investigation*. 1972, 51(7), 1731–1742.

[166] PATNAIK, S. and LAI, Y. K. Just hypercalcaemia or acute ST elevation myocardial infarction? a review of hypercalcaemia-related electrocardiographic changes. *BMJ Case Reports*. 2015, bcr2015211177.

[167] MARTINEZ-VEA, A., BARDAJÍ, A., GARCIA, C., and OLIVER, J. A. Severe hyperkalemia with minimal electrocardiographic manifestations. *Journal of Electrocardiology*. 1999, 32(1), 45–49.

[168] HUBER, L. and GENNARI, F. J. Severe metabolic alkalosis in a hemodialysis patient. *American Journal of Kidney Diseases*. 2011, 58(1), 144–149.

[169] COE, F. L. Metabolic alkalosis. *JAMA: The Journal of the American Medical Association*. 1977, 238(21), 2288.

[170] MESA, M. H., PILIA, N., DÖSSEL, O., and LOEWE, A. Influence of ECG lead reduction techniques for extracellular potassium and calcium concentration estimation. *Current Directions in Biomedical Engineering*. 2019, 5(1), 69–72.

[171] LAMPERT, R. ECG signatures of psychological stress. *Journal of Electrocardiology*. 2015, 48(6), 1000–1005.

[172] AKHRAS, F. and RICKARDS, A. F. The relationship between QT interval and heart rate during physiological exercise and pacing. *Japanese Heart Journal*. 1981, 22(3), 345–351.

[173] BURTON, F. Dispersion of ventricular repolarization and refractory period. *Cardiovascular Research*. 2001, 50(1), 10–23.

[174] ACAR, B., YI, G., HNATKOVA, K., and MALIK, M. Spatial, temporal and wavefront direction characteristics of 12-lead t-wave morphology. *Medical & Biological Engineering & Computing*. 1999, 37(5), 574–584.

[175] CHEN, Y.-W. and JAIN, L. C., Eds. *Deep Learning in Healthcare*. Springer International Publishing, 2020.

[176] WU, M., LU, Y., YANG, W., and WONG, S. Y. A study on arrhythmia via ECG signal classification using the convolutional neural network. *Frontiers in Computational Neuroscience*. 2021, 14.

[177] HSIEH, C.-H., LI, Y.-S., HWANG, B.-J., and HSIAO, C.-H. Detection of atrial fibrillation using 1d convolutional neural network. *Sensors*. 2020, 20(7), 2136.

[178] HANNUN, A. Y., RAJPURKAR, P., HAGHPANAHI, M., TISON, G. H., BOURN, C. *et al.* Cardiologist-level arrhythmia detection and classification in ambulatory electrocardiograms using a deep neural network. *Nature Medicine*. 2019, 25(1), 65–69.

[179] CHANG, H.-Y., YEH, C.-Y., LEE, C.-T., and LIN, C.-C. A sleep apnea detection system based on a one-dimensional deep convolution neural network model using single-lead electrocardiogram. *Sensors*. 2020, 20(15), 4157.

[180] GRANDE-FIDALGO, A., CALPE, J., REDÓN, M., MILLÁN-NAVARRO, C., and SORIA-OLIVAS, E. Lead Reconstruction Using Artificial Neural Networks for Ambulatory ECG Acquisition. *Sensors (Basel, Switzerland)*. 2021, 21(16). [Online]. Available: https://pubmed.ncbi.nlm.nih.gov/34450984/

[181] SOHN, J., YANG, S., LEE, J., KU, Y., and KIM, H. C. Reconstruction of 12-lead electrocardiogram from a three-lead patch-type device using a LSTM network. *Sensors*. 2020, 20(11), 3278.

[182] WAGNER, P., STRODTHOFF, N., BOUSSELJOT, R. D., KREISELER, D., LUNZE, F. I. *et al.* PTB-XL, a large publicly available electrocardiography dataset. *Scientific Data*. 2020, 7(1).

[183] ACAR, B. and KOYMEN, H. SVD-based on-line exercise ECG signal orthogonalization. *IEEE Transactions on Biomedical Engineering*. 1999, 46(3), 311–321.

[184] YOUNG, W. J., VAN DUIJVENBODEN, S., RAMÍREZ, J., JONES, A., TINKER, A. *et al.* A method to minimise the impact of ECG marker inaccuracies on the spatial QRS-t angle: Evaluation on 1, 512 manually annotated ECGs. *Biomedical Signal Processing and Control*. 2021, 64, 102305.

[185] HNATKOVA, K., SEEGERS, J., BARTHEL, P., NOVOTNY, T., SMETANA, P. *et al.* Clinical value of different QRS-T angle expressions. *Europace*. 2018, 20(8), 1352–1361.

[186] LAGUNA, P., CORTÉS, J. P. M., and PUEYO, E. Techniques for ventricular repolarization instability assessment from the ecg. *Proceedings of the IEEE*. 2016, 104(2), 392–415.

[187] MIESZCZANSKA, H., PIETRASIK, G., PIOTROWICZ, K., MCNITT, S., MOSS, A. J., and ZAREBA, W. Gender-related differences in electrocardiographic parameters and their association with cardiac events in patients after myocardial infarction. *The American Journal of Cardiology*. 2008, 101(1), 20–24.

[188] SOTOBATA, I., RICHMAN, H., SIMONSON, E., and FUKOMOTO, A. Sex differences in the vectorcardiogram. *Circulation*. 1968, 37(3), 438–448.

[189] CHAUDHRY, S., MUTHURAJAH, J., LAU, K., and XIAO, H. B. The effect of ageing on the frontal QRS-t angle on the 12-lead ECG. *British Journal of Cardiology*. 2019.

[190] GOLDBERGER, A. L., AMARAL, L. A. N., GLASS, L., HAUSDORFF, J. M., IVANOV, P. C. *et al.* PhysioBank, PhysioToolkit, and PhysioNet. *Circulation*. 2000, 101(23).

[191] KLIGFIELD, P., GETTES, L. S., BAILEY, J. J., CHILDERS, R., DEAL, B. J. *et al.* Recommendations for the standardization and interpretation of the electrocardiogram. *Journal of the American College of Cardiology*. 2007, 49(10), 1109–1127.

[192] DILAVERIS, P., GIALAFOS, E., PANTAZIS, A., SYNETOS, A., TRIPOSKIADIS, F., and GIALAFOS, J. The spatial QRS-t angle as a marker of ventricular repolarisation in hypertension. *Journal of Human Hypertension*. 2000, 15(1), 63–70.

[193] AUGUSTAUSKAS, R., LIPNICKAS, A., and SURGAILIS, T. Segmentation of drilled holes in texture wooden furniture panels using deep neural network. *Sensors*. 2021, 21(11), 3633.

[194] AUGUSTAUSKAS, R. and LIPNICKAS, A. Pixel-level road pavement defects segmentation based on various loss functions. In *2021 11th IEEE International Conference on Intelligent Data Acquisition and Advanced Computing Systems: Technology and Applications (IDAACS)*. IEEE, 2021.

[195] MAHESHWARI, S., ACHARYYA, A., SCHIARITI, M., and PUDDU, P. E. Frank vectorcardiographic system from standard 12 lead ECG: An effort to enhance cardiovascular diagnosis. *Journal of Electrocardiology*. 2016, 49(2), 231–242.

[196] HALL, P. and HOROWITZ, J. A simple bootstrap method for constructing nonparametric confidence bands for functions. *The Annals of Statistics*. 2013, 41(4).

[197] EFRON, B. *The Jackknife, the Bootstrap and Other Resampling Plans*. Society for Industrial and Applied Mathematics, 1982.

[198] RIBEIRO, A. H., RIBEIRO, M. H., PAIXÃO, G. M. M., OLIVEIRA, D. M., GOMES, P. R. *et al.* Automatic diagnosis of the 12-lead ECG using a deep neural network. *Nature Communications*. 2020, 11(1).

[199] VONDRAK, J. and PENHAKER, M. Review of processing pathological vectorcardiographic records for the detection of heart disease. *Frontiers in Physiology*. 2022, 13.

[200] VOULGARI, C., PAGONI, S., TESFAYE, S., and TENTOLOURIS, N. The spatial QRS-t angle: Implications in clinical practice. *Current Cardiology Reviews*. 2013, 9(3), 197–210.

[201] ALIVECOR, I., KardiaMobile, 2022. accessed on: 2022-07-14. [Online]. Available: https://store.kardia.com/products/kardiamobil

[202] BACEVICIUS, J., ABRAMIKAS, Z., DVINELIS, E., AUDZIJONIENE, D., PETRYLAITE, M. *et al.* High specificity wearable device with photoplethysmography and six-lead electrocardiography for atrial fibrillation detection challenged by frequent premature contractions: Doublecheck-af. *Frontiers in Cardiovascular Medicine*. 2022, 9. [Online]. Available: https://www.frontiersin.org/article/10.3389/fcvm.2022.869730

[203] NIGUSSE, A. B., MENGISTIE, D. A., MALENGIER, B., TSEGHAI, G. B., and LANGENHOVE, L. V. Wearable smart textiles for long-term electrocardiography monitoring—a review. *Sensors*. 2021, 21(12), 4174.

[204] CORPORATION, B., Bittium OmegaSnap™ ECG Electrodes, 2022. accessed on: 2022-06-23. [Online]. Available: https://www.bittium.com/medical/bittium-ecg-electrodes

[205] PARTNERS, D., Viscero–ecg vest, 2022. accessed on: 2022-06-23. [Online]. Available: https://www.designpartners.com/projects/viscero-ecg-vest/

[206] JAIN, U., BUTCHY, A., LEASURE, M., COVALESKY, V., MCCORMICK, D., and MINTZ, G. 12-lead ECG reconstruction via combinatoric inclusion of fewer standard ECG leads with implications for lead information and significance. In *Proceedings of the 15th International Joint Conference on Biomedical Engineering Systems and Technologies*. SCITEPRESS - Science and Technology Publications, 2022.

[207] RIJNBEEK, P. R., KORS, J. A., and WITSENBURG, M. Minimum bandwidth requirements for recording of pediatric electrocardiograms. *Circulation*. 2001, 104(25), 3087–3090.

[208] BAI, Y., ZHANG, L., WAN, D., XIE, Y., and DENG, H. Detection of sleep apnea syndrome by CNN based on ECG. *Journal of Physics: Conference Series*. 2021, 1757(1), 012043.

[209] ABDOU, A. and KRISHNAN, S. Horizons in single-lead ECG analysis from devices to data. *Frontiers in Signal Processing*. 2022, 2.

[210] JAROSZYŃSKI, A., SCHLEGEL, T. T., MOSIEWICZ, J., STĘPIEŃ, R., and DĄBROWSKI, W. Heat shock protein 27 levels predict myocardial inhomogeneities in hemodialysis patients. *Mediators of Inflammation*. 2022, 2022, 1–6.

[211] JAROSZYNSKI, A., WYSOKINSKI, A., BEDNAREK-SKUBLEWSKA, A., GLOWNIAK, A., KSIAZEK, P. *et al.* The effect of a single dialysis session on spatial QRS-t angle in haemodialysis patients. *Nephrology Dialysis Transplantation*. 2010, 25(11), 3723–3729.

[212] LIPTON, J. A., NELWAN, S. P., VAN DOMBURG, R. T., KORS, J. A., ELHENDY, A. *et al.* Abnormal spatial QRS-t angle predicts mortality in patients undergoing dobutamine stress echocardiography for suspected coronary artery disease. *Coronary Artery Disease*. 2010, 21(1), 26–32.

[213] SWEDA, R., SABTI, Z., STREBEL, I., KOZHUHAROV, N., WUSSLER, D. *et al.* Diagnostic and prognostic values of the QRS-t angle in patients with suspected acute decompensated heart failure. *ESC Heart Failure*. 2020, 7(4), 1817–1829.

[214] BORLEFFS, C. J. W., SCHERPTONG, R. W., MAN, S.-C., VAN WELSENES, G. H., BAX, J. J. *et al.* Predicting ventricular arrhythmias in patients with ischemic heart disease. *Circulation: Arrhythmia and Electrophysiology*. 2009, 2(5), 548–554.

[215] LAGERHOLM, M., PETERSON, C., BRACCINI, G., EDENBRANDT, L., and SORNMO, L. Clustering ECG complexes using hermite functions and self-organizing maps. *IEEE Transactions on Biomedical Engineering*. 2000, 47(7), 838–848.

[216] KIRANYAZ, S., INCE, T., PULKKINEN, J., and GABBOUJ, M. Personalized long-term ECG classification: A systematic approach. *Expert Systems with Applications*. 2011, 38(4), 3220–3226.

[217] LIN, C.-Y., LIN, L.-Y., and CHEN, P.-C. Analysis of t-wave morphology from the 12-lead electrocardiogram for prediction of long-term prognosis in patients initiating haemodialysis. *Nephrology Dialysis Transplantation*. 2007, 22(9), 2645–2652.

[218] MOODY, G. B. and MARK, R. G. The impact of the MIT-BIH arrhythmia database. *IEEE Eng. Med. Biol. Mag.* 2001, 20(3), 45–50.

[219] DALL'OLIO, L., CURTI, N., REMONDINI, D., HARB, Y. S., ASSELBERGS, F. W. *et al.* Prediction of vascular aging based on smartphone acquired PPG signals. *Scientific Reports*. 2020, 10(1).

[220] BATISTA, G. E. A. P. A., KEOGH, E. J., TATAW, O. M., and DE SOUZA, V. M. A. CID: an efficient complexity-invariant distance for time series. *Data Mining and Knowledge Discovery*. 2013, 28(3), 634–669.

[221] LIU, Y., LI, Z., XIONG, H., GAO, X., and WU, J. Understanding of internal clustering validation measures. In *2010 IEEE International Conference on Data Mining*. IEEE, 2010.

CURRICULUM VITAE

Ana Rita Alves dos Santos Rodrigues
ana.rodrigues@ktu.lt

Education:

2011–2015	BSc in Bioengineering, Faculty of Engineering of University of Porto
2015–2017	MSc in Biomedical Engineering, Kaunas University of Technology
2017–Now	Ph.D. candidate in Electrical and Electronics Engineering, Kaunas University of Technology

Professional experience:

2015–2016	Algorithm Engineer, Stream4s
2016–2017	Product Manager, Insoft Services
2017–2019	Curator, Health Horizon, Pty Ltd
2018–2022	Assistant Lecturer at the Department of Electronics Engineering, Kaunas University of Technology
2018–Now	Junior Researcher at the Biomedical Engineering Institute, Kaunas University of Technology
2023–Now	Lecturer at the Department of Electronics Engineering, Kaunas University of Technology

Areas of research interest:

Personalized Medicine, Cardiology, Machine Learning, Wearable Devices, Data Mining, Deep Learning for Cardiovascular Research, Biomedical Signal Processing, Unobtrusive Parameters of Homeostasis, and Electrophysiology.

The list of scientific papers and conferences related to the topic of the dissertation is given below.

LIST OF PUBLICATIONS ON THE DOCTORAL THESIS SUBJECT

Publications in the journals referred in the *Clarivate Analytics Web of Science* database with impact factor

1. **Santos Rodrigues, Ana**; Petrėnas, Andrius; Paliakaitė, Birutė; Kušleikaitė-Pere, Neda; Jaruševičius, Gediminas; Bumblytė, Inga Arūnė; Laguna, Pablo; Marozas, Vaidotas. Noninvasive monitoring of potassium fluctuations during the long interdialytic interval. *IEEE Access*. 2020, vol. 8, p. 188488–188502. [IF 3.367; Q1 2020].

2. **Santos Rodrigues, Ana**; Augustauskas, Rytis; Lukoševičius, Mantas; Laguna, Pablo; Marozas, Vaidotas. Deep-learning-based estimation of the spatial QRS-T angle from reduced-lead ECGs. *Sensors*. 2022, vol. 22, iss. 14, art. no. 5414, p. 1–22. [IF: 3.847; Q1 2021].

Publications referred in the *Clarivate Analytics Web of Science* database without impact factor

1. **Rodrigues, Ana**; Marozas, Vaidotas; Daukantas, Saulius; Kušleikaitė-Pere, Neda; Štramaitytė, Irmantė; Bumblytė, Inga Arūnė; Kaldoudi, Eleni. Differences between model-based electrocardiogram T wave features before and after haemodialysis. In *Proceedings of IEEE biomedical circuits and systems conference (BioCAS)*. 2017, p. 148–151.

2. **Rodrigues, Ana**; Petrėnas, Andrius; Kušleikaitė-Pere, Neda; Laguna, Pablo; Marozas, Vaidotas. ECG-based monitoring of electrolyte fluctuations during the long interdialytic interval. In *Proceedings of 2018 Computing in Cardiology Conference (CinC)*. 2018, vol. 45, p. 1–4.

3. **Santos Rodrigues, Ana**; Lukoševičius, Mantas; Marozas, Vaidotas. A fast algorithm for facilitating heartbeat annotation in long-term ECG signals. In *Proceedings of 2021 Computing in Cardiology Conference (CinC)*. 2021, p. 1–4.

4. **Santos Rodrigues, Ana**; Paliakaitė, Birutė; Daukantas, Saulius; Sološenko, Andrius; Petrėnas, Andrius; Marozas, Vaidotas. Personalized Evaluation of Life-Threatening Conditions in Chronic Kidney Disease Patients: The Concept of Wearable Technology and Case Analysis. In *Proceedings of 15th International Joint Conference on Biomedical Engineering Systems and Technologies (BIOSTEC 2022)*. 2022, p. 244–250.

Conference presentation abstracts

1. **Rodrigues, Ana**; Petrėnas, Andrius; Kušleikaitė-Pere, Neda; Marozas, Vaidotas. Hemodialize gydomų pacientų elektrolitų fluktuacijų stebėsena dėvimu prietaisu. In *Fizinių ir technologijos mokslų tarpdalykiniai tyrimai: 9-oji jaunųjų mokslininkų konferencija*. 2019, p. 24.

List of attended conferences

1. **Rodrigues, Ana**; Petrėnas, Andrius; Kušleikaitė-Pere, Neda; Laguna, Pablo; Marozas, Vaidotas. ECG-based monitoring of electrolyte fluctuations during the long interdialytic interval. *Conference on Computing in cardiology (CinC)*: September 23–26, 2018, Maastricht, Netherlands.

2. **Santos Rodrigues, Ana**; Lukoševičius, Mantas; Marozas, Vaidotas. A fast algorithm for facilitating heartbeat annotation in long-term ECG signals. *Conference on Computing in cardiology (CinC)*: September 12–15, 2021, Brno, Czech Republic.

3. **Santos Rodrigues, Ana**; Paliakaitė, Birutė; Daukantas, Saulius; Sološenko, Andrius; Petrėnas, Andrius; Marozas, Vaidotas. Personalized Evaluation of Life-Threatening Conditions in Chronic Kidney Disease Patients: The Concept of Wearable Technology and Case Analysis. *15th International Joint Conference on Biomedical Engineering Systems and Technologies (BIOSTEC 2022)*: February 9–11, 2022.

ACKNOWLEDGMENTS

Time flew, and it seems that it was only yesterday that I was a scared, freshly-graduate girl who wrapped herself in a trepidatious adventure. Rick Riordan wrote in *The Lost Hero* that *"there is nothing like ADHD and a good fight to the death to make time fly,"* and Dear Lord, how right he is. Amidst two medically-diagnosed burnouts, a pandemic, and a late auDHD diagnosis (comorbid autism and ADHD), here is my entirely written doctoral dissertation. It only took me six years to get it done instead of the typical four. Honestly, I often felt embarrassed for taking so long and believed my work was not nearly as good as my fellow peers, perceiving myself as infinitesimally small in comparison. In all fairness, I am only 164 cm, which is borderline dwarfism by Lithuanian standards, and it took me 30 years to get diagnosed with a neurodevelopment disorder. So I suppose six years is not so bad in retrospect.

As a child, my mother used to call me '*choramingona*,' which roughly translates to 'little miss crybaby.' I did (and still do) often cry due to the unbearing frustrations and difficulties I experienced that other people easily labeled as lazy, quirky, or dramatic. Over the past year, I've slowly learned to embrace those traits as advantages and realized that *too challenging* and *too ambitious* are two adjectives that do not suffice to deter me from achieving my goals. I proudly state this in the last section of my thesis: *Little Miss crying but won't stop trying!*

Nevertheless, I am surrounded by people who have accompanied me in my journey over the last six years and deserve their well-due recognition. First and foremost, quoting the wise words of the great poet Snoop Dogg: "I wanna thank me. [...] I wanna thank me for doing all this hard work. [...] I wanna thank me for never quitting." Wise words, indeed.

Secondly, I'd like to thank my supervisor, Prof. Dr. Vaidotas Marozas, who endured my frustrations, overthinking, and many tears but gave me this opportunity six years ago, and that means the world. I hope I made you proud and that we both made each other better people throughout this journey.

To my fiance Rytis, or my *ambulatory pagalvė* as I affectionately call him, who held my hand and never left my side. I can't wait for us to become Dr. & Dr. Rodrigues-Augustauskai. To our furry girls, Maja and Mija, who warmed my legs (and heart) in the many days I've worked from home.

To my lovely birds, Dalia, Fallon, Samara, and Viktorija, who are just beautiful people, take me to eat pancakes and drink milkshakes and let me vent relentlessly about data collection, thesis template, and any other issue. They are my biggest cheerleaders.

To my friends, Diogo and Miguel, who, along with me, form arguably the best trio to ever study at the Faculty of Engineering of the University of Porto. Some—if not all—of my happiest moments whilst at the university are with you. During the pandemic, you introduced me to Alexandra and Miguel (another one, they multiply fast!),

who made working from home a more pleasant experience, continuously supported me, and gave me endless laughs. Together with João, our friendship is utter chaos, and I'd not have it any other way.

To my friend Marta Rocha who helped me get diagnosed and has been with me along this journey of unmasking my neurodivergence.

To my iron sister Marta Lopes who shares my passion for sports and constantly reminds me how Ph.D. stress affects my training. Also, thank you for letting me vent whenever someone walks before me while I squat.

To my coach, Arnas, who has shaped me into being physically and mentally stronger and, for whatever reason, sees potential in me that everyone else seems to miss, including myself. He trained me to represent Portugal in the 2022 European Powerlifting Championships amidst the Ph.D. stress, an achievement of his own brilliance. I hope I made you proud too.

To Daivaras, my forever lunch-buddy and in-house translator who smooths my workflow at the Institute. To all my colleagues, Andrius R., who enjoys writing last-minute grant proposals with me. Andrius P., who looks out for all of us, always. To Birutė, who is a kindred spirit that lights any room she walks in. To Mantas for allowing me to be myself in our shared office. To Mohammad, who is genuinely kind and fun. To Monika, Vilma, Andrius S., and the rest of the top-notch team with whom I have the pleasure of working at the Biomedical Engineering Institute.

Last but not least, a massive thank you to my sister and parents, who love me unconditionally and have been and will forever be with me every step of the way.

I sincerely adore you all.

UDK 616.15+616.12-008.318+621.317.75](043.3)

SL 344. 2023-07-27, 24,25 leidyb. apsk. l. Tiražas 14 egz. Užsakymas 133.
Išleido Kauno technologijos universitetas, K. Donelaičio g. 73, 44249 Kaunas
Spausdino leidyklos „Technologija“ spaustuvė, Studentų g. 54, 51424 Kaunas